Phase separation in lipid-based nanoparticles: exploring the nano-bio interface

Papadopoulou, P.

Phase Separation in Lipid-based Nanoparticles

Exploring the nano-bio interface

Proefschrift

ter verkrijging van

de graad van doctor aan de Universiteit Leiden,

op gezag van rector magnificus prof.dr.ir. H. Bijl,

volgens besluit van het college voor promoties

te verdedigen op dinsdag 7 november 2023

klokke 16.15 uur

door

Panagiota Papadopoulou

geboren te Athene, Griekenland

in 1990

Promotor
Prof. dr. A. Kros
Co-promotor
Prof. dr. ir. J.S.T. van Noort

Promotiecomissie

Prof. dr. M. Ubbink
Prof. dr. S. Bonnet
Dr. L. Akkari (Netherlands Cancer Institute)
Prof. dr. N.A.J.M Sommerdijk (Radboud University Medical Center)
Dr. T. H. Sharp (Leiden University Medical Center)

This Ph.D. thesis was funded by the 2017 Leiden/Huygens Fellowship prize. Printing of this thesis was funded by the Nederlandse Vereniging voor Microscopie (NVvM, microscopy.nl) and by the Leiden University Library. Printed by Ipskamp printing.

Cover design: Marta Paula Tychoniec

About the cover: the back cover depicts the circle that contains all human knowledge. During a Ph.D. program one will reach the edge of human knowledge and will push at the boundaries. Eventually the boundary will give way and there will be a small dent at the circle. This dent represents the acquired knowledge. The three small circles represent the future knowledge that is yet to be acquired to advance a scientific field even further. Front cover adapts this concept to a phase-separated liposome and three RNA-LNPs.
Inspired by "The illustrated guide to a PhD" by Matt Might.

"Breathe life into that ember of passion and curiosity within you"

To Andy, for helping me find my spark
and
To Iró, for setting it on fire

Table of Contents

CHAPTER 1

Introduction to phase separation in lipid-based nanoparticles: exploring the nano-bio interface

Parts of this chapter were used for the review article:

Escalona Rayo, O.[#]; **Papadopoulou, P.**[#]; Slutter, B.; Kros, A.* Biological recognition and cellular trafficking of targeted RNA-lipid nanoparticles. Current Opinion in Biotechnology 2023.

# denotes equal contribution
under revision

"There is plenty of room at the bottom" - Richard Feynman, 1959

1.1 Nanotechnology in life sciences

Nanotechnology (from the Greek νανοτεχνολογία: νάνο, lit. 'dwarf', -τέχνη, lit. 'craft, art' and -λογία, lit. 'study, knowledge') is a multidisciplinary field that involves the engineering of materials at the nanoscale level, typically ranging from 1 to 100 nanometers (nm). At this scale, materials exhibit unique properties attributed to surface and quantum effects, that differ from those from the bulk scales allowing for the development of novel materials, devices, and systems. Richard Feynman is considered the father of Nanotechnology, as he was the first to introduce the concept of manipulating matter even at an atomic level. In an iconic presentation with the title "There is plenty room at the bottom" Richard Feynman suggested the concept of scaling down bulk materials, such as copying the whole encyclopedia in the size of a headpin.[1] Ever since, several pioneers established the term and field of Nanotechnology. Importantly, nanotechnology is an emerging field for several biomedical applications in life sciences, including therapeutics, diagnostics, theranostics, imaging, regenerative medicine, and tissue engineering.

1.2 Nanotechnology in medicine

Nanoparticles as Drug Delivery systems

Nanomedicine is the field of medicine which employs nanotechnology, mainly as a drug delivery system or as a tool in photothermal therapy. Nanomedicines have been proposed to be beneficial as drug delivery systems for several reasons. Firstly, nanoparticles offer the advantage of increasing the solubility of poorly soluble drugs and protecting sensitive cargo from degradation. Additionally, nanoparticles allow for the slow controlled release of drugs, enabling sustained drug delivery and lowering the required drug dose and frequency. Therapeutics delivered using nanoparticles typically have different biodistribution, pharmacodynamics and pharmacokinetics compared to the free drug. Nanoparticle-based therapeutics also have reduced toxicity, improved bioavailability and drug half-life, and sometimes

the ability to cross biological and cellular barriers enabling drugs to reach difficult, inaccessible targets. Additionally, a desired concept around nanomedicines is targeted drug delivery, which proposes nanoparticles to act as "magic bullets", targeting predominantly specific (diseased) tissues or cells, while leaving other (healthy) tissues unaffected.[2] By delivering medicines directly to the desired site, the therapeutic window is increased and off-target effects are minimized, leading to better outcomes, a reduced required dose, and fewer adverse side effects. Targeted nanomedicine will be extensively discussed in a separate section.

1.3 Nanoparticle design

Nanoparticles used in life sciences consist of inorganic, organic or hybrid materials. Inorganic nanoparticles based on gold, silver, iron oxide or others – such as quantum dots – have unique plasmonic, magnetic and electronic properties influenced by their shape and size.[3–5] Inorganic nanoparticles are employed in drug delivery, however their properties mostly render them attractive for imaging, diagnosis and photothermal therapies, *i.e.,* photodynamic therapy and hyperthermia. In contrast, organic nanoparticles show the biggest potential in drug delivery, due to their high drug encapsulation capacity and biocompatibility. Organic nanoparticles can be divided in lipid-based, polymer-based, carbon and hybrid (*i.e.,* lipid-polymer, lipopeptide-based)[6] (**Figure 1a**). Additionally, bio-mimetic or bio-derived materials such as virus-like particles (VLPs),[7] extracellular vesicles (EVs),[8] or apolipoprotein-based nanomaterials,[9] are studied as drug delivery systems. Different nanocarrier designs – *i.e.,* micellar, disc, sphere, fiber – are suitable for specific therapeutic cargo encapsulation depending on cargo properties – *i.e.,* size, hydrophobicity, charge –. Therapeutic cargos can be small molecule drugs, nucleic acid-based therapeutics, or protein/peptide based (**Figure 1b**).[10] Additionally, surface coating on nanocarriers with a small amount of the polymer polyethylene glycol (PEG) is a common strategy for stabilization and prevention of opsonization and rapid nanoparticle clearance.[11,12] Other surface functionalities – *i.e.,* antibodies, cell-penetrating peptides, sugar moieties – are utilized to enhance the therapeutic potential by mainly recognizing cell receptors and promoting active cell targeting (**Figure 1c**).

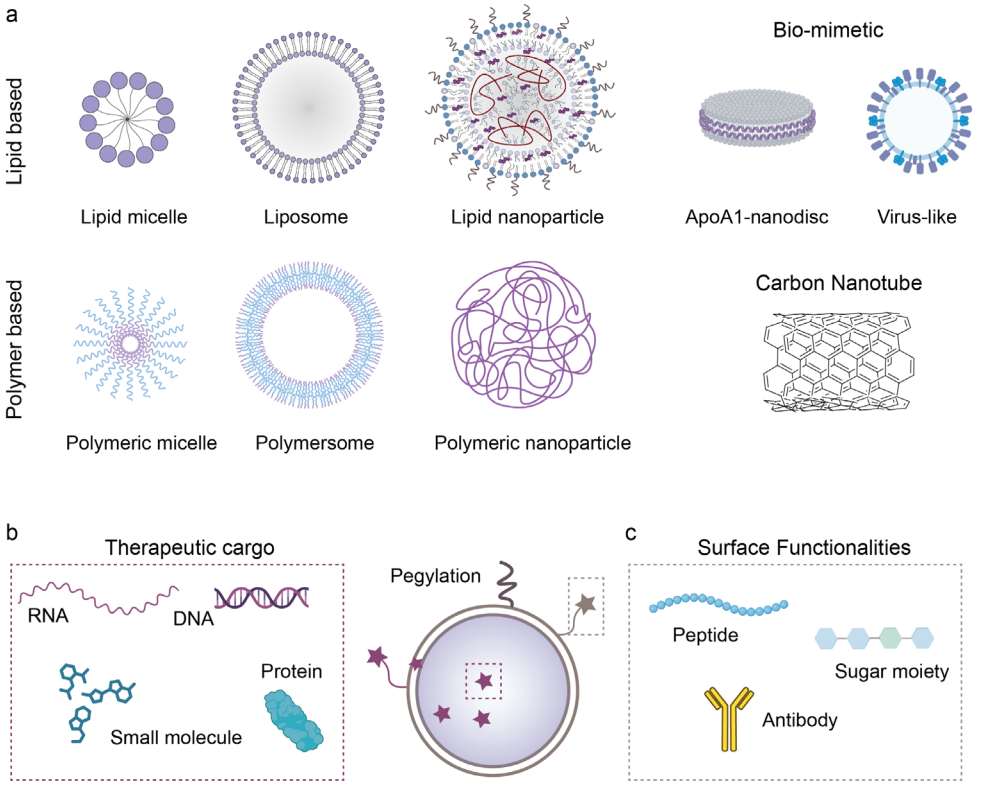

Figure 1. A selection of organic-based nanoparticle designs. a) Depending on the component they mainly consist of, organic-based nanoparticles can be lipid-based (*e.g.,* micelles, liposomes, lipid nanoparticles), polymer-based (*e.g.,* polymeric micelles, polymersomes, polymeric nanoparticles) or lipid-polymer hybrids, biomimetic nanoparticles (*e.g.,* apolipoprotein-based nanodiscs or virus-like particles) and carbon-based (*e.g.,* carbon nanotubes). **b)** Therapeutic cargos usually incorporated in drug nanocarriers are small molecule drugs, nucleic-acid therapeutics and protein/peptide-based therapeutics. **c)** Surface modification of nanoparticle designs are mainly employed for stability (*e.g.,* PEGylation) or targeted performance (*e.g.,* antibodies, sugar moieties and peptides). Polymer based and biomimetic nanoparticle cartoons, therapeutic cargo and surface functionalities cartoons were adapted from Biorender.

1.4 Lipid-based nanoparticles

General description and properties

Lipids are naturally derived molecules which constitute cell membranes and organelles, but are also utilized in energy storage and signaling.[13] Being amphiphilic, lipids self-assemble in physiological environments to create nano- or microstructures. Controlling the natural self-assembly of lipids with various nanofabrication methods (*e.g.*, extrusion, nanoprecipitation, microfluidic mixing) leads to nanomaterials with tunable size and morphology. Due to their biocompatibility, lipid-based nanoparticles typically exhibit low toxicity rendering them suitable as drug carriers. Main lipid classes which can be used for the assembly of lipid-based nanoparticles are phospholipids, sterol lipids, sphingolipids – or other non-phosphate containing lipids *i.e.,* natural diacylglycerols (DAGs) – and synthetic lipids, such as ionizable (amino)lipids (**Figure 2**). Lipid-based nanoparticles are typically in the range of ~20-500 nm in size and can be characterized by i) microscopy techniques – mainly cryo-transmission electron microscopy (cryo-TEM) – for size distribution and morphology, ii) dynamic light scattering (DLS) for size and colloidal stability, and iii) zeta potential measurements for surface charge.[14–18] These physicochemical properties should be the minimum reported on nanoparticle characterization.[19,20]

Nanoparticle complexity in assembly and lipid arrangement is dependent on the number of individual lipid components. One or two-component lipid-based systems usually result in simple liposomal or micellar assemblies. Multicomponent systems exert more intricate morphologies and properties. In general, due to the large variety of all individual lipid components and their combinations, lipid-based nanoparticles are endlessly tunable. A plethora of nanoparticle formulations with different physicochemical properties can be generated, designed to exert specific properties.[21] For example, saturated lipids usually have a high transition temperature (typically ~30-80 °C), therefore these lipids exist in a liquid ordered (gel) phase (L_o) at room or body temperature. This physicochemical property induces tight packing and stiffness in lipid membranes.

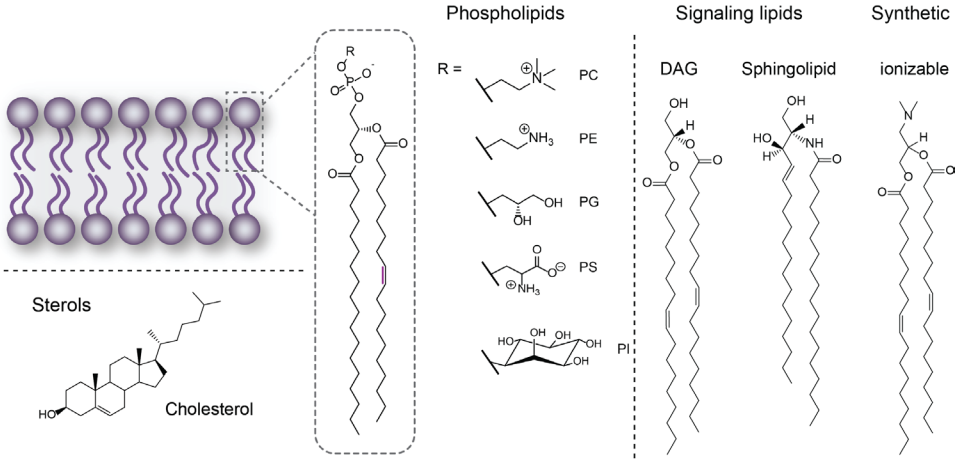

Figure 2. Main lipid classes used in lipid-based nanoparticles. Phospholipids are one of the main lipid components in cell membranes, as they naturally self-assemble into a lipid bilayer. The phospholipid's acyl chains can be i) short, medium or long depending on the number of carbons, and ii) saturated or mono, di- and polyunsaturated depending on double bonds. Their hydrophilic domain consists of a phosphate group along with a polar headgroup – usually a choline, ethanolamine, glycerol and others –. Additional lipids that can be used for lipid-based nanoparticle designs are sterols (*i.e.,* cholesterol), signaling lipids (*i.e.,* diacylglycerols and sphingolipids) or synthetic non-natural lipids (*i.e.,* ionizable lipids). Abbreviations: PC = phosphatidylcholine, PE = phosphatidylethanolamine, PG = phosphatidylglycerol, PS = phosphatidylserine, PI = phosphatidylinositol, DAG = diacylglycerol.

In contrast, unsaturated lipids form more fluid assemblies existing in liquid disordered phase (L_d), giving fluidity on the lipid membrane (**Figure 3a)**. Additionally, for all lipids, polar head groups can be zwitterionic, anionic, or cationic therefore different net surface charge can be presented on the nanoparticle (**Figure 3b**). Lipids also display polymorphism, a biophysical property which gives the ability of lipid systems to exist in various phases depending on lipid geometry (**Figure 3c)**.[22] Lipids with a cylindrical geometry, such as phosphatidylcholines (*i.e.,* both hydrophobic and hydrophilic domains are of similar size) prefer a planar bilayer assembly. In contrast, conical lipids, such as phosphatidylethanolamines (*i.e.,* their polar head group is smaller than the acyl chains) create non-bilayer inverted phases some of which are crystalline *i.e.*, inverse hexagonal (H_{II}) or cubic. Finally, inverse conical lipids, such as lysophosphatidylcholines (*i.e.,* their polar

head group is larger than the acyl chains) induce micellar phases. Conical and inverted conical lipids, when mixed with phospholipids, can respectively decrease, or increase the spontaneous membrane curvature of bilayers (**Figure 3d**).

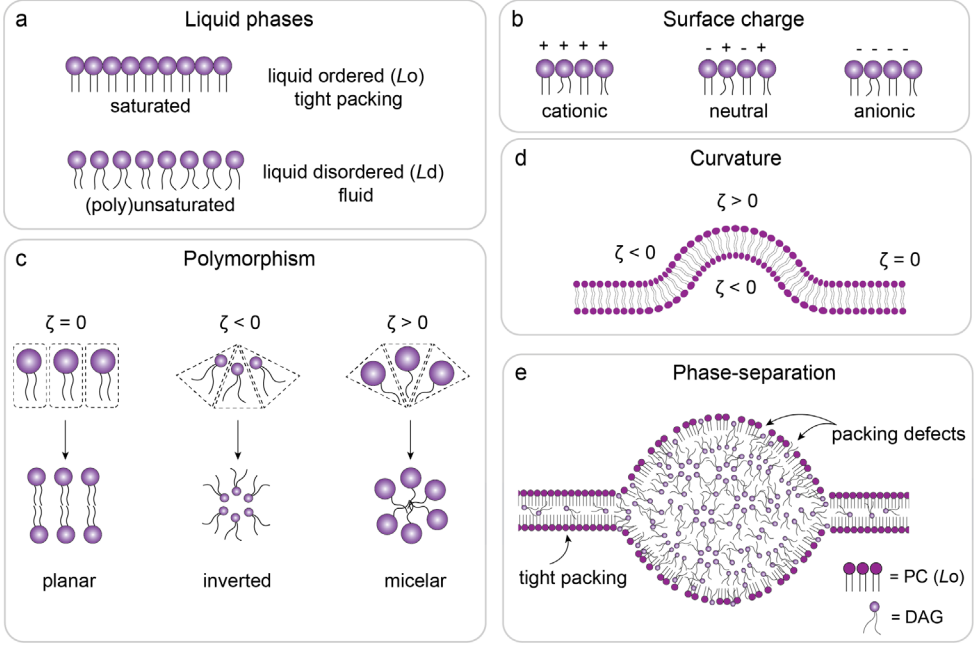

Figure 3. Lipid and membrane properties influencing nanoparticle properties. a) Liquid phases in lipid membranes depend on the degree of (un)saturation and length of individual lipids. Saturated lipids result in tightly packed lipid membranes existing in the liquid ordered phase (L_o). Unsaturated lipids result in a liquid disordered (L_d) phase, making the lipid membranes more fluid. **b)** Net surface charge of nanoparticles (cationic, neutral, anionic) depends on individual lipid charge (cationic, zwitterionic, anionic). **c)** Lipid polymorphism leads to lipid assemblies with various phases and morphologies. Cylindrical lipids tend to assemble in planar bilayers, while conical or inverted conical lipids tend to assemble in inverted or micellar phases, respectively. **d)** Membrane curvature as influenced by lipid polymorphism. **e)** Lipid phase-separation as described when DAGs exceed the miscibility threshold within lipid bilayers. Tight packing of phospholipids – especially of those existing in L_o phase – is impaired and lipid packing defects emerge. Abbreviations: ζ = membrane curvature, PC = phosphatidylcholine, L_o = liquid ordered phase, DAG = diacylglycerol.

DAGs as potential lipid components in lipid based nanoparticles

DAGs are endogenous conical lipids mostly found in cell membranes and lipoproteins, and due to their small polar headgroup and hydrophobicity they embed in lipid bilayers, avoiding exposure to the surrounding environment. [23,24] Upon the miscibility threshold within the lamellar bilayer, DAGs tend to induce distinct, non-bilayer phases within the phospholipid leaflet, resulting in lipid phase separation (**Figure 3e**).[25–28] This phenomenon increases the spacing between adjacent phospholipid headgroups in a lipid membrane, an effect that is amplified by membrane curvature – especially for membranes in L_o phase where high curvature is unfavorable.[29–31] The transient areas resulting from such packing frustrations exposing the apolar domain of the lipid membrane, are known as lipid packing defects.[32] Therefore, the distance between adjacent phospholipids is increased and tight packing is impaired, leaving DAGs exposed to the surrounding environment (**Figure 3e**). Some membrane peripheral proteins have been proposed to rely on these hydrophobic lipid packing defects, – generally caused by factors such as phase separation, lateral tension, or membrane curvature – for membrane binding and activation.[31,33–36]

In cell membranes, DAGs are metabolite products from the hydrolysis of the phospholipid phosphatidylinositol (PI). Their local accumulation in the membrane induces non-bilayer phases potentiating the recruitment and enzymatic activation of Protein Kinase C, which further controls functions of other proteins.[24,37–39] The toxin Equinatoxin-II28 and several lipases also sense DAG-induced phase separation and packing defects, which facilitate membrane binding and subsequent endogenous activity.[40–42] Additionally to their signaling and protein recruitment properties, DAGs act as fusogens due to their ability to increase the negative curvature of lipid membranes. As conical lipids, DAGs have the propensity and ability to induce inverted liquid crystalline phases, especially hexagonal and cubic phases, which contribute to membrane fusion.[43–46]

Finally, DAGs have been found to be main lipoprotein components, especially of high-density lipoproteins (HDLs).[23,47] DAGs, but also triglycerides (TGs) and cholesteryl esters (CEs), are transported in the form of solid lipoprotein particles via endogenous pathways responsible for lipid transport and metabolism.

In summary, DAGs are involved in several biological phenomena, including membrane phase separation, fusion, protein recruitment and communication, signaling, and lipid metabolism. Therefore, DAGs are potentially interesting lipid components for lipid-based nanomedicines, but surprisingly have hardly been studied in depth.[48,49] Fusogenic lipid-based nanoparticles have been proposed to enhance the efficient delivery of therapeutics into cells.[50–52] The same has been proposed for phase-separation.[52–54] Specific nanoparticle-protein communications could be exploited for targeting nanoparticle delivery and signaling could be used for therapeutic purposes.

Evolution of lipid-based nanoparticles

Liposomes are considered the earliest form of lipid-based nanoparticles (**Figure 4a**). They were discovered in the early 1960s, when lipid membrane vesicular assemblies were found to spontaneously form in water.[55,56] Initially, liposomes were used as model membranes to study biological mechanisms including ion transport, fusion and drug-membrane interactions.[57,58] However it became apparent that liposomes could be used to entrap drugs and their potential as drug delivery platforms was established.[59,60] Already by the early 1970s, liposomes were being tested as drug delivery carriers, showing their potential in enzyme entrapment and prevention of immunological reactions.[59,61–63] Later, *in vivo* biodistribution studies revealed their rapid clearance from blood circulation, however further studies showed that their size and unilamellarity, as well as composition and charge, can be tuned to generate liposomes with longer circulation lifetimes.[64–66] Moreover, the addition of cholesterol, as well as PEGylation, increased liposome circulation.[67,68] Almost three decades after their discovery, the first liposomal drug formulations were approved for clinical use (**Table 1**). Examples include the liposomal form of amphotericin B – with the trade name Ambisome® – used to treat severe fungal infections, and the liposomal form of doxorubicin – with the trade name Doxil®/Caelyx® – used for the treatment of several cancer types.

Table 1. A selection of lipid-based nanoparticle therapeutics approved by FDA and/or EMA.[69,70]

Year	Brand name	Formulation	Lipid Composition	Active ingredient	Indication for use
1997	AmBisome®	Liposome	HSPC, DSPG, CHO (2:0.8:1)	amphotericin B	fungal infections
1995	Abelcet®	Liposome	DMPC, DMPG (7:3)	amphotericin B	fungal infections
2021	Comirnaty®	mRNA-LNP	DSPC, CHO, ALC-0315, ALC-0159	tozinameran	vaccine against SARS-CoV-2
1995	Doxil®/Caelyx®	Liposome	HSPC, CHO, DSPE-PEG (5.6:3.9:0.5)	doxorubicin	Kaposi's sarcoma, breast cancer
1996	DaunoXome®	Liposome	DSPC, CHO (2:1)	doxorubicin	Kaposi's sarcoma
2012	Marquibo®	Liposome	Sphyngomyelin, CHO (6:4)	vincristine	acute lymphoblastic leukemia
2009	Mepact®	Liposome	DOPC, DOPS (3:7)	mifamurtide	Osteosarcoma
2000	Myocet®	Liposome	EPC: CHO (5.5:4.5)	doxorubicin	breast cancer
2018	Onpattro®	RNAi-LNP	DSPC, CHO, DLin-MC3-DMA, DMG-PEG2k	patisiran	hATTR amyloidosis
2021	Spikevax®	mRNA-LNP	DSPC, CHO, SM-102, DMG-PEG2k	elasomeran	vaccine against SARS-CoV-2
2000	Visudyne®	Liposome	EPG, DMPC (3:5)	verteporphin	macular degeneration

Abbreviations in Table 1: FDA = Food and Drug Administration, EMA = European Medicines Agency, CHO = cholesterol, HSPC = hydrogenated phosphatidylcholine (soy), DSPG = distearoyl-phospatidylglycerol, DMPC = dimyristoyl-phosphatidylcholine, DMPG = dimyristoyl-phosphatidylglycerol, DSPE-PEG = distearoyl-phosphoethanolamine-polyethylene glycol, DSPC = distearoyl-phospatidylcholine, DOPC = dioleoyl-phospatidylcholine, DOPS = dioleoyl-phospatidylserine, EPC = phospatidylcholine (egg), EPG = phospatidylglycerol (egg), DMG-PEG2k = dimyristoyl-glycerol-polyethylene glycol-2000.

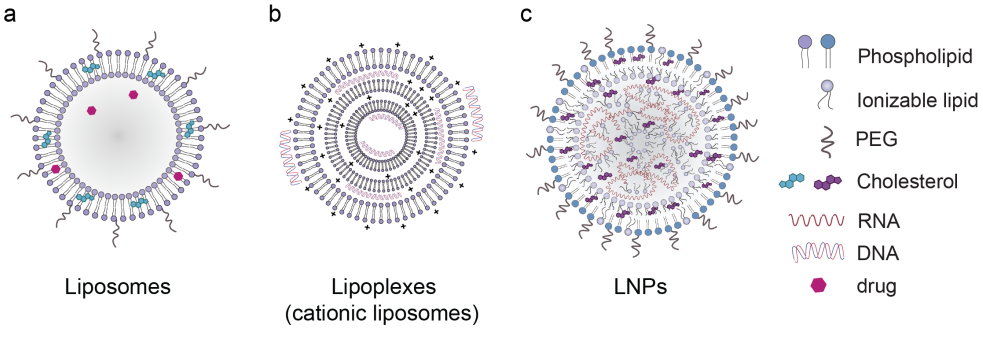

Figure 4. Evolution of lipid-based nanoparticles. a) Liposomes are the first lipid-based nanoparticles developed to mainly entrap small molecule drugs. They are usually spherical, consisting of a phospholipid bilayer and their properties can be tuned by lipid composition and addition of cholesterol or PEGylation. **b)** Cationic liposomes were extensively studied in the 1980s as suitable liposomal carriers for the entrapment of polyanionic nucleotides, mainly DNA. Their intrinsic cytotoxicity due to their charge however, led to the development of ionizable aminolipids with low pKa, which can complex with nucleic acids in acidic pH and become neutral at physiological conditions. The development of **c)** RNA-based ionizable LNPs led to stable, robust entrapment of nucleic acids, lower toxicity, and higher transfection efficiency.

In the field of gene therapy, DNA encapsulation and cell transfection using liposomes proved to be a major challenge in the 1980s. Eventually, the development of the synthetic cationic lipid DOTMA (1,2-di-O-octadecenyl-3-trimethylammonium propane) led to lipofection, where resulting cationic liposomes complex with DNA and transfect cells with high efficiency (**Figure 4b**).[71] Cationic liposomes however, were found to be toxic and rapidly cleared from circulation due to their high surface charge and large size, hindering *in vivo*

systemic use.[72,73] This led to the development of ionizable aminolipids such as DODAP (1,2-dioleoyl-3-dimethylammonium propane), DLin-MC3-DMA, SM-102 and ALC-0315 (**Table 2**). The ionizable lipids allowed for the development of more sophisticated lipid nanoparticle assemblies, known as lipid nanoparticles (LNPs), enabling encapsulation of RNA-based therapeutics, lower toxicity and higher transfection efficiency (**Figure 4c**).[69,74–76] Ionizable amino lipids have an optimal pKa between 6-7 which allows for complexation with RNA in acidic pH, followed by LNP assembly.[77,78] Subsequently, pH can be adjusted to physiological values enabling the deprotonation of ionizable lipids, giving LNPs a relatively neutral surface and avoiding therefore rapid opsonization or toxicity. LNPs have recently shown tremendous potential in gene therapies, especially after the first clinically approved siRNA-based LNP formulation Onpattro® – which is used to treat polyneuropathies resulting from the hereditary transthyretin (hATTR) amyloidosis – and the mRNA-LNP vaccines against SARS-CoV-2, Spikevax® and Comirnaty® (**Table 1**).[79–82]

1.5 Targeted drug delivery

The concept of targeted drug delivery

The concept of using lipid-based nanoparticles in targeted delivery has been proposed since the 1970s.[60,83,84] Nanoparticles can be engineered to exert tailored properties that enable the targeting of specific cells or tissues, hence enhancing their therapeutic efficacy, lowering the dose, and reducing off-target adverse effects. As mentioned previously, nanoparticle modification with targeting ligands – such as antibodies, peptides and sugar moieties – can facilitate nanoparticle recognition by receptors expressed on the surface of specific cell types, to promote active targeting and transport (*i.e.,* receptor-mediated endocytosis). Furthermore, nanoparticles can be designed to respond to specific stimuli such as pH, temperature or light, which allow for spatiotemporal control of drug release and enhanced therapeutic efficacy. Also, a top-down approach is commonly used for targeted lipid nanoparticle discovery, where empirical screenings by altering nanoparticle size and composition, or design of experiment (DOE) methods,[85] narrow down formulations with optimal *in vivo* behavior.

Table 2. Molecular structures of a selection of ionizable lipids.

Ionizable lipid	Molecular structure and name
DODAP First developed	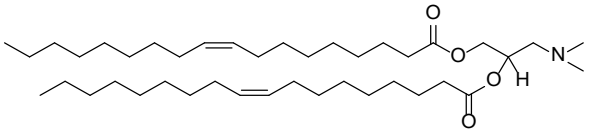 1,2-dioleoyl-3-dimethylammonium propane
DLin-MC3-DMA Clinically approved (Onpattro®)	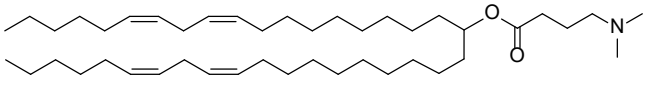 heptatriaconta-6,9,28,31-tetraen-19-yl-4-(dimethylamino) butanoate
SM-102 Clinically approved (Spikevax®)	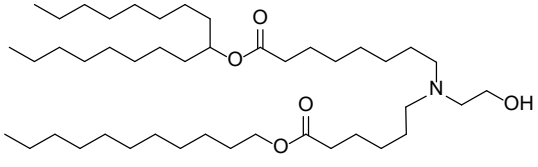 Heptadecan-9-yl 8-((2-hydroxyethyl) (6-oxo-6-(undecyloxy) hexyl) amino)octanoate
ALC-0315 Clinically approved (Comirnaty®)	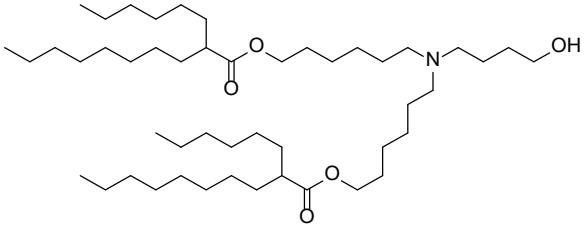 (4-hydroxybutyl)azanediyl)bis(hexane-6,1-diyl)bis(2-hexyldecanoate)

Challenges in targeted drug delivery

Liposomes and LNPs have so far been the most clinically advanced drug delivery platforms. Several liposome drug formulations have been approved for use in patients, mostly because they exhibit lower adverse effects than the free drug. For example, it was found that Doxil® reduces the cardiotoxicity otherwise observed during treatment with doxorubicin.[86,87] Liposomal drug formulations exhibit lower toxicity or slower drug release, however they do not particularly show higher therapeutic potential.[88] Despite the exciting advancements made in the field of lipid-based nanomedicines, several challenges remain. The biggest challenge continues to be the active targeting of (diseased) tissues and cell types. All clinically approved lipid-based nanomedicines are non-targeted delivery systems; Doxil® is a long circulating liposome, PEGylated to prevent rapid clearance, and mainly relies on the enhanced permeation and retention (EPR) effect to accumulate in solid tumors. Other liposomal drug formulations require similar biological mechanisms for accumulation, or they rely on passive uptake due to their size. For example, Mepact® (1-5 μm) has been used to activate the complement system and accumulate in macrophages, similarly to other nanoparticles that are cleared from circulation due to size.[89] Also, the two mRNA-LNP COVID-19 vaccines are administered intramuscularly and therefore immune responses are induced locally.

Consequently, no significant developments leading to selective nanoparticle targeting have yet resulted in a clinical product. Despite five decades of liposome research, discussions reflecting the reasons of the systematic failure to achieve selective therapies is only recently addressed.[88,90–92] Firstly, rapid clearance of systemically administered nanoparticles from circulation, attributed to their opsonization and uptake by cells of the mononuclear phagocyte (MPS) and reticuloendothelial system (RES), lowers their therapeutic efficiency in tissues and organs other than the liver and kidneys. On the other hand, local nanoparticle administration has been shown to enhance drug delivery in tissues and reduce off-targets.[93,94] Often however, areas of pathology are not accessible for local administration and when they are, procedures may be invasive, lowering the patient's quality of life. Secondly, targeting ligands are often erroneously assumed

they act as "magic bullets". They can indeed increase cell specificity within a tissue and actively target cell types, but the poor penetrability of nanoparticles in the tissue – even by local administration – bypassing several cell and tissue barriers, is often ignored. Moreover, the EPR effect, mostly used to target tumors, is often overrated as it shows great potential on animal models due to their faster-growing tumors (especially on xenograft models), but fails to successfully and accurately predict translation in humans.[95] Taken together with the lack of knowledge on the tumor pathophysiology and diversity, which are not carefully considered during nanoparticle design, studies show that only 0.7% of intravenously (*i.v.*) administered nanoparticles reach solid tumors.[91] Finally, nanoparticle designs utilizing targeting ligands such as antibodies, often exhibit relatively similar therapeutic outcomes to non-targeting formulations, but not higher enough to offset bottlenecks such as developmental costs (manufacturing, quality control *etc.*). The high complexity of such nanoparticle designs, containing multiple biologically active compounds, also requires extensive regulation for authorization and makes them unappealing to regulatory offices.[88,90] Similarly, uncharted territories in nanomedicine, especially for the more recent LNP-based therapeutics, could lead to several implications in drug development. For example, it is not yet clear whether LNP components should be considered as active ingredients or drug excipients, and as a result regulation can be complex.[96]

1.6 Overcoming challenges in nanomedicine

Bridging the translational gap

The preclinical development pipeline of nanomedicines usually follows that of traditional drug discovery, *i.e.,* physicochemical characterization, *in vitro* evaluation, and finally *in vivo* validation in relevant animal models. However, given the high complexity of nanomaterials – properties are different from a drug molecule – size, morphology, surface charge and surface modifications will profoundly determine the fate of nanomedicines *in vivo*.[97,98] Taken together that *in vitro* testing fails to reflect a realistic environment, wherein serum proteins, immune cells, clearance mechanisms and dynamic blood flow are present, myriad

preclinical nanoparticle studies achieve very poor translational prediction.[99] Also, exhaustive large-scale experiments, high costs and ethical considerations involved in animal testing, force to narrow down nanoparticle candidates for evaluation in rodents. Consequently many "poor *in vitro* performers" are disregarded and the potential of a plethora of lipid nanoparticle formulations is not assessed further.

Zebrafish are a robust *in vivo* model that can bridge the existing gap and improve the translational prediction.[100] As an animal model to screen and assess nanoparticle behavior *in vivo*, zebrafish offer several advantages over *in vitro* testing, or organs-on-chips, and can be used prior to (but not replacing) testing in higher animal models. Firstly, zebrafish have 76% homology to human genes, compared to a similar percentage for mice (84%) and many organs and functional systems such as the liver, blood-brain-barrier, vascular and immune system share physiological similarities with mammalian counterparts.[101–104] Also, plasma proteomes including main apolipoprotein families, as well as lipid transport and metabolism pathways (*i.e.,* several lipases, scavenging and lipoprotein receptors) are conserved.[105,106] Secondly, zebrafish offer the advantage of optical transparency in early embryonic stages, enabling real-time visualization of nanoparticle behavior *in vivo*, across the whole living embryo and at cellular resolution.[107] Additionally, fast generation of large embryo numbers allows for high-throughput *in vivo* screenings. Another important advantage is the external fertilization, which eases genetic manipulation and generation of numerous transgenic lines (*i.e.,* fluorescent transporter lines, mutants, transparent lines).[108,109] All these biological features allow for total nanoparticle assessment including toxicity studies, inflammatory responses and biodistribution. More specifically for the latter, embryonic zebrafish lines and biological manipulation (*i.e.,* inhibition of biological pathways) lead to observation of circulation lifetimes and clearance, extravasation, specific cell association, mechanisms of uptake, and transport across biological barriers. They also allow for evaluation of therapeutic outcomes such as gene delivery and cell transfection, gene silencing, drug release or others.

Zebrafish embryos, however, have an immature adaptive immune system which does not entirely reflect the nanoparticle clearance in higher animal models. They also have a slower blood flow and lower body temperature than rodents and humans, which can affect nanomedicine pharmacokinetics. Also, of particular note is that several biological pathways observed in zebrafish embryos are associated with developmental stages and are not conserved in adult stages. Therefore, a proper evaluation of the desired study and the correct selection of line and experimental setup is needed to effectively exploit these animal models. Since substantial differences in nanoparticle biodistribution has been observed across species,[110] a combination of models is desired/should be considered, to evaluate and validate research outcomes.

Overall, zebrafish embryos can bridge the gap between *in vitro* and *in vivo* testing in higher animal models. They present more complex biological conditions and have bigger informative value than *in vitro* testing; at the same time, they are easier to manipulate, and are more applicable to high-throughput screenings, more cost/time effective, and require less regulation than higher *in vivo* organisms.

Understanding nanoparticle behavior

Besides the aforementioned translational gap, the stymied progression on nanoparticle targeting also lies on the lack of fundamental knowledge at the nano-bio interface.[95,98] A better translation of nanomedicines can be achieved by understanding key molecular interactions – *i.e.*, specific nanoparticle-protein interactions – that drive biological mechanisms underpinning nanoparticle fate, biodistribution and clearance. For example, it was recently shown that surface charge can remarkably affect clearance and uptake of nanoparticles by different cell types.[111–113] Particularly anionic lipid-based nanoparticles have been found to preferentially accumulate in liver-sinusoidal endothelial cells (LSECs) through an interaction with two transmembrane receptors, Stablin-1 and Stabilin-2.[111,112] Instead of endless nanoparticle screenings, by simply understanding the effect of nanoparticle charge in cell selectivity, and by generating LNPs with anionic surface charge, it was possible to redirect nanoparticle accumulation towards LSECs over hepatocytes.[114] This event was found to be conserved across different animal models. Additionally, the formation of a protein corona on lipid-based

nanoparticles profoundly affects nanoparticle fate.[115,116] Interestingly, the protein corona of several lipid-based nanoparticles has been recently found to be rich in apolipoproteins – the main structural and functional components of lipoproteins which regulate lipid transport and metabolism – as opposed to previous assumptions that larger, more abundant proteins (*i.e.,* albumin) are the main corona components.[117] Importantly, many lipid-based nanoparticles have been found to have diverse apolipoprotein classes adsorbed onto their surface, or have no corona at all – depending on lipid composition – diverging therefore nanoparticle biodistribution. Interestingly, personalized nanoparticle protein coronas (*i.e.,* every individual may exhibit different plasma proteomes and therefore coronas) could be exploited in favor of the nanoparticle design and development.[118,119]

By acquiring a more comprehensive picture on the biological identity of lipid-based nanoparticles influenced by their physicochemical properties, nanoparticle *in vivo* behavior can be more accurately predicted.[98] In summary, lipid composition, morphology, size, colloidal stability and charge, will all affect *in vivo* performance, corona formation, selective nanoparticle-protein communications, and promote different interactions with endogenous mechanisms. Having therefore a biocentric approach on lipid-based nanoparticle development, considering how physicochemical properties affect the nano-bio interface, could help overcome current challenges on nanoparticle targeting and lead to more precise technologies.

Hijacking endogenous mechanisms of lipid transport and metabolism for targeted drug delivery

In contrast to conventional empirical screenings, exploiting endogenous lipid transport mechanisms to guide lipid-based nanoparticles to specific tissues or cells, is an enticing strategy but largely unexplored. A highlight of this approach is the clinically relevant formulation Onpattro®.[79] Here, selective recognition and uptake within target hepatocytes rely on the adsorption of soluble apolipoprotein E (apoE) to the surface of circulating siRNA-LNPs. This, in turn, guides LNPs to low-density lipoprotein receptors (LDLr) that are heavily expressed on the sinusoidal surface of hepatocytes.[120] Similar strategies can employ other

apolipoproteins for enhanced cellular uptake *i.e.*, by scavenger or other apolipoprotein receptors.[9,121,122] An even more unexplored strategy is employing triglyceride lipase-mediated pathways for nanoparticle cell specific targeting and transport. Triglyceride lipases (TGLs) are extracellular, endothelial lumen-bound hydrolytic enzymes which regulate lipid metabolism throughout the body.[123–126] TGLs metabolize lipoproteins by hydrolyzing the ester bonds of TGs, DAGs and CEs to release free fatty acids, which in turn are taken up locally by cells; or facilitate lipoprotein margination and holoparticle uptake by the cell (**Figure 5**).[127–129] The three main members of the TGLs, sharing significant structural homology, are lipoprotein lipase (LPL), endothelial lipase (EL) and hepatic lipase (HL).[130–135] Once expressed, TGLs are localized on endothelial cells and are mainly connected to cell membranes onto heparan sulfate proteoglycans (HSPG) or the glycosylphosphatidylinositol anchored high density lipoprotein binding protein 1 (GPIHBP1) via electrostatic interactions.[136–138] Spatiotemporal regulation of TGLs makes them interesting targets for nanoparticle cell specificity. TGLs are present in organs such as liver, heart, reproductive organs, but also highly present in several cancer types, promoting tumor growth and proliferation through lipid transport.[139–143]

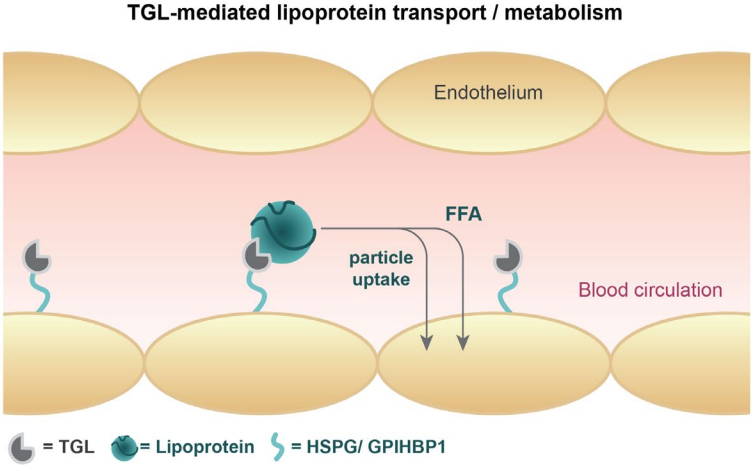

Figure 5. TGL-mediated lipoprotein transport/metabolism. TGLs are electrostatically bound to HSPG or GPIHBP1 and are exposed to the luminal side of endothelial cells. TGLs recognize lipoproteins in blood circulation and facilitate their endocytosis or hydrolyze them to release free fatty acids (FFA) that will be subsequently endocytosed.

1.7 Scope and motivation of this thesis

This doctoral thesis is an effort to understand how lipid phase-separation induced by DAG analogues in lipid-based nanoparticles affects their *in vivo* behavior, leading to specific nanoparticle-protein communications and selective cell targeting. By studying how lipid composition affects morphology and this in turn affects the nano-bio interface, a comprehensive picture and prediction of nanoparticle behavior and cell selectivity is provided.

Chapter 2 of this thesis describes the discovery of a novel liposome formulation consisting of just two lipids, a phospholipid and a synthetic DAG analogue (termed DOaG). This liposome formulation is capable of accumulating within brain endothelial cells of zebrafish embryos, by hijacking a pathway of lipid transport and metabolism mediated by TGL. Cryo-TEM imaging reveals a novel morphology in liposomes, characterized by lipid phase-separation, which is found to be responsible for the selective targeting. Zebrafish embryos are used as the primary *in vivo* model to unravel the biological mechanism underpinning the specific nanoparticle cell uptake, which is also found to be partially conserved in higher animal models (mice).

Chapter 3 describes an in-depth mechanistic understanding of the compositional and morphological changes that the phase-separated liposomes undergo in the presence of TGLs. A combination of cryo-TEM, molecular dynamic simulations and *in vitro* experiments, reveal that liposomes undergo remodeling after liposome-lipase interaction. Additionally, membrane packing defects – which are a result of phase-separation – facilitate the recognition and binding of the lipase onto the liposome surface.

Chapter 4 describes the detailed investigation of the underlying molecular principles underpinning the phase-separation and selective *in vivo* targeting, as induced by DOaG in liposomal membranes. Here, a library of DOaG analogues varying molecular properties is synthesized to investigate the structure- function relationship of DOaG in liposomal formulations. Cryo-TEM and biodistribution studies in zebrafish embryos reveal that only certain analogues can create phase-

separation leading to selective *in vivo* behavior, and that some contribute to the improvement of the formulation in terms of colloidal stability.

Chapter 5 describes the development of a novel mRNA-LNP formulation capable of delivering mRNA preferentially to the brain endothelial cells of zebrafish embryos, with subsequent transfection and protein expression. Guided by the knowledge acquired from the previous chapters, DOaG is used in this study to generate a novel phase-separated LNP formulation, as characterized by cryo-TEM. Zebrafish embryos are used for a biodistribution screening study to determine the exact lipid composition of DOaG-based LNP formulation that leads to specific cell targeting and gene delivery.

Chapter 6 summarizes all main findings generated over the course of this research and reflects on their importance for future studies and applications.

Appendix I describes a developed modified protocol for the *in-situ* formation and encapsulation of gold nanoparticles in phase separated, DOaG-containing liposomes.

1.8 References

1. Feynman, R. P. There's Plenty of Room at the Bottom. *Resonance* **2011**, *16* (9), 890–905.
2. Tewabe, A.; Abate, A.; Tamrie, M.; Seyfu, A.; Siraj, E. A. Targeted Drug Delivery — From Magic Bullet to Nanomedicine: Principles, Challenges, and Future Perspectives. *J Multidiscip Healthc* **2021**, *14*, 1711–1724.
3. Hu, X.; Zhang, Y.; Ding, T.; Liu, J.; Zhao, H. Multifunctional Gold Nanoparticles: A Novel Nanomaterial for Various Medical Applications and Biological Activities. *Front Bioeng Biotechnol* **2020**, *8*, 990.
4. Theodosiou, M.; Sakellis, E.; Boukos, N.; Kusigerski, V.; Kalska-Szostko, B.; Efthimiadou, E. Iron Oxide Nanoflowers Encapsulated in Thermosensitive Fluorescent Liposomes for Hyperthermia Treatment of Lung Adenocarcinoma. *Sci Rep* **2022**, *12* (1), 8697.
5. Dreaden, E. C.; Austin, L. A.; MacKey, M. A.; El-Sayed, M. A. Size Matters: Gold Nanoparticles in Targeted Cancer Drug Delivery. *Ther Deliv* **2012**, *3* (4), 457–478.
6. Dong, Y.; Love, K. T.; Dorkin, J. R.; Sirirungruang, S.; Zhang, Y.; Chen, D.; Bogorad, R. L.; Yin, H.; Chen, Y.; Vegas, A. J.; Alabi, C. A.; Sahay, G.; Olejnik, K. T.; Wang, W.; Schroeder, A.; Lytton-Jean, A. K. R.; Siegwart, D. J.; Akinc, A.; Barnes, C.; Barros, S. A.; Carioto, M.; Fitzgerald, K.; Hettinger, J.; Kumar, V.; Novobrantseva, T. I.; Qin, J.; Querbes, W.; Koteliansky, V.; Langer, R.; Anderson, D. G. Lipopeptide Nanoparticles for Potent and Selective siRNA Delivery in Rodents and Nonhuman Primates. *PNAS* **2014**, *111* (11), 3955–3960.
7. Mohsen, M. O.; Bachmann, M. F. Virus-like Particle Vaccinology, from Bench to Bedside. *Cell Mol Immunol* **2022**, *19* (9), 993–1011.
8. Herrmann, I. K.; Wood, M. J. A.; Fuhrmann, G. Extracellular Vesicles as a Next-Generation Drug Delivery Platform. *Nat Nanotechnol* **2021**, *16* (7), 748–759.
9. Schrijver, D. P.; De Dreu, A.; Hofstraat, S. R. J.; Kluza, E.; Zwolsman, R.; Deckers, J.; Anbergen, T.; De Bruin, K.; Trines, M. M.; Nugraha, E. G.; Ummels, F.; Röring, R. J.; Beldman, T. J.; Teunissen, A. J. P.; Fayad, Z. A.; Van Der Meel, R.; Mulder, W. J. M. Nanoengineering Apolipoprotein A1-Based Immunotherapeutics. *Adv Ther* **2021**, *4* (8), 2100083.
10. Ledesma, F.; Ozcan, B.; Sun, X.; Medina, S. M.; Landry, M. P.; Ledesma, F.; Ozcan, B.; Sun, X.; Medina, S. M.; Landry, M. P.; Biohub, C.-Z. Nanomaterial Strategies for Delivery of Therapeutic Cargoes. *Adv Funct Mater* **2022**, *32* (4), 2107174.
11. Papahadjopoulos, D.; Allen, T. M.; Gabizon, A.; Mayhew, E.; Matthay, K.; Huang, S. K.; Lee, K. D.; Woodle, M. C.; Lasic, D. D.; Redemann, C.; Martin, F. J. Sterically Stabilized Liposomes: Improvements in Pharmacokinetics and Antitumor Therapeutic Efficacy. *PNAS* **1991**, *88* (24), 11460–11464.

12. Klibanov, A. L.; Maruyama, K.; Torchilin, V. P.; Huang, L. Amphipathic Polyethyleneglycols Effectively Prolong the Circulation Time of Liposomes. *FEBS Lett* **1990**, *268* (1), 235–237.
13. Van Meer, G.; Voelker, D. R.; Feigenson, G. W. Membrane Lipids: Where They Are and How They Behave. *Nat Rev Mol Cell Biol* **2008**, *9* (2), 112–124.
14. Crawford, R.; Dogdas, B.; Keough, E.; Haas, R. M.; Wepukhulu, W.; Krotzer, S.; Burke, P. A.; Sepp-Lorenzino, L.; Bagchi, A.; Howell, B. J. Analysis of Lipid Nanoparticles by Cryo-EM for Characterizing siRNA Delivery Vehicles. *Int J Pharm* **2011**, *403*, 237–244.
15. Stewart, P. L. Cryo-Electron Microscopy and Cryo-Electron Tomography of Nanoparticles. *Wiley Interdiscip Rev Nanomed Nanobiotechnol* **2017**, *9* (2), e1417.
16. Frederik, P. M.; Hubert, D. H. W. Cryoelectron Microscopy of Liposomes. *Methods Enzymol* **2005**, *391*, 431–448.
17. Almgren, M.; Edwards, K.; Karlsson, G. Cryo Transmission Electron Microscopy of Liposomes and Related Structures. *Colloids Surf A Physicochem Eng Asp* **2000**, *174* (1–2), 3–21.
18. Bhattacharjee, S. DLS and Zeta Potential – What They Are and What They Are Not? *J Control Release* **2016**, *235*, 337–351.
19. Mahmoudi, M. The Need for Robust Characterization of Nanomaterials for Nanomedicine Applications. *Nat Commun* **2021**, *12* (1), 1–5.
20. Faria, M.; Björnmalm, M.; Thurecht, K. J.; Kent, S. J.; Parton, R. G.; Kavallaris, M.; Johnston, A. P. R.; Gooding, J. J.; Corrie, S. R.; Boyd, B. J.; Thordarson, P.; Whittaker, A. K.; Stevens, M. M.; Prestidge, C. A.; Porter, C. J. H.; Parak, W. J.; Davis, T. P.; Crampin, E. J.; Caruso, F. Minimum Information Reporting in Bio–Nano Experimental Literature. *Nat Nanotechnol* **2018**, *13* (9), 777–785.
21. Poste, G.; Papahadjopoulos, D. Lipid Vesicles as Carriers for Introducing Materials into Cultured Cells: Influence of Vesicle Lipid Composition on Mechanism(s) of Vesicle Incorporation into Cells. *PNAS* **1976**, *73* (5), 1603–1607.
22. Cullis, P. R.; Hope, M. J.; Tilcock, C. P. S. Lipid Polymorphism and the Roles of Lipids in Membranes. *Chem Phys Lipids* **1986**, *40* (2–4), 127–144.
23. Coffill, C. R.; Ramsamy, T. A.; Hutt, D. M.; Schultz, J. R.; Sparks, D. L. Diacylglycerol Is the Preferred Substrate in High Density Lipoproteins for Human Hepatic Lipase. *J Lipid Res* **1997**, *38* (11), 2224–2231.
24. Goñi, F. M.; Alonso, A. Structure and Functional Properties of Diacylglycerols in Membranes. *Prog Lipid Res* **1999**, *38* (1), 1–48.
25. Campomanes, P.; Zoni, V.; Vanni, S. Local Accumulation of Diacylglycerol Alters Membrane Properties Nonlinearly Due to Its Transbilayer Activity. *Commun Chem* **2019**, *2* (1), 1–8.
26. Goldberg, E. M.; Lester, D. S.; Borchardt, D. B.; Zidovetzki, R. Effects of Diacylglycerols on Conformation of Phosphatidylcholine Headgroups in Phosphatidylcholine/Phosphatidylserine Bilayers. *Biophys J* **1995**, *69* (3), 965–973.

27. Alwarawrah, M.; Hussain, F.; Huang, J. Alteration of Lipid Membrane Structure and Dynamics by Diacylglycerols with Unsaturated Chains. *Biochim Biophys Acta Biomembr* **2016**, *1858* (2), 253–263.
28. Bilayers Edward Goldberg, P. M.; Lester, D. S.; Borchardt, D. B.; Zidovetzki, R. Effects of Diacylglycerols and Ca2+ on Structure of Phosphatidylcholine/Phosphatidylserine Bilayers. *Biophys J* **1994**, *66*, 382–393.
29. Alwarawrah, M.; Dai, J.; Huang, J. Modification of Lipid Bilayer Structure by Diacylglycerol: A Comparative Study of Diacylglycerol and Cholesterol. *J Chem Theory Comput* **2012**, *8* (2), 749–758.
30. Szule, J. A.; Fuller, N. L.; Peter Rand, R. The Effects of Acyl Chain Length and Saturation of Diacylglycerols and Phosphatidylcholines on Membrane Monolayer Curvature. *Biophys J* **2002**, *83* (2), 977–984.
31. Vanni, S.; Hirose, H.; Barelli, H.; Antonny, B.; Gautier, R. A Sub-Nanometre View of How Membrane Curvature and Composition Modulate Lipid Packing and Protein Recruitment. *Nat Commun* **2014**, *5* (1), 1–10.
32. Vamparys, L.; Gautier, R.; Vanni, S.; Bennett, W. F. D.; Tieleman, D. P.; Antonny, B.; Etchebest, C.; Fuchs, P. F. J. Conical Lipids in Flat Bilayers Induce Packing Defects Similar to That Induced by Positive Curvature. *Biophys J* **2013**, *104* (3), 585–593.
33. Cui, H.; Lyman, E.; Voth, G. A. Mechanism of Membrane Curvature Sensing by Amphipathic Helix Containing Proteins. *Biophys J* **2011**, *100* (5), 1271–1279.
34. Drin, G.; Casella, J.-F.; Gautier, R.; Boehmer, T.; Schwartz, T. U.; Antonny, B. A General Amphipathic A-Helical Motif for Sensing Membrane Curvature. *Nat Struct Mol Biol* **2007**, *14* (2), 138–146.
35. van Hilten, N.; Methorst, J.; Verwei, N.; Risselada, H. J. Physics-Based Generative Model of Curvature Sensing Peptides; Distinguishing Sensors from Binders. *Sci Adv* **2023**, *9* (11), eade8839.
36. Bohr, S. S. R.; Thorlaksen, C.; Kühnel, R. M.; Günther-Pomorski, T.; Hatzakis, N. S. Label-Free Fluorescence Quantification of Hydrolytic Enzyme Activity on Native Substrates Reveals How Lipase Function Depends on Membrane Curvature. *Langmuir* **2020**, *36* (23), 6473–6481.
37. Gómez-Fernández, J. C.; Corbalán-García, S. Diacylglycerols, Multivalent Membrane Modulators. *Chem Phys Lipids* **2007**, *148* (1), 1–25.
38. Eichmann, T. O.; Lass, A. DAG Tales: The Multiple Faces of Diacylglycerol—Stereochemistry, Metabolism, and Signaling. *Cell Mol Life Sci* **2015**, *72* (20), 3931–3952.
39. Dawson, R. M. C.; Hemington, N. L.; Irvine, R. F. Diacylglycerol Potentiates Phospholipase Attack upon Phospholipid Bilayers: Possible Connection with Cell Stimulation. *Biochem Biophys Res Commun* **1983**, *117* (1), 196–201.
40. Barlič, A.; Gutiérrez-Aguirre, I.; Caaveiro, J. M. M.; Cruz, A.; Ruiz-Argüello, M. B.; Pérez-Gil, J.; González-Mañas, J. M. Lipid Phase Coexistence Favors Membrane

Insertion of Equinatoxin-II, a Pore-Forming Toxin from Actinia Equina. *J Biol Chem* **2004**, *279* (33), 34209–34216.

41. Ahyayauch, H.; Sot, J.; Collado, M. I.; Huarte, N.; Requejo-Isidro, J.; Alonso, A.; Goñi, F. M. End-Product Diacylglycerol Enhances the Activity of PI-PLC through Changes in Membrane Domain Structure. *Biophys J* **2015**, *108* (7), 1672–1682.
42. Dawson, R. M. C.; Irvine, R. F.; Bray, J.; Quinn, P. J. Long-Chain Unsaturated Diacylglycerols Cause a Perturbation in the Structure of Phospholipid Bilayers Rendering Them Susceptible to Phospholipase Attack. *Biochem Biophys Res Commun* **1984**, *125* (2), 836–842.
43. Basáñez, G.; Nieva, J. L.; Rivas, E.; Alonso, A.; Goñi, F. M. Diacylglycerol and the Promotion of Lamellar-Hexagonal and Lamellar-Isotropic Phase Transitions in Lipids: Implications for Membrane Fusion. *Biophys J* **1996**, *70* (5), 2299–2306.
44. Siegel, D. P.; Epand, R. M. The Mechanism of Lamellar-to-Inverted Hexagonal Phase Transitions in Phosphatidylethanolamine: Implications for Membrane Fusion Mechanisms. *Biophys J* **1997**, *73* (6), 3089–3111.
45. Nieva, J. L.; Alonso, A.; Basáñez, G.; Goñi, F. M.; Gulik, A.; Vargas, R.; Luzzati, V. Topological Properties of Two Cubic Phases of a Phospholipid : Cholesterol: Diacylglycerol Aqueous System and Their Possible Implications in the Phospholipase C-Induced Liposome Fusion. *FEBS Lett* **1995**, *368* (1), 143–147.
46. Siegel, D. P.; Banschbach, J.; Alford, D.; Bentz, J.; Ellens, H.; Lis, L. J.; Quinn, P. J.; Yeagle, P. L. Physiological Levels of Diacylglycerols in Phospholipid Membranes Induce Membrane Fusion and Stabilize Inverted Phases. *Biochemistry* **1989**, *28* (9), 3703–3709.
47. Vieu, C.; Jaspard, B.; Barbaras, R.; Manent, J.; Chap, H.; Perret, B.; Collet, X. Identification and Quantification of Diacylglycerols in HDL and Accessibility to Lipase. *J Lipid Res* **1996**, *37* (5), 1153–1161.
48. Bae, C. S.; Ahn, T. Diacylglycerol in Cationic Nanoparticles Stimulates Oxidative Stress-Mediated Death of Cancer Cells. *Lipids* **2018**, *53* (11–12), 1059–1067.
49. Ibarguren, M.; Bomans, P. H. H.; Ruiz-Mirazo, K.; Frederik, P. M.; Alonso, A.; Goñi, F. M. Thermally-Induced Aggregation and Fusion of Protein-Free Lipid Vesicles. *Colloids Surf B Biointerfaces* **2015**, *136*, 545–552.
50. Kim, B.; Sun, S.; Varner, J. A.; Howell, S. B.; Ruoslahti, E.; Sailor, M. J. Securing the Payload, Finding the Cell, and Avoiding the Endosome: Peptide-Targeted, Fusogenic Porous Silicon Nanoparticles for Delivery of siRNA. *Adv Mat* **2019**, *31* (35), 1902952.
51. Yang, J.; Tu, J.; Lamers, G. E. M.; Olsthoorn, R. C. L.; Kros, A. Membrane Fusion Mediated Intracellular Delivery of Lipid Bilayer Coated Mesoporous Silica Nanoparticles. *Adv Healthc Mater* **2017**, *6* (20), 201700759.
52. Hafez, I. M.; Cullis, P. R. Roles of Lipid Polymorphism in Intracellular Delivery. *Adv Drug Deliv Rev* **2001**, *47* (2–3), 139–148.

53. Cheng, M. H. Y.; Leung, J.; Zhang, Y.; Strong, C.; Basha, G.; Momeni, A.; Chen, Y.; Jan, E.; Abdolahzadeh, A.; Wang, X.; Kulkarni, J. A.; Witzigmann, D.; Cullis, P. R. Induction of Bleb Structures in Lipid Nanoparticle Formulations of mRNA Leads to Improved Transfection Potency. *Adv mat* **2023**, e2303370.
54. Imam, Z. I.; Kenyon, L. E.; Ashby, G.; Nagib, F.; Mendicino, M.; Zhao, C.; Gadok, A. K.; Stachowiak, J. C. Phase-Separated Liposomes Enhance the Efficiency of Macromolecular Delivery to the Cellular Cytoplasm. *Cell Mol Bioeng* **2017**, *10* (5), 387–403.
55. Bangham, A. D.; Standish, M. M.; Watkins, J. C. Diffusion of Univalent Ions across the Lamellae of Swollen Phospholipids. *J Mol Biol* **1965**, *13* (1), 238–252.
56. Weissig, V. Liposomes Came First: The Early History of Liposomology. *Methods Mol Biol* **2017**, *1522*, 1–15.
57. Bangham, A. D.; Hill, M. W.; Miller, N. G. A. Preparation and Use of Liposomes as Models of Biological Membranes. In *Methods Membr Biol*; Springer, Boston, MA, 1974; 1–68.
58. Bangham, A. D.; Hill, M. W. The Proton Pump/Leak Mechanism of Unconsciousness. *Chem Phys Lipids* **1986**, *40* (2–4), 189–205.
59. Gregoriadis, G.; Buckland, R. A. Enzyme-Containing Liposomes Alleviate a Model for Storage Disease. *Nature* **1973**, *244* (5412), 170–172.
60. Gregoriadis, G. The Carrier Potential of Liposomes in Biology and Medicine (First of Two Parts). *N Engl J Med* **1976**, *295* (13), 704–710.
61. Gregoriadis, G.; Allison, A. C. Entrapment of Proteins in Liposomes Prevents Allergic Reactions in Pre-Immunised Mice. *FEBS Lett* **1974**, *45* (1), 71–74.
62. Allison, A. C.; Gregoriadis, G. Liposomes as Immunological Adjuvants. *Nature* **1974**, *252* (5480), 252–252.
63. Gregoriadis, G. Liposomes in Drug Delivery: How It All Happened. *Pharmaceutics* **2016**, *8* (2), 19.
64. Hwang, K. J.; Luk, K. F. S.; Beaumier, P. L. Hepatic Uptake and Degradation of Unilamellar Sphingomyelin/Cholesterol Liposomes: A Kinetic Study. *PNAS* **1980**, *77* (7), 4030–4034.
65. Gregoriadis, G.; Senior, J. The Phospholipid Component of Small Unilamellar Liposomes Controls the Rate of Clearance of Entrapped Solutes from the Circulation. *FEBS Lett* **1980**, *119* (1), 43–46.
66. Juliano, R. L.; Stamp, D. The Effect of Particle Size and Charge on the Clearance Rates of Liposomes and Liposome Encapsulated Drugs. *Biochem Biophys Res Commun* **1975**, *63* (3), 651–658.
67. Kirby, C.; Clarke, J.; Gregoriadis, G. Effect of the Cholesterol Content of Small Unilamellar Liposomes on Their Stability in Vivo and in Vitro. *Biochemical Journal* **1980**, *186* (2), 591–598.

68. Gabizon, A.; Papahadjopoulos, D. Liposome Formulations with Prolonged Circulation Time in Blood and Enhanced Uptake by Tumors. *PNAS* **1988**, *85* (18), 6949–6953.
69. Cullis, P. R.; Hope, M. J. Lipid Nanoparticle Systems for Enabling Gene Therapies. *Mol Ther* **2017**, *25* (7), 1467–1475.
70. Crommelin, D. J. A.; van Hoogevest, P.; Storm, G. The Role of Liposomes in Clinical Nanomedicine Development. What Now? Now What? *J Control Release* **2020**, *318*, 256–263.
71. Felgner, P. L.; Gadek, T. R.; Holm, M.; Roman, R.; Chan, H. W.; Wenz, M.; Northrop, J. P.; Ringold, G. M.; Danielsen, M. Lipofection: A Highly Efficient, Lipid-Mediated DNA-Transfection Procedure. *PNAS* **1987**, *84* (21), 7413–7417.
72. Filion, M. C.; Phillips, N. C. Toxicity and Immunomodulatory Activity of Liposomal Vectors Formulated with Cationic Lipids toward Immune Effector Cells. *Biochim Biophys Acta* **1997**, *1329* (2), 345–356.
73. Allen, T. M.; Cullis, P. R. Liposomal Drug Delivery Systems: From Concept to Clinical Applications. *Adv Drug Deliv Rev* **2013**, *65* (1), 36–48.
74. Semple, S. C.; Klimuk, S. K.; Harasym, T. O.; Dos Santos, N.; Ansell, S. M.; Wong, K. F.; Maurer, N.; Stark, H.; Cullis, P. R.; Hope, M. J.; Scherrer, P. Efficient Encapsulation of Antisense Oligonucleotides in Lipid Vesicles Using Ionizable Aminolipids: Formation of Novel Small Multilamellar Vesicle Structures. *Biochim Biophys Acta* **2001**, *1510* (1–2), 152–166.
75. Semple, S. C.; Akinc, A.; Chen, J.; Sandhu, A. P.; Mui, B. L.; Cho, C. K.; Sah, D. W. Y.; Stebbing, D.; Crosley, E. J.; Yaworski, E.; Hafez, I. M.; Dorkin, J. R.; Qin, J.; Lam, K.; Rajeev, K. G.; Wong, K. F.; Jeffs, L. B.; Nechev, L.; Eisenhardt, M. L.; Jayaraman, M.; Kazem, M.; Maier, M. A.; Srinivasulu, M.; Weinstein, M. J.; Chen, Q.; Alvarez, R.; Barros, S. A.; De, S.; Klimuk, S. K.; Borland, T.; Kosovrasti, V.; Cantley, W. L.; Tam, Y. K.; Manoharan, M.; Ciufolini, M. A.; Tracy, M. A.; De Fougerolles, A.; MacLachlan, I.; Cullis, P. R.; Madden, T. D.; Hope, M. J. Rational Design of Cationic Lipids for siRNA Delivery. *Nat Biotechnol* **2010**, *28* (2), 172–176.
76. Horejs, C. From Lipids to Lipid Nanoparticles to mRNA Vaccines. *Nat Rev Mater* **2021**, *6* (12), 1075–1076.
77. Patel, P.; Ibrahim, N. M.; Cheng, K. The Importance of Apparent pKa in the Development of Nanoparticles Encapsulating siRNA and mRNA. *Trends Pharmacol Sci* **2021**, *42* (6), 448–460.
78. Hald Albertsen, C.; Kulkarni, J. A.; Witzigmann, D.; Lind, M.; Petersson, K.; Simonsen, J. B. The Role of Lipid Components in Lipid Nanoparticles for Vaccines and Gene Therapy. *Adv Drug Deliv Rev* **2022**, *188*, 114416.
79. Akinc, A.; Maier, M. A.; Manoharan, M.; Fitzgerald, K.; Jayaraman, M.; Barros, S.; Ansell, S.; Du, X.; Hope, M. J.; Madden, T. D.; Mui, B. L.; Semple, S. C.; Tam, Y. K.; Ciufolini, M.; Witzigmann, D.; Kulkarni, J. A.; van der Meel, R.; Cullis, P. R. The

Onpattro Story and the Clinical Translation of Nanomedicines Containing Nucleic Acid-Based Drugs. *Nat Nanotechnol* **2019**, *14* (12), 1084–1087.

80. Schoenmaker, L.; Witzigmann, D.; Kulkarni, J. A.; Verbeke, R.; Kersten, G.; Jiskoot, W.; Crommelin, D. J. A. mRNA-Lipid Nanoparticle COVID-19 Vaccines: Structure and Stability. *Int J Pharm* **2021**, *601*, 120586.
81. Szabó, G. T.; Mahiny, A. J.; Vlatkovic, I. COVID-19 mRNA Vaccines: Platforms and Current Developments. *Mol Ther* **2022**, *30* (5), 1850–1868.
82. Khurana, A.; Allawadhi, P.; Khurana, I.; Allwadhi, S.; Weiskirchen, R.; Banothu, A. K.; Chhabra, D.; Joshi, K.; Bharani, K. K. Role of Nanotechnology behind the Success of mRNA Vaccines for COVID-19. *Nano Today* **2021**, *38*, 101142.
83. Gregory Gregoriadis, E.; Neerunjun, D. Homing of Liposomes to Target Cells. *Biochem Biophys Res Commun* **1975**, *65* (2), 537–544.
84. Gregoriadis, G. Targeting of Drugs. *Nature* **1977**, *265* (5593), 407–411.
85. Bevers, S.; Kooijmans, S. A. A.; Van de Velde, E.; Evers, M. J. W.; Seghers, S.; Gitz-Francois, J. J. J. M.; van Kronenburg, N. C. H.; Fens, M. H. A. M.; Mastrobattista, E.; Hassler, L.; Sork, H.; Lehto, T.; Ahmed, K. E.; El Andaloussi, S.; Fiedler, K.; Breckpot, K.; Maes, M.; Van Hoorick, D.; Bastogne, T.; Schiffelers, R. M.; De Koker, S. mRNA-LNP Vaccines Tuned for Systemic Immunization Induce Strong Antitumor Immunity by Engaging Splenic Immune Cells. *Mol Ther* **2022**, *30* (9), 3078–3094.
86. O'Brien, M. E. R.; Wigler, N.; Inbar, M.; Rosso, R.; Grischke, E.; Santoro, A.; Catane, R.; Kieback, D. G.; Tomczak, P.; Ackland, S. P.; Orlandi, F.; Mellars, L.; Alland, L.; Tendler, C. Reduced Cardiotoxicity and Comparable Efficacy in a Phase III Trial of Pegylated Liposomal Doxorubicin HCl (Caelyx™/Doxil®) versus Conventional Doxorubicin for First-Line Treatment of Metastatic Breast Cancer. *Annals of Oncology* **2004**, *15* (3), 440–449.
87. Northfelt, D. W.; Dezube, B. J.; Thommes, J. A.; Miller, B. J.; Fischl, M. A.; Friedman-Kien, A.; Kaplan, L. D.; Du Mond, C.; Mamelok, R. D.; Henry, D. H. Pegylated-Liposomal Doxorubicin versus Doxorubicin, Bleomycin, and Vincristine in the Treatment of AIDS-Related Kaposi's Sarcoma: Results of a Randomized Phase III Clinical Trial. *J Clin Oncol* **1998**, *16* (7), 2445–2451.
88. Lammers, T.; Kiessling, F.; Hennink, W. E.; Storm, G. Drug Targeting to Tumors: Principles, Pitfalls and (Pre-) Clinical Progress. *J Control Release* **2012**, *161* (2), 175–187.
89. Hoshyar, N.; Gray, S.; Han, H.; Bao, G. The Effect of Nanoparticle Size on in Vivo Pharmacokinetics and Cellular Interaction. *Nanomedicine* **2016**, *11* (6), 673–692.
90. Guidolin, K.; Zheng, G. Nanomedicines Lost in Translation. *ACS Nano* **2019**, *13* (12), 13620–13626.
91. Wilhelm, S.; Tavares, A. J.; Dai, Q.; Ohta, S.; Audet, J.; Dvorak, H. F.; Chan, W. C. W. Analysis of Nanoparticle Delivery to Tumours. *Nat Rev Mater* **2016**, *1* (5), 1–12.

92. Bae, Y. H.; Park, K. Targeted Drug Delivery to Tumors: Myths, Reality and Possibility. *J Control Release* **2011**, *153* (3), 198–205.
93. Pardi, N.; Tuyishime, S.; Muramatsu, H.; Kariko, K.; Mui, B. L.; Tam, Y. K.; Madden, T. D.; Hope, M. J.; Weissman, D. Expression Kinetics of Nucleoside-Modified mRNA Delivered in Lipid Nanoparticles to Mice by Various Routes. *J control release* **2015**, *217*, 345–351.
94. Bastiancich, C.; Bozzato, E.; Henley, I.; Newland, B. Does Local Drug Delivery Still Hold Therapeutic Promise for Brain Cancer? A Systematic Review. *J Control Release* **2021**, *337*, 296–305.
95. Björnmalm, M.; Thurecht, K. J.; Michael, M.; Scott, A. M.; Caruso, F. Bridging Bio-Nano Science and Cancer Nanomedicine. *ACS Nano* **2017**, *11* (10), 9594–9613.
96. Hemmrich, E.; McNeil, S. Active Ingredient vs Excipient Debate for Nanomedicines. *Nat Nanotechnol* **2023**, *18* (7), 692–695.
97. Dai, Q.; Bertleff-Zieschang, N.; Braunger, J. A.; Björnmalm, M.; Cortez-Jugo, C.; Caruso, F. Particle Targeting in Complex Biological Media. *Adv Healthc Mater* **2018**, *7* (1), 1700575.
98. Nel, A. E.; Mädler, L.; Velegol, D.; Xia, T.; Hoek, E. M. V.; Somasundaran, P.; Klaessig, F.; Castranova, V.; Thompson, M. Understanding Biophysicochemical Interactions at the Nano–Bio Interface. *Nat Mater* **2009**, *8* (7), 543–557.
99. Paunovska, K.; Sago, C. D.; Monaco, C. M.; Hudson, W. H.; Castro, M. G.; Rudoltz, T. G.; Kalathoor, S.; Vanover, D. A.; Santangelo, P. J.; Ahmed, R.; Bryksin, A. V.; Dahlman, J. E. A Direct Comparison of in Vitro and in Vivo Nucleic Acid Delivery Mediated by Hundreds of Nanoparticles Reveals a Weak Correlation. *Nano Lett* **2018**, *18* (3), 2148–2157.
100. Sieber, S.; Grossen, P.; Bussmann, J.; Campbell, F.; Kros, A.; Witzigmann, D.; Huwyler, J. Zebrafish as a Preclinical in Vivo Screening Model for Nanomedicines. *Adv Drug Deliv Rev* **2019**, *151–152*, 152–168.
101. Howe, K.; Clark, M. D.; Torroja, C. F.; Torrance, J.; Berthelot, C.; Muffato, M.; Collins, J. E.; Humphray, S.; McLaren, K.; Matthews, L.; McLaren, S.; Sealy, I.; Caccamo, M.; Churcher, C.; Scott, C.; Barrett, J. C.; Koch, R.; Rauch, G. J.; White, S.; Chow, W.; Kilian, B.; Quintais, L. T.; Guerra-Assunção, J. A.; Zhou, Y.; Gu, Y.; Yen, J.; Vogel, J. H.; Eyre, T.; Redmond, S.; Banerjee, R.; Chi, J.; Fu, B.; Langley, E.; Maguire, S. F.; Laird, G. K.; Lloyd, D.; Kenyon, E.; Donaldson, S.; Sehra, H.; Almeida-King, J.; Loveland, J.; Trevanion, S.; Jones, M.; Quail, M.; Willey, D.; Hunt, A.; Burton, J.; Sims, S.; McLay, K.; Plumb, B.; Davis, J.; Clee, C.; Oliver, K.; Clark, R.; Riddle, C.; Eliott, D.; Threadgold, G.; Harden, G.; Ware, D.; Mortimer, B.; Kerry, G.; Heath, P.; Phillimore, B.; Tracey, A.; Corby, N.; Dunn, M.; Johnson, C.; Wood, J.; Clark, S.; Pelan, S.; Griffiths, G.; Smith, M.; Glithero, R.; Howden, P.; Barker, N.; Stevens, C.; Harley, J.; Holt, K.; Panagiotidis, G.; Lovell, J.; Beasley, H.; Henderson, C.; Gordon, D.; Auger, K.; Wright, D.; Collins, J.; Raisen, C.; Dyer, L.; Leung, K.; Robertson, L.; Ambridge, K.; Leongamornlert, D.; McGuire, S.;

Gilderthorp, R.; Griffiths, C.; Manthravadi, D.; Nichol, S.; Barker, G.; Whitehead, S.; Kay, M.; Brown, J.; Murnane, C.; Gray, E.; Humphries, M.; Sycamore, N.; Barker, D.; Saunders, D.; Wallis, J.; Babbage, A.; Hammond, S.; Mashreghi-Mohammadi, M.; Barr, L.; Martin, S.; Wray, P.; Ellington, A.; Matthews, N.; Ellwood, M.; Woodmansey, R.; Clark, G.; Cooper, J.; Tromans, A.; Grafham, D.; Skuce, C.; Pandian, R.; Andrews, R.; Harrison, E.; Kimberley, A.; Garnett, J.; Fosker, N.; Hall, R.; Garner, P.; Kelly, D.; Bird, C.; Palmer, S.; Gehring, I.; Berger, A.; Dooley, C. M.; Ersan-Ürün, Z.; Eser, C.; Geiger, H.; Geisler, M.; Karotki, L.; Kirn, A.; Konantz, J.; Konantz, M.; Oberländer, M.; Rudolph-Geiger, S.; Teucke, M.; Osoegawa, K.; Zhu, B.; Rapp, A.; Widaa, S.; Langford, C.; Yang, F.; Carter, N. P.; Harrow, J.; Ning, Z.; Herrero, J.; Searle, S. M. J.; Enright, A.; Geisler, R.; Plasterk, R. H. A.; Lee, C.; Westerfield, M.; De Jong, P. J.; Zon, L. I.; Postlethwait, J. H.; Nüsslein-Volhard, C.; Hubbard, T. J. P.; Crollius, H. R.; Rogers, J.; Stemple, D. L. The Zebrafish Reference Genome Sequence and Its Relationship to the Human Genome. *Nature* **2013**, *496* (7446), 498–503.

102. Isogai, S.; Horiguchi, M.; Weinstein, B. M. The Vascular Anatomy of the Developing Zebrafish: An Atlas of Embryonic and Early Larval Development. *Dev Biol* **2001**, *230* (2), 278–301.
103. Chu, J.; Sadler, K. C. A New School in Liver Development: Lessons from Zebrafish. *Hepatology* **2009**, *50* (5), 1656–1663.
104. Kim, S. S.; Im, S. H.; Yang, J. Y.; Lee, Y. R.; Kim, G. R.; Chae, J. S.; Shin, D. S.; Song, J. S.; Ahn, S.; Lee, B. H.; Woo, J. C.; Ahn, J. H.; Yun, C. S.; Kim, P.; Kim, H. R.; Lee, K. R.; Bae, M. A. Zebrafish as a Screening Model for Testing the Permeability of Blood-Brain Barrier to Small Molecules. *Zebrafish* **2017**, *14* (4), 322–330.
105. Otis, J. P.; Zeituni, E. M.; Thierer, J. H.; Anderson, J. L.; Brown, A. C.; Boehm, E. D.; Cerchione, D. M.; Ceasrine, A. M.; Avraham-Davidi, I.; Tempelhof, H.; Yaniv, K.; Farber, S. A. Zebrafish as a Model for Apolipoprotein Biology: Comprehensive Expression Analysis and a Role for ApoA-IV in Regulating Food Intake. *Dis Model Mech* **2015**, *8* (3), 295–309.
106. Li, C.; Tan, X. F.; Lim, T. K.; Lin, Q.; Gong, Z. Comprehensive and Quantitative Proteomic Analyses of Zebrafish Plasma Reveals Conserved Protein Profiles between Genders and between Zebrafish and Human. *Sci Rep* **2016**, *6* (1), 1–15.
107. Karlsson, J.; Von Hofsten, J.; Olsson, P. E. Generating Transparent Zebrafish: A Refined Method to Improve Detection of Gene Expression during Embryonic Development. *Marine biotechnology* **2001**, *3* (6), 522–527.
108. Nasevicius, A.; Ekker, S. C. Effective Targeted Gene 'Knockdown' in Zebrafish. *Nature Genetics* **2000**, *26* (2), 216–220.
109. Wienholds, E.; van Eeden, F.; Kosters, M.; Mudde, J.; Plasterk, R. H. A.; Cuppen, E. Efficient Target-Selected Mutagenesis in Zebrafish. *Genome Res* **2003**, *13* (12), 2700–2707.

110. Hatit, M. Z. C.; Lokugamage, M. P.; Dobrowolski, C. N.; Paunovska, K.; Ni, H.; Zhao, K.; Vanover, D.; Beyersdorf, J.; Peck, H. E.; Loughrey, D.; Sato, M.; Cristian, A.; Santangelo, P. J.; Dahlman, J. E. Species-Dependent in Vivo mRNA Delivery and Cellular Responses to Nanoparticles. *Nat Nanotechnol* **2022**, *17* (3), 310–318.
111. Arias-Alpizar, G.; Koch, B.; Hamelmann, N. M.; Neustrup, M. A.; Paulusse, J. M. J.; Jiskoot, W.; Kros, A.; Bussmann, J. Stabilin-1 Is Required for the Endothelial Clearance of Small Anionic Nanoparticles. *Nanomedicine* **2021**, *34*, 102395.
112. Campbell, F.; Bos, F. L.; Sieber, S.; Arias-Alpizar, G.; Koch, B. E.; Huwyler, J.; Kros, A.; Bussmann, J. Directing Nanoparticle Biodistribution through Evasion and Exploitation of Stab2-Dependent Nanoparticle Uptake. *ACS Nano* **2018**, *12* (3), 2138–2150.
113. Arias-Alpizar, G.; Kong, L.; Vlieg, R. C.; Rabe, A.; Papadopoulou, P.; Meijer, M. S.; Bonnet, S.; Vogel, S.; van Noort, J.; Kros, A.; Campbell, F. Light-Triggered Switching of Liposome Surface Charge Directs Delivery of Membrane Impermeable Payloads in Vivo. *Nat Commun* **2020**, *11*, 3638.
114. Pattipeiluhu, R.; Arias-Alpizar, G.; Basha, G.; Chan, K. Y. T.; Bussmann, J.; Sharp, T. H.; Moradi, M.-A.; Sommerdijk, N.; Harris, E. N.; Cullis, P. R.; Kros, A.; Witzigmann, D.; Campbell, F. Anionic Lipid Nanoparticles Preferentially Deliver mRNA to the Hepatic Reticuloendothelial System. *Advanced Materials* **2022**, *34* (16), e2201095.
115. Ritz, S.; Schöttler, S.; Kotman, N.; Baier, G.; Musyanovych, A.; Kuharev, J.; Landfester, K.; Schild, H.; Jahn, O.; Tenzer, S.; Mailänder, V. Protein Corona of Nanoparticles: Distinct Proteins Regulate the Cellular Uptake. *Biomacromolecules* **2015**, *16* (4), 1311–1321.
116. Lundqvist, M.; Stigler, J.; Elia, G.; Lynch, I.; Cedervall, T.; Dawson, K. A. Nanoparticle Size and Surface Properties Determine the Protein Corona with Possible Implications for Biological Impacts. *PNAS* **2008**, *105* (38), 14265–14270.
117. Pattipeiluhu, R.; Crielaard, S.; Klein-Schiphorst, I.; Florea, B. I.; Kros, A.; Campbell, F. Unbiased Identification of the Liposome Protein Corona Using Photoaffinity-Based Chemoproteomics. *ACS Cent Sci* **2020**, *6* (4), 535–545.
118. Corbo, C.; Molinaro, R.; Tabatabaei, M.; Farokhzad, O. C.; Mahmoudi, M. Personalized Protein Corona on Nanoparticles and Its Clinical Implications. *Biomater Sci* **2017**, *5* (3), 378–387.
119. Hajipour, M. J.; Laurent, S.; Aghaie, A.; Rezaee, F.; Mahmoudi, M. Personalized Protein Coronas: A "Key" Factor at the Nanobiointerface. *Biomater Sci* **2014**, *2*, 1210–1221.
120. Akinc, A.; Querbes, W.; De, S.; Qin, J.; Frank-Kamenetsky, M.; Jayaprakash, K. N.; Jayaraman, M.; Rajeev, K. G.; Cantley, W. L.; Dorkin, J. R.; Butler, J. S.; Qin, L.; Racie, T.; Sprague, A.; Fava, E.; Zeigerer, A.; Hope, M. J.; Zerial, M.; Sah, D. W.; Fitzgerald, K.; Tracy, M. A.; Manoharan, M.; Koteliansky, V.; Fougerolles, A. De;

Maier, M. A. Targeted Delivery of RNAi Therapeutics with Endogenous and Exogenous Ligand-Based Mechanisms. *Mol Ther* **2010**, *18* (7), 1357–1364.

121. Kadiyala, P.; Li, D.; Nuñez, F. M.; Altshuler, D.; Doherty, R.; Kuai, R.; Yu, M.; Kamran, N.; Edwards, M.; Moon, J. J.; Lowenstein, P. R.; Castro, M. G.; Schwendeman, A. High-Density Lipoprotein-Mimicking Nanodiscs for Chemo-Immunotherapy against Glioblastoma Multiforme. *ACS Nano* **2019**, *13* (2), 1365–1384.
122. Alam, S. B.; Wang, F.; Qian, H.; Kulka, M. Apolipoprotein C3 Facilitates Internalization of Cationic Lipid Nanoparticles into Bone Marrow-Derived Mouse Mast Cells. *Sci Rep* **2023**, *13* (1), 1–16.
123. Watt, M. J.; Steinberg, G. R. Regulation and Function of Triacylglycerol Lipases in Cellular Metabolism. *Biochemical Journal* **2008**, *414* (3), 313–325.
124. Watt, M. J.; Spriet, L. L. Triacylglycerol Lipases and Metabolic Control: Implications for Health and Disease. *Am J Physiol Endocrinol Metab* **2010**, *299* (2), 162–168.
125. Beisiegel, U. New Aspects on the Role of Plasma Lipases in Lipoprotein Catabolism and Atherosclerosis. *Atherosclerosis* **1996**, *124* (1), 1–8.
126. Olivecrona, G.; Olivecrona, T. Triglyceride Lipases and Atherosclerosis. *Curr Opin Lipidol* **2010**, *21* (5), 409–415.
127. Goulbourne, C. N.; Gin, P.; Tatar, A.; Nobumori, C.; Hoenger, A.; Jiang, H.; Grovenor, C. R. M.; Adeyo, O.; Esko, J. D.; Goldberg, I. J.; Reue, K.; Tontonoz, P.; Bensadoun, A.; Beigneux, A. P.; Young, S. G.; Fong, L. G. The GPIHBP1–LPL Complex Is Responsible for the Margination of Triglyceride-Rich Lipoproteins in Capillaries. *Cell Metab* **2014**, *19* (5), 849–860.
128. Strauss, J. G.; Zimmermann, R.; Hrzenjak, A.; Zhou, Y.; Kratky, D.; Levak-Frank, S.; Kostner, G. M.; Zechner, R.; Frank, S. Endothelial Cell-Derived Lipase Mediates Uptake and Binding of High-Density Lipoprotein (HDL) Particles and the Selective Uptake of HDL-Associated Cholesterol Esters Independent of Its Enzymic Activity. *Biochem J* **2002**, *368* (Pt 1), 69–79.
129. Merkel, M.; Kako, Y.; Radner, H.; Cho, I. S.; Ramasamy, R.; Brunzell, J. D.; Goldberg, I. J.; Breslow, J. L. Catalytically Inactive Lipoprotein Lipase Expression in Muscle of Transgenic Mice Increases Very Low Density Lipoprotein Uptake: Direct Evidence That Lipoprotein Lipase Bridging Occurs in Vivo. *PNAS* **1998**, *95* (23), 13841–13846.
130. Connelly, P. W. The Role of Hepatic Lipase in Lipoprotein Metabolism. *Clin Chim Acta* **1999**, *286* (1–2), 243–255.
131. Feng, D.; Huang, Q. Y.; Liu, K.; Zhang, S. C.; Liu, Z. H. Comparative Studies of Zebrafish Danio Rerio Lipoprotein Lipase (Lpl) and Hepatic Lipase (Lipc) Genes Belonging to the Lipase Gene Family: Evolution and Expression Pattern. *J Fish Biol* **2014**, *85* (2), 329–342.

132. Mead, J. R.; Irvine, S. A.; Ramji, D. P. Lipoprotein Lipase: Structure, Function, Regulation, and Role in Disease. J *Mol Med* **2002**, *80* (12), 753–769.
133. Khetarpal, S. A.; Vitali, C.; Levin, M. G.; Klarin, D.; Park, J.; Pampana, A.; Millar, J. S.; Kuwano, T.; Sugasini, D.; Subbaiah, P. V.; Billheimer, J. T.; Natarajan, P.; Rader, D. J. Endothelial Lipase Mediates Efficient Lipolysis of Triglyceride-Rich Lipoproteins. *PLoS Genet* **2021**, *17* (9), e1009802.
134. Choi, S. Y.; Hirata, K.; Ishida, T.; Quertermous, T.; Cooper, A. D. Endothelial Lipase. *J Lipid Res* **2002**, *43* (11), 1763–1769.
135. Jaye, M.; Lynch, K. J.; Krawiec, J.; Marchadier, D.; Maugeais, C.; Doan, K.; South, V.; Amin, D.; Perrone, M.; Rader, D. J. A Novel Endothelial-Derived Lipase That Modulates HDL Metabolism. *Nat Genet 1999 21:4* **1999**, *21* (4), 424–428.
136. Birrane, G.; Beigneux, A. P.; Dwyer, B.; Strack-Logue, B.; Kristensen, K. K.; Francone, O. L.; Fong, L. G.; Mertens, H. D. T.; Pan, C. Q.; Ploug, M.; Young, S. G.; Meiyappan, M. Structure of the Lipoprotein Lipase–GPIHBP1 Complex That Mediates Plasma Triglyceride Hydrolysis. *PNAS* **2019**, *116* (5), 1723–1732.
137. Young, S. G.; Fong, L. G.; Beigneux, A. P.; Allan, C. M.; He, C.; Jiang, H.; Nakajima, K.; Meiyappan, M.; Birrane, G.; Ploug, M. GPIHBP1 and Lipoprotein Lipase, Partners in Plasma Triglyceride Metabolism. *Cell Metab* **2019**, *30* (1), 51–65.
138. Fuki, I. V.; Blanchard, N.; Jin, W.; Marchadier, D. H. L.; Millar, J. S.; Glick, J. M.; Rader, D. J. Endogenously Produced Endothelial Lipase Enhances Binding and Cellular Processing of Plasma Lipoproteins via Heparan Sulfate Proteoglycan-Mediated Pathway. *J Biol Chem* **2003**, *278* (36), 34331–34338.
139. Kuemmerle, N. B.; Rysman, E.; Lombardo, P. S.; Flanagan, A. J.; Lipe, B. C.; Wells, W. A.; Pettus, J. R.; Froehlich, H. M.; Memoli, V. A.; Morganelli, P. M.; Swinnen, J. V.; Timmerman, L. A.; Chaychi, L.; Fricano, C. J.; Eisenberg, B. L.; Coleman, W. B.; Kinlaw, W. B. Lipoprotein Lipase Links Dietary Fat to Solid Tumor Cell Proliferation. *Mol Cancer Ther* **2011**, *10* (3), 427–436.
140. Carter, S. A.; Foster, N. A.; Scarpini, C. G.; Chattopadhyay, A.; Pett, M. R.; Roberts, I.; Coleman, N. Lipoprotein Lipase Is Frequently Overexpressed or Translocated in Cervical Squamous Cell Carcinoma and Promotes Invasiveness through the Non-Catalytic C Terminus. *Br J Cancer* **2012**, *107* (4), 739–747.
141. Gago-Dominguez, M.; Redondo, C. M.; Calaza, M.; Matabuena, M.; Bermudez, M. A.; Perez-Fernandez, R.; Torres-Español, M.; Carracedo, Á.; Castelao, J. E. LIPG Endothelial Lipase and Breast Cancer Risk by Subtypes. *Sci Rep* **2021**, *11* (1), 1–10.
142. Trost, Z.; Sok, M.; Marc, J.; Cerne, D. Increased Lipoprotein Lipase Activity in Non-Small Cell Lung Cancer Tissue Predicts Shorter Patient Survival. *Arch Med Res* **2009**, *40* (5), 364–368.
143. Wang, W.; Bai, L.; Li, W.; Cui, J. The Lipid Metabolic Landscape of Cancers and New Therapeutic Perspectives. *Front Oncol* **2020**, *10*, 605154.

CHAPTER 2

Phase-separated liposomes hijack endogenous lipoprotein transport and metabolism pathways to target subsets of endothelial cells *in vivo*

This chapter was published as a research article:

Gabriela Arias-Alpizar[#], **Panagiota Papadopoulou[#]**, Xabier Rios, Krishna Reddy Pulagam, Mohammad-Amin Moradi, Roy Pattipeiluhu, Jeroen Bussmann, Nico Sommerdijk, Jordi Llop, Alexander Kros[*], Frederick Campbell[*]. Advanced Healthcare Materials 2022, 12(10), e2202709.

# denotes equal contribution

Abstract | Plasma lipid transport and metabolism is essential to ensure correct cellular function throughout the body. Dynamically regulated in time and space, the well characterized mechanisms underpinning plasma lipid transport and metabolism offer an enticing, but as yet underexplored, rationale to design synthetic lipid nanoparticles with inherent cell/tissue selectivity. Herein, we describe a systemically administered liposome formulation, composed of just two lipids, that is capable of hijacking a triglyceride lipase-mediated lipid transport pathway, resulting in liposome recognition and uptake within specific endothelial cell subsets. In the absence of targeting ligands, liposome-lipase interactions are mediated by a unique, phase-separated ('parachute') liposome morphology. Within the embryonic zebrafish, selective liposome accumulation is observed at the developing blood-brain-barrier. In mice, extensive liposome accumulation within the liver and spleen – which is reduced but not eliminated following small molecule lipase inhibition – supports a role for endothelial lipase, but highlights these liposomes are also subject to significant 'off-target' by reticuloendothelial system organs. Overall, these compositionally simplistic liposomes offer new insights into the discovery and design of lipid-based nanoparticles that can exploit endogenous lipid transport and metabolism pathways to achieve cell selective targeting *in vivo*.

2.1 Introduction

All cells rely on plasma lipid transport to maintain a correct intracellular balance of essential and non-essential fatty acids. This requires the dynamic regulation of the secretion, transport, and metabolism of water-insoluble fats throughout the body. Often packaged, secreted, and transported as nanometer-sized, solid lipid particles (*i.e.*, lipoproteins), many of the biological mechanisms underpinning endogenous plasma lipid transport and metabolism are now well understood.[1]

Despite compositional and structural similarities of lipoproteins and synthetic lipid-based nanoparticles however, there are currently only a few examples of nanoparticles that explicitly hijack endogenous lipid transport mechanisms to achieve target cell specificity. One notable example, however, is Onpattro® – a clinically approved lipid nanoparticle (LNP)-RNAi therapy used to treat polyneuropathies resulting from transthyretin-mediated amyloidosis (hATTR). In this case, selective recognition and uptake within target hepatocytes relies on the adsorption of soluble apolipoprotein E (apoE) to the surface of circulating LNPs. This, in turn, guides Onpattro® to low density lipoprotein receptors (LDLr) that are heavily expressed on the sinusoidal surface of hepatocytes.[2,3] This clinically relevant lipid nanoparticle formulation highlights the enticing, but largely unexplored,[4,5] potential of exploiting endogenous lipid transport to guide nanoparticles to specific tissues and cells within the body.

The three main plasma lipid transport forms are free fatty acids (FFAs), triglycerides (TGs) and cholesteryl esters (CEs).[1] FFAs are generally transported as a complex with serum albumin, whereas TGs and CEs are transported within the core of plasma lipoproteins – solid lipid particles surrounded by a lipid monolayer rich in phospholipids – and stabilized by apolipoprotein(s). The five major classes of lipoproteins are chylomicrons (secreted by intestine, *size*: 100 – 1000 nm); very-low density lipoproteins (VLDLs, secreted by liver, *size*: 50 – 200 nm); intermediate and low density lipoproteins (IDLs and LDLs, lipoprotein metabolites enriched in cholesterol, and, at high levels, associated with atherogenic disorders [6,7] *size*: 20 – 50 nm); and high density lipoproteins (HDLs, involved in reverse cholesterol transport,[8] size 8 – 12 nm). In the case of VLDL and chylomicrons, a single, surface-

bound apolipoprotein B – apoB100 or apoB48 respectively – stabilizes each secreted lipoprotein. HDLs, in contrast, are stabilized by apolipoprotein A-I (apoAI).[9,10] Once secreted into the bloodstream, soluble and exchangeable apolipoproteins (*e.g.*, apoA, C, D and E) recognize and bind to the surface of a circulating lipoprotein. These apolipoproteins guide lipoproteins to specific targets within the body. For example, apoE is a ligand for LDLr, promoting uptake primarily in hepatocytes,[11] lipoprotein-bound apoC2 functions as an obligatory cofactor of lipoprotein lipase (LPL),[12,13] whereas apoA1 binds a wide range of cognate receptors and enzymes including LDLr,[14] scavenger receptor B-1 (SRB-1),[15–17] ATP-binding cassette transporters A1 (ABCA1) and G1 (ABCG1),[18–20] and endothelial lipase (EL).[21,22]

Following transport, lipoproteins are generally metabolized to release free fatty acids that are then taken up locally by cells. TG lipases are key extracellular, hydrolytic enzymes that regulate lipid metabolism throughout the body. The three main members of the TG lipase family are LPL,[23] hepatic lipase (HL),[24] and EL[21,25] (encoded by the human genes *LPL*, *LIPC,* and *LIPG* respectively). All three share significant structural homology, including a conserved catalytic triad of amino acids (serine, aspartate and histidine), as well as conserved heparin and lipoprotein binding domains.[21,25] LPL is predominantly synthesized in adipose tissue, heart and skeletal muscle; HL in hepatocytes; and EL in vascular endothelial cells.[21] Once expressed, TG lipases are secreted and actively transported (in the case of LPL and HL) to the local endothelium where they anchor to heparan sulfate proteoglycans (HSPG) *via* electrostatic interactions.[22] As hydrolytic enzymes, LPL primarily hydrolyzes TGs,[26] HL – TGs and phospholipids,[24,27] and EL – phospholipids.[21] Substrate specificity is determined by sequence variation in the lid region of each enzyme.[21,28,29] However, whereas LPL and HL metabolize fats primarily derived from VLDL and chylomicrons, the principle function of EL is the regulation of HDL metabolism *via* interactions with apoA-1.[21,30–33] In addition, all three TG lipase family members are capable of internalizing lipoproteins *via* proteoglycan- or receptor-mediated pathways in a non-enzymatic fashion.[22,34,35]

Herein, we describe a systemically administered liposome formulation, composed of just two lipids, that preferentially targets a specific subset of endothelial cells *in vivo*. Most notably, these liposomes accumulate at the brain endothelium of an

embryonic zebrafish. Mechanistically, we show that target selectivity is linked to the ability of these liposomes to interact with endogenous (endothelial) lipase, although whether cell selectivity arises as a result of direct (*e.g.*, non-enzymatic lipase-mediated recognition and uptake) or indirect (*i.e.,* lipase mediated metabolism prior to cellular uptake) lipase engagement is not yet clear. With no additional 'targeting' functionality, lipase-liposome interactions are mediated through a unique, phase-separated ("parachute") liposome morphology, onto the surface of which preferentially adsorb apolipoproteins A1, A4 and E. Within 6-8 week old mice, liposomes predominantly accumulate within the liver and spleen. While in the liver, we show liposome accumulation is in part mediated by lipase interaction, these observations ultimately reaffirm that the capacity of these RES organs to clear nanoparticles from circulation is both proficient and mechanistically multipronged.

2.2 Results

PAP3 liposomes accumulate at the brain endothelium of embryonic zebrafish

Zebrafish embryos are convenient, accurate and cost effective animals to study the behavior and pharmacokinetics of nanoparticles *in vivo*,[36,37] to assess and predict key nanoparticle-liver interactions within higher vertebrates and to identify endogenous biological pathways underpinning nanoparticle fate *in vivo*.[38–40] From a preliminary screen of intravenously (*i.v.*) administered liposomes, we unexpectedly observed selective accumulation of a liposomal formulation, PAP3, within the head region of a ~78 hours post fertilization (hpf) zebrafish embryo (**Figure 1a, b)**. PAP3 liposomes (size: ~120 nm) were composed of an equimolar mixture of just two lipids: a novel synthetic lipid, 2-hydroxy-3-oleamidopropyl oleate (DOaG), and the naturally occurring, 1,2-distearyl-*sn*-glycero-3-phosphocholine (DSPC) (**Figure 1c**). These liposomes contained no additional targeting functionality. Looking closely within the head region of the zebrafish embryo, PAP3 liposomes clearly accumulated within some (*e.g.*, mesencephalic vein (MsV), mesencephalic artery (MsA), middle mesencephalic central artery (MMCtA), middle cerebral vein (MCeV), primordial

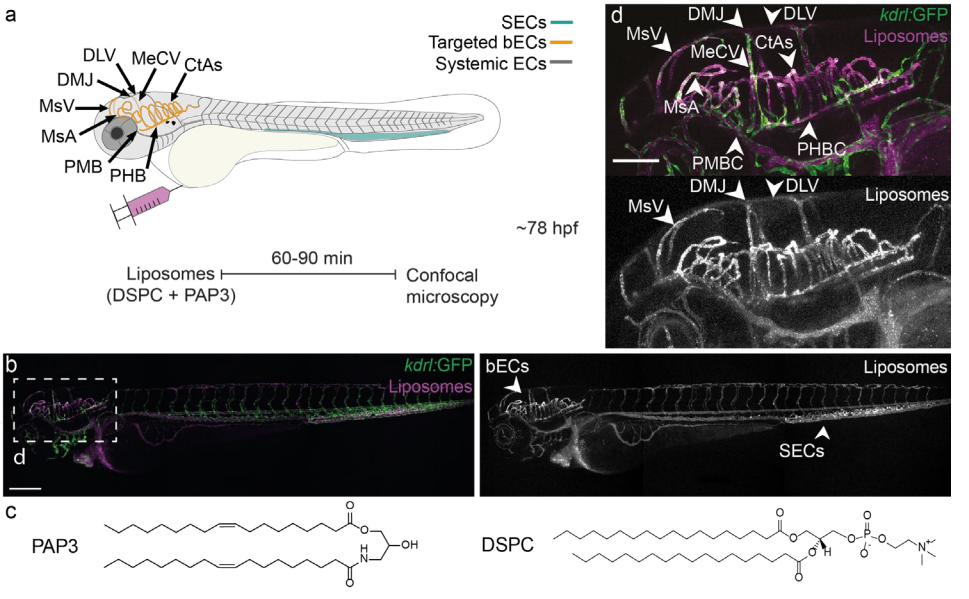

Figure 1. Biodistribution of PAP3 liposomes within zebrafish embryos (78 hpf). a) Schematic zebrafish larvae in lateral (whole body) view, showing the site of microinjection and key cranial vessels. Fluorescently labeled liposomes are imaged with confocal microscopy after 60-90 min. The vasculature as follows, liposome targeted bECs in yellow and systemic endothelium in dark gray, scavenging endothelial cells (SECs) in cyan, at ~78 hours post fertilization (hpf). **b)** Biodistribution (10x magnification, lateral view) of PAP3 liposomes within a Tg(kdrl:GPF) zebrafish embryo at 1.5 hours post injection (hpi). **c)** Molecular structure of lipids used in equimolar mixture for the formulation of PAP3 liposomes, DOaG and DSPC. **d)** Zoom of the cranial region in lateral view. bECs = brain endothelial cells; CtAs = central arteries; DLV = dorsal longitudinal vein; DMJ = dorsal midline junction; MCeV = middle cerebral vein; MsA = mesencephalic artery; MsV = mesencephalic vein; PMBC = primordial midbrain channel; PHBC = primordial hindbrain channel; SECs = scavenging endothelial cells. Liposomes formulated by extrusion (5 mM, 0.2% mol DOPE-LR). Scale bars: 200 µm (lateral view) and 100 µm (zoom).

hindbrain channels (PHBC) and cerebral arteries (CtAs)), but not all (*e.g.*, dorsal longitudinal vein (DLV), primordial midbrain channel (PMBC)) blood vessels and capillaries within the embryo head (**Figure 1d** and **Figure 2a)**. The specific blood vessels and capillaries in which PAP3 liposomes accumulated have been previously characterized as the brain endothelial cells (bECs), constituting the blood-brain-barrier (BBB) of the developing embryo.[41–43]

To verify selective liposome accumulation with bECs, PAP3 liposomes were administered (*i.v.*) within embryonic zebrafish at different developmental stages (2, 3 and 4 dpf) (**Figure 2b-d**). This two-day timeframe spans the onset and maturation of the embryonic BBB, most prominently within the mid- and forebrain, following complete hindbrain vascular invasion by 48 hpf (characterized by CtA capillary loops connecting both PHBCs with the central basilar artery (BA)).[41] Accordingly, at 2 dpf, PAP3 liposomes mainly accumulated in functional bECs, within blood vessels and capillaries of the hindbrain, namely CtAs, BA and PHBCs (**Figure 2b**). At 3 dpf, as blood vessels irrigate rostrally throughout the brain,[50] PAP3 liposomes accumulated within newly formed capillaries of the mid- and forebrain (**Figure 2c, e**), as well as within the continually expanding BBB vasculature of the hindbrain (**Figure 2f, h, i** and **Figure S1a-b** for a Z-stack depth color-coded of the vasculature in dorsal view). By 4 dpf, PAP3 liposomes extensively accumulated throughout the brain endothelium of the embryonic zebrafish (**Figure 2d**). Notably at all developmental stages, liposomes did not drastically accumulate in systemic blood vessels (*e.g.,* PMBC and DLV) within the head region (**Figure 2g**), confirming a specific preference of PAP3 liposomes for bECs at all developmental timepoints. Indeed, colocalization of PAP3 liposome accumulation and Claudin-5 expression, notably within the CtAs, MMCtA (**Figure 2h-i**) and MsA, was confirmed in Tg*(cldn5a:*eGFP*)*[42] embryos, stably expressing an integrated eGFP-Claudin5a fusion protein (**Figure 2j-k** and **Figure S1c**). In addition to bEC target selectivity, PAP3 liposomes also accumulated in the tail within the caudal hematopoietic tissue (CHT) and caudal vein (CV) of the embryo (**Figure 1a, b**). We have previously shown that these blood vessels are composed of scavenger endothelial cells (SECs) and blood resident macrophages, equivalent to hepatic reticuloendothelial (RES) cells (*i.e.,* liver sinusoidal endothelial cells (LSECs) and Kupffer cells (KCs)) in mammals.[38] SECs, in particular, proficiently recognize and clear anionic nanoparticles, as well as neutral DSPC liposomes, from circulation *via* the conserved scavenger receptors, Stabilin-1 and -2.

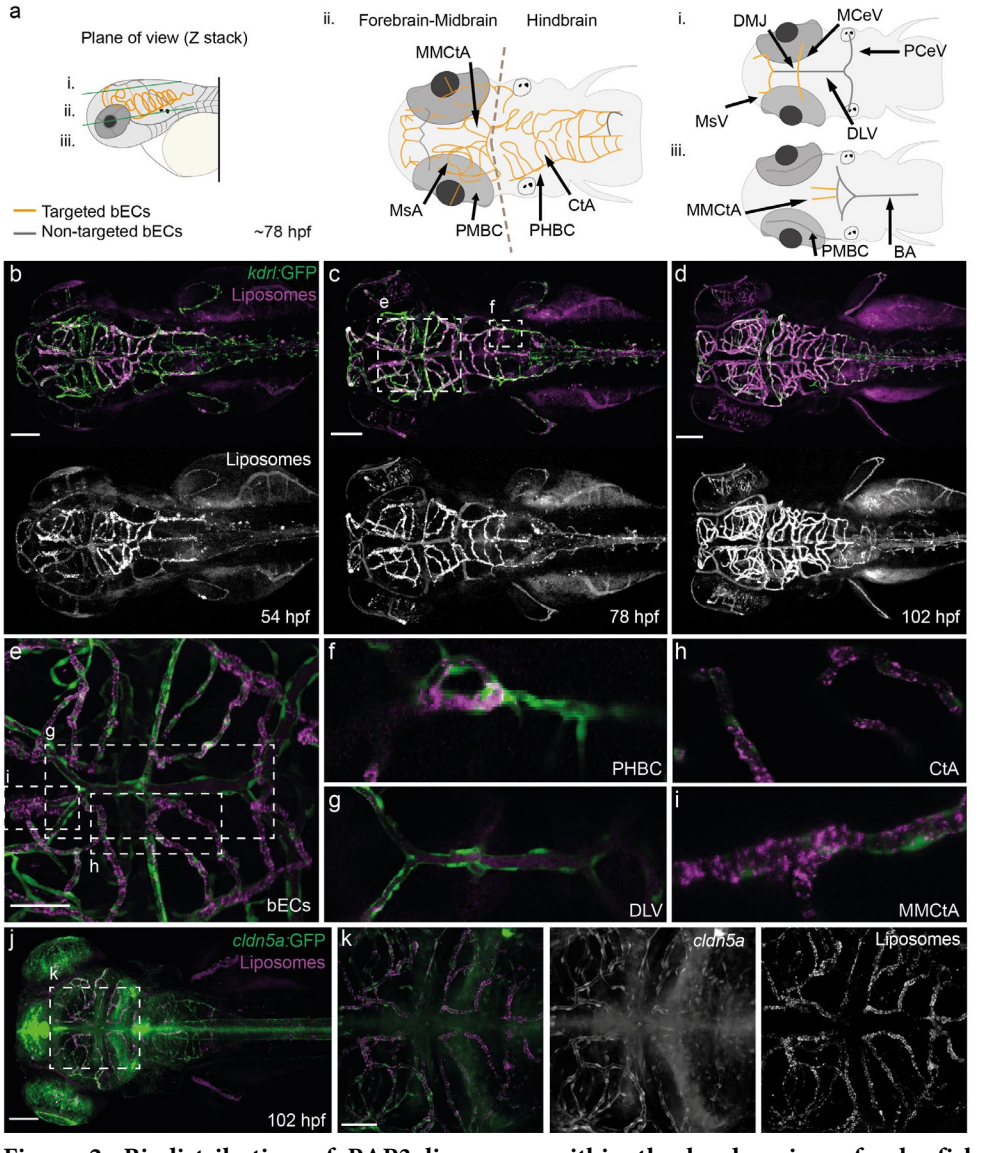

Figure 2. Biodistribution of PAP3 liposomes within the head region of zebrafish embryos. a) Schematic zebrafish larvae with key blood vessels in different planes of view. See **Figure S1a-b** for a Z-stacks depth color-coded zebrafish vasculature. Dorsal view, showing the **i.** top, **ii.** middle and **iii.** bottom layer diagram. The vasculature as follows, targeted brain endothelial cells (bECs) in yellow and non-targeted systemic endothelium in dark gray, at ~78 hpf. PHBC = primordial hindbrain channel; CtA = central artery; DLV = dorsal longitudinal vein; MsA = mesencephalic artery; MsV = mesencephalic vein; MMCtA = middle mesencephalic central artery. **b)** Biodistribution (10x magnification, dorsal view, 1.5 hpi) of PAP3 liposomes within the head region of a Tg(*kdrl:*GFP) zebrafish embryo at 54

hpf, **c)** 78 hpf, **d)** 102 hpf. **e)** High magnification view of **c** (inset, 40x, zoom) showing PAP3 liposomes accumulating within bECs. **f)** Posterior part of the PHBC, **g)** DLV, **h)** CtA, **i)** MMCtA. **j-k)** Biodistribution of PAP3 liposomes in a Tg*(cldn5a:*GFP*)*[42] zebrafish embryo (102 hpf) with GFP-labeling in blood and choroid plexus brain barrier showing colocalization of *cldn5a* with fluorescent liposomes. Zoom in of the region that includes the hindbrain vasculature and colocalization with *cldn5a* expression is shown in **Figure S1c**. Liposomes formulated by extrusion (5 mM, 0.2 mol% DOPE-LR). Scale bars: 100 µm (dorsal view), 50 µm (tissue level).

Accordingly, systemic administration of DSPC-containing PAP3 liposomes in zebrafish mutants lacking functional scavenger receptors Stabilin-1 and Stabilin-2 (*stabilin-1*^{ibl3} *stabilin-2*^{ibl1})[39] resulted in reduced liposome accumulation within the CHT and CV of the embryo without significantly affecting bEC targeting (**Figure S2**). This confirmed that (off-)targeting of PAP3 liposomes to RES-like cell types, but not bECs, was, at least in part, Stabilin-dependent. However, persistent liposome accumulation within blood resident macrophages of the mutant *stabilin-1/-2* double knockout embryo, suggested potentially significant and competitive pathways of PAP3 RES clearance.

Cryo-TEM revealed a novel 'parachute' liposome morphology that is essential for BBB targeting in embryonic zebrafish

To rationalize bEC-liposome specificity, and in the absence of any additional targeting functionality (*e.g.,* targeting ligands), cryogenic transmission electron microscopy (cryo-TEM) was performed to characterize PAP3 liposome ultrastructure. Unexpectedly, these images revealed a highly unusual phase-separated, "parachute" morphology, characterized by a single electron-dense protrusion within each liposomal membrane (**Figure 3a-c** and **Figure S3**). Such parachute-like structures have been previously reported for lipid-polymer hybrid nanoparticles,[51,52] propofol-containing liposomes,[53] and mRNA encapsulated LNPs[54,55] but, to the best of our knowledge, have not been reported for purely lipidic nanoparticles. Given the flat, bilayer preference of amphipathic DSPC, the observed phase-separated protrusion was hypothesized to be rich in DOaG. Indeed, at a molecular level, DOaG is structurally very similar to diacylglycerols (DAGs) whose hydrophobicity and geometry are known to alter the spontaneous curvature of PC

lipid membranes and perturb lamellar membrane structures resulting in the formation of non-bilayer phases.[56–60]

To investigate the possible association of phase separation and liposome-bEC selectivity, PAP3 liposomes were formulated at varying molar ratios (10-50 mol% DOaG) to correlate liposome morphology with *in vivo* biodistribution (**Figure 3d-i**). Of note, >50 mol% DOaG resulted in liposome aggregation. Cryo-TEM images of 10% DOaG liposomes (10-90 mol% DOaG-DSPC) revealed a mixture of non-spherical, bi-layered and multilamellar particles with no evident phase separation (**Figure 3d** and **Figure S4a**). 10% DOaG liposomes mostly accumulated within SECs in the CV and CHT of the embryo (**Figure S5a**) and did not target bECs (**Figure 3e**). Likewise, 20% DOaG liposomes (20-80 mol% DOaG-DSPC) were predominantly non-spherical (**Figure 3f** and **Figure S4b**), mainly accumulated within SECs (**Figure S5b**) and did not target bECs (**Figure 3g**). However, at 20% DOaG, small electron-dense protrusions within the liposome membrane indicated a liposome formulation approaching its miscibility threshold (**Figure 3f, Figure S4b** – white arrows). This was confirmed by the clear phase separation of 30% DOaG liposomes (30-70 mol% DOaG-DSPC) in which a single lipid protrusion was now clearly evident within each discreet liposome membrane (**Figure 3h, Figure S4c**). 30% DOaG liposomes, as for PAP3 liposomes (*i.e.,* 50-50 mol% DOaG-DSPC), proficiently targeted bECs of the zebrafish larvae (**Figure 3i** and **Figure S5c**). A 30 mol% DOaG miscibility threshold (within a DSPC bilayer) closely mirrors that previously reported for structurally similar DAGs (*i.e.,* 25 mol% miscibility threshold within a PC bilayer).[61]

Accordingly, to better understand the molecular details of DOaG lipid that facilitate the phase separation, we replaced the amide bond in DOaG to an ester bond, resulting in the naturally occurring diacylglycerol analogue, dioleyolglycerol (DOG). This also led to phase-separated liposomes and bEC targeting (**Figure S6a-d**). However, creating an analogue with two amides or replacing the oleic chains to stearyl chains (**Figure S6e-f**) resulted in lipids which cannot formulate liposomes. In addition, lipid phase separation is known to be dependent on the gel phase state

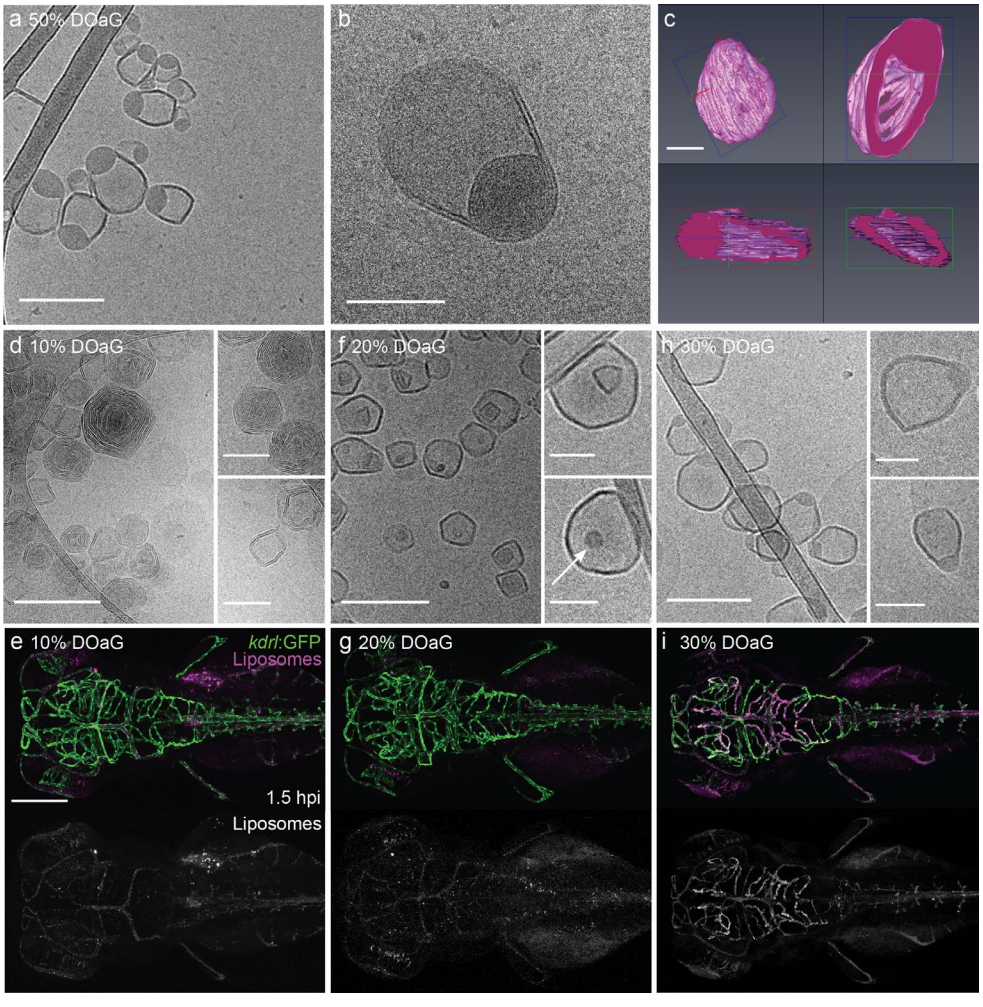

Figure 3. Cryo-TEM images of PAP3 liposomes and correlation of morphology with bECs targeting in zebrafish larvae (~78 hpf). a-b) Cryo-TEM images of PAP3 (50-50 mol% DOaG-DSPC) liposomes and **c)** 3D model of a representative PAP3 liposome, reconstructed based on the electron density derived from cryo-electron tomography, demonstrating the whole body and different plane sections of the particle**.** Cryo-TEM and biodistribution (in a Tg*(kdrl:*GFP*)* zebrafish embryo at 1.5 hpi) of liposomes containing DSPC and **d-e**) DOaG 10 mol%, **f-g)** 20 mol%, and **h-i)** 30 mol%. Liposomes (5 mM, 0.2% mol DOPE-LR) described in all panels formulated by ethanol injection except panel **b** and **c** - formulated by extrusion. Scale bars: 200 nm and 100 nm for higher magnification insets for cryo-TEM, 100 nm for 3D reconstruction and 200 μm for dorsal zebrafish view.

of a lipid bilayer. Consequently, switching co-formulant phospholipid from saturated DSPC (phase transition temperature (T*m*) 55°C) to unsaturated DOPC (T*m* -17°C) resulted in liposomes (at room temperature) with no apparent phase separation and severely ablated bEC targeting (**Figure S7**). Notably, incorporation of polyethylene glycol (PEG)-conjugated lipid (*e.g.* 1,2-distearoyl-sn-glycero-3-phosphatidylethanolamine DSPE-PEG, 5 mol% as commonly used)[62,63] to the PAP3 liposome results in the loss of selective targeting, as observed in the zebrafish (**Figure S8a-b**). Altogether, these experiments confirmed the critical requirement of phase-separated lipid protrusions for bEC selective liposome accumulation within the embryonic zebrafish.

PAP3 liposome targeting and uptake by bECs in zebrafish larvae is mediated by (endothelial) lipase

In the absence of any additional targeting functionality (*i.e.,* targeting ligands), we next investigated whether PAP3 liposomes could be hijacking an endogenous plasma lipid transport pathway to selectively target bECs of the embryonic zebrafish. Importantly, all major elements of mammalian plasma lipid transport and metabolism, including the expression of apolipoproteins, lipoprotein receptors (*e.g.*, low density lipoprotein receptor, LDLr) and hydrolytic enzymes (*e.g.*, lipases), are present and functional in a three day old zebrafish embryo.[64–66] These conserved features have led to the zebrafish being used as an *in vivo* model to investigate various lipid disorders,[67–69] including hypertriglyceridemia, a disease caused by a malfunction in lipase-mediated plasma lipid transport and metabolism.[70] Following secretion into blood, the typical first step of lipoprotein-mediated plasma lipid transport is the binding of soluble apolipoproteins.[1] To identify serum proteins preferentially adsorbed to PAP3 liposomes, we performed a photoaffinity-based capture of the PAP3 liposome protein corona.[71] For consistency, this experiment should be performed using zebrafish serum collected during embryonic stages; however, given the practical difficulties in obtaining sufficient embryonic zebrafish serum, these experiments were performed in human serum and do not necessarily reflect the exact composition and abundance of serum proteins in the developing zebrafish embryo. Importantly, functional conservation between the most abundant serum proteins in humans and zebrafish has been previously reported, including

similar profiles in apolipoproteins and complement proteins.[72] For this method, it was necessary to incorporate the photoaffinity probe, IKS02 (5 mol%),[71] within the PAP3 liposome formulation. Incorporation of this probe did not significantly alter the physicochemical properties or *in vivo* behavior of PAP3 liposomes (**Table S1**). Following protein corona capture, isolation and subsequent proteomic analysis, we identified soluble apolipoproteins as the major protein corona components of both PAP3 and control (100% mol) DSPC liposomes (**Figure S9**). However, while no obvious differences in protein corona composition could easily explain the very different *in vivo* fates of these two liposome formulations, a significant enrichment of apoA1, A4 and apoE on the surface of both PAP3 and DSPC liposomes, at least, conformed to a lipoprotein-like transport and metabolism targeting rationale.

Given the presence of apolipoproteins on the surface of PAP3 liposomes, we next investigated the potential role of extracellular, TG lipases in the selective accumulation of PAP3 liposomes at the BBB of the zebrafish larvae. Lipases are heparin-releasable[24,73] and following heparin pre-injection (*i.v.*; 30 minutes prior to PAP3 liposome administration), PAP3 liposomes remained freely circulating with no apparent bEC targeting (**Figure 4a-f**). While this suggested TG lipase involvement, heparin is also known to bind a wide range of other proteins that could (in)directly disrupt liposome-bEC accumulation.[74] We therefore selectively inhibited TG lipase enzymatic activity using the small molecule inhibitor, XEN445.[75,76] Following XEN445 pre-treatment (1 nL, 50 μM at 24 h and 1 h prior to PAP3 liposome administration), we observed a significant decrease in bEC targeting of liposomes. This result confirmed TG lipases play a fundamental role in determining the fate of PAP3 liposomes within the embryonic fish (**Figure 4g-i**).

Surprisingly, however, we found that PAP3 liposomes associated with bECs were no longer heparin-releasable (**Figure 5a-c**). This indicated that PAP3 liposomes, following initial lipase interaction, were internalized by bECs. To confirm this hypothesis, we incorporated the (endosomal) pH-sensitive dye, pHrodo™, within the PAP3 liposome membrane *via* a phospholipid anchor (as in reference [37]) (see **SI** for characterization and **Figure S10** for pH-dependent emission).

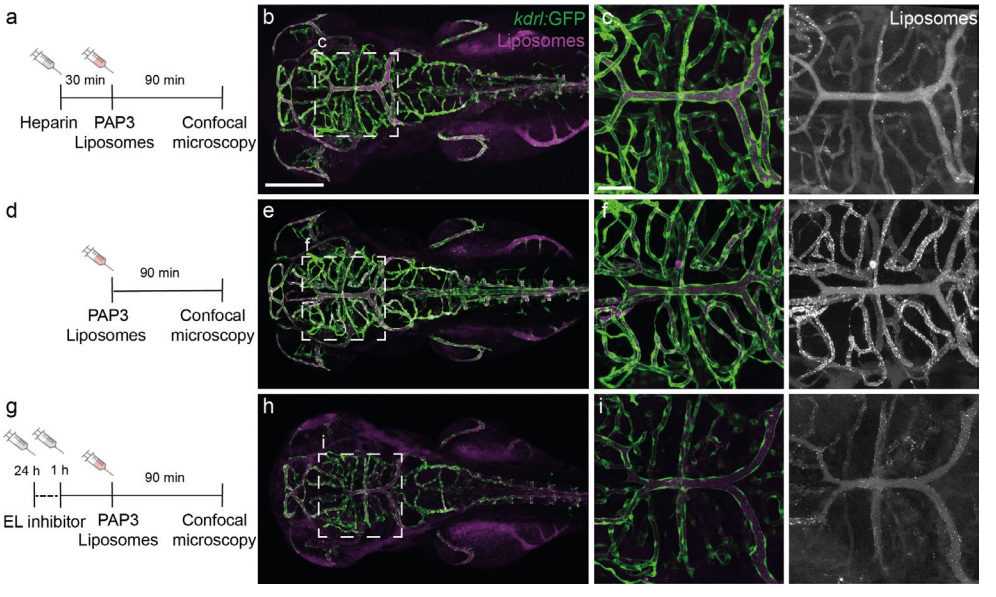

Figure 4. bECs targeting by PAP3 liposomes is inhibited by heparin and an TG lipase inhibitor. a) Timeline of injection and imaging. **b-c)** Biodistribution (10 and 40x magnification) of PAP3 liposomes at 1.5 hpi, after heparin (1 nl, 50 mg/ml) administration. **d)** Timeline of injection and imaging. **e-f)** Biodistribution (10 and 40x magnification) of PAP3 liposomes, as a reference, at 1.5 hpi. **g)** Timeline of injection and imaging. **h-i)** Biodistribution (10 and 40x magnification) of PAP3 liposomes at 1.5 hpi, after a double administration (24 h and 1 h prior liposome injection) of a TG lipase inhibitor (XEN445, 1 nL, 50 μM). All zebrafish larvae, Tg*(kdrl:*GFP*)* at ~78 hpi. Liposomes (5 mM, 0.2% mol DOPE-LR) formulated by extrusion. Scale bars: 200 μm (whole embryo) and 50 μm (tissue level).

Incorporation up to 0.5% mol of this fluorescent probe did not significantly alter the size or bEC targeting proficiency of PAP3 liposomes (**Table S1**). Following liposome administration, pHrodo™-associated fluorescence was clearly observed within bECs, *e.g.* CtAs and MMCtA, but not the systemic endothelium, *e.g.* DLV or PMBC (**Figure 5e-f**), mirroring the observed biodistribution of PAP3 liposomes and confirming PAP3 liposomes are endocytosed by bECs following initial lipase-liposome interaction.

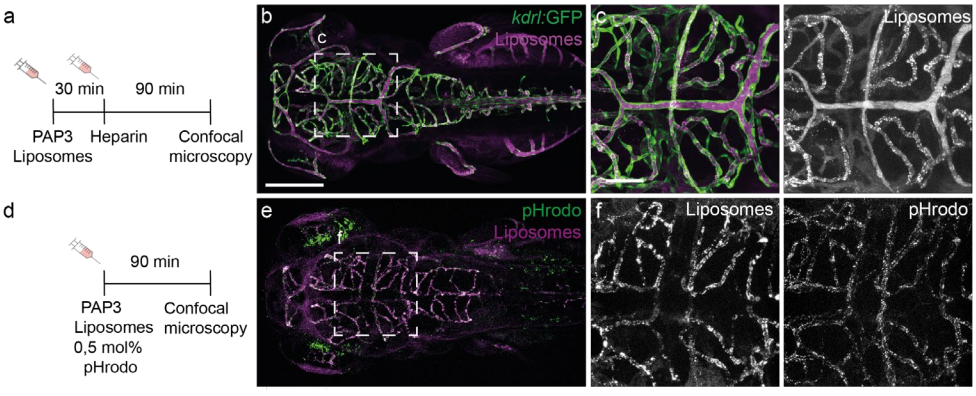

Figure 5. Internalization of PAP3 in zebrafish bECs. a) Timeline of injection and imaging. **b-c)** Biodistribution (10 and 40x magnification) of PAP3 liposomes (5 mM, 0.2 mol% DOPE-LR) after post-administration of heparin (1 nl, 50 mg/ml) in a Tg(kdrl:GFP) zebrafish embryo at 1.5 hpi. **d)** Timeline of injection and imaging. **e-f)** Biodistribution of PAP3 liposomes (10 mM), containing 0.5 mol% of pH sensitive DOPE-pHrodo (green/grey) to indicate endocytosis and 0.5 mol% of pH non-sensitive dye DOPE-NBD (magenta/grey) to label liposomes, in a AB/TL zebrafish embryo at 1.5 hpi. All zebrafish larvae at ~78 hpi. Liposomes formulated by extrusion. Scale bars: 200 µm (whole embryo) and 50 µm (tissue level).

PAP3 liposomes accumulate within the liver and spleen in mice, mediated (partially) by triglyceride lipase

Finally, we quantified the dynamic biodistribution of systemically administered PAP3 liposomes in 6-8 week old male mice. For these experiments, both XEN445 pre-treated (30 mg/kg XEN445 orally *b.i.d.* for 9 days prior to liposome administration) and untreated mice were used. As positron emission tomography (PET) tracer, a non-exchangeable ^{64}Cu ($T_{1/2}$= 12,7 h) radionuclide was incorporated within the PAP3 liposome formulation, chelated *via* the lipid-NOTA conjugate, NOTA-Bz-SCN-C18 (0.2 % mol). Based on 'cold' experiments using stable Cu isotopes, the incorporation of this lipid and/or Cu chelation protocol did not affect the physicochemical properties, morphology and/or bEC targeting proficiency of PAP3 liposomes in embryonic zebrafish (**Figure S11**, **Table S1**). Of note, phase-separation on PAP3 liposomes is also maintained upon incubation in mouse serum (**Figure S12**). Following tail vein injection (2845 ± 185 and 2480 ± 260 kBq/100 µL,

XEN445 treated and non-treated mice respectively; n=2 per group), PET scans were obtained, from 1 min to 6 hours post-injection, to visualize liposome biodistribution (**Figure 6a**). These values were corroborated through *ex vivo* radioanalysis (% ID/g, n=3) of the (major) organs (heart, brain, liver, spleen, kidneys, lungs, stomach and testes) and blood, following cardiac perfusion and organ collection at 10 min, 2 h and 6 hpi (**Figures 6b, c** and **Figure S13**). This data revealed rapid and extensive liposome accumulation within the murine liver (*ca.* 53% ID/g, 10 min post-injection) and spleen (*ca.* 106% ID/g) with low levels of PAP3 liposome accumulation in all other organs.

Following XEN445 pre-treatment (n=3 per time point), however, a significant increase of liposomes in circulation was observed at 2 h and a significant decrease in liposome accumulation within the murine liver, but not the spleen, was observed (**Figure 6b, c**). This reduction in PAP3 liposome liver accumulation, following small molecule TG lipase inhibition, confirmed at least a partial role for (endothelial) lipase in determining the fate of systemically administered PAP3 liposomes in mice. However, the failure of XEN445 to reduce liposome uptake in the spleen, as well as negligible PAP3 liposome accumulation in other EL-expressing organs (*e.g.,* lungs and testes), was equally indicative of significant 'off-target' and lipase-independent pathways of PAP3 liposome processing within RES organs of the mouse. As observed in the zebrafish embryo (**Figure 1b**), these 'off-target' interactions in the murine liver and spleen are most likely mediated by scavenging cell types, namely LSECs, KCs and splenic macrophages,[77,78] and these interactions are, in turn, mediated by a distinct array of receptors and enzymes, including Stabilins, class B scavenger receptors, ATP-binding cassette transporters, as well as TG lipases. To this end, it is noteworthy that apoA1-decorated nanobiologics have been specifically developed to preferentially target myeloid cells, notably in the liver and spleen.[79–81]

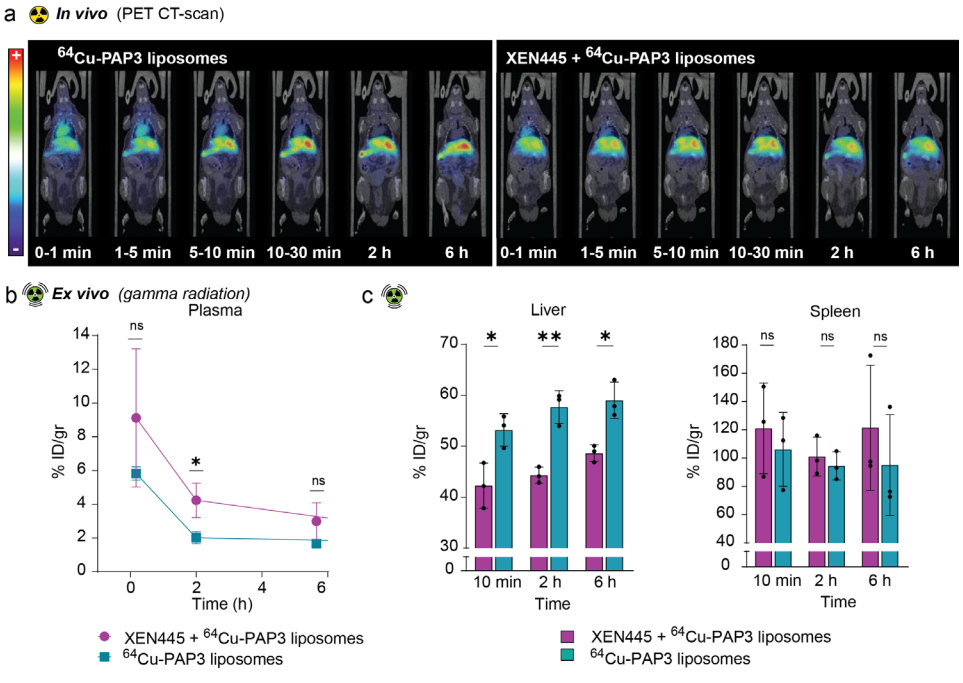

Figure 6. Biodistribution of radiolabeled PAP3 liposomes in mice. a) Representative positron emission tomography (PET) images (coronal projections) obtained at 0-1, 1-5, 5-10, 10-30 min, 2 h and 6 h after injection of radiolabeled PAP3 liposomes containing 0.2 mol% of ^{64}Cu-NOTA-Bz-SCN-C18 in 6-8 weeks male mice treated (or not treated) with XEN445 (30 mg/kg orally, *b.i.d.* for 9 days) prior to liposomal injection (n=2 per group and timepoint). PET images have been co-registered with representative CT slices for anatomical localization of the radioactive signal. **b)** *Ex vivo* gamma radiation counter of plasma in mice treated (or not treated) with XEN445. Concentration of radioactivity in plasma at 10 min, 2 h and 6 h after *i.v.* administration of radiolabeled PAP3 liposomes (n=3 per time point). **c)** *Ex vivo* gamma radiation counter of liver and spleen in mice treated (or not treated) with XEN445 at 10 min, 2 h and 6 h after *i.v.* administration of radiolabeled PAP3 liposomes (n=3 per group and time point). Statistical significance was evaluated using a two-tailed unpaired Student's t-test. ns: not significant ($P > 0.05$). Significantly different *$P < 0.05$, **$P < 0.01$; ***$P < 0.001$. Exact P values for **b**: 0.2379, 0.0242, 0.1095. Exact P values for **c**: 0.0259, 0.0029, and 0.0103 at 10 min, 2 h and 6 h respectively for the liver and 0.5668, 0.5323, 0.4659 for the spleen.

2.3 Discussion and Conclusion

Herein, we describe a liposome formulation, consisting of just two lipids, that is capable of hijacking an endogenous lipase-mediated pathway of lipid transport and metabolism to selectively target, and be taken up by, specific subsets of endothelial cells. While lipases, in particular small secretory phospholipase A_2 (sPLA2), have been previously exploited to achieve localized, stimuli-responsive drug release within target tissues (*e.g.*, solid tumors),[82,83] lipid nanoparticle targeting of TG lipases has, to the best of our knowledge, not been described before.

Lacking any additional targeting functionality, lipase recognition of PAP3 liposomes is mediated through a unique phase-separated, 'parachute' morphology. Such extreme phase-separated morphologies have not been described before for purely lipid nanoparticles. The discrete lipid-rich protrusion of each liposome resembles, in both structure and size, a solid lipid nanoparticle (*i.e.,* lipoprotein-like) and, as for analogous DAG/PC lipid mixtures, is likely characterized by increased stress on the bended membrane and increased surface hydrophobicity.[84,85] Although stable in water and Tris Buffer (**Figure S14** and **Table S1**), PAP3 liposomes tend to aggregate in physiologically relevant saline-containing buffers (**Table S1**). This is in line with observations showing that increased DAG concentrations in PC bilayers decreases the ability of PC to coordinate sodium ions.[86] However, PAP3 liposomes are stable in serum (**Figure S12**). Presumably, this is due to the rapid adsorption of soluble apolipoproteins (apoA1, A4 and E) to the liposome surface, as is required for the stabilization of endogenous secreted lipoproteins.[1] While greater molecular understanding is required as to how these lipid-rich, phase-separated protrusions are stably incorporated within the PAP3 liposome membrane, their compositional simplicity, unique morphology and unprecedented *in vivo* behavior provides an important proof-of-concept of a selective, lipase-mediated uptake pathway *in vivo*.

A key outstanding question is the precise mechanism of PAP3 liposome recognition and uptake within endothelial cells following lipase interaction. Here, we propose three plausible pathways. Pathway 1 – TG lipase binds to and directly internalizes PAP3 liposomes *via* cell surface proteoglycans (*e.g.* HSPG). This non-enzymatic, lipase-mediated pathway of endogenous lipoprotein uptake is known to be

particularly proficient in the case of lipase-mediated uptake of HDL particles.[22,34] Pathway 2 – TG lipase binds to PAP3 liposomes and acts as bridging molecule to a secondary receptor on the same cell, *e.g.,* apoER2, LRP1. Lipase-mediated bridging interactions are also known to facilitate lipoprotein intracellular uptake. [22,34,87] Pathway 3 – TG lipase binds to and enzymatically remodels PAP3 liposomes. Released PAP3 liposome metabolites are then recognized and internalized by alternative receptors expressed on target cells.

In zebrafish embryo, liposome selectivity for TG lipases is represented by bEC specific targeting, particularly for EL and LPL over HL. Expression of EL and LPL within the head of the zebrafish embryo is high from 2 to 4 dpf.[88,89] Together with the observed prevalence of ApoA1 -a cofactor of EL – on the PAP3 liposome surface (**Figure S9**) and XEN445 being 50-100 fold more selective inhibitor of EL (IC_{50} = 237 nM) over LPL (IC_{50} = 20 μM) and HL (IC_{50} = 9.5 μM).[75] This strongly suggests PAP3 liposomes preferentially hijack an EL-mediated pathway of endogenous lipoprotein recognition and metabolism.[21,31] We cannot however exclude the recognition of PAP3 liposomes similarly by other lipases, namely lipoprotein lipase (LPL) and hepatic lipase (HL) and by cell types other than endothelial cells due to competing interactions. In mice, EL expression is dynamically restricted in both time and space and is particularly high between embryonic stages E8.5 and E11.5 (but not later[90]) within the developing murine brain. In healthy adults, EL expression is mainly restricted to the lungs, liver, spleen, testes and ovaries (during pregnancy) and is particularly high in the placenta of pregnant mice.[21,31,90,91] A similar restricted pattern of EL expression has been reported in humans.[21]

Here, it is important to mention the significant decrease of PAP3 liposome uptake in the mouse liver after XEN445 treatment. This signifies the uptake acts – at least partially – as a liposome clearance mechanism via a lipase-mediated pathway. While other pathways, involving lipoprotein and more general scavenger receptors in hepatocytes and liver sinusoidal endothelial cells, as well as macrophage uptake via opsonization processes, are well established as lipid nanoparticle clearance mechanisms,[77] the role of TG lipases on nanoparticle clearance pathways, to our knowledge, has not been described before. However, additionally to the selective lipase-mediated clearance/uptake pathways, the significant competing off-target

interactions by liver and spleen have to be addressed and minimized to fully exploit this system. To this end, it will be fascinating to see if EL-mediated liposome targeting can be enhanced *via* local PAP3 liposome administration and/or dietary control of lipase expression.

Finally, this work again highlights the unique opportunities the zebrafish embryo can offer within nanomedicine discovery and development pipelines. Beyond the benefits of size, transparency, fecundity and ease of genetic manipulation,[92] in this case, the very discovery of ('irrational') PAP3 liposomes and the biological mechanism revealing the involvement of lipase-mediated pathways was only possible through our ability to screen and visualize large numbers of liposome formulations *in vivo*, at high resolution and across an entire living organism.

2.4 Materials and Methods

General reagents: 1,2-dioleoyl-*sn*-glycero-3-phosphocholine(DOPC), 1,2-distearoyl-*sn*-glycero-3 phosphocholine (DSPC), 1,2-dioleoyl-*sn*-glycero-3-phosphoethanolamine-N-(lissamine rhodamine B sulfonyl) (DOPE-LR) and NOTA-Bz-SCN-C18 (custom made), were purchased from Avanti Polar Lipids (Alabaster, AL, US). Additional DSPC was purchased from Lipoid GmbH. pHrodo™ Red, succinimidyl ester (pHrodo™ Red, SE) was purchased from Thermo Fisher Scientific. DOPE-pHrodo was synthesized as previously reported.[93] All other chemical reagents were purchased at the highest grade available from Sigma Aldrich and used without further purification. All solvents were purchased from Biosolve Ltd. Ultrapure MilliQ® water, purified by a MilliQ Advantage A10 water purification system from MilliPore, was used throughout. Heparin sodium salt from porcine intestinal mucosa, sodium carboxymethyl-cellulose (average Mw 90,000) and Tween 20 were purchased from Sigma Aldrich. XEN445 was purchased from AdooQ Bioscience (Irvine, CA, USA) and from Sigma Aldrich.

Synthesis and characterization of DOaG and DOG lipid: Column chromatography was performed using silica gel (40-63 μm, 60 Å, Screening Devices, The Netherlands). TLC analysis was performed on Merck silica gel 60/Kieselguhr

F254, 0.25 mm TLC plates. Compounds were visualized by KMnO4 stain (K_2CO_3 (15 g), $KMnO_4$ (2 g), and H_2O (200 mL)). 1 H spectra were recorded on a Bruker AV 400 MHz spectrometer. Chemical shifts are reported in ppm (δ), relative to the deuterated solvent as internal standard. Data are reported as follows: chemical shifts (δ), multiplicity (s=singlet, d=doublet, dd=doublet of doublet, td=triple of doublet, t=triplet, q=quartet, m=multiplet), coupling constants (J) reported in Hz. High resolution mass spectra were recorded by direct injection (2 μL of a 1 mM solution in methanol) using a mass spectrometer (Thermo Finnigan LTQ Orbitrap) with an electrospray ion source run in positive mode (source voltage 3.5 kV, sheath gas flow 10, capillary temperature 250°C).

2-hydroxy-3-oleamidopropyl oleate (Dioleoylamidoglycerol, DOaG)

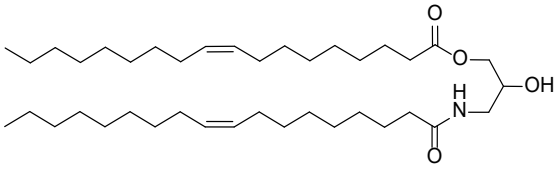

To a round bottom flask containing stirred solution of (±)-3-Amino-1,2-propanediol (100 mg, 1.10 mmol) in CH_2Cl_2:THF (5:1) (~15 mL), Oleic Acid (621.5 mg, 2.20 mmol), EDCI (527.1mg, 2.75 mmol), DMAP (336 mg, 2.75 mmol) and DIPEA (479 μL, 2.75 mmol) were added. After overnight stirring at room temperature (rt), the reaction mixture was diluted with DCM, washed with sat. NH_4Cl (~20 mL) and brine (~20 mL) and subsequently was dried (Na_2SO_4), filtered *in vacuo* and concentrated, so the crude compound was obtained. Purification by column chromatography (CH_2Cl_2 to 10% EtOAc in CH_2Cl_2) yielded the target material (248.5 mg, 0.40 mmol) isolated as a mixture of two regioisomers (substitution at 1° alcohol *vs.* 2° alcohol) at a ratio of 8:2 with a white waxy structure.

TLC (CH_2Cl_2: EtOAc, 8:2 v/v) : R_f = 0.3 ; **^{1}H NMR** (400 MHz, $CDCl_3$) δ 5.94 (t, *J* = 5.6 Hz, 1H), 5.40 – 5.28 (m, 4H), 4.86 – 4.78 (m, 0.2H), 4.15 (dd, *J* = 11.5, 5.2 Hz, 1H), 4.05 (dd, *J* = 11.5, 5.8 Hz, 1H), 3.97 – 3.88 (m, 0.8H), 3.64 – 3.46 (m, 1H), 3.27 – 3.19 (m, 1H), 2.34 (t, *J* = 7.6 Hz, 2H), 2.26 – 2.17 (t, *J* = 7.6 Hz, 2H), 2.00 (q, *J* = 6.4 Hz, 8H), 1.63 (dd, *J* = 11.1, 6.8 Hz, 4H), 1.28 (d, *J* = 14.6 Hz, 40H), 0.88 (t, *J* = 6.9 Hz, 6H) ; **ESI-HRMS** (m/z) $[M+H]^+$: calcd. for $C_{39}H_{73}NO_4$, 620.56; found 620.56, delta=0.1ppm.

2-hydroxypropane-diyl dioleate (Dioleoyl Glycerol, DOG)

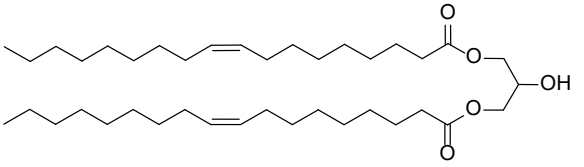

To a round bottom flask containing stirred solution of 1,2,3-Propanetriol (glycerol) (100 mg, 1.09 mmol) in CH_2Cl_2 : THF (5:1) (~15 mL), Oleic Acid (585 mg, 2.07 mmol), EDCI (527 mg, 2.75 mmol), DMAP (336 mg, 2.75 mmol) and DIPEA (479 µL, 2.75 mmol) were added. After overnight stirring at RT, the reaction mixture was diluted with DCM, washed with sat. NH_4Cl (~20 mL) and brine (~20 mL) and subsequently was dried (Na_2SO_4), filtered *in vacuo* and concentrated, so the crude lipid was obtained. Purification by column chromatography (CH_2Cl_2 to 2% EtOAC in CH_2Cl_2) yielded the target material (75.2 mg, 0.12 mmol) isolated as a mixture of two regioisomers (substitution at 1º alcohol *vs.* 2º alcohol) at a ratio of 8:2, as colorless oil.

TLC (CH_2Cl_2: EtOAc, 9.5:0.5 v/v) R_f = 0.8 ; **^{1}H NMR** (400 MHz, $CDCl_3$) δ 5.39 – 5.26 (m, 4H), 4.23 – 4.01 (m, 4.8H), 2.76 (t, *J* = 6.4 Hz, 0.2H), 2.34 (t, *J* = 7.6 Hz, 4H), 2.03 – 1.96 (m, 8H), 1.61 (dd, *J* = 14.6, 7.2 Hz, 4H), 1.28 (d, *J* = 14.3 Hz, 40H), 0.87 (t, *J* = 6.7 Hz, 6H).

Liposome formulation: Liposomes were formulated by extrusion or by ethanol injection (Note: DOPC:DOaG liposomes could be only formulated by ethanol injection) in ddH_2O at a total lipid concentration of 5 mM and containing 0.2 mol% DOPE-Lissamine Rhodamine (DOPE-LR) for fluorescent visualization, unless otherwise stated. In the case of extrusion, individual lipids as stock solutions (1-10 mM) in chloroform, were combined to the desired molar ratios and dried to a thin film, first under N_2 stream, then >1 h under vacuum. Lipid films were hydrated above the T_m of all lipids (65-70ºC), with gentle vortexing if necessary, to form a suspension. Large unilamellar vesicles were formed through extrusion (mini extruder, Avanti Polar Lipids) above the T_m of all lipids (*i.e.* 65-70ºC). Hydrated lipids were passed 11 times through 2 x 400 nm polycarbonate (PC) membranes (Nucleopore Track-Etch membranes, Whatman), followed by 11 times through 2 x 100 nm PC membranes. All liposomes were stored at 4 ºC and used within 1 week.

In the case of ethanol injection, lipid films were re-dissolved in absolute ethanol to a total lipid concentration of 50 mM. Using a glass micro-syringe (Hamilton, syringe series 700, volume 50 or 500 µl) 50 or 100 µL of the ethanolic solution was submerged in a water bath of 70 °C for 1-2 sec and then was rapidly injected in a glass vial containing 0.5 mL or 1mL ddH_2O, respectively, (1:10 v/v; EtOH:H_2O) at 70°C under constant vigorous stirring (650 rpm – stirring bar dimensions: 12 x 4 x 4 cm), to form large unilamellar vesicles. Liposomes were then transferred to a dialysis tube (Spectrum labs, 3.5k MWCO) or a dialysis cassette (slide-A-Lyzer™ 3.5k MWCO, Thermo Fisher Scientific) and dialyzed against ddH_2O overnight at 4°C, to ensure complete ethanol removal. All liposomes were stored at 4 °C and used within 1 week.

Size and zeta potential measurements: Particle size and zeta potentials were measured using a Malvern Zetasizer Nano ZS. For DLS (operating wavelength = 633 nm), measurements were carried out at room temperature in water at a total lipid concentration of approx. 100 µM. Zeta potentials were measured at 500 µM total lipid concentration, using a dip-cell electrode (Malvern), at room temperature. For liposomes formulated in water, aq. NaCl was added to the liposome solution to a final concentration of 10 mM before zeta potential measurement. All reported DLS measurements and zeta potentials are the average of three measurements.

Cryogenic transmission electron microscopy and 3D tomography: Liposomes (3 µL, 5 mM total lipid concentration) were applied to a freshly glow-discharged carbon 200 mesh Cu grid (Lacey carbon film, Electron Microscopy Sciences, Aurion, The Netherlands). Grids were blotted for 3 sec at 99% humidity in a Vitrobot plunge-freezer (FEI VitrobotTM Mark III, Thermo Fisher Scientific). Cryo-EM images were collected on a Talos L120C or a KRIOS (NeCEN, Leiden University) operating at 120 kV or 300 kV, respectively. In the case of Talos, images were recorded manually at a nominal magnification of 17500x or 28000x yielding a pixel size at the specimen of 5.83 or 3.56 ångström (Å), respectively. In the case of KRIOS, images were recorded manually at a nominal magnification of 33000x yielding a pixel size at the specimen of 3.48 ångström (Å). Alternatively, imaging and cryo-ET was performed on a Titan operating at 300kV (TU Eindhoven). Images were recorded manually at a nominal magnification of 6500x or 24000x yielding a pixel size at the specimen of 13.87 or 3.86 ångström (Å),

respectively. Tomographic tilt series acquisition was performed with Inspect3D software from Thermo Fisher Scientific with a total electron dose of less than 100 e/nm2. Alignment and reconstruction of the series were performed using IMOD[94] and Avizo 9 (Thermo Fisher Scientific).

Zebrafish husbandry and injections: Zebrafish (*Danio rerio*, strain AB/TL) were maintained and handled according to the guidelines from the Zebrafish Model Organism Database (http://zfin.org) and in compliance with the directives of the local animal welfare committee of Leiden University. Fertilization was performed by natural spawning at the beginning of the light period, and eggs were raised at 28.5 °C in egg water (60 μg/ mL Instant Ocean Sea salts). The following previously established zebrafish lines were used: Tg*(cldn5a:*eGFP)[42], Tg*(kdrl:*eGFP)^{s843},[95] Tg*(mpeg1:*GFP)^{gl22},[96] Tg*(mpeg1:*mCherry)^{gl23},[96] and a previously generated zebrafish mutant (*stabilin-1*^{ibl3} *stabilin-2*^{ibl1}).[39] Liposomes were injected into 54-120 hours post fertilization zebrafish embryos using a modified microangiography protocol.[97] Embryos were anesthetized in 0.01% tricaine and embedded in 0.4% agarose containing tricaine before injection. To improve reproducibility of microangiography experiments, 1 nl volume was calibrated and injected into the sinus venosus/Duct of Cuvier or the primary head sinus. A small injection space was created by penetrating the skin with the injection needle and gently pulling the needle back, thereby creating a small pyramidal space in which the liposomes were injected. Successfully injected embryos were identified through the backward translocation of venous erythrocytes and the absence of damage to the yolk ball. More details about the protocol used or injections in the zebrafish embryo are provided in reference [97]. Heparin (1 nl of 50 mg/ml) was injected 30 min before/after liposome injection. XEN445 (first dissolved in DMSO to obtain a 10 mM stock solution and then diluted in water to a final concentration of 50 μM) was administered 24 h and 1 h prior liposome injection.

Confocal imaging acquisition and editing: Zebrafish embryos were randomly picked from a dish of 20-60 successfully injected embryos. Confocal z-stacks were captured on a Leica TCS SPE or SP8 confocal microscope, using a 10x air objective (HCX PL FLUOTAR), a 40x water-immersion objective (HCX APO L) or 63x water-immersion objective (HC PL APO CS). For whole-embryo views, 3/4 overlapping z-stacks were captured to cover the complete embryo in lateral view.

Laser intensity, gain and offset settings were identical between stacks and each experiment. Images were processed and quantified using the Fiji distribution of ImageJ.[98,99]

Studies in mice: Male mice weighting *ca.* 18-20 g (C57BL6, 6-8 weeks, Janvier; see below for number of animals) were used. Animals were treated with 30 mg/kg XEN445 (as a suspension in 0.2% Tween-20/1% carboymethyl-cellulose) orally *b.i.d.* for 9 days[75] prior to liposome administration.

For radiolabeling studies, PAP3 liposomes (10 mM total lipid concentration) were made by ethanol injection as described above, with only difference that 0.2 mol% of NOTA-Bz-SCN-C18 (custom made, Avanti Polar Lipids) was added to the lipid film. Additionally, the required total volume of liposomes was made in two batches of 500 µl to ensure avoidance of aggregation. After formation of particles and removal of ethanol, $^{64}CuCl_2$ in 0.1 M aq. ammonium acetate pH=5.5 was added to the liposome solution and the mixture was incubated at room temperature (20 mins) (1:4 v/v ammonium acetate/liposomes). Subsequently, the free $^{64}CuCl_2$ was removed by size exclusion chromatography (SEC) (NAP™-25 columns Sephadex™, GE Healthcare) equilibrated with 10 mM Tris buffer pH=7.4. Elution fractions of 500 µl containing the radiolabeled liposomes were collected from the SEC column and their radioactivity was checked using a dose calibrator (CPCRC-25R, Capintec Inc., NJ, USA). The fraction containing the higher concentration of radioactivity was measured in size by DLS and was used for subsequent *in vivo* imaging and *ex vivo* studies.

For PET imaging studies, anesthesia was induced by inhalation of 3% isoflurane in pure O_2 and maintained by 1.5-2% isofluorane in 100% O_2. With the animal under anesthesia, the labelled liposomes were injected *via* one of the lateral tail veins (2845 ± 185 kBq/100 µl for treated animals; 2480 ± 260 kBq/100 µl for non-treated animals; n=2 per group). Dynamic whole-body images (20 min duration) were acquired list-mode in one bed position in a 511 keV ± 30% energetic window immediately after administration of the labelled liposomes using a MOLECUBES β-CUBE scanner. Static 10 min images were also acquired at 2 h and 6 h after administration. After each PET scan, whole body high resolution computed tomography (CT) acquisitions were performed on the MOLECUBES X-CUBE scanner, to provide anatomical information as well as the attenuation map for the later reconstruction

of the PET images. Dynamic PET images were reconstructed with OSEM-3D iterative algorithm, using the following frames: 4 × 30 s, 4 × 60 s, 4 × 120 s, 2 × 180 s. Static images were reconstructed as a single frame using the same method. Images were analyzed using π-MOD image analysis software (π-MOD Technologies Ltd, Zurich, Switzerland).

For *ex vivo* biodistribution studies, animals (n=3 per compound and time point) were anesthetized with isoflurane 3% isoflurane in pure O_2 and maintained by 1.5-2% isoflurane in 100% O_2. A solution containing the labelled liposomes (2640 ± 370 kBq/100 µl for treated animals; 2530 ± 385 kBq/100 µl for non-treated animals; n=3 per group and time point) was injected through one of the lateral tail veins. Animals were recovered from anesthesia and at pre-determined time points (t=10 min, and 2, 6 and 24 h), animals were anesthetized again and sacrificed by perfusion using saline solution and brain, liver, kidneys, spleen, lungs, heart, and stomach were quickly removed and rinsed with water. The amount of radioactivity in each organ was measured in an automatic gamma counter (2470 Wizard, PerkinElmer). Blood samples were obtained just before perfusion. Part of the blood was processed to separate the plasma, which was also counted in the gamma counter. Results were normalized to injected dose and organ weight to express the results as percentage of injected dose per gram of tissue (% ID/g).

Statistical analysis: All experiments performed in zebrafish embryo/larvae presented in this chapter were repeated at least twice and were performed using freshly prepared liposomes. For all experiments performed in zebrafish, at least four embryos were randomly selected (from a pooled of ~20-60 successfully injected embryos) and visualized at low resolution microscopy. From these four embryo/larva zebrafish, at least one was selected for confocal microscopy. The imaged zebrafish was representative for the data and showed consistent results confirming the presented data. No statistical analysis is performed in this work. All experiments performed in mice were approved by the ethical committee of CIC biomaGUNE and by local authorities (Diputación Foral de Guipúzcoa), authorization number PRO-AE-SS-207, maintained and handled in accordance with the guidelines and regulations (Guidelines for Accommodation and Care of Animals). Statistical analysis as follows: for the *ex vivo* gamma radiation studies, results were normalized to injected dose and organ weight to express the results as

percentage of injected dose per gram of tissue (% ID/g). Data is presented as mean ± SD values. Sample size used for mice studies was n=2 per group per timepoint for the PET images and n=3 per group per time point for the *ex vivo* gamma radiation experiments. Statistical significance was evaluated using a two-tailed unpaired Student's t-test. ns: not significant ($P > 0.05$). Significantly different *$P < 0.05$, **$P < 0.01$; ***$P < 0.001$. Exact P values are included in the figure captions. GraphPad was used as a software for the statistical analysis.

Protein corona analysis: Proteomic corona analysis of PAP3 and DSPC liposomes was performed as described in reference [71]. Briefly, liposomes were formulated by extrusion incorporating 5 mol% of the IKS02 diazirene-based photoaffinity lipid probe and incubated in human serum at 37°C for 1h (1:1 volumetric ratio). Proteins adsorbed to the surface of the liposomes were *in situ* photo-cross linked with the IKS02 probe of the liposomes. Afterwards, the captured proteins were isolated and quantified with LC-MS/MS.

2.5 Supplementary Information

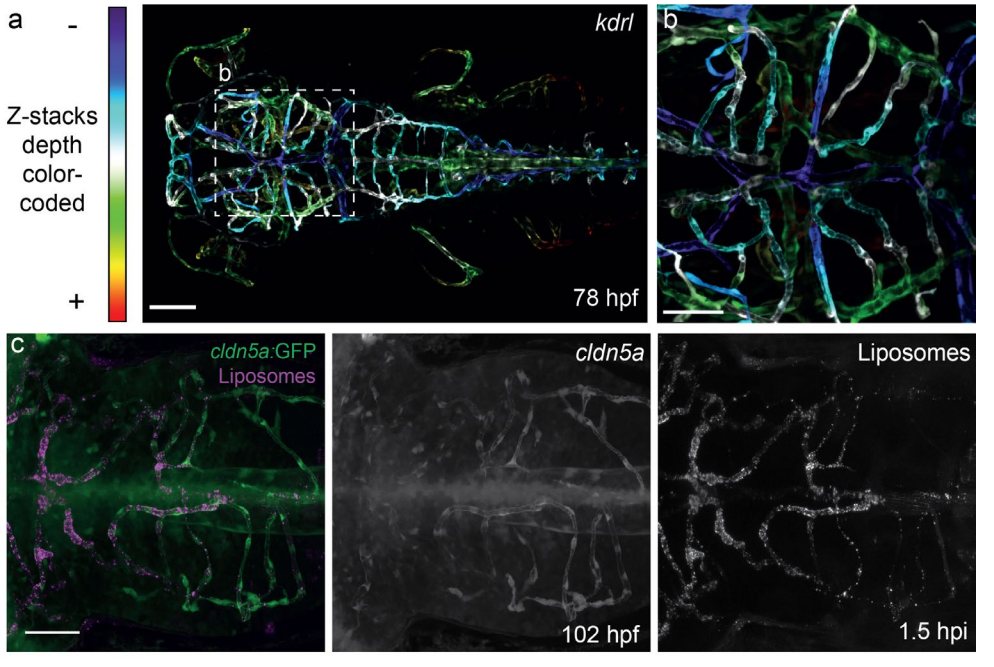

Figure S1. Vascularization within the head region of a zebrafish embryo (3 dpf) and biodistribution of PAP3 liposomes in Tg*(cldn5a:*eGFP) embryos (4 dpf). a-b) Depth color-coded z-stacks of the head region of a Tg(*kdrl*:GFP) zebrafish embryo, in dorsal view, at approx. 3 days post fertilization (dpf). Depth color scale: blue (dorsal) to red (ventral). **c)** Colocalization of *cldn5a* and PAP3 liposomes (5 mM, 0.2 mol% DOPE-LR) within the hindbrain region (magnification 40x, zoom) of a 4 day-old Tg*(cldn5a:eGFP)* zebrafish at 1.5 hpi (whole embryo, 10x shown in **Figure 2j**). Liposomes formulated by extrusion. Scale bars: 100 μm (a) and 50 μm (b-c).

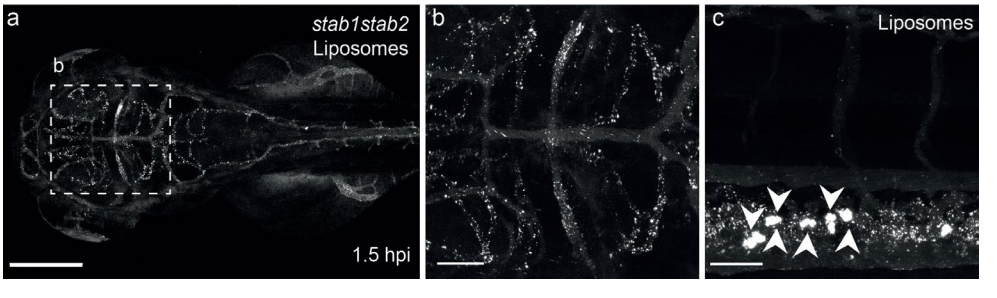

Figure S2. Biodistribution of PAP3 liposomes within *stabilin-1/-2* double knockout zebrafish embryos (3 dpf). a) Biodistribution (10x magnification) of PAP3 liposomes (5

mM, 0.2 mol% DOPE-LR) within the head region of a mutant *stab1*^{ibl3}*stab2*^{ibl1} zebrafish embryo at 1.5 hpi. **b)** High magnification (40x, zoom) dorsal view of PAP3 liposome biodistribution showing accumulation within bECs. **c)** High magnification (40x), lateral view, showing accumulation of PAP3 liposomes within blood-resident macrophages (white arrows) of the CHT of a mutant *stab1*^{ibl3}*stab2*^{ibl1} zebrafish embryo at 1.5 hpi. Liposomes formulated by extrusion. Scale bar: 200 µm (a) and 50 µm (b-c).

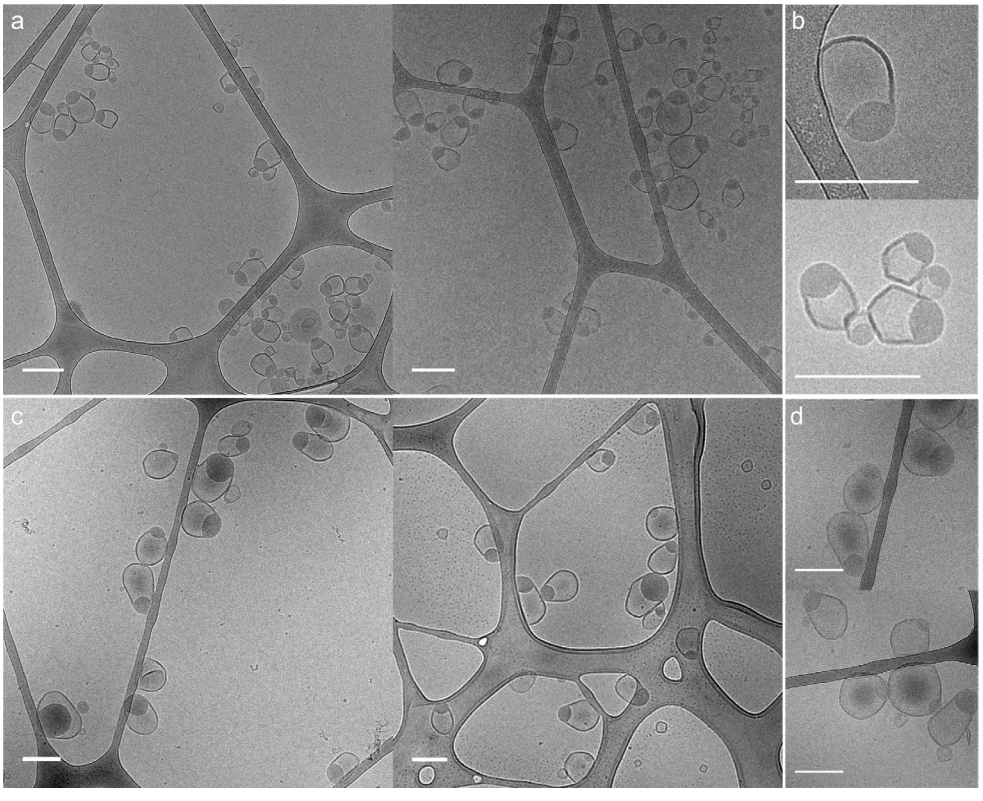

Figure S3. Cryo-TEM images of 'parachute' PAP3 liposomes formulated by two methods. a, b) PAP3 liposomes formulated by ethanol injection. **c, d)** PAP3 liposomes formulated by extrusion. Scale bars: 200 nm.

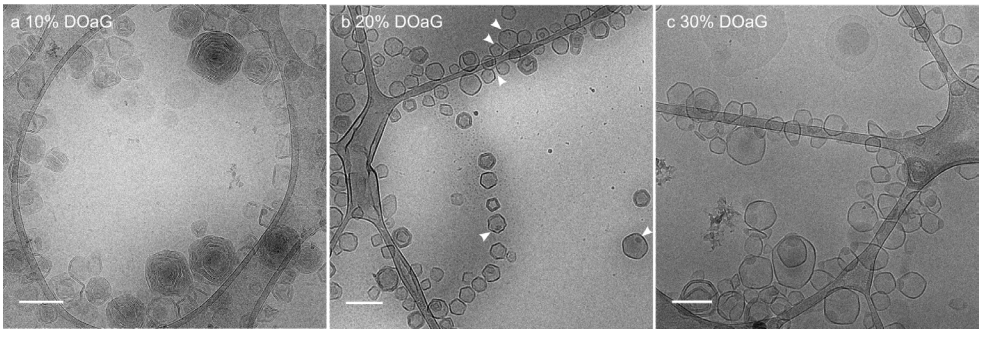

Figure S4. Cryo-TEM images of PAP3 liposomes formulated at varying molar ratios. Liposomes composed of DSPC and **a)** 10 mol%, **b)** 20 mol% or **c)** 30 mol% DOaG. White arrows indicate small electron rich protrusions. Liposomes formulated by ethanol injection. Scale bars: 200 nm.

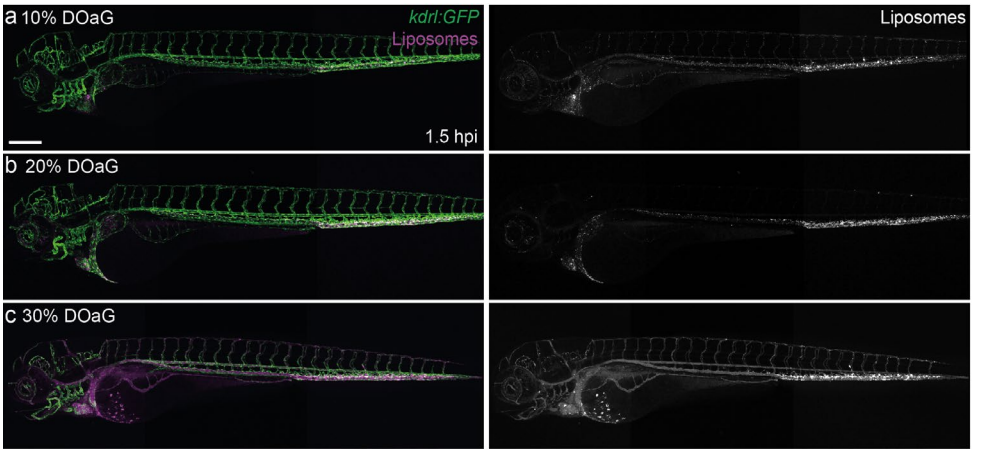

Figure S5. Biodistribution of PAP3 liposomes formulated at varying molar ratios within zebrafish embryos (3 dpf). a) Biodistribution (10x magnification) of liposomes (5 mM, 0.2 mol% DOPE-LR) composed of DSPC and 10 mol%, **b)** 20 mol%, or **c)** 30 mol% DOaG within the whole body of Tg(*kdrl*:GFP) zebrafish embryos at 1.5 hpi. Liposomes formulated by ethanol injection. Scale bar: 200 μm.

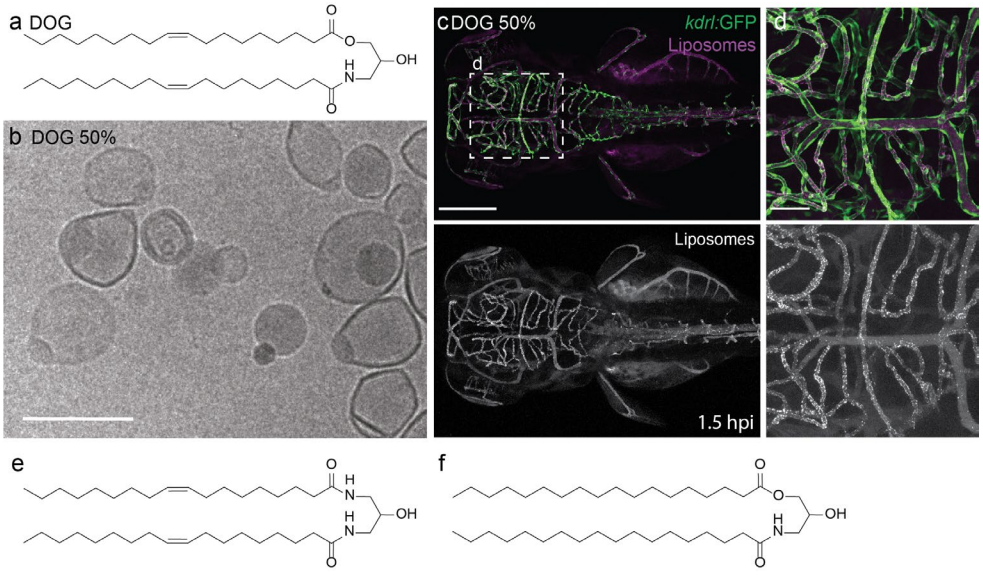

Figure S6. Cryo-TEM and biodistribution of DSPC:DOG liposomes within zebrafish embryos (3 dpf). a) Chemical structure of dioleoyl glycerol (DOG(18:1/0:0/18:1). **b)** Cryo-TEM of liposomes containing DSPC and DOG in equal ratios. **c)** Biodistribution (10x magnification) of DSPC:DOG liposomes (5 mM, 0.2 mol% DOPE-LR) within the head region of a Tg(*kdrl*:GFP zebrafish embryo at 1.5 hpi. **d)** High magnification (40x, zoom) view of DSPC:DOG liposome biodistribution showing accumulation within bECs. Liposomes formulated by extrusion. Scale bars: 200 nm (cryo-TEM), 200 µm (dorsal view) and 50 µm (tissue level). **e)** Chemical structure of variant with two amides. **f)** Chemical structure of variant with two stearyl chains.

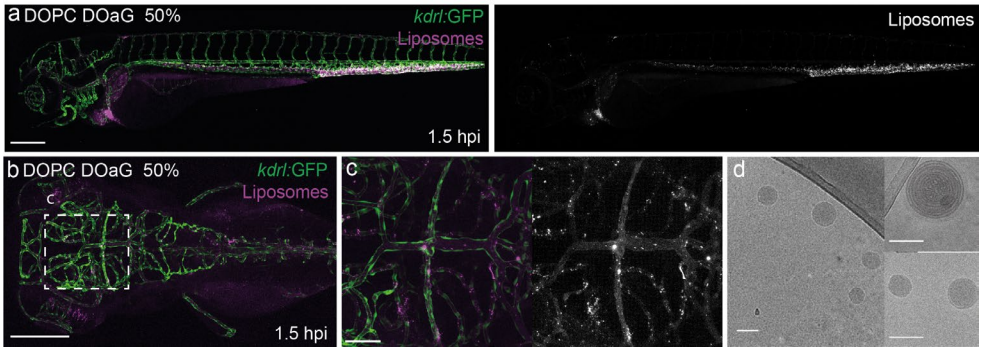

Figure S7. Cryo-TEM and biodistribution of DOPC:DOaG liposomes within zebrafish embryos (3 dpf). a) Biodistribution (10x magnification) of DOPC:DOaG liposomes (composed in equal ratios, 5 mM, 0.2 mol% DOPE-LR) within the whole body of a

Tg(*kdrl*:GFP) zebrafish embryo at 1.5 hpi. **b)** Dorsal view (10x magnification) of DOPC:DOaG liposome biodistribution within the head region. **c)** High magnification (40x, zoom) view of DOPC:DOaG liposome biodistribution showing no accumulation within bECs. **d)** Cryo-TEM images of DOPC:DOaG liposomes showing multilamellar with solid core or solid lipid-like morphology. Liposomes formulated by ethanol injection. Scale bars: 200 μm (dorsal and lateral views), 50 μm (tissue level) and 100 nm (cryo-TEM).

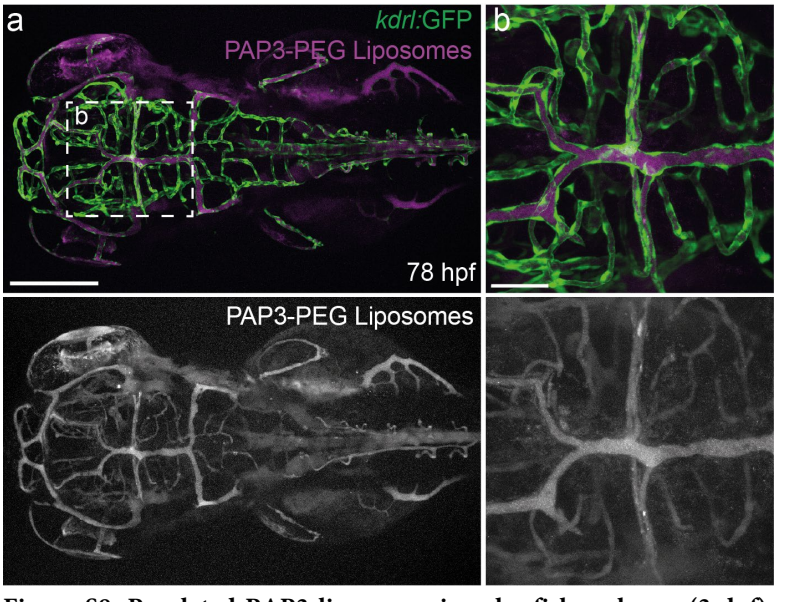

Figure S8. Pegylated-PAP3 liposomes in zebrafish embryos (3 dpf). a) Biodistribution (10x magnification) of PAP3 liposomes (5 mM, 0.2 mol% DOPE-LR) containing DSPE-PEG (5 mol%) in a Tg(*kdrl*:GFP) zebrafish embryo at 1.5 hpi. Liposomes formulated by extrusion. Scale bars: 200 μm (lateral view), 50 μm (tissue level).

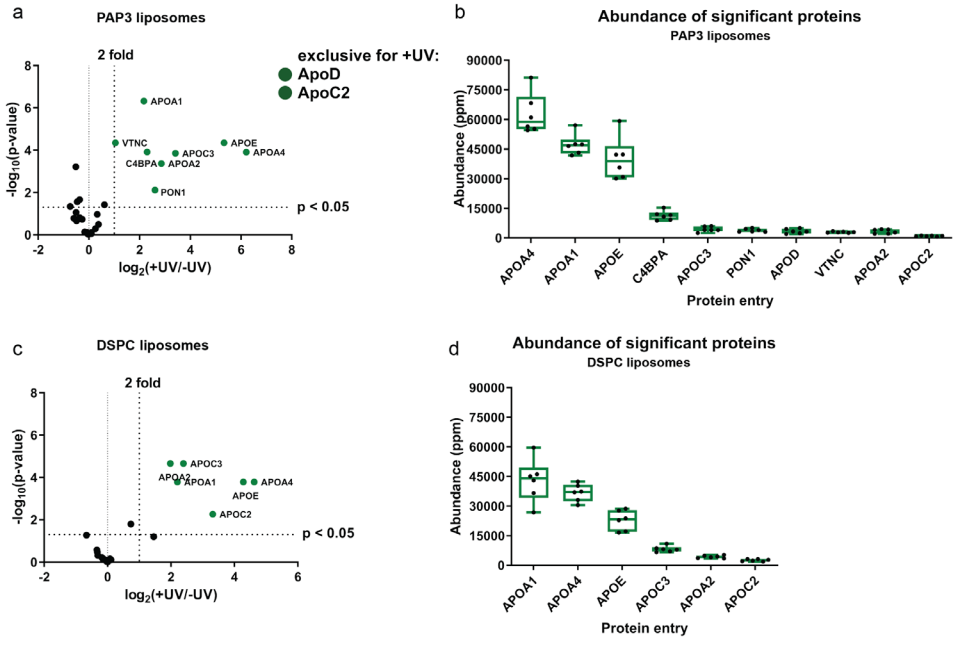

Figure S9. Identification of the PAP3 liposome protein corona, isolated via photoaffinity-based method. a, c) Volcano plots of enrichment over background (log_2(+UV/-UV) plotted against the statistical significance of this comparison (-log_{10}(*p*-value)) of PAP3 and 100% DSPC liposomes, respectively. Proteins meeting all selection criteria labeled in green. Proteins without background labeling are listed as exclusive for +UV. **b, d)** Abundance plots of proteins (replicate abundancies of the top10 proteins (ppm) withing the +UV samples) identified in PAP3 and DSPC liposomes respectively. Liposomes with affinity probe (IKS02 5 mol%) incorporated into the liposome membrane were formulated by extrusion.

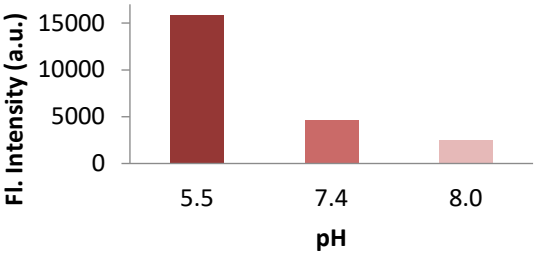

Figure S10. Fluorescence intensity of PAP3 liposomes containing 0.5% mol DOPE-pHrodo™ at different pH (5.5, 7.4 and 8.0). Fluorescence intensity of liposomes containing 0.5% mol DOPE-pHrodo™ in buffer solutions of different pH (ammonium acetate for pH 5.5, and Tris Buffer for pH 7.4 and 8.0) was measured on a plate reader at 585nm (ex/em of pHrodo™: 560/585nm).

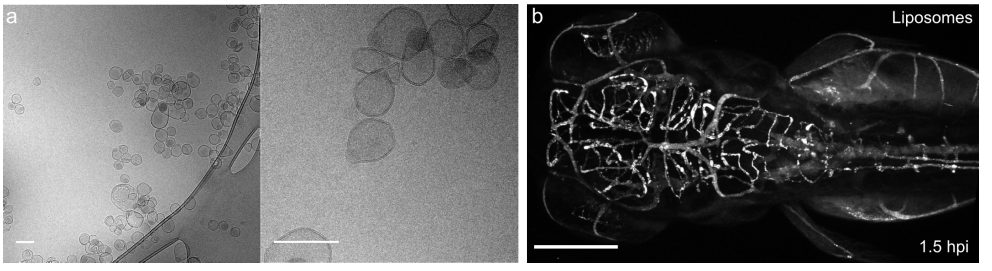

Figure S11. Cryo-TEM and biodistribution of ^{64}Cu - PAP3 liposomes containing NOTA-Bz-SCN-C18 within zebrafish embryos (3 dpf). a) Cryo-TEM images of PAP3 liposomes containing 0.2% mol NOTA-Bz-SCN-C18 after Cu chelation (stable Cu isotope). **b)** Biodistribution (10x magnification) of PAP3 liposomes (0.1% mol DOPE-LR, 0.2% mol NOTA-Bz-SCN-C18, after ^{64}Cu chelation) within the head region of an AB/TL zebrafish embryo at 1.5 hpi, showing accumulation in bECs. Two weeks after ^{64}Cu chelation and administration in mice (to ensure radioactivity decay), the remaining sample was injected in zebrafish embryos to confirm bEC targeting was retained. Liposomes containing NOTA-Bz-SCN-C18 were formulated by ethanol injection. Scale bars: 200 nm (cryo-TEM), 200 μm (dorsal view).

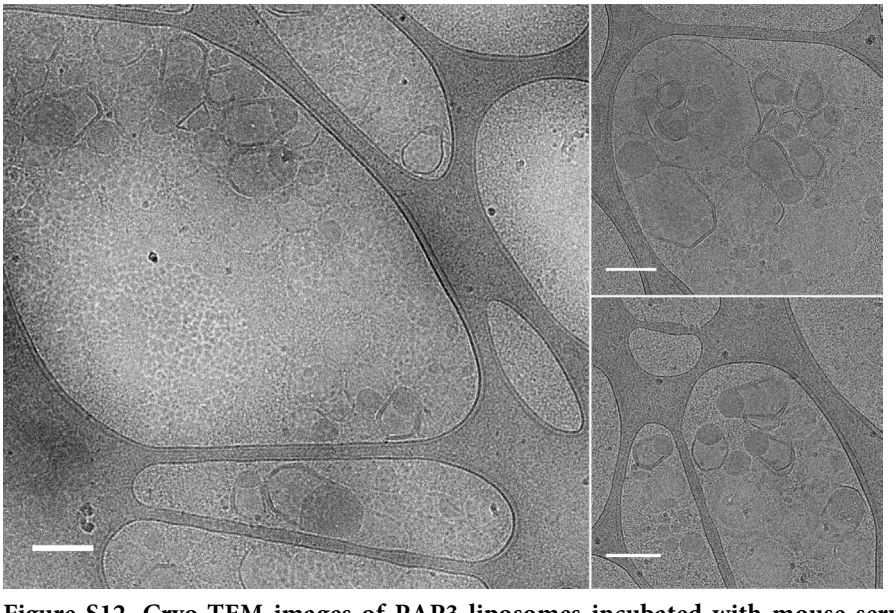

Figure S12. Cryo-TEM images of PAP3 liposomes incubated with mouse serum (2:1 volumetric ratio). Liposomes were incubated with mouse serum at 37 °C for 30 min. Liposomes formulated by extrusion. Scale bars: 200 nm.

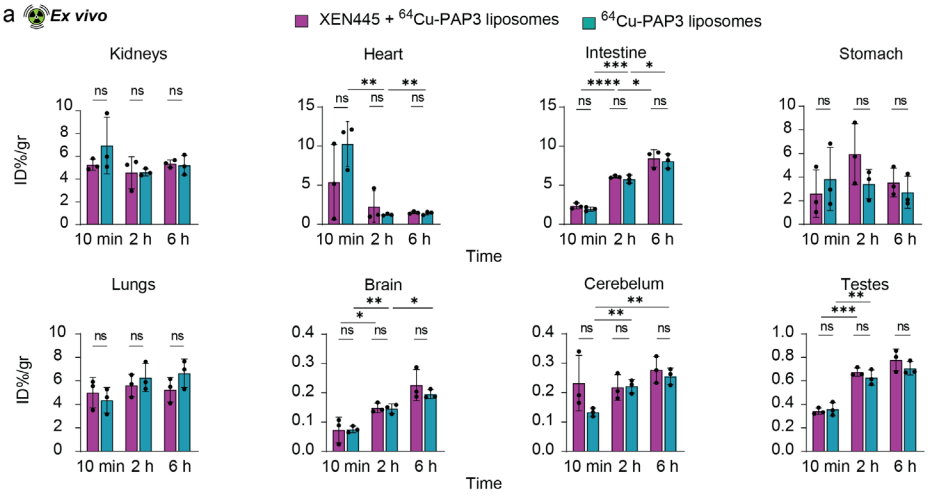

Figure S13. Biodistribution of radiolabeled PAP3 liposomes in male mice. a) *Ex vivo* gamma radiation counter (%ID/gr) of kidneys, heart, intestine, stomach, lungs, brain, cerebellum and testes in mice after XEN445 treatment or in mice without treatment at 10 min, 2 h and 6 h after *i.v.* administration of ^{64}Cu-labelled PAP3 liposomes (n=3 per group and time point). Statistical significance was evaluated using a two-tailed unpaired Student's t-test. ns: not significant (P > 0.05). Significantly different *P < 0.05, **P < 0.01; ***P < 0.001 and P<0.0001****. Exact P values for the heart 0.0057**, 0.0061**, for the intestine <0.0001****, 0.0003***, 0.0191* and 0,0237*; for the brain 0.0496*, 0.0033**, 0.0194*; for the cerebellum 0.0048** and 0.0024**; and for the testes 0.0002***, 0.0056**.

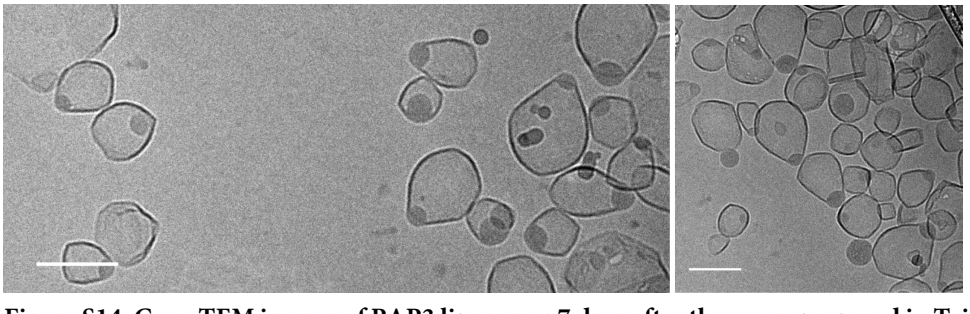

Figure S14. Cryo-TEM images of PAP3 liposomes 7 days after they were prepared in Tris Buffer. PAP liposomes were prepared by extrusion in 10mM Tris Buffer pH = 7.4 and cryo-TEM images were taken 7 days after preparation.

Chemical characterization – ^{1}H-NMRs

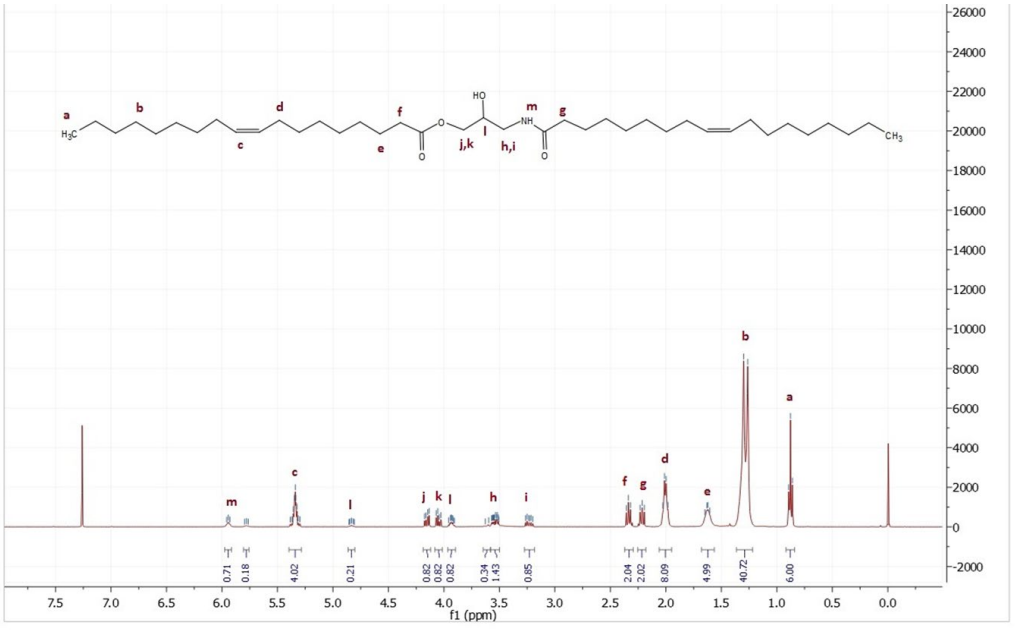

^{1}H-NMR of DOaG

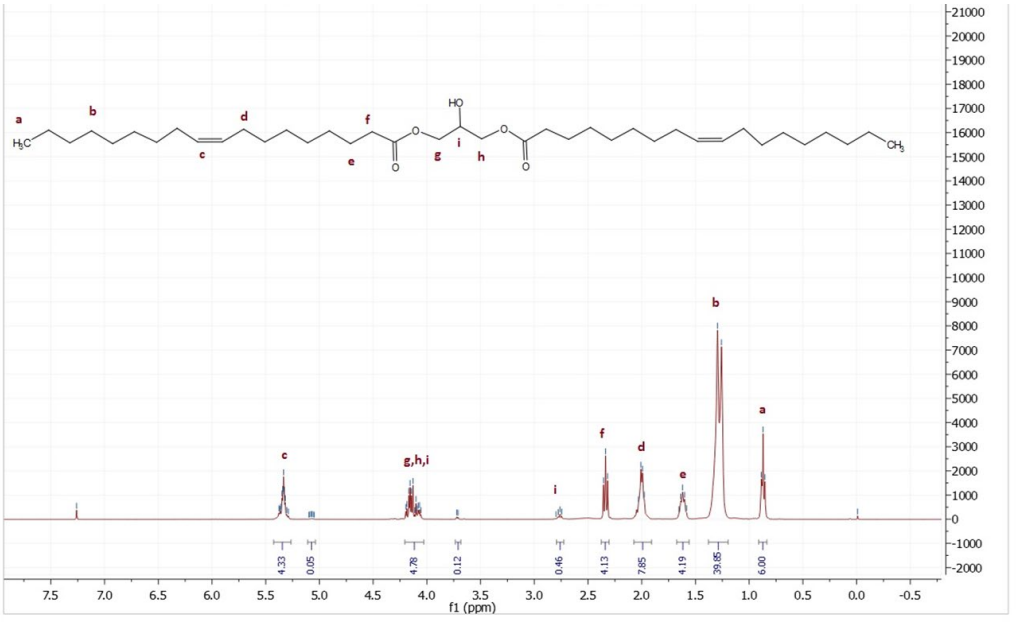

^{1}H-NMR of DOG

Table S1. Physicochemical properties of liposomes

Formulation	Preparation method		Size (nm)	PDI	ζ-potential* (mV)
10% DOaG liposomes	Ethanol injection		± 137.5	0.179	ND
20% DOaG liposomes	Ethanol injection		± 107.5	0.181	ND
30% DOaG liposomes	Ethanol injection		± 136.5	0.281	ND
PAP3 liposomes (50% DOaG)	Extrusion	Day 0	± 142.2	0.123	-6.1*
		Day 5	±157.5	0.225	ND
	Ethanol injection		± 123.0	0.218	-11.2*
PAP3 (*formulated in PBS)*	Extrusion		± 249.1	0.495	ND
PAP3 (*formulated in 10mM Tris pH= 7.4)*	Extrusion		± 124.8	0.218	ND
DSPC:DOaG:IKS02 (45:50:5)	Extrusion		± 129.4	0.163	ND
DSPC:DOG (50:50)	Extrusion		± 161.7	0.318	-7.2
DOPC:DOaG (50:50)	Ethanol injection		± 200.2	0.141	ND
PAP3 liposomes:DSPE-PEG (5 %)	Extrusion		± 113.1	0.060	ND
DSPC:DOaG:NOTA (49.9:49.9:0.2)	Ethanol injection		± 151.3	0.207	ND
DSPC:DOaG:NOTA (49.9:49.9:0.2) *after labeling with Cu^{2+} (cold)*	Ethanol injection		± 260.8	0.231	-8.7
DSPC:DOaG:NOTA (49.9:49.9:0.2) *radiolabeled with $^{64}Cu^{2+}$ just before administration in mice*	Ethanol injection		± 152.2	0.220	ND
DSPC:DOaG:DOPE-pHrodo:DOPE-NBD (49.5:49.5:0.5:0.5)	Extrusion		± 126.2	0.227	ND

* Addition of NaCl for surface charge measurement increases the PAP3 liposome size and PDI (180.8 nm, 0.8 PDI). ND: Not determined.

2.6 References

1. Feingold, K. R.; Grunfeld, C. Introduction to Lipids and Lipoproteins. *Endotext* **2021**.
2. Akinc, A.; Maier, M. A.; Manoharan, M.; Fitzgerald, K.; Jayaraman, M.; Barros, S.; Ansell, S.; Du, X.; Hope, M. J.; Madden, T. D.; Mui, B. L.; Semple, S. C.; Tam, Y. K.; Ciufolini, M.; Witzigmann, D.; Kulkarni, J. A.; van der Meel, R.; Cullis, P. R. The Onpattro Story and the Clinical Translation of Nanomedicines Containing Nucleic Acid-Based Drugs. *Nat Nanotechnol* **2019**, *14* (12), 1084–1087.
3. Akinc, A.; Querbes, W.; De, S.; Qin, J.; Frank-Kamenetsky, M.; Jayaprakash, K. N.; Jayaraman, M.; Rajeev, K. G.; Cantley, W. L.; Dorkin, J. R.; Butler, J. S.; Qin, L.; Racie, T.; Sprague, A.; Fava, E.; Zeigerer, A.; Hope, M. J.; Zerial, M.; Sah, D. W.; Fitzgerald, K.; Tracy, M. A.; Manoharan, M.; Koteliansky, V.; Fougerolles, A. De; Maier, M. A. Targeted Delivery of RNAi Therapeutics with Endogenous and Exogenous Ligand-Based Mechanisms. *Mol Ther* **2010**, *18* (7), 1357–1364.
4. Schrijver, D. P.; de Dreu, A.; Hofstraat, S. R. J.; Kluza, E.; Zwolsman, R.; Deckers, J.; Anbergen, T.; de Bruin, K.; Trines, M. M.; Nugraha, E. G.; Ummels, F.; Röring, R. J.; Beldman, T. J.; Teunissen, A. J. P.; Fayad, Z. A.; van der Meel, R.; Mulder, W. J. M. Nanoengineering Apolipoprotein A1-Based Immunotherapeutics. *Adv Ther* **2021**, *4* (8), 2100083.
5. Wolfrum, C.; Shi, S.; Jayaprakash, K. N.; Jayaraman, M.; Wang, G.; Pandey, R. K.; Rajeev, K. G.; Nakayama, T.; Charrise, K.; Ndungo, E. M.; Zimmermann, T.; Koteliansky, V.; Manoharan, M.; Stoffel, M. Mechanisms and Optimization of in vivo Delivery of Lipophilic siRNAs. *Nat Biotechnol* **2007**, *25* (10), 1149–1157.
6. Ference, B. A.; Ginsberg, H. N.; Graham, I.; Ray, K. K.; Packard, C. J.; Bruckert, E.; Hegele, R. A.; Krauss, R. M.; Raal, F. J.; Schunkert, H.; Watt, G. F.; Borén, J.; Fazio, S.; Horton, J. D.; Masana, L.; Nicholls, S. J.; Nordestgaard, B. G.; Van De Sluis, B.; Taskinen, M. R.; Tokgözoğlu, L.; Landmesser, U.; Laufs, U.; Wiklund, O.; Stock, J. K.; Chapman, M. J.; Catapano, A. L. Low-Density Lipoproteins Cause Atherosclerotic Cardiovascular Disease. Evidence from Genetic, Epidemiologic, and Clinical Studies. A Consensus Statement from the European Atherosclerosis Society Consensus Panel. *Eur Heart J* **2017**, *38* (32), 2459–2472.
7. Goldstein, J. L.; Brown, M. S. A Century of Cholesterol and Coronaries: From Plaques to Genes to Statins. *Cell* **2015**, *161* (1), 161–172.

8. Fielding, C. J.; Fieldinst, P. E. Molecular Physiology of Reverse Cholesterol Transport. *J Lipid Res* **1995**, *36*, 211–228.
9. Allan, C. M.; Fidge, N. H.; Morrison, J. R.; Kanellos, J. Monoclonal Antibodies to Human Apolipoprotein AI: Probing the Putative Receptor Binding Domain of Apolipoprotein AI. *Biochem J* **1993**, *290*, 449–455.
10. Vadiveloo, P. K.; Allan, C. M.; Murray, B. J.; Fidge, N. H. Interaction of Apolipoprotein AII with the Putative High-Density Lipoprotein Receptor. *Biochemistry* **1993**, *32* (36), 9480–9485.
11. Hussain, M. M.; Strickland, D. K.; Bakillah, A. The Mammalian Low-Density Lipoprotein Receptor Family. *Annu Rev Nutr* **1999**, *19*, 141–172.
12. Shen, Y.; Lookene, A.; Zhang, L.; Olivecrona, G. Site-Directed Mutagenesis of Apolipoprotein CII to Probe the Role of Its Secondary Structure for Activation of Lipoprotein Lipase. *J Biol Chem* **2010**, *285* (10), 7484–7492.
13. Amar, M. J. A.; Sakurai, T.; Sakurai-Ikuta, A.; Sviridov, D.; Freeman, L.; Ahsan, L.; Remaley, A. T. A Novel Apolipoprotein C-II Mimetic Peptide That Activates Lipoprotein Lipase and Decreases Serum Triglycerides in Apolipoprotein E-Knockout Mice. *J Pharmacol Exp Ther* **2015**, *352* (2), 227–235.
14. Saito, H.; Lund-Katz, S.; Phillips, M. C. Contributions of Domain Structure and Lipid Interaction to the Functionality of Exchangeable Human Apolipoproteins. *Prog Lipid Res* **2004**, *43* (4), 350–380.
15. Xu, S.; Laccotripe, M.; Huang, X.; Rigotti, A.; Zannis, V. I.; Krieger, M. Apolipoproteins of HDL Can Directly Mediate Binding to the Scavenger Receptor SR-BI, an HDL Receptor That Mediates Selective Lipid Uptake. *J. Lipid Res* **1997**, *3*, 1289–1298.
16. Williams, D. L.; De La Llera-Moya, M.; Thuahnai, S. T.; Lund-Katz, S.; Connelly, M. A.; Azhartt, S.; Anantharamaiah, G. M.; Phillips, M. C. Binding and Cross-Linking Studies Show That Scavenger Receptor BI Interacts with Multiple Sites in Apolipoprotein A-I and Identify the Class A Amphipathic Alpha-Helix as a Recognition Motif. *J Biol Chem* **2000**, *275* (25), 18897–18904.
17. Thuahnai, S. T.; Lund-Katz, S.; Anantharamaiah, G. M.; Williams, D. L.; Phillips, M. C. A Quantitative Analysis of Apolipoprotein Binding to SR-BI: Multiple Binding Sites for Lipid-Free and Lipid-Associated Apolipoproteins. *J Lipid Res* **2003**, *44* (6), 1132–1142.
18. Chroni, A.; Liu, T.; Gorshkova, I.; Kan, H. Y.; Uehara, Y.; Von Eckardstein, A.; Zannis, V. I. The Central Helices of ApoA-I Can Promote ATP-Binding Cassette Transporter A1 (ABCA1)-Mediated Lipid Efflux. Amino Acid Residues 220-231 of

the Wild-Type ApoA-I Are Required for Lipid Efflux in vitro and High Density Lipoprotein Formation in vivo. *J Biol Chem* **2003**, *278* (9), 6719–6730.

19. Wang, N.; Silver, D. L.; Costet, P.; Tall, A. R. Specific Binding of ApoA-I, Enhanced Cholesterol Efflux, and Altered Plasma Membrane Morphology in Cells Expressing ABC1. *J Biol Chem* **2000**, *275* (42), 33053–33058.
20. Denis, M.; Haidar, B.; Marcil, M.; Bouvier, M.; Krimbou, L.; Genest, J. Molecular and Cellular Physiology of Apolipoprotein A-I Lipidation by the ATP-Binding Cassette Transporter A1 (ABCA1). *J Biol Chem* **2004**, *279* (9), 7384–7394.
21. Jaye, M.; Lynch, K. J.; Krawiec, J.; Marchadier, D.; Maugeais, C.; Doan, K.; South, V.; Amin, D.; Perrone, M.; Rader, D. J. A Novel Endothelial-Derived Lipase That Modulates HDL Metabolism. *Nat Genet* **1999**, *21* (4), 424–428.
22. Fuki, I. V.; Blanchard, N.; Jin, W.; Marchadier, D. H. L.; Millar, J. S.; Glick, J. M.; Rader, D. J. Endogenously Produced Endothelial Lipase Enhances Binding and Cellular Processing of Plasma Lipoproteins via Heparan Sulfate Proteoglycan-Mediated Pathway. *J Biol Chem* **2003**, *278* (36), 34331–34338.
23. Mead, J. R.; Irvine, S. A.; Ramji, D. P. Lipoprotein Lipase: Structure, Function, Regulation, and Role in Disease. *J Mol Med* **2002**, *80* (12), 753–769.
24. Connelly, P. W. The Role of Hepatic Lipase in Lipoprotein Metabolism. *Clin Chim Acta* **1999**, *286* (1–2), 243–255.
25. Hirata, K. I.; Dichek, H. L.; Cioffi, J. A.; Choi, S. Y.; Leeper, N. J.; Quintana, L.; Kronmal, G. S.; Cooper, A. D.; Quertermous, T. Cloning of a Unique Lipase from Endothelial Cells Extends the Lipase Gene Family. *J Biol Chem* **1999**, *274* (20), 14170–14175.
26. Santamarina-Fojo, S.; Dugi, K. A. Structure, Function and Role of Lipoprotein Lipase in Lipoprotein Metabolism. *Curr Opin Lipidol* **1994**, *5* (2), 117–125.
27. Landin, B.; Nilsson, Å. Metabolism of Chylomicron Phosphatidylethanolamine in the Rat. *Biochim Biophys Acta* **1984**, *793* (1), 105–113.
28. Dugi, K. A.; Dichek, H. L.; Santamarina-Fojo, S. Human Hepatic and Lipoprotein Lipase: The Loop Covering the Catalytic Site Mediates Lipase Substrate Specificity. *J Biol Chem* **1995**, *270* (43), 25396–25401.
29. McCoy, M. G.; Sun, G. S.; Marchadier, D.; Maugeais, C.; Glick, J. M.; Rader, D. J. Characterization of the Lipolytic Activity of Endothelial Lipase. *J Lipid Res* **2002**, *43* (6), 921–929.
30. Yu, J. E.; Han, S. Y.; Wolfson, B.; Zhou, Q. The Role of Endothelial Lipase in Lipid Metabolism, Inflammation, and Cancer. *Histol Histopathol* **2018**, *33* (1), 1–10.

31. Ishida, T.; Choi, S.; Kundu, R. K.; Hirata, K. ichi; Rubin, E. M.; Cooper, A. D.; Quertermous, T. Endothelial Lipase Is a Major Determinant of HDL Level. *J Clin Invest* **2003**, *111* (3), 347–355.
32. Paradis, M. E.; Lamarche, B. Endothelial Lipase: Its Role in Cardiovascular Disease. *Can J Cardiol* **2006**, *22*, 31B-34B.
33. Jin, W.; Millar, J. S.; Broedl, U.; Glick, J. M.; Rader, D. J. Inhibition of Endothelial Lipase Causes Increased HDL Cholesterol Levels in vivo. *J Clin Invest* **2003**, *111* (3), 357–362.
34. Strauss, J. G.; Zimmermann, R.; Hrzenjak, A.; Zhou, Y.; Kratky, D.; Levak-Frank, S.; Kostner, G. M.; Zechner, R.; Frank, S. Endothelial Cell-Derived Lipase Mediates Uptake and Binding of High-Density Lipoprotein (HDL) Particles and the Selective Uptake of HDL-Associated Cholesterol Esters Independent of Its Enzymic Activity. *Biochem J* **2002**, *368* (Pt 1), 69–79.
35. Merkel, M.; Kako, Y.; Radner, H.; Cho, I. S.; Ramasamy, R.; Brunzell, J. D.; Goldberg, I. J.; Breslow, J. L. Catalytically Inactive Lipoprotein Lipase Expression in Muscle of Transgenic Mice Increases Very Low Density Lipoprotein Uptake: Direct Evidence That Lipoprotein Lipase Bridging Occurs in vivo. *PNAS* **1998**, *95* (23), 13841–13846.
36. Sieber, S.; Grossen, P.; Detampel, P.; Siegfried, S.; Witzigmann, D.; Huwyler, J. Zebrafish as an Early Stage Screening Tool to Study the Systemic Circulation of Nanoparticulate Drug Delivery Systems in vivo. *J Control Release* **2017**, *264*, 180–191.
37. Arias-Alpizar, G.; Kong, L.; Vlieg, R. C.; Rabe, A.; Papadopoulou, P.; Meijer, M. S.; Bonnet, S.; Vogel, S.; van Noort, J.; Kros, A.; Campbell, F. Light-Triggered Switching of Liposome Surface Charge Directs Delivery of Membrane Impermeable Payloads in vivo. *Nat Commun* **2020**, *11*, 3638.
38. Campbell, F.; Bos, F. L.; Sieber, S.; Arias-Alpizar, G.; Koch, B. E.; Huwyler, J.; Kros, A.; Bussmann, J. Directing Nanoparticle Biodistribution through Evasion and Exploitation of Stab2-Dependent Nanoparticle Uptake. *ACS Nano* **2018**, *12* (3), 2138–2150.
39. Arias-Alpizar, G.; Koch, B.; Hamelmann, N. M.; Neustrup, M. A.; Paulusse, J. M. J.; Jiskoot, W.; Kros, A.; Bussmann, J. Stabilin-1 Is Required for the Endothelial Clearance of Small Anionic Nanoparticles. *Nanomedicine* **2021**, *34*, 102395.
40. Hayashi, Y.; Takamiya, M.; Jensen, P. B.; Ojea-Jiménez, I.; Claude, H.; Antony, C.; Kjaer-Sorensen, K.; Grabher, C.; Boesen, T.; Gilliland, D.; Oxvig, C.; Strähle, U.; Weiss, C. Differential Nanoparticle Sequestration by Macrophages and Scavenger

Endothelial Cells Visualized in vivo in Real-Time and at Ultrastructural Resolution. *ACS Nano* **2020**, *14* (2), 1665–1681.

41. Quiñonez-Silvero, C.; Hübner, K.; Herzog, W. Development of the Brain Vasculature and the Blood-Brain Barrier in Zebrafish. *Dev Biol* **2020**, *457* (2), 181–190.
42. Van Leeuwen, L. M.; Evans, R. J.; Jim, K. K.; Verboom, T.; Fang, X.; Bojarczuk, A.; Malicki, J.; Johnston, S. A.; van der Sar, A. M. A Transgenic Zebrafish Model for the in Vivo Study of the Blood and Choroid Plexus Brain Barriers Using Claudin 5. *Biol Open* **2018**, *7* (2), bio.030494.
43. Ulrich, F.; Ma, L. H.; Baker, R. G.; Torres-Vázquez, J. Neurovascular Development in the Embryonic Zebrafish Hindbrain. *Dev Biol* **2011**, *357* (1), 134–151.
44. Zhang, J.; Liss, M.; Wolburg, H.; Blasig, I. E.; Abdelilah-Seyfried, S. Involvement of Claudins in Zebrafish Brain Ventricle Morphogenesis. *Ann N Y Acad Sci* **2012**, *1257* (1), 193–198.
45. Zhang, J.; Piontek, J.; Wolburg, H.; Piehl, C.; Liss, M.; Otten, C.; Christ, A.; Willnow, T. E.; Blasig, I. E.; Abdelilah-Seyfried, S. Establishment of a Neuroepithelial Barrier by Claudin5a Is Essential for Zebrafish Brain Ventricular Lumen Expansion. *PNAS* **2010**, *107* (4), 1425–1430.
46. Ando, K.; Fukuhara, S.; Izumi, N.; Nakajima, H.; Fukui, H.; Kelsh, R. N.; Mochizuki, N. Clarification of Mural Cell Coverage of Vascular Endothelial Cells by Live Imaging of Zebrafish. *Development* **2016**, *143* (8), 1328–1339.
47. Lyons, D. A.; Talbot, W. S. Glial Cell Development and Function in Zebrafish. *Cold Spring Harb perspect biol* **2014**, *7* (2), a020586.
48. Umans, R. A.; Henson, H. E.; Mu, F.; Parupalli, C.; Ju, B.; Peters, J. L.; Lanham, K. A.; Plavicki, J. S.; Taylor, M. R. CNS Angiogenesis and Barriergenesis Occur Simultaneously. *Dev Biol* **2017**, *425* (2), 101–108.
49. O'Brown, N. M.; Megason, S. G.; Chenghua, G. Suppression of Transcytosis Regulates Zebrafish Blood-Brain Barrier Function. *Elife* **2019**, *8*, e47326.
50. Isogai, S.; Horiguchi, M.; Weinstein, B. M. The Vascular Anatomy of the Developing Zebrafish: An Atlas of Embryonic and Early Larval Development. *Dev Biol* **2001**, *230* (2), 278–301.
51. Moradi, M. A.; Bomans, P. H. H.; Jackson, A. W.; van Herk, A. M.; Heuts, J. P. A. A Quantitative CryoTEM Study on Crosslinked Nanocapsule Morphology in RAFT-Based Vesicle Polymerization. *Eur Polym J* **2018**, *108*, 329–336.

52. Moradi, M. A.; Tempelaar, S.; Van Herk, A. M.; Heuts, J. P. A. Morphology Control of Liposome - RAFT Oligomer Precursors to Complex Polymer Nanostructures. *Macromolecules* **2019**, *52* (24), 9476–9483.
53. Wu, Y.; Manna, S.; Petrochenko, P.; Koo, B.; Chen, L.; Xu, X.; Choi, S.; Kozak, D.; Zheng, J. Coexistence of Oil Droplets and Lipid Vesicles in Propofol Drug Products. *Int J Pharm* **2020**, *577*, 118998.
54. Leung, A. K. K.; Tam, Y. Y. C.; Chen, S.; Hafez, I. M.; Cullis, P. R. Microfluidic Mixing: A General Method for Encapsulating Macromolecules in Lipid Nanoparticle Systems. *J Phys Chem B* **2015**, *119* (28), 8698–8706.
55. Brader, M. L.; Williams, S. J.; Banks, J. M.; Hui, W. H.; Hong Zhou, Z.; Jin, L. Encapsulation State of Messenger RNA inside Lipid Nanoparticles. *Biophysj* **2021**, *120*, 2766–2770.
56. De Boeck, H.; Zidovetzki, R. Effects of Diacylglycerols on the Structure of Phosphatidylcholine Bilayers: A 2H and 31P NMR Study. *Biochemistry* **1989**, *28* (18), 7439–7446.
57. Goldberg, E. M.; Lester, D. S.; Borchardt, D. B.; Zidovetzki, R. Effects of Diacylglycerols and Ca2+ on Structure of Phosphatidylcholine/Phosphatidylserine Bilayers. *Biophys J* **1994**, *66*, 382–393.
58. Jiménez-Monreal, A. M.; Villalaín, J.; Aranda, F. J.; Gómez-Fernández, J. C. The Phase Behavior of Aqueous Dispersions of Unsaturated Mixtures of Diacylglycerols and Phospholipids. *Biochim Biophys Acta* **1998**, *1373* (1), 209–219.
59. Goñi, F. M.; Alonso, A. Structure and Functional Properties of Diacylglycerols in Membranes. *Prog Lipid Res* **1999**, *38* (1), 1–48.
60. Szule, J. A.; Fuller, N. L.; Peter Rand, R. The Effects of Acyl Chain Length and Saturation of Diacylglycerols and Phosphatidylcholines on Membrane Monolayer Curvature. *Biophys J* **2002**, *83* (2), 977–984.
61. Campomanes, P.; Zoni, V.; Vanni, S. Local Accumulation of Diacylglycerol Alters Membrane Properties Nonlinearly Due to Its Transbilayer Activity. *Commun Chem* **2019**, *2* (1), 1–8.
62. Allen, T. M.; Hansen, C.; Martin, F.; Redemann, C.; Yau-Young, A. Liposomes Containing Synthetic Lipid Derivatives of Poly(Ethylene Glycol) Show Prolonged Circulation Half-Lives in vivo. *Biochim Biophys Acta* **1991**, *1066* (1), 29–36.
63. Working, P. K.; Newman, M. S.; Huang, S. K.; Mayhew, E.; Vaage, J.; Lasic, D. D. Pharmacokinetics, Biodistribution and Therapeutic Efficacy of Doxorubicin Encapsulated in Stealth® Liposomes (Doxil®). *J Liposome Res* **2008**, *4* (1), 667–687.

64. Otis, J. P.; Zeituni, E. M.; Thierer, J. H.; Anderson, J. L.; Brown, A. C.; Boehm, E. D.; Cerchione, D. M.; Ceasrine, A. M.; Avraham-Davidi, I.; Tempelhof, H.; Yaniv, K.; Farber, S. A. Zebrafish as a Model for Apolipoprotein Biology: Comprehensive Expression Analysis and a Role for ApoA-IV in Regulating Food Intake. *Dis Model Mech* **2015**, *8* (3), 295–309.

65. Miyares, R. L.; De Rezende, V. B.; Farber, S. A. Zebrafish Yolk Lipid Processing: A Tractable Tool for the Study of Vertebrate Lipid Transport and Metabolism. *Dis Model Mech* **2014**, *7* (7), 915–927.

66. Kim, J. Y.; Seo, J.; Cho, K. H. Aspartame-Fed Zebrafish Exhibit Acute Deaths with Swimming Defects and Saccharin-Fed Zebrafish Have Elevation of Cholesteryl Ester Transfer Protein Activity in Hypercholesterolemia. *Food Chem Toxicol* **2011**, *49* (11), 2899–2905.

67. Song, Y.; Cone, R. D. Creation of a Genetic Model of Obesity in a Teleost. *FASEB journal* **2007**, *21* (9), 2042–2049.

68. Nishio, S. I.; Gibert, Y.; Bernard, L.; Brunet, F.; Triqueneaux, G.; Laudet, V. Adiponectin and Adiponectin Receptor Genes Are Coexpressed during Zebrafish Embryogenesis and Regulated by Food Deprivation. *Dev Dyn* **2008**, *237* (6), 1682–1690.

69. Anderson, J. L.; Carten, J. D.; Farber, S. A. Zebrafish Lipid Metabolism: From Mediating Early Patterning to the Metabolism of Dietary Fat and Cholesterol. *Methods Cell Biol* **2011**, *101*, 111–141.

70. Liu, C.; Gates, K. P.; Fang, L.; Amar, M. J.; Schneider, D. A.; Geng, H.; Huang, W.; Kim, J.; Pattison, J.; Zhang, J.; Witztum, J. L.; Remaley, A. T.; Dong, P. D.; Miller, Y. I. Apoc2 Loss-of-Function Zebrafish Mutant as a Genetic Model of Hyperlipidemia. *Dis Model Mech* **2015**, *8* (8), 989–998.

71. Pattipeiluhu, R.; Crielaard, S.; Klein-Schiphorst, I.; Florea, B. I.; Kros, A.; Campbell, F. Unbiased Identification of the Liposome Protein Corona Using Photoaffinity-Based Chemoproteomics. *ACS Cent Sci* **2020**, *6* (4), 535–545.

72. Li, C.; Tan, X. F.; Lim, T. K.; Lin, Q.; Gong, Z. Comprehensive and Quantitative Proteomic Analyses of Zebrafish Plasma Reveals Conserved Protein Profiles between Genders and between Zebrafish and Human. *Sci Rep* **2016**, *6*, 24329.

73. Muller, D. P. R.; Gamlen, T. R. The Activity of Hepatic Lipase and Lipoprotein Lipase in Glycogen Storage Disease: Evidence for a Circulating Inhibitor of Postheparin Lipolytic Activity. *Pediatr Res* **1984**, *18* (9), 881–885.

74. Ori, A.; Wilkinson, M. C.; Fernig, D. G. A Systems Biology Approach for the Investigation of the Heparin/Heparan Sulfate Interactome. *J Biol Chem* **2011**, *286* (22), 19892–19904.

75. Sun, S.; Dean, R.; Jia, Q.; Zenova, A.; Zhong, J.; Grayson, C.; Xie, C.; Lindgren, A.; Samra, P.; Sojo, L.; Van Heek, M.; Lin, L.; Percival, D.; Fu, J. M.; Winther, M. D.; Zhang, Z. Discovery of XEN445: A Potent and Selective Endothelial Lipase Inhibitor Raises Plasma HDL-Cholesterol Concentration in Mice. *Bioorg Med Chem* **2013**, *21* (24), 7724–7734.

76. Lo, P. K.; Yao, Y.; Zhou, Q. Inhibition of LIPG Phospholipase Activity Suppresses Tumor Formation of Human Basal-like Triple-Negative Breast Cancer. *Sci Rep* **2020**, *10* (1), 8911.

77. Zhang, Y. N.; Poon, W.; Tavares, A. J.; McGilvray, I. D.; Chan, W. C. W. Nanoparticle-Liver Interactions: Cellular Uptake and Hepatobiliary Elimination. *J Control Release* **2016**, *240*, 332–348.

78. Wilhelm, S.; Tavares, A. J.; Dai, Q.; Ohta, S.; Audet, J.; Dvorak, H. F.; Chan, W. C. W. Analysis of Nanoparticle Delivery to Tumours. *Nat Rev Mater* **2016**, *1* (5), 1–12.

79. Kuai, R.; Subramanian, C.; White, P. T.; Timmermann, B. N.; Moon, J. J.; Cohen, M. S.; Schwendeman, A. Synthetic High-Density Lipoprotein Nanodisks for Targeted Withalongolide Delivery to Adrenocortical Carcinoma. *Int J Nanomedicine* **2017**, *12*, 6581–6594.

80. Lameijer, M.; Binderup, T.; Van Leent, M. M. T.; Senders, M. L.; Fay, F.; Malkus, J.; Sanchez-Gaytan, B. L.; Teunissen, A. J. P.; Karakatsanis, N.; Robson, P.; Zhou, X.; Ye, Y.; Wojtkiewicz, G.; Tang, J.; Seijkens, T. T. P.; Kroon, J.; Stroes, E. S. G.; Kjaer, A.; Ochando, J.; Reiner, T.; Pérez-Medina, C.; Calcagno, C.; Fischer, E. A.; Zhang, B.; Temel, R. E.; Swirski, F. K.; Nahrendorf, M.; Fayad, Z. A.; Lutgens, E.; Mulder, W. J. M.; Duivenvoorden, R. Efficacy and Safety Assessment of a TRAF6-Targeted Nanoimmunotherapy in Atherosclerotic Mice and Non-Human Primates. *Nat Biomed Eng* **2018**, *2* (5), 279–292.

81. van Leent, M. M. T.; Meerwaldt, A. E.; Berchouchi, A.; Toner, Y. C.; Burnett, M. E.; Klein, E. D.; Verschuur, A. V. D.; Nauta, S. A.; Munitz, J.; Prévot, G.; van Leeuwen, E. M.; Ordikhani, F.; Mourits, V. P.; Calcagno, C.; Robson, P. M.; Soultanidis, G.; Reiner, T.; Joosten, R. R. M.; Friedrich, H.; Madsen, J. C.; Kluza, E.; van der Meel, R.; Joosten, L. A. B.; Netea, M. G.; Ochando, J.; Fayad, Z. A.; Pérez-Medina, C.; Mulder, W. J. M.; Teunissen, A. J. P. A Modular Approach toward Producing Nanotherapeutics Targeting the Innate Immune System. *Sci Adv* **2021**, *7* (10), eabe7853.

82. Zhu, G.; Mock, J. N.; Aljuffali, I.; Cummings, B. S.; Arnold, R. D. Secretory Phospholipase A_2 Responsive Liposomes. *J Pharm Sci* **2011**, *100* (8), 3146–3159.
83. Sharipov, M.; Tawfik, S. M.; Gerelkhuu, Z.; Huy, B. T.; Lee, Y. I. Phospholipase A2-Responsive Phosphate Micelle-Loaded UCNPs for Bioimaging of Prostate Cancer Cells. *Sci Rep* **2017**, *7* (1), 16073.
84. Gómez-Fernández, J. C.; Corbalán-García, S. Diacylglycerols, Multivalent Membrane Modulators. *Chem Phys Lipids* **2007**, *148* (1), 1–25.
85. Alwarawrah, M.; Dai, J.; Huang, J. Modification of Lipid Bilayer Structure by Diacylglycerol: A Comparative Study of Diacylglycerol and Cholesterol. *J Chem Theory Comput* **2012**, *8* (2), 749–758.
86. Holme, M. N.; Rashid, M. H.; Thomas, M. R.; Barriga, H. M. G.; Herpoldt, K. L.; Heenan, R. K.; Dreiss, C. A.; Bañuelos, J. L.; Xie, H. N.; Yarovsky, I.; Stevens, M. M. Fate of Liposomes in the Presence of Phospholipase C and D: From Atomic to Supramolecular Lipid Arrangement. *ACS Cent Sci* **2018**, *4* (8), 1023–1030.
87. Tacken, P. J.; De Beer, F.; Van Vark, L. C.; Havekes, L. M.; Hofker, M. H.; Van Dijk, K. W. Very-Low-Density Lipoprotein Binding to the Apolipoprotein E Receptor 2 Is Enhanced by Lipoprotein Lipase, and Does Not Require Apolipoprotein E. *Biochem J* **2000**, *347*, 357–361.
88. Thisse, B.; Thisse, C. Fast Release Clones: A High Throughput Expression Analysis. *ZFIN Direct Data Submission* **2004**.
89. Liu, C.; Han, T.; Stachura, D. L.; Wang, H.; Vaisman, B. L.; Kim, J.; Klemke, R. L.; Remaley, A. T.; Rana, T. M.; Traver, D.; Miller, Y. I. Lipoprotein Lipase Regulates Hematopoietic Stem Progenitor Cell Maintenance through DHA Supply. *Nat Commun* **2018**, *9* (1), 1–14.
90. Lindegaard, M. L. S.; Nielsen, J. E.; Hannibal, J.; Nielsen, L. B. Expression of the Endothelial Lipase Gene in Murine Embryos and Reproductive Organs. *J Lipid Res* **2005**, *46* (3), 439–444.
91. Lindegaard, M. L. S.; Olivecrona, G.; Christoffersen, C.; Kratky, D.; Hannibal, J.; Petersen, B. L.; Zechner, R.; Damm, P.; Nielsen, L. B. Endothelial and Lipoprotein Lipases in Human and Mouse Placenta. *J Lipid Res* **2005**, *46* (11), 2339–2346.
92. Sieber, S.; Grossen, P.; Bussmann, J.; Campbell, F.; Kros, A.; Witzigmann, D.; Huwyler, J. Zebrafish as a Preclinical in vivo Screening Model for Nanomedicines. *Adv Drug Deliv Rev* **2019**, *151–152*, 152–168.
93. Kemmer, G. C.; Bogh, S. A.; Urban, M.; Palmgren, M. G.; Vosch, T.; Schiller, J.; Günther Pomorski, T. Lipid-Conjugated Fluorescent PH Sensors for Monitoring PH Changes in Reconstituted Membrane Systems. *Analyst* **2015**, *140* (18), 6313–6320.

94. Kremer, J. R.; Mastronarde, D. N.; McIntosh, J. R. Computer Visualization of Three-Dimensional Image Data Using IMOD. *J Struct Biol* **1996**, *116* (1), 71–76.
95. Jin, S. W.; Beis, D.; Mitchell, T.; Chen, J. N.; Stainier, D. Y. R. Cellular and Molecular Analyses of Vascular Tube and Lumen Formation in Zebrafish. *Development* **2005**, *132* (23), 5199–5209.
96. Ellett, F.; Pase, L.; Hayman, J. W.; Andrianopoulos, A.; Lieschke, G. J. Mpeg1 Promoter Transgenes Direct Macrophage-Lineage Expression in Zebrafish. *Blood* **2011**, *117* (4), e49–e56.
97. Arias-Alpizar, G.; Bussmann, J.; Campbell, F. Zebrafish Embryos as a Predictive Animal Model to Study Nanoparticle Behavior in vivo. *Bio Protoc* **2021**, *11* (19), e4173.
98. Schindelin, J.; Arganda-Carreras, I.; Frise, E.; Kaynig, V.; Longair, M.; Pietzsch, T.; Preibisch, S.; Rueden, C.; Saalfeld, S.; Schmid, B.; Tinevez, J. Y.; White, D. J.; Hartenstein, V.; Eliceiri, K.; Tomancak, P.; Cardona, A. Fiji: An Open-Source Platform for Biological-Image Analysis. *Nat Methods* **2012**, *9* (7), 676–682.
99. Schneider, C. A.; Rasband, W. S.; Eliceiri, K. W. NIH Image to ImageJ: 25 Years of Image Analysis. *Nat Methods* **2012**, *9* (7), 671–675.

CHAPTER 3

Lipase-mediated selective hydrolysis of lipid droplets in phase-separated liposomes

This chapter was published as a preprint:

Panagiota Papadopoulou[#], Rianne van der Pol[#], Niek van Hilten[#], Mohammad-Amin Moradi, Maria J. Ferraz, Johannes M.F.G. Aerts, Nico Sommerdijk, H. Jelger Risselada, G.J. Agur Sevink, Alexander Kros* ChemRxiv 2023, DOI: 10.26434/chemrxiv-2023-9q9wh-v3

# denotes equal contribution
currently under revision with Advanced Materials

Abstract | The membrane-protein interface in lipid-based nanoparticles is important for their *in vivo* behavior. Better understanding may assist to evolve current drug delivery methods to more precise, cell- or tissue-selective nanomedicine. Previously, we demonstrated how phase separation can drive liposomes to cell specific accumulation *in vivo*, through the selective recognition of phase separation by triglyceride lipases (TGLs). This exemplified how liposome morphology and composition can determine the preferential interaction of nanoparticles with biologically relevant proteins. Here, we investigate in detail the lipase-induced compositional and morphological changes of phase-separated liposomes – which bear a lipid droplet in their bilayer – and unravel how lipase recognizes and binds to the particles at a molecular level. We find that phase-separated liposomes undergo selective lipolytic degradation of their lipid droplet while overall nanoparticle integrity remains intact. Next, we combine MD simulations and *in vitro* experiments to identify the Tryptophan-rich loop of the lipase – a region which is involved endogenously in lipoprotein binding – as the region through which the enzyme binds to the particle. We demonstrate that this preferential binding is due to the lipid packing defects induced on the membrane by phase separation. These findings are a significant example of selective nanoparticle-protein communication and interaction, aspects that may further the control of the *in vivo* behavior of lipid-based nanoparticles.

3.1 Introduction

Lipid-based nanomedicine is undoubtably a research field of growing importance, with various liposomal drug formulations marketed and used in the clinic over the last decades.[1] More recently, the development of RNA-based lipid nanoparticles (LNPs) has shown great potential, paving the way for future innovations.[2–6] To push this technology forward, towards simpler, yet more efficient and tissue specific formulations for drug delivery, better understanding of nanoparticle behavior must be acquired *i.e.*, how lipid organization determines morphology and influences (desired) nano-bio interactions. A key step is to study the interactions of lipid-based nanoparticles with biologically relevant proteins, and how these are determined by lipid composition and morphology. It is well known that such interactions *i.e.*, lead to the formation of a protein corona which controls the *in vivo* fate of nanoparticles to a great extent;[7–10] or they can lead to preferential protein binding or induce morphological changes in the membrane and affect the supramolecular assembly,[11,12] which in turn can affect their *in vivo* fate.

Previously,[13] in a liposome screening study in zebrafish embryos, a novel liposome formulation (named PAP3) was found to selectively interact with (capillary) lumen-bound triglyceride lipases (TGLs), enzymes involved in lipid transport and metabolism. The interaction led to the selective accumulation of PAP3 liposomes in brain endothelial cells (bECs) of zebrafish embryos which, at this developmental stage, are rich in TGLs. Liposome-lipase interactions are mediated solely through a unique phase-separated lipid nanoparticle morphology, in which liposomes bare a single lipid droplet inside each bilayer (**Figure 1a**). This morphology was found to be the key element for the cell specific accumulation and for interaction with TGLs. This is, to our knowledge, the first time that phase separation is used to target specific cells *in vivo*. PAP3 liposomes consist of an equimolar mixture of 1,2-distearyl-*sn*-glycero-3-phosphatidylcholine (DSPC) – a naturally occurring phospholipid – and 2-hydroxy-3-oleamidopropyl-oleate (DOaG), a synthetic lipid structurally analogous to a diacylglycerol (DAG) (**Figure 1b**). DAGs are endogenous signaling lipids and their conical shape, attributed to the small polar hydroxyl group and bulky fatty acid tails, is associated with negative curvature.

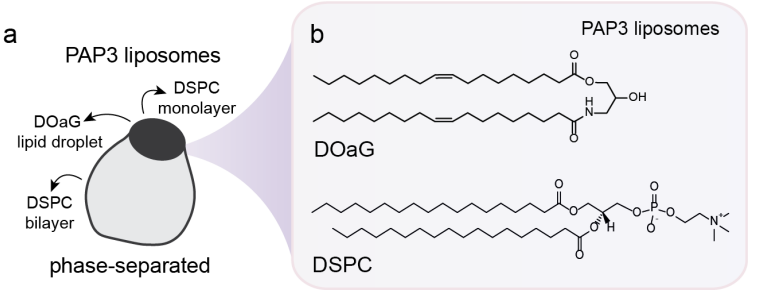

Figure 1. Molecular details of PAP3 liposomes. a) Schematic representation of phase-separated liposomes (named PAP3). **b)** Molecular structures of DOaG and DSPC combined in an equimolar mixture (1:1) to form PAP3 liposomes.

Endogenously, their local accumulation in the cell membrane induces morphological changes, which in turn potentiate recruitment and activation of proteins *e.g.*, Protein Kinase C (PKC) or Phospholipase C.[14–16] When added to phospholipid membranes, they are known to perturb lamellar bilayers and even induce phase separation and formation of non-bilayer phases (*i.e.,* lipid droplets) above a threshold (miscibility) concentration.[17,18] Our particular liposomal formulation follows the same principles and is an example of how DAG analogues can generate lipid droplets within DSPC leaflets (*i.e.,* lipid droplet is surrounded by a DSPC monolayer). Another important aspect of DAGs is that they increase the spacing between adjacent phospholipid headgroups in a lipid membrane, even below the threshold concentration, an effect that is amplified by curvature.[19] The domains that form as a consequence of such packing frustrations, and transiently expose the apolar domain of the lipid membrane, are known as lipid packing defects.[18,20–22] Some membrane peripheral proteins have been proposed to rely on these hydrophobic lipid packing defects – caused by factors such as phase separation, lateral tension, or membrane curvature – for membrane binding and activation.[23,24] Examples include the Golgi-associated protein ArfGAP1, that senses curvature-induced packing defects through an amphipathic lipid packing sensor motif [25,26] and the CTP:phosphocholine cytidylyltransferase (CCT), that binds to large packing defects on lipid droplets.[27] Also, the toxin Equinatoxin-II [28] and several lipases [29,30] have been found to sense packing defects induced by DAGs in particular.

Triglyceride lipases (TGLs) are lipolytic enzymes bound at the luminal surface of capillaries, and are involved in lipid transport and metabolism primarily through their interaction with freely circulating lipoproteins. They either hydrolyze tri- and di-acylglycerols and cholesteryl esters or phospholipids, remodeling lipoprotein particles and promoting influx of fatty acids into the cell; or they act as bridging molecules to facilitate lipoprotein uptake.[31,32] The family consists mainly of hepatic lipase (HL),[33] lipoprotein lipase (LPL),[34] and endothelial lipase (EL).[35] The main functional domains – the lipid (or lipoprotein) binding domain for substrate binding, the lid region containing the catalytic triad of Serine (Ser), Aspartate (Asp), Histidine (His) and the heparin binding domain – are all structurally homologous throughout the lipase protein family (see [36,37] and **Figure S24** for protein alignment). The lipid binding domain is rich in hydrophobic residues, mainly tryptophans (Trp), forming a hydrophobic Trp-rich loop that is responsible for insertion of the protein in the hydrophobic lipid core of lipoproteins.[33,38–41] Importantly, lipases have been found to depend on lipids on the lipoprotein membrane, but not apolipoproteins, for binding.[42]

Therefore, in this study, we combine experimental characterization and (coarse-grained) molecular dynamics (MD) simulations to investigate the molecular mechanism through which the TGL lipoprotein lipase (LPL) interacts with the DOaG-rich phase separated liposomes, and the subsequent morphological changes of the liposomes upon incubation. First, by combining morphological liposome analysis by cryo-Transmission Electron Microscopy (cryo-TEM) and enzymatic activity analysis of LPL, we observe selective lipolytic degradation of the DOaG-rich lipid droplet of PAP3 liposomes, while the overall nanoparticle integrity and structure is maintained. Mass spectrometry analysis confirms the selective hydrolysis of DOaG over DSPC, consistent with the known preference of LPL for hydrolyzing Tri- and Di-acylglycerols. Next, we built upon earlier insight in the role of defects for protein binding, [23,24] and study lipid packing defects in PAP3 liposomes and their role in recognition and binding of LPL. By combining cryo-TEM with MD simulations we confirm and quantify increased packing defects on the curved DSPC monolayer surrounding the DOaG lipid droplet, leading to the insight that (induced) curvature and DOaG availability are the two likely ingredients for

selective LPL binding. Finally, free energy calculations and enzymatic activity analysis reveal that the Trp-rich loop of LPL acts as a lipid packing defect sensing motif, that prefers to interact with the defected PAP3 membrane (DSPC/DOaG), over the (flat) pure DSPC counterpart.

3.2 Results

DOaG lipid droplet selectively depleted by lipoprotein lipase

To determine any morphological changes on PAP3 liposomes upon incubation with a TGL, the phase-separated liposomes were incubated with LPL at physiological conditions (pH = 7.4, 37 °C) for 3 h and changes in the morphology were assessed by cryo-TEM imaging (**Figure 2a**). As expected, without addition of LPL nearly 80% of PAP3 liposomes incubating at 37 °C for 3 h were phase-separated (**Figure 2b, e, f** and **Figure S1a**), with only ~20% of the population having another morphology *i.e.*, either (multi-) lamellar, solid-lipid or unidentifiable. Strikingly, after PAP3 liposomes were incubated with LPL they lacked their lipid droplet (**Figure 2c** and **Figure S1b**); less than 10% of the population appeared to be phase-separated (**Figure 2g, h**), and almost 80% of the population were lamellar. This indicated that LPL could deplete the phase-separated droplet possibly through its lipolytic activity, therefore selectively hydrolyzing the DOaG lipid. Accordingly, when the denatured and therefore inactive form of LPL was added to PAP3 liposomes, no change of the phase-separated morphology or the percentage in the population was observed (**Figure 2d, i, j** and **Figure S1c**), implying the catalytically active LPL to be responsible for the selective droplet digestion. Interestingly, despite the major morphological change on PAP3 liposomes, the nanoparticles remained intact in terms of structural integrity, retaining their initial average hydrodynamic diameter of ~120 nm over time, as determined by dynamic light scattering (DLS) (**Figure S2** and **table S1**). Of note, liposomes without DOaG, (*i.e.,* 100% DSPC), did not display any changes in morphology or size before and after addition of LPL (**Figure S3** and **table S1**), suggesting no interaction and as before, signifying LPL to be selective for DOaG or for the phase separation induced by DOaG.

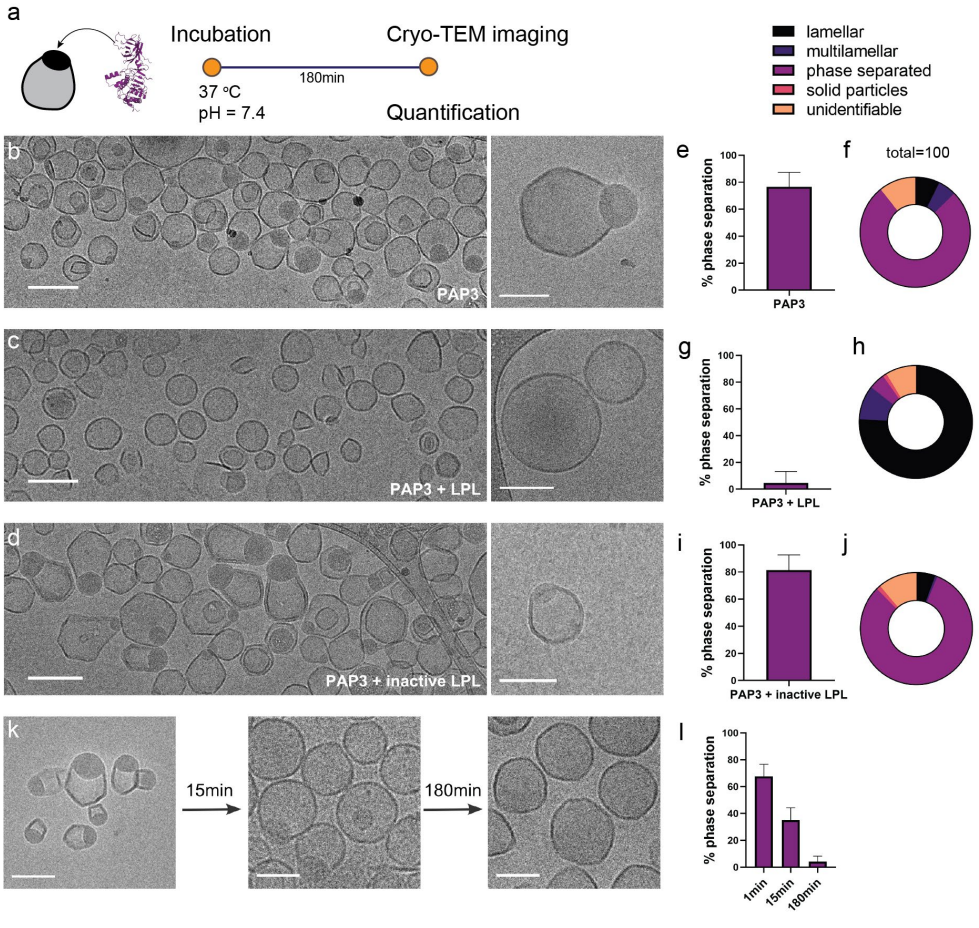

Figure 2. Selective depletion of DOaG lipid droplets in PAP3 liposomes. a) Schematic for conditions and timeline of cryo-TEM imaging. Low and high magnification cryo-TEM images depicting PAP3 liposomes incubating at 37 °C for 180 min **b)** without LPL, **c)** with LPL or d) with inactive LPL. Percentage of phase separation and quantification, based on cryo-TEM (N=200), of all populations found on PAP3 liposomal formulation incubating at 37 °C for 180 min **e, f)** without LPL, **g, h)** with LPL or **i, j)** with inactive LPL. **k)** Cryo-TEM images of PAP3 liposomes incubating with LPL at 37 °C for 1, 15 and 180 min. **l)** Percentage of phase separation on PAP3 liposomes, based on cryo-TEM quantification (N=200), after incubation with LPL at 37 °C for 1, 15 and 180 min. The data set generated for this figure is a result of the same liposome formulation. Size and PDI values (as determined by DLS) can be found in supporting table S1. Scale bars: 200 nm for b, c, d and 100 nm for k and insets on b, c, d.

LPL selectively hydrolyzes DOaG but not DSPC

Subsequently, to assess the evolution and timeline of the observed morphological change, PAP3 liposomes were imaged after incubating with LPL for 1, 15 and 180 min, and the percentage of phase separation was found to progressively decrease over time (**Figure 2k-l** and **Figure S4**). This indicated the observed phenomenon was a dynamic process, and lipolysis could be monitored over time by quantifying the amount of free fatty acids (FFA),[43,44] released as metabolite products from the hydrolysis of the co-formulants DOaG and/or DSPC (**Figure 3a**). For this, a non-esterified free fatty acid measurement kit (NEFA-kit) was used, along with mass spectrometry which was used to determine which lipid is preferentially hydrolyzed (**Figure 3b**). As expected, PAP3 liposomes incubated with LPL released ~0.9 mmoL/L of FFA over a period of 300 min (**Figure 3c**) and hydrolysis continued beyond this point (**Figure S5**). Incubation of PAP3 liposomes without LPL, or incubation of PAP3 liposomes with inactivated LPL, as well as incubation of 100% DPSC liposomes with LPL, did not release any significant amount of FFA over the same period, again indicating the specificity of LPL for DOaG (**Figure 3c**). Here, to also verify the LPL preference on naturally occurring DAGs – along DOaG as a DAG analogue – we formulated phase-separated liposomes consisting of dioleoylglycerol (DOG) and DSPC (1:1). Subsequently, we monitored the FFA release and structural changes of the DSPC/DOG liposomes upon LPL incubation (**Figure S6**). The results showed similar preference of LPL on DOG-containing liposomes as on PAP3. Similarly, to assess the influence of LPL on liposomes that are known to freely circulate *in vivo* and not particularly interact with cells types and proteins,[8] a formulation based on the clinically approved Myocet®[45] (composition: POPC:CHO, 55:45) was also incubated at 37 °C with LPL for 180 min, which did not result in FFA release, indicating no interaction with LPL (**Figure S7**).

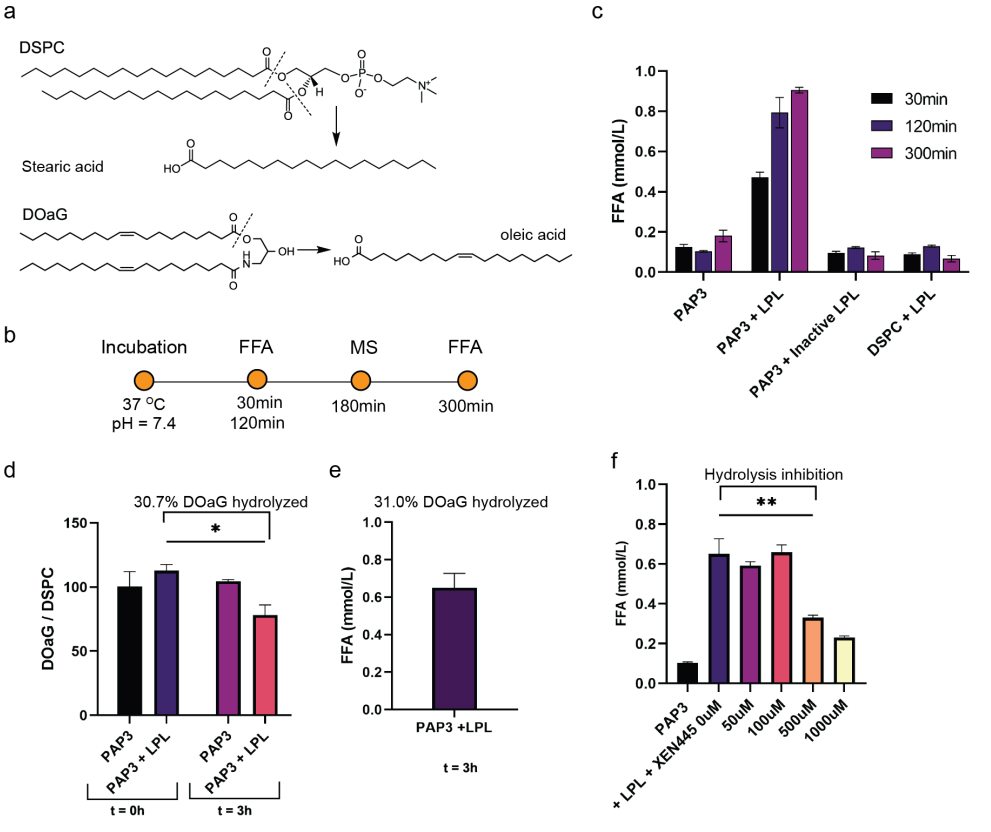

Figure 3. **Hydrolysis of lipids in PAP3 liposomes. a)** Potential hydrolysis of DSPC and/or DOaG co-formulants by LPL resulting in free fatty acid (FFA) release. **b)** Timeline of measurement of LPL hydrolytic activity. **c)** Quantification of released FFA after incubation of PAP3 liposomes without and with LPL, or PAP3 with inactive LPL, or DSPC liposomes with LPL at 37 °C after 30, 120, and 300 min. **d)** Quantification of DOaG / DSPC lipid ratio in PAP3 liposomes as measured by mass spectrometry at t = 0 h and t = 3 h incubating at 37 °C with and without LPL. DOaG / DSPC ratio of PAP3 at t = 0 h was set as 100. Analysis indicated the % of DOaG hydrolyzed. **e)** Quantification of released FFA in PAP3 liposomes incubating with LPL at 37 °C for 3 h, indicating the % of DOaG hydrolyzed. FFA release was measured immediately after the mass spectrometry analysis. The difference on the released FFA of PAP3 between Figure 3c and 3e is attributed to the different concentrations of LPL used for each measurement and therefore hydrolysis must be designated as a range (0.6-0.9 mmoL/L). **f)** XEN445-mediated inhibition of LPL and effect on FFA release after PAP3 liposomes incubated with LPL and 0, 50, 100, 500 or 1000 μM XEN445. Size and PDI values (as determined by DLS) can be found in supporting table S1. Statistical significance was evaluated using a two-tailed unpaired Student's t-test. ns: not significant ($P > 0.05$). Significantly different: *$P \leq 0.05$, **$P \leq 0.01$, ***$P < 0.001$. Exact P value for d : 0.0337 and for f : 0.0020.

Next, mass spectrometry analysis was used to investigate the hydrolysis of the lipids in PAP3 liposomes. The DOaG/DSPC ratio was measured before and after addition of LPL, indicating a decrease only for the DOaG lipid, after addition of LPL, and signifying that 30.7% of DOaG was hydrolyzed (**Figure 3d** and **Figure S8**). Given that DOaG is the only lipid hydrolyzed, FFA was again measured immediately after the mass spectrometry and found to correspond to 31% of hydrolyzed DOaG, in agreement with the mass spectrometry value (**Figure 3e**). In our previous studies,[13] lipase-mediated uptake of PAP3 liposomes was inhibited *in vivo* (zebrafish embryos and adult mice) by the TGL inhibitor XEN445.[46] Therefore, we investigated the influence of XEN445 on the lipolytic activity of LPL on PAP3. LPL was incubated with XEN445 at room temperature for 30 min, prior to the addition of LPL to PAP3 liposomes at 37 °C, and DOaG hydrolysis was found to be inhibited by ~50% at 500 μM XEN445 (**Figure 3f** and **Figure S9**).

Simulations confirm lipase binds on PAP3 liposomes through lipid packing defects and via its Trp-rich lipid binding domain

Having confirmed that LPL selectively hydrolyzes liposomes containing DOaG, we sought to investigate the role of the characteristic phase-separated morphology. Previously, we showed that the concentration of DOaG lipid in the PAP3 formulation determines whether liposomes phase-separate. When PAP3 was formulated with DSPC and 0, 10, or 20% mol DOaG, liposomes did not show phase separation, while above 30% mol DOaG liposomes were found to be phase-separated, causing a directed *in vivo* biodistribution towards TGL-rich endothelial cells.[13] Therefore, we hypothesized phase separation to be essential – or at least preferable – for TGL recognition. To assess this hypothesis, released FFA after LPL incubation was measured for liposomes with varying % mol of DOaG. Up to 20% mol, *i.e.,* for mixed membranes, FFA release was observed to increase linearly, but it steeply increased after this point (**Figure 4a**). This suggested enhanced LPL action for PAP3 liposomes with ≥30% mol DOaG, which coincides with the concentration threshold relating to phase separation as quantified by cryo-TEM (**Figure 4a insets, Figure 4b right y-axis** and **Figure S10**). The finding that the phase change coincides with a non-linear jump in the LPL-induced FFA release, signifies the role of phase separation in LPL hydrolysis.

As reported earlier for DAGs,[17-19] increasing the DOaG content in a PC bilayer across a phase boundary, could substantially increase the membrane curvature in the surroundings of the lipid droplet. Curvature is known to notably increase the lipid packing defect number and area, an effect that has been suggested to promote protein binding.[17,47] Moreover, compared to a mixed membrane, the local concentration of DOaG in the curved membrane around the lipid droplet is also significantly higher. Therefore, to quantify the role of phase separation, curvature, and packing defects at a molecular level – that is not directly accessible by experiments or atomistic MD due to long time scales – we generated a coarse-grained (CG) representation for DSPC/DOaG at different DOaG concentrations (**snapshots** in **Figure 4b** and **Figure S11a**). As detailed in the SI (sections **S12-S15**), the CG DOaG lipid representation was adapted from the similar DOG lipid.[48] In agreement with standard practice, we employed the observed phase separation onset at 29 % mol (**Figure 4b, left y-axis**) to match the experimental findings. Phase separation in CGMD was quantified by the (time-averaged) relative fraction of contacts between the DOaG lipid and the DSPC lipid (see Materials and Methods for more details and **Figure S14**) following a recently developed method.[49] The DOaG parametrization described here was used for all simulations in the remainder of this study.

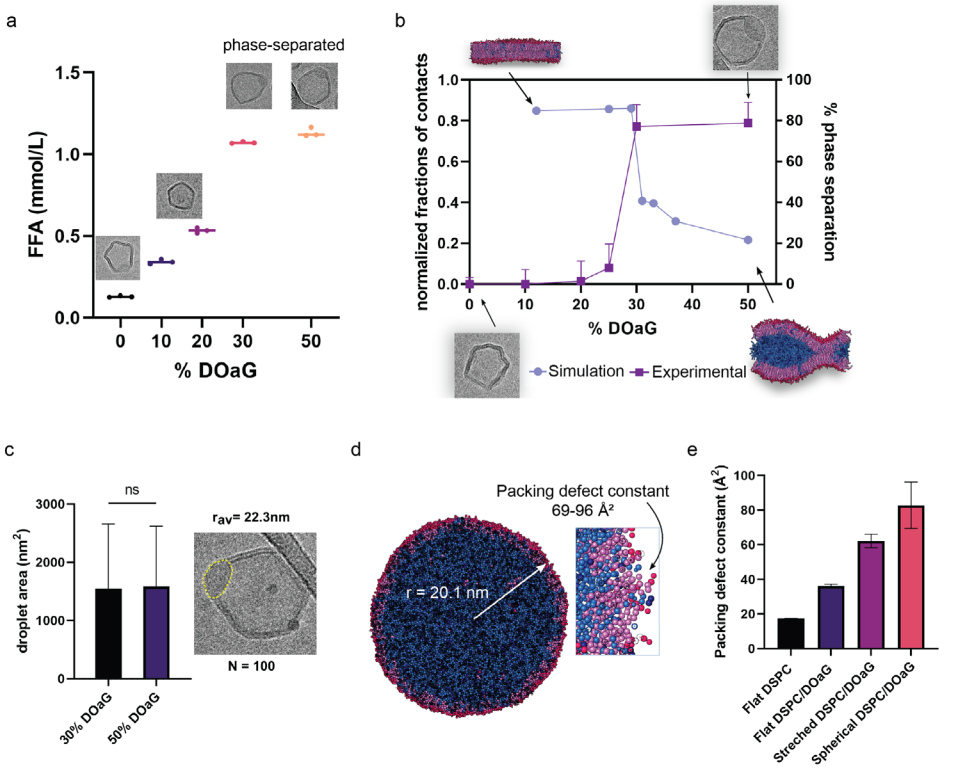

Figure 4. Experimental findings and simulations confirm phase separation as an important aspect for LPL preferential binding on PAP3 liposomes a) Quantification of released FFA of formulations containing DSPC and varying % mol of DOaG, after incubation with LPL at 37 °C for 120 min. Insets show the morphology of liposomes at a particular % mol DOaG (0% = gel phase, 20% = small droplet indicate initiation of phase separation, 30-50% = phase-separated). **b)** Double plot showing correlation of experimental and simulation data. Phase separation starts after 25% mol DOaG according to cryo-TEM quantification (N=200) and 29% according to the coarse-grained simulation. DOaG is shown in blue and DSPC is shown in pink/red. **Correlation of simulated PAP3 droplet and experimental values. c)** Average radius of phase-separated PAP3 liposomes (containing 30% or 50% mol DOaG) as calculated by cryo-TEM quantification of the droplet area (N=100). Area was measured in Fiji software, by drawing the perimetry of each droplet (yellow dashed line) according to the electron density. **d)** Simulated PAP3 spherical droplet with radius approximately matching the experimental value in (c) and zoom-in inset depicting the lipid packing defects. Packing defect constant determined as the effective average area of hydrophobic defects and calculated to be 69-96 Å^2 for the spherical droplet. DOaG is shown in blue and DSPC is shown in pink/red. **e)** Packing defect constants of flat DSPC, flat DSPC/DOaG, streched DSPC/DOaG and spherical DSPC/DOaG (see d). Size and PDI values (as determined by DLS) can be found in supporting table S1. Statistical

significance was evaluated using a two-tailed unpaired Student's t-test. ns: not significant ($P > 0.05$). Significantly different: $^{*}P \leq 0.05$, $^{**}P \leq 0.01$, $^{***}P < 0.001$. Exact P value for c: 0.8152, e: 0.0002 and <0.0001. For graphs in b, lines were drawn for the clear visualization of the phase separation point.

To capture the role of curvature and to quantify the defect characteristics for a DOaG droplet of a typical diameter of – *i.e.*, an average of 22.3 nm for ≥30 % mol DOaG (see **Figure 4c**) as quantified by cryo-TEM – we performed a droplet simulation with this initial radius for a 82/18 DOaG/DSPC ratio (**Figure 4d** and **Figure S11b**). Since demixing is strongly diffusion limited, we started from a pre-structured droplet and performed 2 microsecond of simulated annealing, to quickly reach a stable structure, with the droplet radius stabilizing to 20.1 nm. Using a modified protocol (see Materials and Methods), we calculated the packing defect constant, which is a measure of the effective average area of hydrophobic defects (**Figure 4d, e** and **Figure S16**). For a flat DSPC membrane the constant was found to be ~17 $Å^2$ while adding the DOaG to the system (1:1 ratio) increased the constant to ~36 $Å^2$ indicating phase separation increases the packing defects. Also, adding curvature increased the packing defect constant even further – as calculated by the defect constant on the curved droplet (**Figure 4d, e**). For the latter, however, we give a range since the lipid composition in the droplet monolayer varies, depending on the starting configuration and size, and because there is an uncertainty in the fitting parameter. The range for the packing defect constant was between 69 to 96 $Å^2$, showing that the packing defects in the curved droplet are more prevalent than in the flat pure DSPC and flat DSPC/DOaG membranes (**Figure 4d zoom in, and Figure 4e**). We next used the lower bound of this value range as a reference value for simulating LPL binding to stretched DOaG/DSPC membranes (**Figure 4e and 5c**). Stretched membranes are used to approximate curved membranes, since the lipid packing defects on their outer leaflet surface correlate, as we explain in reference [50] (*vide infra*).

Following the proof that the DOaG droplet increases both the number and area of lipid packing defects in the curved DSPC monolayer – due to the condensing of DOaG and the accompanying high curvature of the outer leaflet – we next sought to investigate whether LPL specifically binds to PAP3 via these packing defects. The structure of LPL is well studied and identified by X-ray crystallography[51] and cryo-TEM[52] (**Figure 5a**). Functional parts include the lipid binding domain which is rich in Trp as mentioned previously (hence called the Trp-rich loop, **Figure 5a, inset**), and the catalytic lid with the active site (**Figure 5a, inset**). The C-terminus, where the lipid binding domain is located, is responsible for substrate binding but not for heparin binding or catalysis.[53] We first proceeded to investigate which regions of the LPL protein may be involved in interacting with the lipid packing defects of the phase-separated membrane. Hereto, we employed a recently developed neural network (NN) model that is trained on MD data and is able to predict the lipid packing defect sensing free energy (ΔΔF) for peptide sequences.[54] ΔΔF is defined as the difference in free energy of a peptide binding to a tensionless membrane versus a stretched membrane that bares lipid packing defects, such as the curved DSPC monolayer around a DOaG droplet. The higher the magnitude of the ΔΔF value, the more favorably it binds to the defected membrane. We first used a sliding window of 15 residues to fragmentize the LPL protein structure and then predicted the ΔΔF for the overlapping fragments. From this, we derived a per-residue average ΔΔF (given the residue is solvent accessible, see section **S17** and **Figure S18**) and color-coded the protein structure accordingly (**Figure 5b**).

Residues Ser416-Ser426, comprising the Trp-rich loop, was the highest scoring solvent-accessible peptide motif we identified (**Figure 5b** and section **S19**). As previously described in the context of membrane curvature sensing, Trp residues can indeed play a key role in complementing the hydrophobic lipid packing defects on lipid leaflets,[25] and we argue that the Trp-rich loop of LPL might fulfill a similar function. Notably, this argument is in line with the Trp-rich loop being part of the lipid binding domain of LPL, which is responsible for endogenous lipoprotein binding.[38–40]

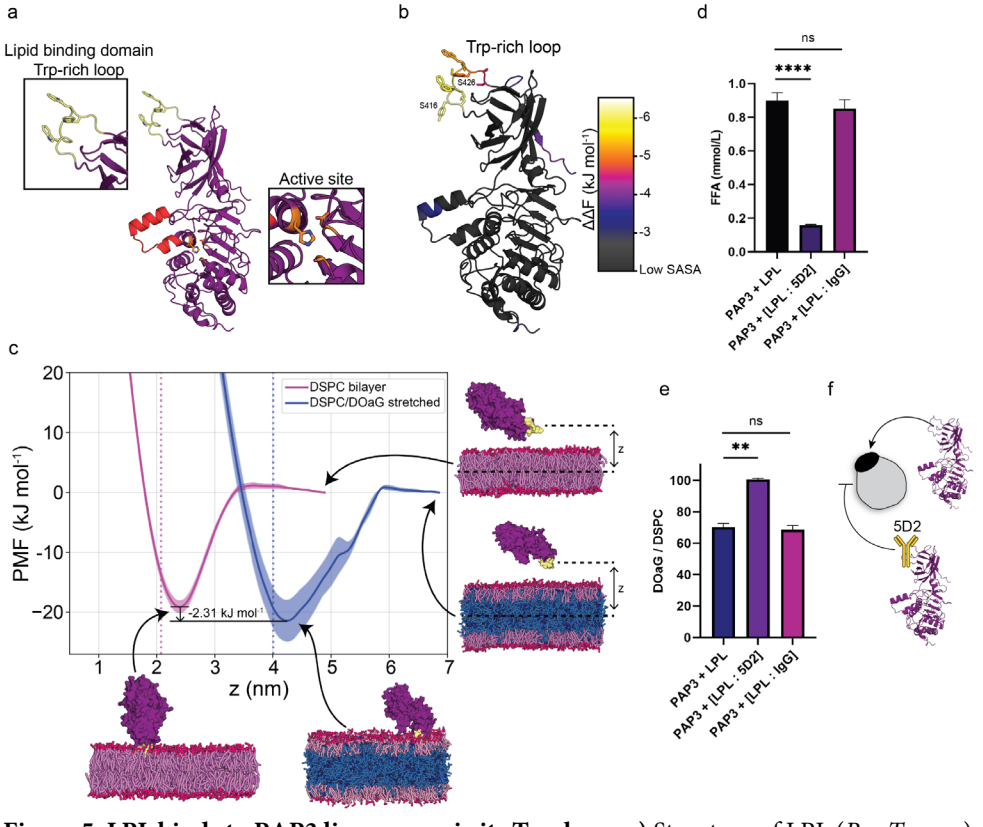

Figure 5. LPL binds to PAP3 liposomes via its Trp-loop. a) Structure of LPL (*Bos Taurus*). Insets indicate the Trp-rich loop (yellow) – which comprises the lipid binding domain – and active site (orange). Lid region indicated in red. **b)** Color-map of predicted lipid packing defect sensing regions on LPL (all values are given in **S19**). Bright colors indicate putative sensing motifs, according to NN-predicted relative binding free energy (ΔΔF) and solvent-accessible surface area (SASA) values. **c)** Potential of mean force (PMF) profiles of LPL binding to a DSPC membrane (in red-pink) and a DSPC/DOaG phase-separated membrane (in red-pink/blue). The umbrella sampling (US) reaction coordinate is the z-distance between the center-of-mass (COM) of the Trp-rich loop (in yellow) and the COM of the lipids (*i.e.,* center plane of the membrane). Snapshots are the final frames of the trajectories and indicate that the protein is completely unbound at high z (free energy = 0 kJ mol^{-1}) and membrane-bound through the Trp-rich loop at the minima. Dotted lines indicate the position of the DSPC head groups (NC3 beads). **d)** Quantification of released FFA from PAP3 liposomes and **e)** mass spectrometry quantification of DOaG / DSPC ratio of PAP3 liposomes after incubation at 37 °C for 120 min with LPL, LPL + 5D2 antibody and LPL + IgG control antibody. DOaG/DSPC ratio of liposomes that did not undergo hydrolysis incubating with LPL + 5D2 was set as 100. **f)** Schematic of LPL binding to PAP3 liposomes via its Trp-rich loop and 5D2 mediated inhibition of binding. Size and PDI values (as determined by DLS) can be found in supporting table S1. Statistical significance was

evaluated using a two-tailed unpaired Student's t-test. ns: not significant ($P > 0.05$). Significantly different: *$P \leq 0.05$, **$P \leq 0.01$, ***$P < 0.001$. Exact P value for d: <0.0001 and 0.3222 and for e: 0.0029 and 0.5654.

To further investigate lipid packing defect sensing by LPL and to see whether the Trp-loop is preferably binding to defected membranes such as the PAP3 liposomes, we calculated the potential of mean force (PMF) profiles for the entire LPL protein binding to the PAP3 phase-separated membrane – with lipid packing defect constants that are in a similar range as those for the earlier simulated PAP3 droplet (*vide supra*, **Figure 4e**). We performed umbrella sampling (US) simulations with the z-distance between the Trp-rich loop and the center plane of the membrane as the reaction coordinate. The resulting PMF profiles showed that LPL binds to the PAP3 phase-separated membrane (having enhanced lipid packing defects) indeed more favorably than to a flat pure DSPC bilayer, with a small free energy difference of 2.31 kJ mol^{-1} (~1 k_BT) between the minima (**Figure 5c**). The propensity for binding that is observed for the flat pure DSPC membrane (about 20 kJ mol^{-1}) corresponds exactly to the curvature sensing transition point from a recent study,[54] which showed that a 2 kJ mol^{-1} increase in binding free energy has a pronounced effect on the membrane binding probability (**Figure S20**).

Moreover, although a conformational change in the binding domain may contribute a few kJ mol^{-1} to the actual binding affinity,[55] this shift is likely very similar for both membranes. Beyond this binding preference, the enzymatic preference of LPL to hydrolyze DAGs over phospholipids[56] *is not* captured by our MD simulations but *does* contribute to our experimental observations. From the MD trajectories, it is clear that LPL indeed interacts with the membranes through its Trp-rich loop (**snapshots** in **Figure 5c**), in line with the NN-predictions (**Figure 5b**), and mechanistically similar to previously reported lipid droplet sensing proteins.[57,58]

To experimentally prove the involvement of the Trp-rich loop in the recognition and hydrolysis of PAP3 liposomes, we measured the hydrolytic activity of LPL on PAP3 liposomes, while blocking the Trp-rich loop with the monoclonal anti-LPL antibody 5D2. The 5D2 monoclonal antibody has been identified to bind specifically

to the Trp-loop of the lipid binding domain of LPL, inhibiting binding and catalysis of lipoproteins.[40,59–61] Indeed, after incubation of LPL with 5D2 in a 1:1 ratio at room temperature for 30 min and subsequent addition to PAP3 liposomes at 37 °C, hydrolysis of DOaG as quantified by the release of FFA and mass spectrometry was strongly reduced (**Figure 5d-f**). To ensure that inhibition of hydrolysis was due to the specific inhibition of the Trp-rich loop by the 5D2 antibody, a negative isotype control antibody (matching 5D2 antibody's host species and class - IgG1) was used to measure the non-specific binding in LPL and non-specific interactions with PAP3. As expected, the control antibody did not inhibit the hydrolysis (**Figure 5d, e**), supporting the specific interaction of LPL with PAP3 liposomes through its Trp-rich loop. Similarly, when a non-mammalian LPL (derived from *Burkholderia sp.*) – which lacks the lipid binding domain of mammalian TGLs – was used with the 5D2 antibody (**Figure S21** for complete sequence), hydrolysis was not inhibited (**Figure S22**), indicating again the specificity of 5D2 to the Trp-rich loop. Despite the hydrolysis of PAP3 liposomes taking place with the non-mammalian lipase, it appears to occur via a different mechanism, and it is therefore not relevant for the study of mammalian LPL species. It *does* however signify that 5D2 inhibits the Trp-loop specifically, and non-specific interactions between antibody-protein-liposomes do not take place.

3.3 Discussion and Conclusion

In this work, we combine experimental findings and MD simulation data to describe the selective lipolytic degradation of lipid droplets in phase-separated liposomes by LPL. We show LPL recognizes the enhanced lipid packing defects on the liposomal membrane induced by phase separation. The liposomes, named PAP3, consist of the naturally occurring DPSC and the synthetic DAG analogue DOaG, in a 1:1 ratio, with the latter being responsible for the phase separation and constitution of a lipid droplet within each liposome bilayer. PAP3 liposomes have been seen to interact with TGLs and specifically accumulate in cell subsets *in vivo*,[13] a phenomenon attributed to their phase-separated morphology. Therefore, the observation of their structural evolution after interaction with LPL, as well as the mechanism of enzyme

binding was of great interest. Here, we confirm the selective hydrolysis of DOaG by LPL, leading to degradation of the lipid droplet and to reorganization of the assembly to a lamellar bilayer, while the overall integrity of the nanoparticle is maintained. Contrarily, the other co-formulant – DSPC – does not undergo hydrolysis. These observations exemplify selective nanoparticle-protein interactions and subsequent nanoparticle rearrangement. As TGLs endogenously remodel lipoproteins without nanoparticle collapse – *i.e.,* LPL remodels very low-density lipoproteins to low-density lipoproteins[34,62,63] – here we similarly show the depletion of a large part of the nanoparticle without bilayer disruption.

Additionally, we show that LPL is selective for PAP3 liposomes (DSPC/DOaG) and for liposomes containing the natural DAG counterpart (DSPC/DOG). LPL is not selective for 100% DSPC liposomes, or typical spherical LUVs with high circulation lifetimes *in vivo* (*i.e.,* Myocet®-like). One reason for this could be the inherent preference of LPL to hydrolyze DAGs and therefore DAG analogues, such as DOaG. Synergistically, another reason could be the preference of LPL to recognize membranes with high curvature – and thus higher packing defect constants – induced by phase separation.[15,16,24] This hypothesis is supported by the non-linear increased hydrolysis on liposomes consisting of ≥ 30% mol DOaG (phase-separated), over liposomes consisting of < 25% mol DOaG (non-phase separated). Lipid packing defects were then quantified in our coarse-grained MD simulations and found to be higher when phase separation and high curvature are present in the membrane system. Finally, we show that LPL preferentially binds to the defected membrane of PAP3 liposomes, and we identified the Trp-rich loop of LPL as a lipid packing defect sensing motif. Preventing the Trp-loop to bind to PAP3 (by blocking the region with the selective antibody 5D2)[59], abolishes the lipolysis and confirms the involvement of the Trp-rich loop in the recognition of PAP3 liposomes. Hereby, we expand our knowledge of the Trp-rich loop to act as a lipid packing defect sensor, beyond its role in lipoprotein binding.[38] PAP3 liposomes, having lipid packing defects that arise upon phase separation, appear to hijack the natural pathway in which LPL recognizes lipoproteins via its Trp-rich loop.

Additionally, we have previously shown PAP3 liposomes to be endocytosed by a TGL-mediated pathway *in vivo*.[13] A possible pathway for this could be the selective recognition of DOaG by TGL – with a significantly higher chance of DOaG being transiently exposed to the aqueous environment due to the increased packing defects in the phase-separated membrane – and subsequent endocytosis. Our current study shows the selective lipolysis and remodeling of the particle by LPL, something that may also occur *in vivo* before nanoparticle uptake by the cell. However, given the complex *in vivo* environment and the spatiotemporal regulation of lipase function in lipid metabolism, further studies should be performed *in vivo* and in real time to solidly prove this hypothesis. Here it should be noted, apolipoprotein CII (APOCII) is an essential co-factor of LPL and, in a physiological environment, it will play a central role on efficient lipase activity.[34] This is an aspect that is not presented in the current study. However, the presence of apolipoproteins is not vital for LPL binding on lipid membranes[42] and, although APOCII would enhance the LPL lipolytic efficiency (or would even be essential in an *in vivo* environment), it is not required for overall LPL activity; especially not for comparison of relative activity on different targets (*i.e.*, different liposomal formulations).

In the case of *in vivo* selective lipolysis of the PAP3 lipid droplet – without nanoparticle collapse as this study suggests – these nanoparticles can exert unique properties for drug delivery *i.e.*, the lipid droplet could be used as a guide "moiety" for cell selective accumulation through a lipase-mediated pathway, while the hydrophilic core could incorporate functional drugs. Alternatively, pro-drugs could be incorporated within the lipid droplet exploiting the selective lipase interaction for specific drug release *i.e.*, lipase-mediated prodrug hydrolysis and subsequent drug release. However, the most important aspect of this work is not to address potential drug-delivery designs, but to overall understand in detail how interactions with the biological environment influences lipid-based nanoparticle properties. Ultimately this will lead to more rational drug-delivery designs. Another noteworthy observation is the visible remnants of the hydrolyzed droplet on some nanoparticles (**Figure S23, arrows**). Such thickness mismatches in cryo-TEM have been recently described as nanodomains in liposomal membranes.[64,65] Therefore,

although PAP3 liposomes can be seen as lamellar and non-phase separated macromolecularly after LPL incubation, a more in-depth investigation of the molecular details is required – *e.g.*, the existence of nanodomains or lipid rafts remaining after LPL hydrolysis. The question that arises here is whether such nanodomains can be still recognizable by TGLs *in vivo*.

Finally, the selection of LPL as a representative TGL was purely due to the extensive literature on LPL structure, regulation and function in health and disease, and therefore was the most relevant protein to base our studies on. However, all (mammalian) lipases from the TGL family have very similar amino acid sequences ([36] and **Figure S24** for protein alignment), structural homology, and similar functional roles on triglyceride metabolism.[33,66–68] This allows the assumption that other TGLs will behave similarly on PAP3 liposomes as the LPL studied here. On the same note, the LPL chosen for these studies was derived from bovine milk (*Bos Taurus*), yet the sequence homology with human LPL (*Homo Sapiens*) is > 90%, with high structural similarity and a conserved Trp-loop (see **Figure S25-S26** for protein structure alignment), which allows to assume that it will similarly affect PAP3 liposomes as bovine LPL. To support this, we show that incubating PAP3 liposomes with human LPL releases a substantial amount of FFA (**Figure S27**). Also, similar PMF profiles were calculated for human LPL interacting with the DOaG/DSPC phase-separated membrane and a flat DSPC bilayer through its Trp-rich loop, showing even a more substantial binding preference for the phase-separated system in terms of the free energy difference between the minima (13.48 kJ mol^{-1}) (**Figure S28**).

Overall, this study explains in detail the how and the why of the preferential interaction of TGLs with unique phase-separated liposomes. Such interaction has been recently found responsible for cell specific targeting *in vivo*. Particularly, it serves an important proof-of-concept for selective protein interaction on lipid nanoparticle membranes, owing to lipid packing defects. Comparable to the formulation studied here, some RNA-based lipid nanoparticles (RNA-LNPs) have membranes with high curvature. They consist of a solid lipid core, surrounded by a phospholipid monolayer and – depending on composition – they may be prone to such packing defects. Therefore, this study could open new avenues for exploration

of novel LNP formulations, that could preferentially interact with packing-defect sensing motifs in proteins of interest. Most notably, this work presents a selective lipid-based nanoparticle - protein communication and emphasizes the morphological changes nanoparticles undergo after interaction with physiologically relevant proteins. Persistent and limited understanding of the key nano-bio interactions has so far stymied progression from empirical discovery towards rational nanoparticle design. Therefore, understanding the nanoparticle - protein interface is an aspect that could lead to more advanced and precise nanomedicines in the future.

3.4 Materials and Methods

General reagents: 1,2-distearoyl-*sn*-glycero-3-phosphatidylcholine (DSPC) was purchased from Avanti Polar Lipids (Alabaster, AL, US). Additional DSPC was purchased from Lipoid GmbH. XEN445, Lipoprotein Lipase derived from Bovine milk and Lipoprotein Lipase derived from *Burkholderia Sp.* was purchased from Sigma Aldrich. Human LPL (recombinant derived from CHO cells) was purchased from R&D systems, Bio-techne. Non-Esterified Fatty Acid measurement kit (NEFA-HR2, FUJIFILM Wako chemicals) was purchased from Sopachem, the Netherlands. Anti-lipoprotein lipase monoclonal antibody – 5D2 clone and negative IgG isotype control – was purchased from Biorad, United Kingdom. All other chemical reagents were purchased at the highest grade available from Sigma Aldrich and used without further purification. All solvents were purchased from Biosolve Ltd. Ultrapure MilliQ® water, purified by a MilliQ Advantage A10 water purification system from MilliPore, was used throughout.

Synthesis of DOaG and DOG lipids: DOaG and DOG lipids were synthesized as previously reported (chapter 2 and reference [13]) and isolated as regioisomeric mixtures: 80% isomer where acyl chains substituting the *sn*-1 and *sn*-3 positions of the backbone and 20% isomer where acyl chains substituting the *sn*-1 and *sn*-2 positions of the backbone):

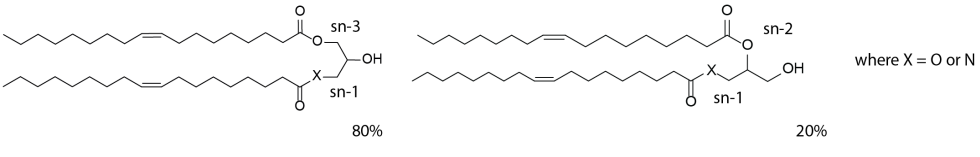

Lipoprotein Lipase: Lipoprotein Lipase (from bovine milk) in ammonium sulfate suspension was centrifuged in a low protein binding tube (DNA Lobind, Eppendorf) for 15 min at 15.000 g (at 4 °C) and the supernatant was removed. The precipitate was then dissolved gently in Tris Buffer 10mM, pH 7.4 and spun again for 15 min at 15000 g. The supernatant containing the dissolved protein was then kept and concentrated with spin filtration (Amicon, MWCO 10 kDa). The new concentration was determined using a NanoDrop™ One/One^{C} Microvolume UV-Vis Spectrophotometer (Thermo Scientific) according to Lambert's beer equation (A = ε b c) with an extinction coefficient ε = 71040 L/moL.

To ensure retrieval of all LPL from the manufacture's bottle, any leftover precipitate in the bottle was dissolved in Tris Buffer (10 mM, pH = 7.4) and dialyzed against the same buffer to remove residual ammonium sulfate (dialysis cassettes, Slide-A-Lyzer™, 20K MWCO, ThermoFisher Scientific). The solution was then centrifuged at 15000 g for 15 min and the supernatant was kept, concentrated and concentration was determined as stated above. LPL was then aliquoted in low protein binding tubes (DNA Lobind, Eppendorf) and kept at -80 °C until usage. Lipoprotein Lipase in PBS (Human, derived from CHO cells) was firstly dialyzed against Tris Buffer 10 mM pH = 7.4 and then concentrated. The new concentration was determined as described above. Similarly, it was kept at -80 °C aliquoted for further use.

Liposome formulation: Large unilamellar vesicles (LUVs) were formed through extrusion (mini extruder, Avanti Polar Lipids) above the T_m of all lipids (*i.e.,* 65-70 °C) in 10mM Tris Buffer pH = 7.4 and at a total lipid concentration of 5 mM (3.5 mg/mL), unless if stated otherwise. Individual lipids as stock solutions (10 mM) in chloroform, were combined to the desired molar ratios and dried to a thin film, first under N_2 stream, then >1 h under vacuum. Lipid films were hydrated with 1 mL Tris Buffer above the T_m of all lipids (65-70 °C), with gentle vortexing, to form a suspension. Hydrated lipids were passed 11 times through 2 x 400 nm polycarbonate (PC) membranes (Nucleopore Track-Etch membranes, Whatman), followed by 11 times through 2 x 100 nm PC membranes. All liposomes were stored at 4 °C and used within 5 days.

Liposome - Lipase Incubation: Liposomes (3.5 mg/mL, in 10mM Tris Buffer, pH = 7.4) were transferred in a low protein binding tube (3 mg/mL final lipid concentration after lipase incubation) and subsequently Lipoprotein Lipase (in

10mM Tris Buffer pH = 7.4) was added to the tube to reach 0.03 mg/mL final concentration. Liposome-lipase mixture was left to incubate at 37 °C in a thermomixer (Eppendorf) for up to 20 h with gentle occasional mixing.

Inactivation of LPL: Lipase in Tris Buffer (10mM, pH=7.4) was added in a low protein binding tube (DNA LoBind, Eppendorf) and heated up to 95 °C for 10 min in a thermomixer (Eppendorf) to ensure denaturation.

Inhibition of LPL by XEN445 inhibitor: To inhibit the catalytic activity of LPL before incubation with PAP3 liposomes, the lipase was incubated for 30 min at room temperature with the TGL inhibitor XEN445 at different concentrations (titration). The inhibitor was freshly dissolved in DMSO as a stock solution of 10 mM and subsequently added to a low-protein binding Eppendorf tube (DNA-LoBind) containing LPL, to reach final concentration of 0, 50, 100, 500 or 1000 μM and at a constant DMSO content of 5% v/v. LPL concentration was so that it would reach 0.03 mg/mL final concentration after incubation with liposomes, as stated previously.

Size and polydispersity measurements: Particle size and polydispersity were measured using a Malvern Zetasizer Nano ZS (operating wavelength = 633 nm). Measurements were carried out at room temperature (25 °C) or at 37 °C in Tris Buffer 10 mM, pH = 7.4 and at a total lipid concentration of approx. 100 μM. All reported DLS measurements are the average of three measurements.

FFA release measurement: For each time point of interest, the amount of FFA resealed in the sample was measured with a non-esterified fatty acid assay kit (NEFA kit – Fujifilm Wako Chemicals) with a protocol provided for 96 well plates (Greiner) using a microplate spectrophotometer set to 37 °C (Infinite®, M1000 pro, TECAN). Briefly and for each sample, 9 μL were taken and diluted 2x in Tris Buffer 10 mM (pH = 7.4). 5 μL were then put in each well and mixed with 200 μL of Reagent 1 and incubated for 5 min. The absorbance (Abs1) was then measured in each well at 550 nm (Sub: 660 nm). Immediately after, 100 μL of Reagent 2 was added and the mixture was incubated for another 5 min. The absorbance (Abs2) was again then measured in each well at 550 nm (Sub: 660 nm). Final absorbance was calculated by subtracting Abs1 from Abs2. Concentration of FFA (mmoL/L) was calculated by constructing each time a new calibration curve. All measurements were the average of three measurements.

Cryogenic Transmission Electron Microscopy: Freshly glow-discharged carbon grids supported on Cu (Lacey carbon film, 200 mesh, Electron Microscopy Sciences, Aurion, The Netherlands) were used for vitrification inside a Vitrobot plunge-freezer (FEI VitrobotTM Mark III, Thermo Fisher Scientific) regulating steady temperature and humidity conditions (22 °C or 37 °C and 99% humidity). Liposomes incubating with LPL at 37 °C were immediately taken and applied to the grid and the excess liquid was blotted for 3 s and subsequently plunge frozen in liquid ethane below -160 °C to ensure formation of vitreous ice. cryo-TEM images were collected on a Talos L120C (NeCEN, Leiden University) operating at 120 kV or on a Titan (TU Eindhoven) operating at 300 kV, with working temperature below -180 °C. Images were recorded manually at a nominal magnification of 13500x, 22000x or 36000x yielding a pixel size at the specimen of 7.41, 4.44, or 2.86 ångström (Å), respectively.

Cryo-TEM Quantification: Software Fiji (ImageJ) was used for image processing and quantification. Individual low magnification images (up to 3 images per sample) were used to provide a big population of 200 nanoparticles. Particles were then counted and divided into categories (lamellar, multilamellar, phase-separated, solid particles), according to their morphology. Liposomes whose morphology was not able to be identified (due to image quality) were marked as "unidentifiable" and the value obtained was used as standard deviation for the rest of population. Liposomes that were seen to be on top or in close contact with the copper grid or overlapping with each other, were excluded from the quantification. Particles consisting of two distinct liposomal cores and one lipid droplet (*i.e.*, sharing the droplet) were quantified as one phase-separated particle. For quantification and calculation of the radius of the PAP3 droplet, the area A (nm^2) of each individual droplet (N = 100) was measured by the 2D projection of liposomes as obtained by cryo-TEM imaging. The average droplet radius r (nm) was then calculated from the formula: $A = \pi r^2$.

Simulation details: All simulations were performed with GROMACS 2019.3 [69] and the Martini 3.0.0 force field,[48] at a 20-fs time step. Temperature (T = 303.15 K, τ_T = 1 ns) and pressure coupling (compressibility = $4.5 \cdot 10^{-5}$ bar^{-1}, τ_p = 12 ns) were applied by the velocity rescaling thermostat and the Berendsen barostat, respectively. The neighbor list was updated every 20 steps. A 1.1 nm cutoff was used for the Van der Waals interactions (shifted Verlet cutoff scheme) and Coulomb interactions (reaction-field electrostatics).

Coarse-grained model for PAP3 liposomes: Phase separation on PAP3 liposomes was determined from the MD trajectories, using the time-averaged contact fraction between the DOaG and the DSPC lipid. Following a general procedure,[49] a relative contact fraction was calculated by counting contacts between DOaG and DSPC lipids and dividing it by the total number of DOaG contacts (see sections **S12-S15** for details). A cutoff of 1.1 nm was used to identify contacts between lipids via selected beads on both lipid types that are roughly at the same depth within the membrane. In addition, we normalized by the total concentration of DOaG to enable direct comparison for different DOaG concentrations. Consequently, complete phase separation always corresponds to a value of zero, and ideal mixing to unity.

Droplet simulation: For the simulation of the droplet, the droplet configuration was made with PackMol[70] with - on the inside - purely DOaG and on the outside a monolayer of DSPC. The simulated annealing was run for 1.5μs, with a starting temperature of 450 K and cooled to a temperature of 303 K, after which the temperature was kept stable for 500 ns at the final temperature. After the simulated annealing the droplet was ran for analysis for 1.5 μs at the same temperature and settings as the bilayer simulations.

Packing defects: While previous work used the PackMem package[71] to identify a linearly increasing defect size constant with total curvature for both single component and mixed membranes,[19] the role of (de)mixing remains less quantified. Here, we developed a new computational protocol to clarify this relation for our highly curved DOaG/DSPC membranes of arbitrary (non-symmetric) shapes. Packing defect constants for the simulated PAP3 droplet can in principle be determined using standard PackMem routines, by employing a spherical instead of the usual rectangular grid.[19] However, since droplets do not necessarily adopt a

purely spherical shape, even tiny mismatches in the determination of the relevant reference interface may bias the calculated constants in a non-predictable fashion. For this reason, we developed a protocol that can deal with arbitrary shapes. Briefly, a closed 2D interface is fitted through the positions of relevant GL beads, subsequently triangulated, and used as a reference for identifying shallow and deep defects following the recommended PackMem settings.[71] Details and examples of this procedure will be published in a separate study.

Protein modeling and lipid packing defect sensing prediction: The 3D models of human and bovine LPL were downloaded from the AlphaFold2 database.[72,73] Both structures closely overlap with the human crystal structure[51] (**Figure S26**). The unstructured N-terminal signal sequence (residue 1-34) was excluded. To predict which regions of the protein may play a role in lipid packing defect sensing, a previously developed neural network model was applied. [54] A sliding window of 15 residues was used to predict binding free energy values (ΔΔF) for peptide motifs along the sequence of the bovine LPL protein (sections **S17**-**S19**). In order to exclude buried protein regions (that are unavailable to interact with membranes), only peptide motifs with an average solvent-accessible surface area (SASA, as calculated using BioPython[74]) of greater than 0.8 nm^2 were considered. To visualize putative regions of interest, the B-factor field in the PDB file format was used to adjust the coloring accordingly.

Umbrella sampling: A DSPC bilayer (361 molecules per leaflet) was prepared using the *insane* python script[75] and the Martini 3 CG force field.[48] After solvation with Martini 3 water and ions (0.15 M NaCl), steepest decent energy minimization and 10 ns of semiisotropic NpT equilibration (p_{ref} = 1 bar) were performed. Next, a layer of 1444 randomly oriented DOaG molecules was inserted between the two DSPC leaflets. The resulting 1:2 DSPC:DOaG membrane was energy minimized and equilibrated. A 75 bar·nm surface tension was applied to the membrane system to match the lipid packing defects (measured with a protocol based on PackMem (same as the one calculating defects on the spherical droplet and with the recommended settings[71]) to the ones found on a DSPC/DOaG spherical lipid droplet (see **Figure S16**). A CG Martini representation of the LPL protein was obtained with Martinize2/VerMOUTH.[76] Secondary structure was predicted with DSSP[77] and constrained by an elastic network between the backbone beads (k_{force} =

500 kJ mol^{-1}). The CG protein was inserted into the DSPC or DSPC/DOaG systems with ~4 nm separation between the Trp-rich loop of the protein (Ile413-Pro427) and the upper leaflet's lipid head groups. The resulting set-ups were resolvated with water and ions (0.15 M NaCl). After steepest decent energy minimization, both systems were equilibrated for 100 ns with position restraints (k_{force} = 1,000 kJ mol^{-1}) on all protein beads. The initial frames for US were generated by running a pulling simulation in which the z-distance between the centers-of-mass (COM) of the Trp-rich loop and the lipids was decreased gradually, and then selecting 24 frames that span the range from the solvated to the membrane-bound state with 0.2 nm increments. For each umbrella window, a 50 ns equilibration followed by a 2 μs production run was performed in which the Lipid-Trp-rich loop COM z-distance was constrained to its initial value (k_{force} = 500 kJ mol^{-1}). To dampen membrane deformations during US runs, a soft harmonic flat-bottom potential (k_{force} = 100 kJ mol^{-1}) was applied on the lipid head groups to restrain the lipids within its initial thickness range (+0.5 nm on each side of the membrane). Free energy profiles were obtained through umbrella integration[78] with 10,000 bins. Averages and standard deviations were calculated by using block-averaging over 3 blocks.

Mass spectrometry analysis: DSPC and DOaG were analyzed by Liquid Chromatography tandem Mass Spectrometry (LC-MS/MS). Solutions of DSPC and DOaG (1 pmol/μL) were prepared in 5 mM ammonium formate, in methanol. The compounds were introduced in the mass spectrometer and the tuning conditions for both compounds were determined as indicated below.

Lipid extraction: For the MS analysis and for each time point, 9 μL of each sample (PAP3 liposomes incubating at 37 °C with or without LPL) was flush frozen in liquid nitrogen to ensure discontinuation of the hydrolysis. Subsequently the samples were extracted by a modified Bligh and Dyer extraction[79] using acidic buffer (100 mM ammonium formate buffer, pH = 3.1). Briefly, in an Eppendorf tube, 400 μL methanol and 200 μL of chloroform were added to the sample. The sample was vortexed for 30 min at room temperature and centrifuged for 10 min at 15,700 g to spin down precipitated protein.

MS/MS parameters

Mass Spectrometer	Xevo TQ-S micro (Waters)
Capillary voltage	3.50 kV
Source temperature	150°C
Desolvation temperature	450°C
Cone gas	50 L/h
Desolvation gas	950 L/h

Compound	Retention time (min)	Parent (m/*z*)	Daughter (m/*z*)	Cone Voltage (V)	Collision energy (V)
DOaG	2.51	620.9	602.9	15	15
DSPC	4.45	790.7	184.0	15	20

The supernatant was transferred to a new Eppendorf tube and 200 µL chloroform and 350 µL water were added for extraction of the lipids. After centrifugation (5 min at 15,700 g), the lower (organic) phase was transferred to a clean Eppendorf tube and the upper (aqueous) phase was re-extracted by adding 400 µL of chloroform. Organic phases were pooled and taken to dryness at 45 °C under a nitrogen stream. Next, the residue was dissolved in 600 µL of butanol and 600 µL of water, mixed and centrifuged for 10 min at 15,700 g. The butanol phase was transferred to a clean tube and taken to dryness in Eppendorf Concentrator Plus at 45 °C. The residue was dissolved in 100 µL methanol, stirred and sonicated in a bath for 30 s and centrifuged for 10 min at 15,700 × g. Finally, 10 µL of the supernatant was applied to the UPLC-MS/MS. Data are the average of 2 experiments.

LC-MS/MS: Measurements were performed by reverse-phase liquid chromatography using a Waters UPLC-Xevo-TQS micro and a BEH C18 column, 2.1 × 50 mm with 1.7 µm particle size (Waters, USA), by applying an isocratic elution of methanol containing 10 mM ammonium formate. The UPLC program was applied for 7 min at a flow rate of 0.250 mL/min. The temperature of the column and of the autosampler were kept at 23 °C and 10 °C, respectively, during the run. Data were analyzed with Masslynx 4.2 Software (Waters Corporation; Milford MA).

3.5 Supplementary Information

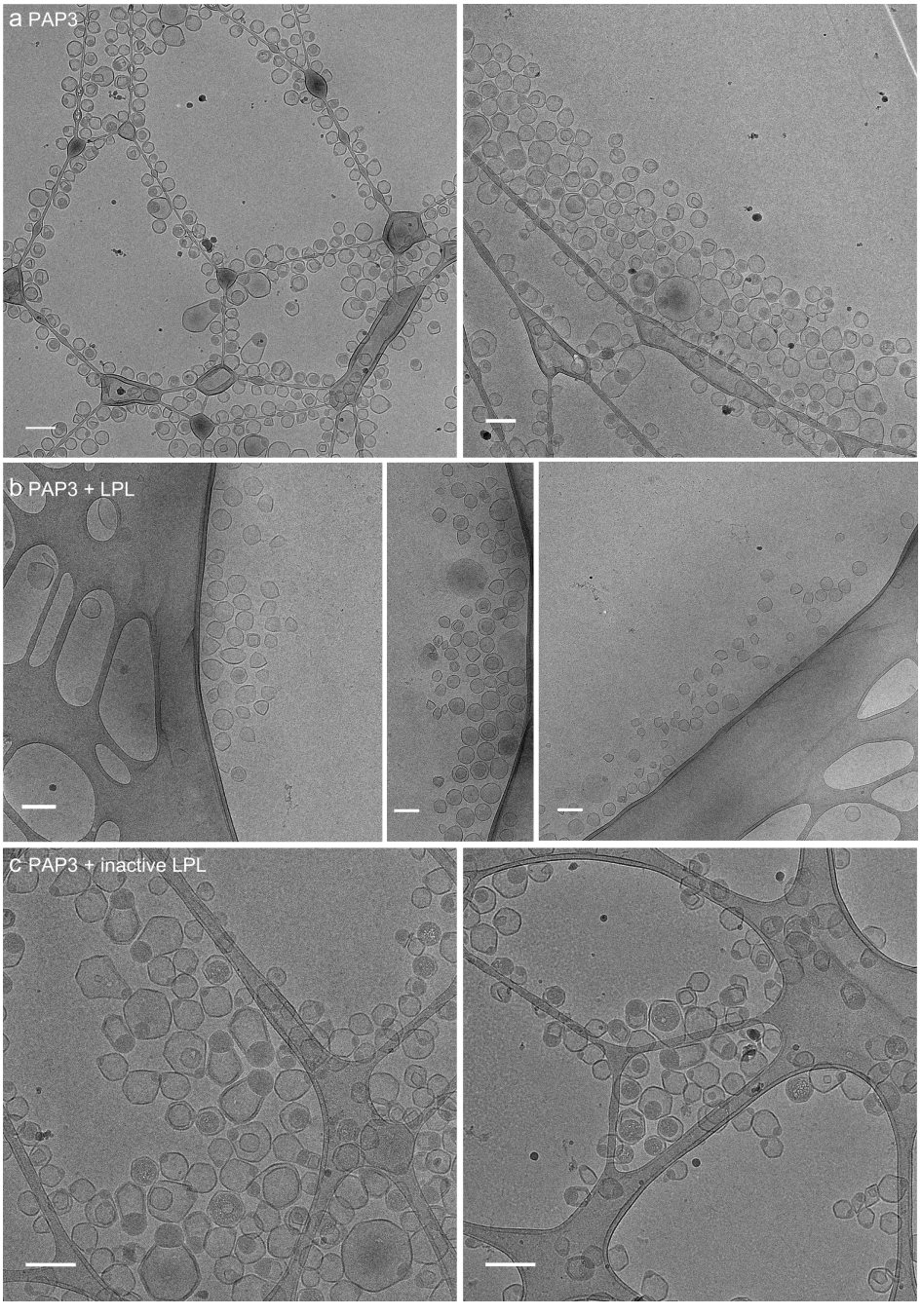

Figure S1. Cryo-TEM images of PAP3 liposomes a) without LPL, **b)** with LPL and **c)** with inactive LPL incubating for 180 min at 37 ºC. Images as chosen for quantification of the whole population. Scale bars: 200 nm.

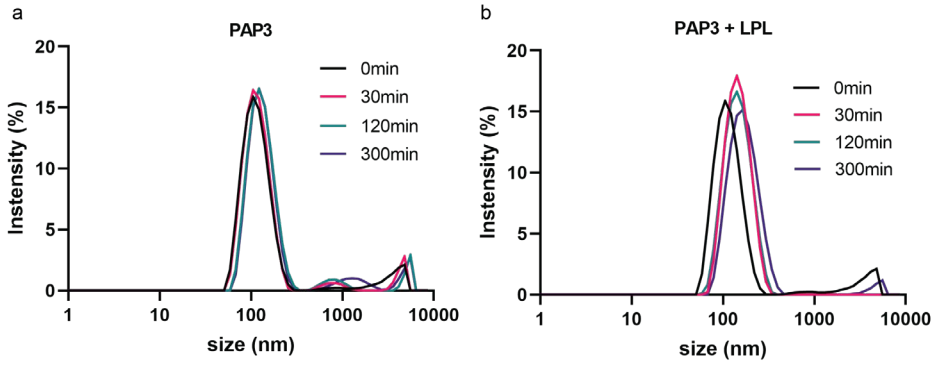

Figure S2. Size of PAP3 liposomes overtime as measured by dynamic light scattering (DLS). a) before and **b)** after addition of LPL. Liposomes incubating at 37 °C for 0, 30, 120 and 300 min.

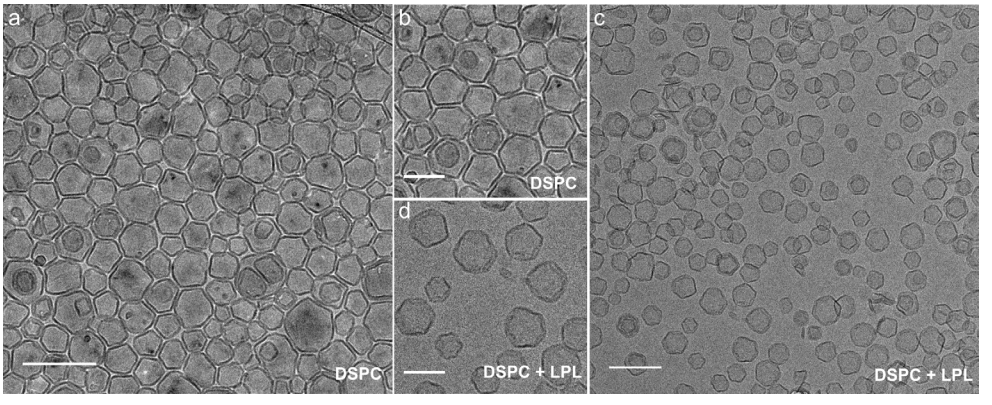

Figure S3. Cryo-TEM images of DSPC liposomes a, b) before and **c, d)** after addition of LPL. Liposomes incubating at 37 °C for 180 min. Scale bars: 200 nm for a, c and 100 nm for b, d.

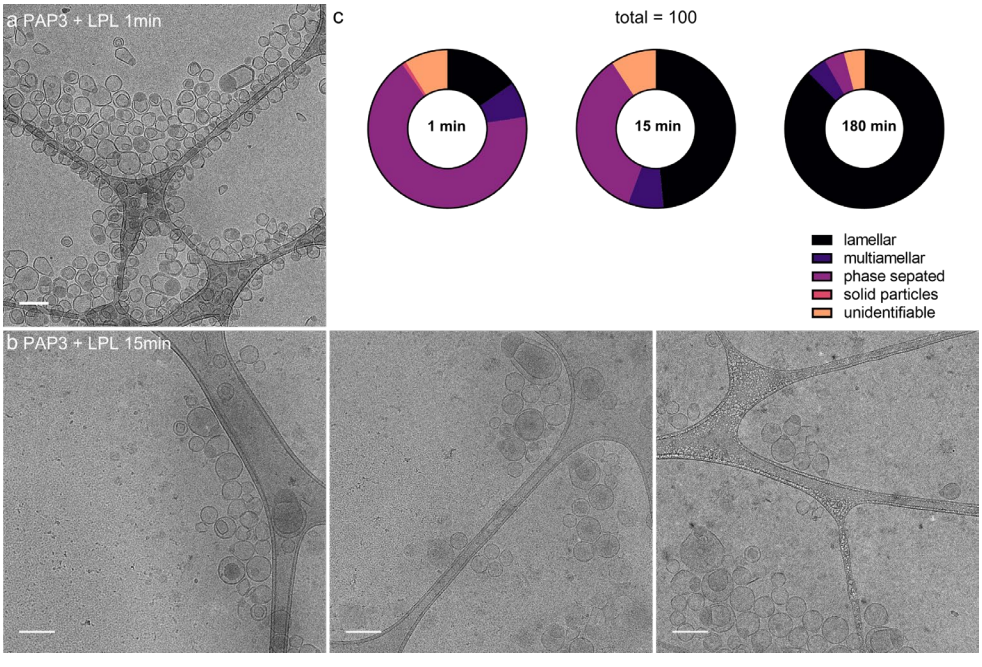

Figure S4. Cryo-TEM images of PAP3 liposomes with LPL incubating at 37ºC for a) 1 min or **b)** 15 min and **c)** Quantification of the whole population of PAP3 liposomes with LPL incubating at 37 ºC for 1, 15 and 180 min. Images as chosen for quantification. Scale bars: 200 nm.

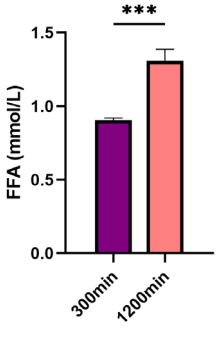

Figure S5. Release of FFA from PAP3 liposomes incubating with LPL. PAP3 liposomes incubating at 37 ºC with LPL for 300 and 1200 min. Statistical significance was evaluated using a two-tailed unpaired Student's t-test. ns: not significant ($P > 0.05$). Significantly different: *$P \leq 0.05$, **$P \leq 0.01$; ***$P < 0.001$. Exact P value 0.0009.

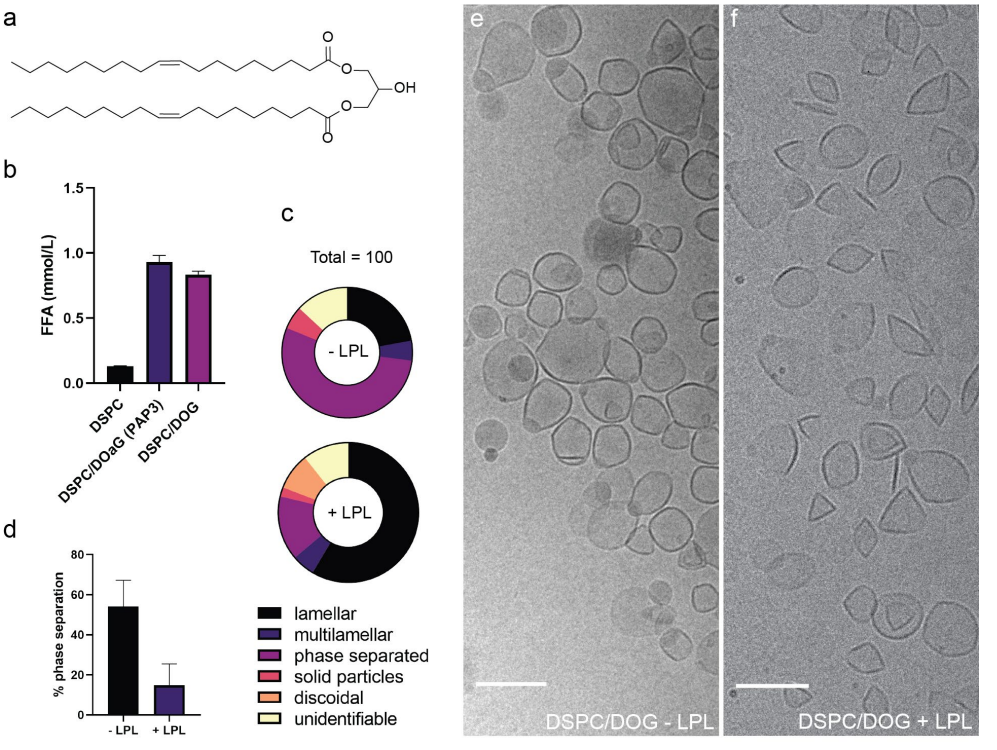

Figure S6. Effect of LPL on DOG containing liposomes. a) Molecular structure of dioleoylglycerol (DOG). **b)** Release of FFA from liposomes containing DSPC (100%), DSPC/DOaG (1:1), or DSPC/DOG (1:1) after incubation with LPL at 37 °C for 120 min. **c)** Quantification (N=100) of the whole population of liposomes consisting of DSPC/DOG (1:1) without LPL or with LPL, incubating at 37 °C for 120 min. **d)** Percentage of phase separation of liposomes consisting of DSPC/DOG (1:1) incubating at 37 °C for 120 min without or with LPL. **e)** Cryo-TEM images of liposomes consisting of DSPC/DOG (1:1) incubating at 37 °C for 120 min without LPL and **f)** with LPL. Scale bars: 200 nm.

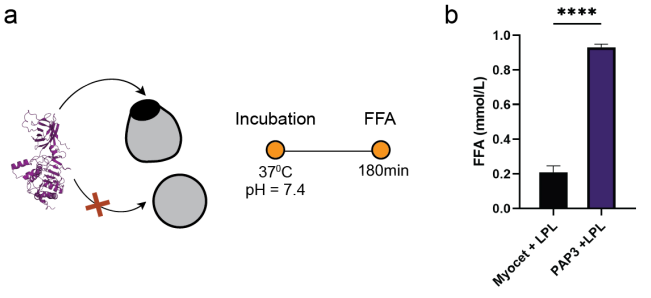

Figure S7. Release of FFA from Myocet®-based formulation in comparison to PAP3 liposomes. a) Schematic of LPL interacting with PAP3 or Myocet®-like liposomes and

timeline of measurement of released FFA. **b)** Quantification of released FFA from Myocet®-like or PAP3 liposomes after incubating with LPL at 37 °C for 180 min. Statistical significance was evaluated using a two-tailed unpaired Student's t-test. ns: not significant (P > 0.05). Significantly different: *P ≤ 0.05, **P ≤ 0.01; ***P < 0.001, ****P < 0.0001. Exact P value : < 0.0001.

			DOaG/DSPC	% Abundance
PAP3	.-LPL	t = 0h	0,830483	86,50863
PAP3	.-LPL	t = 0h	0,977713	101,8451
PAP3	.+LPL	t = 0h	1,046577	109,0185
PAP3	.+LPL	t = 0h	0,984694	102,5723
PAP3	.-LPL	t = 3h	0,932472	97,13248
PAP3	.-LPL	t = 3h	0,950282	98,98767
PAP3	.+LPL	t = 3h	0,753585	78,49848
PAP3	.+LPL	t = 3h	0,65356	68,07916

Figure S8. Mass spectrometry analysis of PAP3 liposomes (DOaG:DSPC 1:1). Analysis table of DOaG/DSPC ratio before and after addition of LPL at t = 0 h and t = 3 h (at 37 °C). Abundance (%) was determined by normalizing all PAP3 data against PAP3 at t = 0 h (average of the two measurements was set as 100%).

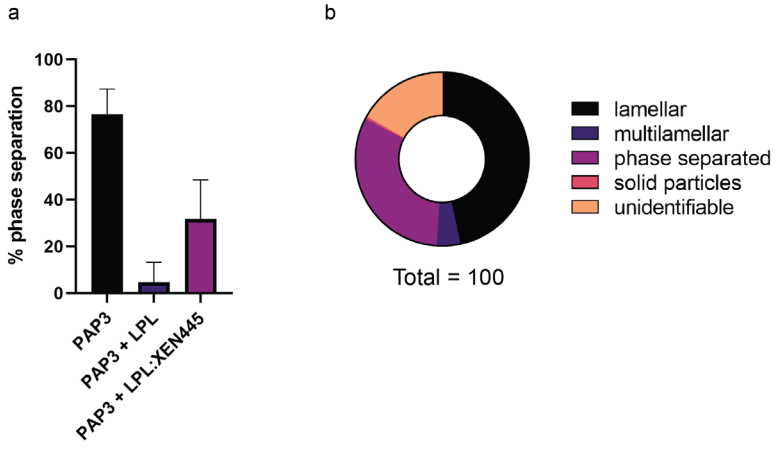

Figure S9. Effect of XEN445 on LPL lipolytic activity. a) Percentage of phase separation of PAP3 liposomes incubating at 37 °C for 120 min without, or with LPL, or with LPL after addition of 1000 µM XEN445 inhibitor. **b)** Quantification of all populations found on PAP3 liposomal formulation incubating with LPL for 120 min after addition of 1000 µM XEN445 inhibitor. Quantification based on cryo-TEM particle count (N=200).

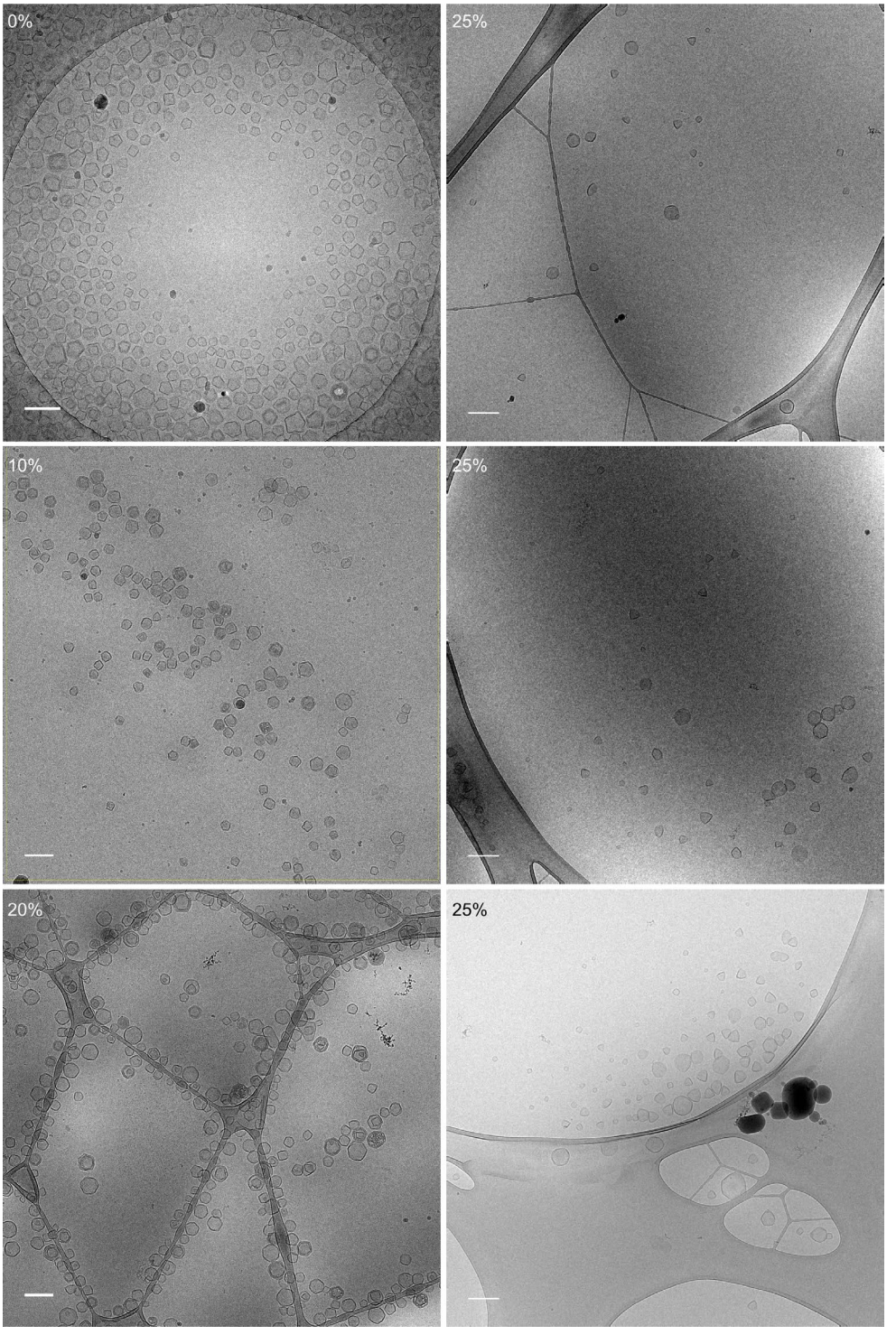
0%
25%
10%
25%
20%
25%

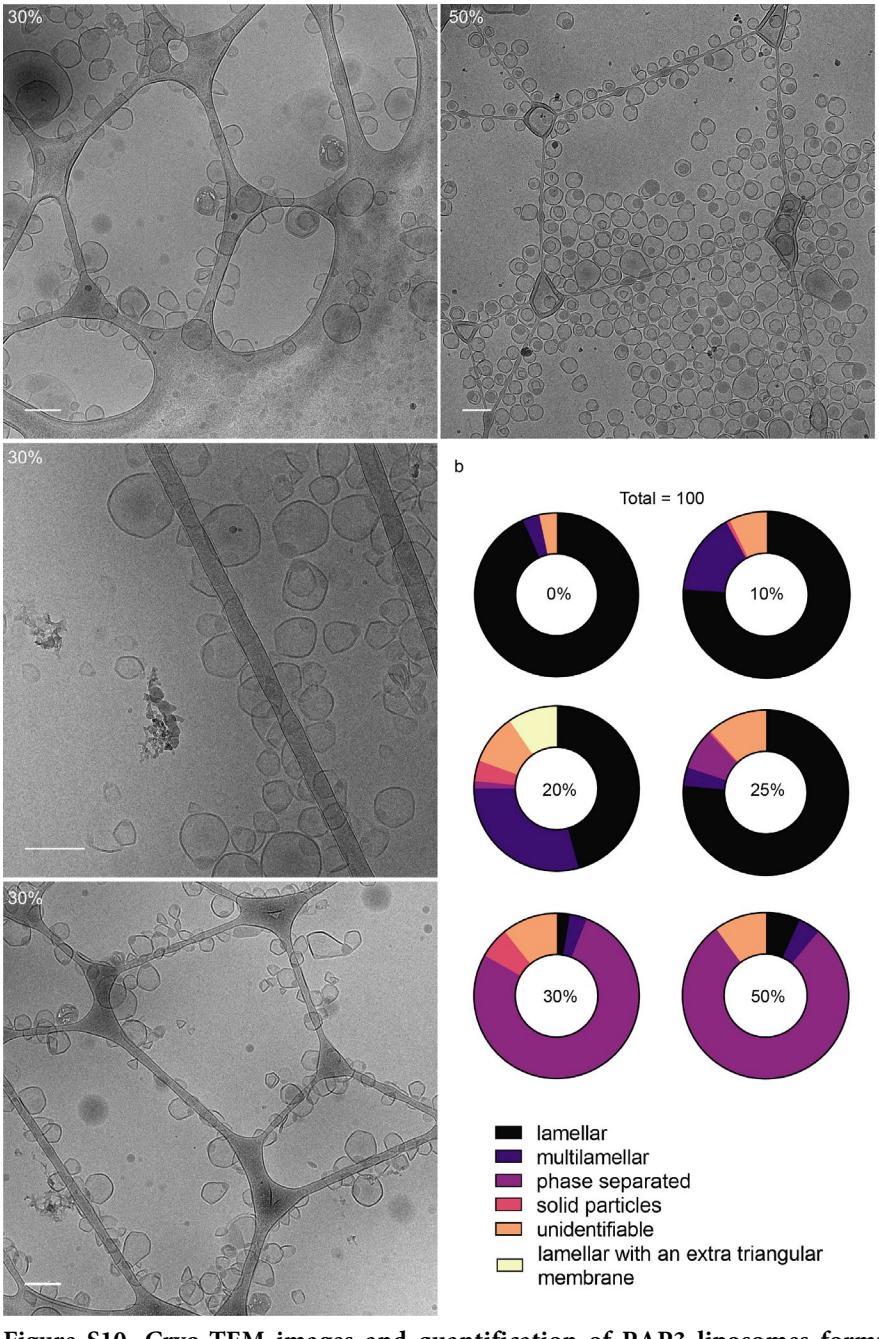

Figure S10. Cryo-TEM images and quantification of PAP3 liposomes formulated at varying molar ratios. a) Cryo-TEM images of liposomes composed of DSPC and 0, 20, 25, 30 and 50 mol % DOaG. Images as chosen for quantification of the whole population. Scale bars: 200 nm. **b)** Quantification of the whole population. Total of each circle chart = 100. Quantification based on cryo-TEM particle count (N=200).

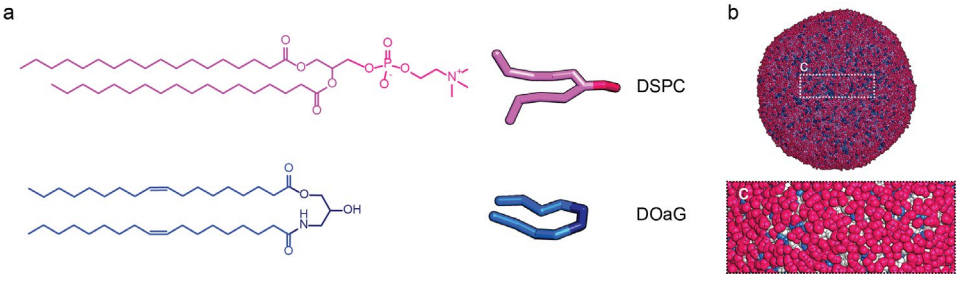

Figure S11. Lipids used for the coarse-grained representation of PAP3 liposomes. a) Molecular structures of DSPC and DOaG lipids and simulated representations. **b)** Modeled lipid droplet of PAP3 liposomes. **c)** Zoom in of b showing the lipid packing defects and the high spacing between DSPC headgroups exposing the DOaG (grey/blue). Size of droplet radius 20.1 nm.

SI 12 Coarse-Grained model

While several lipids have been parametrised within the Martini context, including DSPC, a representation of DOaG is lacking and should be parametrised. Our starting point is an existing representation for a diacylglycerol lipid (DOG), which is very similar to DOaG. Observations by cryo-TEM are used as a reference, and indicate that phase-separated liposomes are formed for mixtures containing > 25 %mol of DOaG, assuming that DOaG is evenly distributed over all liposomes. The ambiguity in the CG representation of DOaG is in the choice of the head beads, *i.e.*, in the non-bonded interactions that are usually estimated from relative partitioning in two different solvents, and we may use the experimental data for phase separation as an alternative. To quantify phase separation *in silico*, the contact fraction between DOaG and DSPC is used:

$$f_{DOaG-DSPC} = \frac{c_{DOaG-DMPC}}{c_{DOaG-DMPC} + c_{DOaG-DOaG}} \times \frac{1}{\phi_{DOaG}}$$

with c_{i-j} representing the number of contacts between two lipid species, and ϕ_{DOaG} the fraction of DOaG lipids. The normalisation by the DOaG fraction, which is not used in the original formulation,[80] is introduced to enable a direct comparison of membranes with different fractions of DOaG, *i.e.*, by normalizing the maximum of the contact fraction to unity. To determine if two lipids are in direct contact, the standard distance threshold of 1.1 nm was used for the GL1 bead (if the lipid is a DSPC lipid) and the GLA bead (in case of DOaG). Density profiles (see **Figure S13**) along the membrane normal indicate that these beads reside roughly at the same depth within the monolayer.

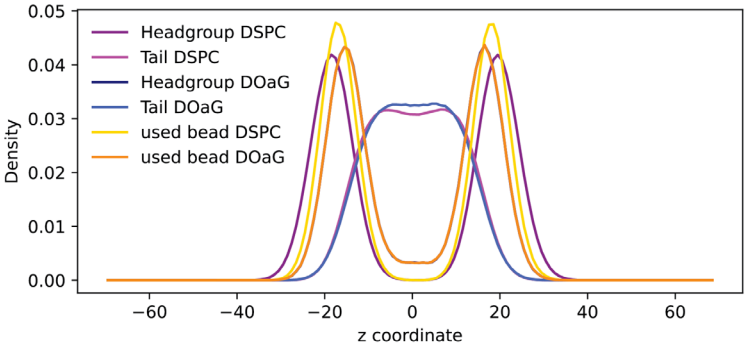

Figure S13. Density profiles of selected bead types across the membrane (along the normal). The contact fraction was subsequently employed to monitor the degree of phase separation for varying DOaG fractions and for different bead-type representations of the DOaG head group in CG Martini. We considered both Martini 2 and 3. Based on the best fit to the experimental data, the DOaG representation with N6a and N6d beads was selected as most appropriate. DPPC = DSPC.

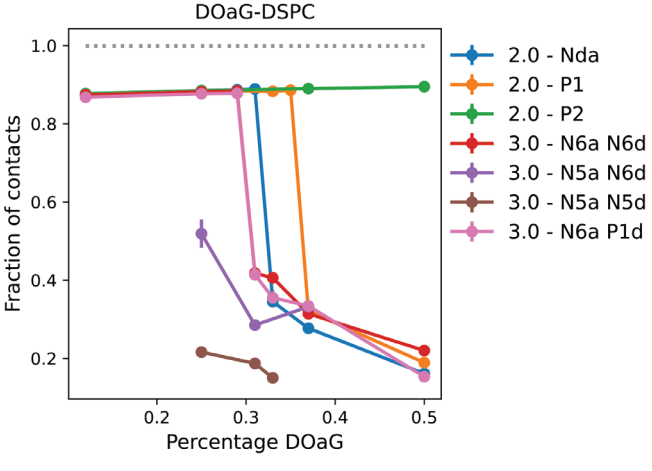

Figure S14. Fractions of contact for increasing composition fractions of DOaG as calculated from CG membrane simulations. Contact fractions have been determined by averaging over the last µs of a 2 µs simulation trajectory.

SI 15. Input file for the CG Martini representation for DOaG used in this study:

```
[moleculetype]; molname     nrexcl
 DOAG        1

[atoms]; id       type      resnr    residu   atom     cgnr
   1       N6a       1       DOAG   GLA      1        0
   2       N6d       1       DOAG   NAB      2        0
   3       C1        1       DOAG   C1A      3        0
   4       C4h       1       DOAG   D2A      4        0
   5       C1        1       DOAG   C3A      5        0
   6       C1        1       DOAG   C4A      6        0
   7       C1        1       DOAG   C1B      7        0
   8       C4h       1       DOAG   D2B      8        0
   9       C1        1       DOAG   C3B      9        0
  10       C1        1       DOAG   C4B      10       0

[bonds];
i         j       funct   length   force.c.
   1  2            1       0.312    2500
   1  3            1       0.47     5000
   3  4            1       0.47     3800
   4  5            1       0.47     3800
   5  6            1       0.47     3800
   2  7            1       0.47     3600
   7  8            1       0.47     3800
   8  9            1       0.47     3800
   9 10            1       0.47     3800

[angles];
    i  j  k  funct   angle    force.c.
   1  3  4  2       180.0    35.0
   3  4  5  2       120.0    35.0
   4  5  6  2       180.0    35.0
   2  7  8  2       180.0    35.0
   7  8  9  2       120.0    35.0
   8  9 10 2       180.0    35.0
```

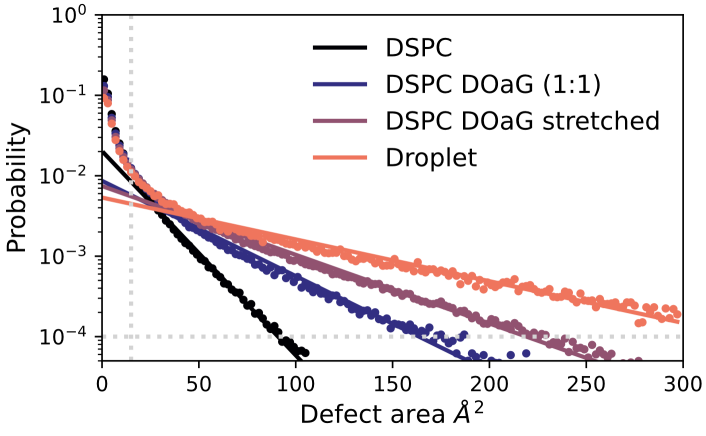

Figure S16. Standard practice when using PackMem is retrieving the packing defect constant from fitting the probability to find a defect of a certain area. This probability of finding a defect of a certain area is given by the formula: $P(A) = b\, e^{-\frac{A}{\pi}}$, where P(A) is the probability of finding a defect area of area Å^2, b is a constant and π is the packing defect constant. The fit is performed on all datapoints where the area of the defect is bigger than 15 Å^2 and the probability is higher than 1e^{-4}. The fit for the flat DSPC, flat but phase-separated DSPC/DOaG layer (1:1 ratio), for the stretched phase-separated DSPC/DOaG layer and spherical DSPC/DOaG system (droplet), are shown in this figure. The solid line of the same color is the fit through the data, which gives the packing defect constant for each system.

SI 17 Identifying lipid packing defect sensing motifs on LPL protein structure

Our previously developed neural network (NN) model is able to predict the relative free energy of a peptide binding to a stretched membrane (high packing defect constant) versus a tensionless membrane (low packing defect constant),[54] only requiring the amino acid sequence. To identify putative regions with lipid packing defect sensing ability within a 3D protein structure of LPL, we used a python script that employs a sliding window of length 15 to screen the protein sequence and predict ΔΔF for every segment. Since the segments overlap, every individual residue is part of more than one segment (except for the termini). By taking the average of these overlapping segment scores at every position we obtained a "per-residue" ΔΔF which can be interpreted as the contribution of that single amino acid to the overall lipid packing defect sensing ability of the respective protein region (**Figure S18a**).

For a residue to bind to a membrane's lipid packing defects, it must be located at the outer shell of the protein structure, *i.e.*, it must be exposed to the solvent. We accounted for this by calculating the solvent-accessible surface area (SASA) for every individual residue (using BioPython)[74], based on the 3D protein structure. Then, we calculated the average SASA of the direct vicinity: a 9 amino acid stretch ($n_{-4} - n_{+4}$) around the respective residue at position n (**Figure S18b**). If this averaged SASA exceeded a threshold value of 0.8 nm^2, we considered that residue to be sufficiently solvent exposed to potentially contribute to lipid packing defect sensing ability. If not, that residue was labeled inactive.

By taking both the averaged per-residue ΔΔF and SASA values into account, we mapped and color-coded the predicted lipid packing defect sensing ability onto the 3D protein structure, as we show in **Figure 5b** in the main text. For this, we used the B-factor field in the PDB file, applying the following rules:

$$if\ SASA < 0.8: \qquad Bfactor = 0.0$$
$$if\ SASA \geq 0.8: \qquad Bfactor = \frac{x - x_{max}}{x_{min} - x_{max}} \times 100$$

In which x is the per-residue ΔΔF score and x_{max} and x_{min} are the maximal and minimal value of x for the entire protein. This formula yields a maximal B-factor of 100.0 for the highest score (most negative ΔΔF , $x=x_{min}$) and the minimal B-factor of 0.0 for the lowest score ($x=x_{max}$). Note that ΔΔF values are always negative.

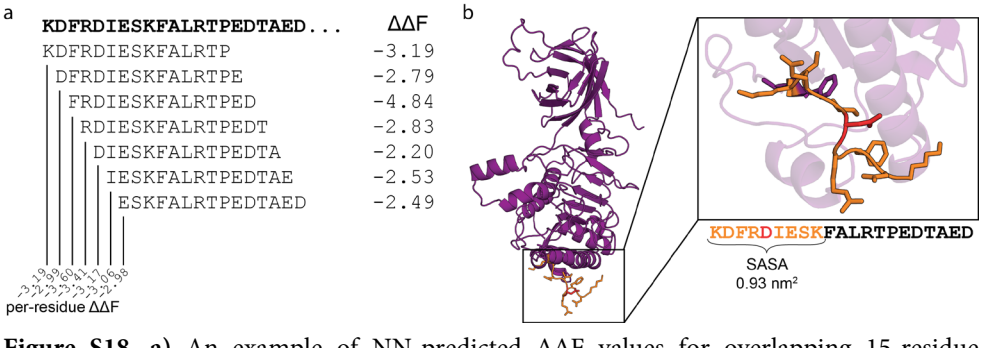

Figure S18. a) An example of NN-predicted ΔΔF values for overlapping 15-residue fragments of LPL (*Bos Taurus*) N-terminal region. The average of the overlapping scores yields the per-residue ΔΔF at every position. **b)** For every amino acid in the 3D protein structure, the individual SASA is calculated. Then, for every position, we compute the average SASA of the 9-residue vicinity (in orange) and assign that value (0.93 nm^2 in this case) to the middle residue (Asp39 in this example, in red).

S19 Residue scores. Per-residue SASA, ΔΔF, and resulting B-factors for LPL (*Bos Taurus*).

		SASA	ΔΔF	B-factor
35	K	1.20	-3.19	22.20
36	D	1.05	-2.99	17.42
37	F	1.04	-3.60	31.98
38	R	0.92	-3.41	27.45
39	D	0.93	-3.17	21.72
40	I	0.73	-3.06	0.00
41	E	0.64	-2.98	0.00
42	S	0.61	-3.00	0.00
43	K	0.39	-3.00	0.00
44	F	0.34	-3.06	0.00
45	A	0.39	-3.00	0.00
46	L	0.46	-3.05	0.00
47	R	0.50	-3.05	0.00
48	T	0.42	-3.06	0.00
49	P	0.47	-3.08	0.00
50	E	0.59	-3.08	0.00
51	D	0.62	-3.09	0.00
52	T	0.73	-2.94	0.00
53	A	0.71	-2.97	0.00
54	E	0.70	-3.05	0.00
55	D	0.52	-3.10	0.00
56	T	0.56	-3.16	0.00
57	C	0.55	-3.20	0.00
58	H	0.55	-3.29	0.00
59	L	0.49	-3.41	0.00
60	I	0.50	-3.46	0.00
61	P	0.51	-3.51	0.00
62	G	0.48	-3.45	0.00
63	V	0.42	-3.45	0.00
64	T	0.49	-3.37	0.00
65	E	0.52	-3.44	0.00
66	S	0.51	-3.44	0.00
67	V	0.63	-3.51	0.00
68	A	0.59	-3.61	0.00
69	N	0.60	-3.78	0.00
70	C	0.57	-3.91	0.00
71	H	0.68	-4.06	0.00
72	F	0.70	-4.17	0.00
73	N	0.69	-4.15	0.00
74	H	0.57	-4.05	0.00
75	S	0.56	-4.16	0.00
90	M	0.54	-4.92	0.00
91	Y	0.54	-5.02	0.00
92	E	0.48	-5.01	0.00
93	S	0.49	-5.08	0.00
94	W	0.47	-5.05	0.00
95	V	0.33	-5.06	0.00
96	P	0.31	-5.05	0.00
97	K	0.27	-5.05	0.00
98	L	0.20	-5.09	0.00
99	V	0.22	-5.01	0.00
100	A	0.39	-4.94	0.00
101	A	0.41	-4.82	0.00
102	L	0.34	-4.76	0.00
103	Y	0.43	-4.62	0.00
104	K	0.55	-4.35	0.00
105	R	0.52	-4.13	0.00
106	E	0.52	-3.90	0.00
107	P	0.52	-3.82	0.00
108	D	0.50	-3.65	0.00
109	S	0.33	-3.64	0.00
110	N	0.28	-3.61	0.00
111	V	0.27	-3.77	0.00
112	I	0.19	-3.90	0.00
113	V	0.09	-4.01	0.00
114	V	0.15	-4.18	0.00
115	D	0.16	-4.28	0.00
116	W	0.16	-4.47	0.00
117	L	0.26	-4.47	0.00
118	S	0.35	-4.41	0.00
119	R	0.50	-4.40	0.00
120	A	0.52	-4.37	0.00
121	Q	0.59	-4.38	0.00
122	Q	0.64	-4.29	0.00
123	H	0.57	-4.26	0.00
124	Y	0.56	-4.17	0.00
125	P	0.60	-4.04	0.00
126	V	0.59	-3.76	0.00
127	S	0.50	-3.56	0.00
128	A	0.46	-3.48	0.00
129	G	0.48	-3.32	0.00
130	Y	0.41	-3.31	0.00

76	S	0.39	-4.21	0.00
77	K	0.37	-4.42	0.00
78	T	0.31	-4.55	0.00
79	F	0.23	-4.73	0.00
80	V	0.11	-4.77	0.00
81	V	0.18	-4.86	0.00
82	I	0.11	-4.88	0.00
83	H	0.20	-4.76	0.00
84	G	0.30	-4.64	0.00
85	W	0.32	-4.57	0.00
86	T	0.45	-4.49	0.00
87	V	0.53	-4.44	0.00
88	T	0.56	-4.54	0.00
89	G	0.62	-4.77	0.00
		SASA	**ΔΔF**	**B-factor**
145	M	0.33	-5.62	0.00
146	A	0.48	-5.54	0.00
147	D	0.48	-5.46	0.00
148	E	0.53	-5.45	0.00
149	F	0.52	-5.70	0.00
150	N	0.57	-5.73	0.00
151	Y	0.60	-5.77	0.00
152	P	0.51	-5.71	0.00
153	L	0.42	-5.62	0.00
154	G	0.36	-5.46	0.00
155	N	0.22	-5.28	0.00
156	V	0.21	-5.27	0.00
157	H	0.15	-5.26	0.00
158	L	0.15	-5.31	0.00
159	L	0.10	-5.37	0.00
160	G	0.04	-5.37	0.00
161	Y	0.04	-5.55	0.00
162	S	0.02	-5.55	0.00
163	L	0.02	-5.58	0.00
164	G	0.02	-5.29	0.00
165	A	0.02	-5.15	0.00
166	H	0.02	-4.90	0.00
167	A	0.01	-4.78	0.00
168	A	0.02	-4.59	0.00
169	G	0.09	-4.47	0.00
170	I	0.17	-4.38	0.00
171	A	0.20	-4.08	0.00
172	G	0.31	-3.93	0.00

131	T	0.33	-3.25	0.00
132	K	0.42	-3.43	0.00
133	L	0.42	-3.55	0.00
134	V	0.38	-3.65	0.00
135	G	0.30	-3.76	0.00
136	Q	0.37	-3.92	0.00
137	D	0.26	-4.10	0.00
138	V	0.19	-4.34	0.00
139	A	0.21	-4.57	0.00
140	K	0.23	-4.87	0.00
141	F	0.13	-5.19	0.00
142	M	0.15	-5.34	0.00
143	N	0.24	-5.42	0.00
144	W	0.35	-5.56	0.00
		SASA	**ΔΔF**	**B-factor**
200	R	0.56	-3.33	0.00
201	L	0.41	-3.22	0.00
202	S	0.37	-3.04	0.00
203	P	0.33	-2.94	0.00
204	D	0.29	-2.85	0.00
205	D	0.26	-2.75	0.00
206	A	0.27	-2.95	0.00
207	D	0.27	-2.95	0.00
208	F	0.22	-3.11	0.00
209	V	0.10	-3.10	0.00
210	D	0.09	-3.19	0.00
211	V	0.11	-3.26	0.00
212	L	0.06	-3.36	0.00
213	H	0.25	-3.38	0.00
214	T	0.30	-3.41	0.00
215	F	0.35	-3.45	0.00
216	T	0.43	-3.40	0.00
217	R	0.44	-3.38	0.00
218	G	0.67	-3.34	0.00
219	S	0.67	-3.34	0.00
220	P	0.72	-3.32	0.00
221	G	0.71	-3.13	0.00
222	R	0.51	-2.96	0.00
223	S	0.51	-2.91	0.00
224	I	0.52	-2.99	0.00
225	G	0.49	-2.98	0.00
226	I	0.47	-3.05	0.00
227	Q	0.25	-3.03	0.00

173	S	0.47	-3.70	0.00
174	L	0.57	-3.53	0.00
175	T	0.56	-3.33	0.00
176	N	0.61	-3.10	0.00
177	K	0.61	-2.92	0.00
178	K	0.54	-2.82	0.00
179	V	0.45	-2.72	0.00
180	N	0.43	-2.76	0.00
181	R	0.32	-2.84	0.00
182	I	0.16	-2.90	0.00
183	T	0.06	-2.93	0.00
184	G	0.06	-3.10	0.00
185	L	0.01	-3.19	0.00
186	D	0.04	-3.36	0.00
187	P	0.15	-3.50	0.00
188	A	0.15	-3.63	0.00
189	G	0.17	-3.70	0.00
190	P	0.34	-3.80	0.00
191	N	0.36	-3.81	0.00
192	F	0.52	-3.95	0.00
193	E	0.55	-3.89	0.00
194	Y	0.66	-3.94	0.00
195	A	0.66	-3.83	0.00
196	E	0.59	-3.73	0.00
197	A	0.58	-3.67	0.00
198	P	0.57	-3.63	0.00
199	S	0.45	-3.46	0.00
		SASA	**ΔΔF**	**B-factor**
255	I	0.84	-3.66	33.41
256	A	0.98	-3.49	29.36
257	E	0.96	-3.27	24.11
258	R	0.93	-3.10	20.05
259	G	0.95	-2.97	16.95
260	L	0.98	-2.94	16.23
261	G	1.00	-2.83	13.60
262	D	0.92	-2.70	10.50
263	V	0.79	-2.65	0.00
264	D	0.79	-2.59	0.00
265	Q	0.68	-2.69	0.00
266	L	0.58	-2.69	0.00
267	V	0.51	-2.67	0.00
268	K	0.46	-2.67	0.00
269	C	0.38	-2.72	0.00

228	K	0.26	-3.17	0.00
229	P	0.19	-3.24	0.00
230	V	0.19	-3.28	0.00
231	G	0.19	-3.35	0.00
232	H	0.15	-3.42	0.00
233	V	0.08	-3.45	0.00
234	D	0.06	-3.57	0.00
235	I	0.07	-3.70	0.00
236	Y	0.07	-3.77	0.00
237	P	0.10	-3.82	0.00
238	N	0.16	-3.85	0.00
239	G	0.16	-3.79	0.00
240	G	0.21	-3.77	0.00
241	T	0.25	-3.79	0.00
242	F	0.26	-3.92	0.00
243	Q	0.32	-3.94	0.00
244	P	0.46	-3.96	0.00
245	G	0.51	-3.99	0.00
246	C	0.53	-4.01	0.00
247	N	0.48	-4.05	0.00
248	I	0.60	-4.06	0.00
249	G	0.67	-3.99	0.00
250	E	0.68	-3.86	0.00
251	A	0.73	-3.82	0.00
252	L	0.73	-3.82	0.00
253	R	0.72	-3.73	0.00
254	V	0.87	-3.72	34.84
		SASA	**ΔΔF**	**B-factor**
310	K	0.70	-2.69	0.00
311	N	0.71	-2.66	0.00
312	R	0.69	-2.61	0.00
313	C	0.65	-2.54	0.00
314	N	0.52	-2.48	0.00
315	N	0.37	-2.42	0.00
316	M	0.29	-2.40	0.00
317	G	0.25	-2.31	0.00
318	Y	0.35	-2.29	0.00
319	E	0.39	-2.26	0.00
320	I	0.53	-2.27	0.00
321	N	0.59	-2.26	0.00
322	K	0.82	-2.26	0.00
323	V	1.01	-2.29	0.72
324	R	1.01	-2.32	1.43

270	S	0.27	-2.81	0.00
271	H	0.22	-2.93	0.00
272	E	0.17	-3.00	0.00
273	R	0.13	-3.09	0.00
274	S	0.09	-3.23	0.00
275	V	0.10	-3.34	0.00
276	H	0.10	-3.48	0.00
277	L	0.08	-3.68	0.00
278	F	0.08	-3.78	0.00
279	I	0.15	-3.79	0.00
280	D	0.21	-3.72	0.00
281	S	0.28	-3.67	0.00
282	L	0.47	-3.70	0.00
283	L	0.57	-3.69	0.00
284	N	0.59	-3.56	0.00
285	E	0.59	-3.48	0.00
286	E	0.65	-3.47	0.00
287	N	0.64	-3.47	0.00
288	P	0.56	-3.44	0.00
289	S	0.62	-3.31	0.00
290	K	0.53	-3.17	0.00
291	A	0.51	-3.11	0.00
292	Y	0.44	-2.99	0.00
293	R	0.50	-2.95	0.00
294	C	0.59	-2.88	0.00
295	N	0.55	-2.86	0.00
296	S	0.55	-2.89	0.00
297	K	0.64	-2.84	0.00
298	E	0.65	-2.87	0.00
299	A	0.63	-2.94	0.00
300	F	0.58	-2.96	0.00
301	E	0.57	-2.88	0.00
302	K	0.49	-2.91	0.00
303	G	0.42	-2.88	0.00
304	L	0.43	-2.96	0.00
305	C	0.59	-2.92	0.00
306	L	0.71	-2.86	0.00
307	S	0.68	-2.80	0.00
308	C	0.81	-2.70	10.50
309	R	0.72	-2.68	0.00
325	A	1.01	-2.35	2.15
326	K	1.00	-2.40	3.34
327	R	0.89	-2.58	7.64
328	S	0.85	-2.64	9.07
329	S	0.69	-2.79	0.00
330	K	0.66	-2.98	0.00
331	M	0.43	-3.26	0.00
332	Y	0.29	-3.37	0.00
333	L	0.29	-3.52	0.00
334	K	0.42	-3.55	0.00
335	T	0.43	-3.73	0.00
336	R	0.51	-3.86	0.00
337	S	0.51	-4.09	0.00
338	Q	0.57	-4.33	0.00
339	M	0.55	-4.62	0.00
340	P	0.57	-4.82	0.00
341	Y	0.50	-4.94	0.00
342	K	0.45	-4.90	0.00
343	V	0.33	-4.98	0.00
344	F	0.24	-5.04	0.00
345	H	0.25	-4.88	0.00
346	Y	0.23	-4.68	0.00
347	Q	0.26	-4.58	0.00
348	V	0.25	-4.47	0.00
349	K	0.25	-4.43	0.00
350	I	0.27	-4.26	0.00
351	H	0.42	-4.20	0.00
352	F	0.53	-4.01	0.00
353	S	0.66	-3.80	0.00
354	G	0.63	-3.50	0.00
355	T	0.72	-3.30	0.00
356	E	0.71	-3.11	0.00
357	S	0.81	-3.07	19.33
358	N	0.91	-2.97	16.95
359	T	0.90	-2.89	15.04
360	Y	0.77	-2.95	0.00
361	T	0.64	-2.93	0.00
362	N	0.55	-2.98	0.00
363	Q	0.48	-2.94	0.00
364	A	0.40	-2.97	0.00

		SASA	ΔΔF	B-factor
365	F	0.34	-2.98	0.00
366	E	0.26	-2.95	0.00
367	I	0.16	-3.08	0.00
368	S	0.24	-3.18	0.00
369	L	0.32	-3.38	0.00
370	Y	0.36	-3.46	0.00
371	G	0.43	-3.59	0.00
372	T	0.45	-3.52	0.00
373	V	0.54	-3.61	0.00
374	A	0.63	-3.55	0.00
375	E	0.62	-3.56	0.00
376	S	0.71	-3.59	0.00
377	E	0.64	-3.66	0.00
378	N	0.62	-3.80	0.00
379	I	0.59	-3.93	0.00
380	P	0.58	-4.13	0.00
381	F	0.65	-4.38	0.00
382	T	0.54	-4.38	0.00
383	L	0.46	-4.44	0.00
384	P	0.46	-4.39	0.00
385	E	0.44	-4.32	0.00
386	V	0.52	-4.28	0.00
387	S	0.50	-4.30	0.00
388	T	0.53	-4.28	0.00
389	N	0.46	-4.28	0.00
390	K	0.40	-4.32	0.00
391	T	0.42	-4.32	0.00
392	Y	0.42	-4.35	0.00
393	S	0.50	-4.35	0.00
394	F	0.41	-4.39	0.00
395	L	0.44	-4.29	0.00
396	L	0.40	-4.11	0.00
397	Y	0.46	-4.05	0.00
398	T	0.42	-4.03	0.00
399	E	0.44	-4.13	0.00
400	V	0.48	-4.34	0.00
401	D	0.49	-4.59	0.00
402	I	0.47	-4.87	0.00
403	G	0.51	-5.07	0.00
404	E	0.38	-5.33	0.00
405	L	0.40	-5.54	0.00
406	L	0.31	-5.78	0.00

		SASA	ΔΔF	B-factor
420	W	1.24	-5.72	82.58
421	S	1.31	-5.56	78.76
422	N	1.12	-5.42	75.42
423	W	1.03	-5.26	71.60
424	W	1.03	-5.06	66.83
425	S	0.83	-4.75	59.43
426	S	0.86	-4.54	54.42
427	P	0.71	-4.36	0.00
428	G	0.47	-4.16	0.00
429	F	0.44	-4.11	0.00
430	D	0.30	-3.83	0.00
431	I	0.44	-3.72	0.00
432	G	0.41	-3.51	0.00
433	K	0.41	-3.50	0.00
434	I	0.43	-3.35	0.00
435	R	0.37	-3.19	0.00
436	V	0.42	-3.06	0.00
437	K	0.48	-3.02	0.00
438	A	0.36	-2.96	0.00
439	G	0.42	-3.04	0.00
440	E	0.36	-3.04	0.00
441	T	0.37	-3.08	0.00
442	Q	0.39	-3.12	0.00
443	K	0.38	-3.22	0.00
444	K	0.41	-3.24	0.00
445	V	0.38	-3.37	0.00
446	I	0.49	-3.43	0.00
447	F	0.63	-3.49	0.00
448	C	0.78	-3.34	0.00
449	S	0.74	-3.36	0.00
450	R	0.74	-3.37	0.00
451	E	0.82	-3.57	31.26
452	K	0.82	-3.72	34.84
453	M	0.85	-3.95	40.33
454	S	0.89	-4.05	42.72
455	Y	0.73	-4.18	0.00
456	L	0.61	-4.22	0.00
457	Q	0.51	-4.19	0.00
458	K	0.50	-4.16	0.00
459	G	0.50	-4.20	0.00
460	K	0.43	-4.21	0.00
461	S	0.43	-4.26	0.00

407	M	0.38	-5.89	0.00
408	L	0.35	-5.92	0.00
409	K	0.34	-5.94	0.00
410	L	0.36	-6.15	0.00
411	K	0.44	-6.31	0.00
412	W	0.46	-6.41	0.00
413	I	0.67	-6.45	0.00
414	S	0.74	-6.33	0.00
415	D	0.76	-6.35	0.00
416	S	0.89	-6.16	93.08
417	Y	0.91	-6.11	91.89
418	F	1.00	-6.01	89.50
419	S	1.23	-5.86	85.92

462	P	0.43	-4.34	0.00
463	V	0.44	-4.44	0.00
464	I	0.49	-4.47	0.00
465	F	0.55	-4.57	0.00
466	V	0.51	-4.48	0.00
467	K	0.58	-4.37	0.00
468	C	0.64	-4.25	0.00
469	H	0.61	-4.09	0.00
470	D	0.74	-4.02	0.00
471	K	0.92	-3.97	40.81
472	S	1.08	-4.14	44.87
473	L	1.13	-4.23	47.02
474	N	1.18	-4.24	47.26

		SASA	ΔΔF	B-factor
475	R	1.25	-4.22	46.78
476	K	1.26	-4.18	45.82
477	S	1.35	-3.83	37.47
478	G	1.56	-3.49	29.36

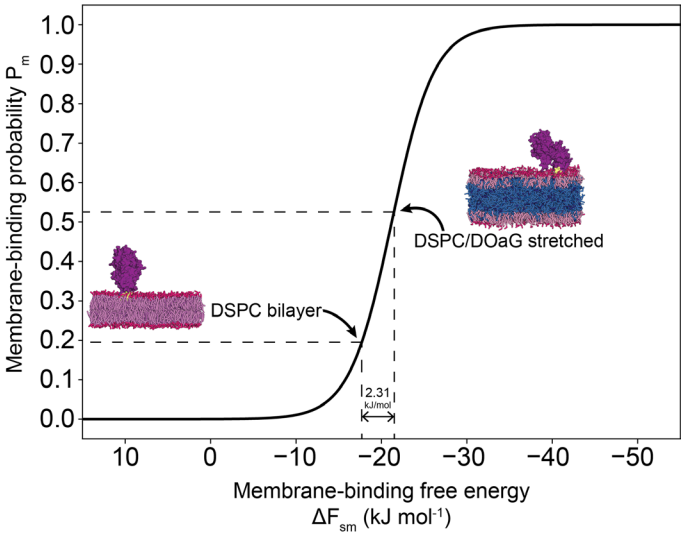

Figure S20. Thermodynamic model describing the relation between membrane-binding free energy ΔF_{sm} and membrane-binding probability P_m, as defined in reference [54]. When we consider the membrane-binding free energies for bovine LPL to a stretched DSPC/DOaG bilayer and a DSPC bilayer as calculated by umbrella sampling (Fig. 5c in main text), we conclude that a seemingly small free energy difference of 2.31 kJ mol-1, indeed constitutes a large change in membrane-binding probability (dashed lines).

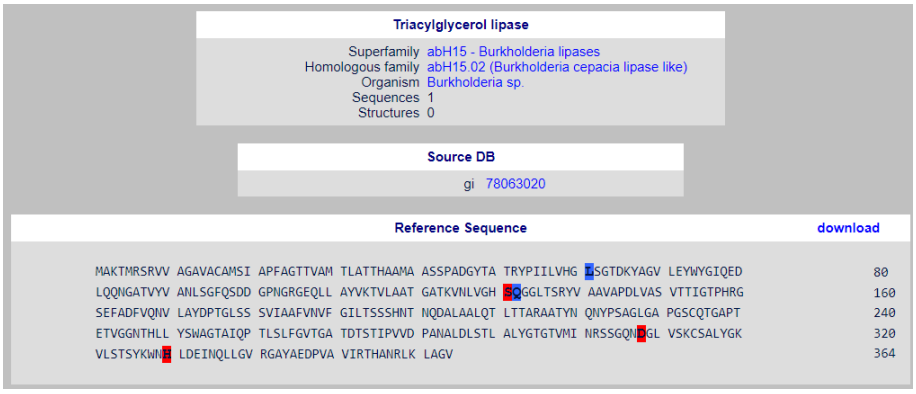

Figure S21. Sequence of Triacylglycerol lipase derived from *Burkholderia sp*. Sequence was obtained by the Lipase engineering Database.[81] Sequence does not indicate a Trp-rich domain. BLAST run does not designate significant matches of the protein with any human protein species.

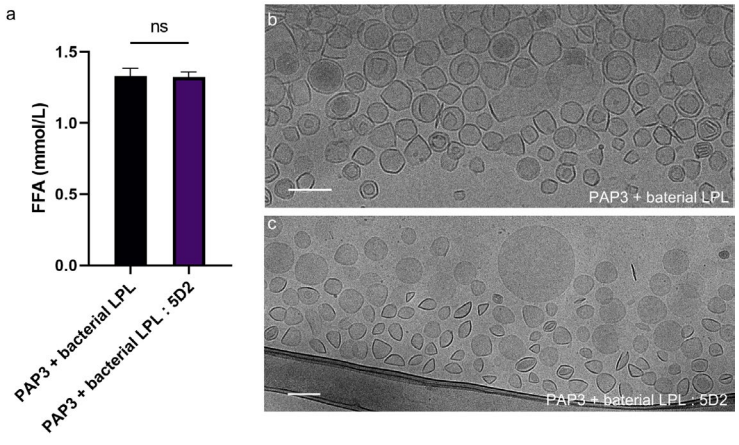

Figure S22. Effect of non-mammalian LPL on PAP3 liposomes with and without 5D2 antibody. a) Release of FFA from PAP3 liposomes incubating at 37 °C with non-mammalian LPL (derived from *Burkholderia sp.*) and non-mammalian LPL + 5D2 antibody (1:1) for 120 min. Cryo-TEM images of PAP3 liposomes after incubating at 37 °C for 120 min with **b)** non-mammalian LPL and **c)** non-mammalian LPL + 5D2 antibody (1:1).

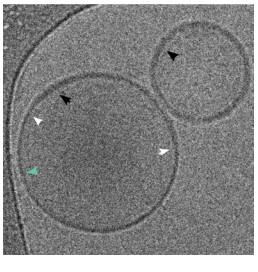

Figure S23. Cryo-TEM image of PAP3 liposomes after incubation with LPL at 37 °C for 180min. Difference of bilayer thickness is indicated with black (thicker part) or green (thinner part) arrows. The point of thickness mismatch is indicated with white arrows.

```
sp|P11150|LIPC_HUMAN
sp|P06858|LIPL_HUMAN
sp|Q9Y5X9|LIPE_HUMAN

MDTSPLCFSILLVLCIFIQSSALGQSLKPEPFGRRAQA------VETNKTLHEMKTRFLL 54
MESKAL---LVLTLAVWLQSLTAS-RGGV-------------AAADQRRDFIDIESKFAL 43
MSN------SVPLLCFWSLCYCFA-AGSPVPFGPEGRLEDKLHKPKATQTEVKPSVRFNL 53
*..       :  *..:  .   .                      .  :   . . :* *

F---GETNQGCQIRINHPDTLQECGFNSSLPLVMIIHGWSVDGVLENWIWQMVAALKSQP 111
RTPEDTAEDTCHLIPGVAESVATCHFNHSSKTFMVIHGWTVTGMYESWVPKLVAALYKRE 103
RTSKDPEHEGCYLSVGHSQPLEDCSFNMTAKTFFIIHGWTMSGIFENWLHKLVSALHTRE 113
    .  .: * :  .  : :  * ** :   .::****:: *: *.*: ::*:** .:

AQPVNVGLVDWITLAHDHYTIAVRNTRLVGKEVAALLRWLEESVQLSRSHVHLIGYSLGA 171
-PDSNVIVVDWLSRAQEHYPVSAGYTKLVGQDVARFINWMEEEFNYPLDNVHLLGYSLGA 162
-KDANVVVVDWLPLAHQLYTDAVNNTRVVGHSIARMLDWLQEKDDFSLGNVHLIGYSLGA 172
    ** :***:  *:: *  :.  *::**:.:* :: *::*. :   .:***:******

HVSGFAGSSIGGTHKIGRITGLDAAGPLFEGSAPSNRLSPDDANFVDAIHTFTREHMGLS 231
HAAGIAGSLTNK--KVNRITGLDPAGPNFEYAEAPSRLSPDDADFVDVLHTFTRGSPGRS 220
HVAGYAGNFVKG--TVGRITGLDPAGPMFEGADIHKRLSPDDADFVDVLHTYTRS-FGLS 229
*.:* **.      .:.****** *** ** :   .*******:***.:**:**   * *

VGIKQPIGHYDFYPNGGSFQPGCHFLELYRHIAQHGFNAITQTIKCSHERSVHLFIDSLL 291
IGIQKPVGHVDIYPNGGTFQPGCNIGEAIRVIAERGLGDVDQLVKCSHERSIHLFIDSLL 280
IGIQMPVGHIDIYPNGGDFQPGCGLNDVLGSI---AYGTITEVVKCEHERAVHLFVDSLV 286
:**: *:** *:***** ***** : :    *   . . : : :**.***::***:***:

HAGTQSMAYPCGDMNSFSQGLCLSCKKGRCNTLGYHVRQEPRSKSKRLFLVTRAQSPFKV 351
NEENPSKAYRCSSKEAFEKGLCLSCRKNRCNNLGYEINKVRAKRSSKMYLKTRSQMPYKV 340
NQDKPSFAFQCTDSNRFKKGICLSCRKNRCNSIGYNAKKMRNKRNSKMYLKTRAGMPFRV 346
:  . * *: * . : *.:*:****:*.***.:**. .:   .:..:::* **:  *::*

YHYQFKIQFINQ-TETPIQTTFTMSLLGTKEKMQKIPITLGKGIASNKTYSFLITLDVDI 410
FHYQVKIHFSGTESETHTNQAFEISLYGTVAESENIPFTLPE-VSTNKTYSFLIYTEVDI 399
YHYQMKIHVFSYKNMGEIEPTFYVTLYGTNADSQTLPLEIVERIEQNATNTFLVYTEEDL 406
:***.**:. .  .    : :* ::* **  . :.:*: : : :  * * :**:  : *:

GELIMIKFKWENSA--VWANVWDTVQTIIPWSTGPRHSGLVLKTIRVKAGETQQRMTFCS 468
GELLMLKLKWKSDSYFSWSDWWSS-------------PGFAIQKIRVKAGETQKKVIFCS 446
GDLLKIQLTWEGASQ-SWYNLWKEFRSYLSQPRNP-GRELNIRRIRVKSGETQRKLTFCT 464
*:*: :::.*:. :   * : *.                : :: ****:****::: **:

ENTDDLLLRPTQEKIFVKCEIKSKTSKRKIR-----  499
REKVSHLQKGKAPAVFVKCHDKSLNKKSG-------  475
EDPENTSISPGRELWFRKCRDGWRMKNETSPTVELP  500
.:  .          * **.     .:
```

Figure S24. Sequence alignment of Triacylglycerol Lipases Hepatic, Lipoprotein and Endothelial Lipase (*Homo Sapiens*). Sequence alignment was run by an alignment tool provided by Uniprot.org database. Uniprot IDs: P11150 (in magenta), P06858 (in blue) and Q9Y5X9 (in black) respectively. Conserved amino acids indicated with *. Similar amino acids indicated with " : " , somewhat similar amino acids indicated with " . " . Tryptophan-rich loop indicated in purple box.

```
sp|P11151|LIPL_BOVIN
sp|P06858|LIPL_HUMAN

MESKALLLLALSVCLQSLTVSRGGLVAADRITGGKDFRDIESKFALRTPEDTAEDTCHLI 60
MESKALLVLTLAVWLQSLTASRGGVAAADQ---RRDFIDIESKFALRTPEDTAEDTCHLI 57
*******:*:*:* *****.****:.***:    :** **********************

PGVTESVANCHFNHSSKTFVVIHGWTVTGMYESWVPKLVAALYKREPDSNVIVVDWLSRA 120
PGVAESVATCHFNHSSKTFMVIHGWTVTGMYESWVPKLVAALYKREPDSNVIVVDWLSRA 117
***:****.**********:****************************************

QQHYPVSAGYTKLVGQDVAKFMNWMADEFNYPLGNVHLLGYSLGAHAAGIAGSLTNKKVN 180
QEHYPVSAGYTKLVGQDVARFINWMEEEFNYPLDNVHLLGYSLGAHAAGIAGSLTNKKVN 177
*:*****************:*:*** :******.*************************

RITGLDPAGPNFEYAEAPSRLSPDDADFVDVLHTFTRGSPGRSIGIQKPVGHVDIYPNGG 240
RITGLDPAGPNFEYAEAPSRLSPDDADFVDVLHTFTRGSPGRSIGIQKPVGHVDIYPNGG 237
************************************************************

TFQPGCNIGEALRVIAERGLGDVDQLVKCSHERSVHLFIDSLLNEENPSKAYRCNSKEAF 300
TFQPGCNIGEAIRVIAERGLGDVDQLVKCSHERSIHLFIDSLLNEENPSKAYRCSSKEAF 297
**********:**********************:******************.*****

EKGLCLSCRKNRCNNMGYEINKVRAKRSSKMYLKTRSQMPYKVFHYQVKIHFSGTESNTY 360
EKGLCLSCRKNRCNNLGYEINKVRAKRSSKMYLKTRSQMPYKVFHYQVKIHFSGTESETH 357
***************:*******************************************:*:

TNQAFEISLYGTVAESENIPFTLPEVSTNKTYSFLLYTEVDIGELLMLKLKWISDSYFSW 420
TNQAFEISLYGTVAESENIPFTLPEVSTNKTYSFLIYTEVDIGELLMLKLKWKSDSYFSW 417
************************************:**************** *******

SNWWSSPGFDIGKIRVKAGETQKKVIFCSREKMSYLQKGKSPVIFVKCHDKSLNRKSG   478
SDWWSSPGFAIQKIRVKAGETQKKVIFCSREKVSHLQKGKAPAVFVKCHDKSLNKKSG   475
*:******* * ********************:*:*****:*.:**********:***
```

Figure S25. Sequence alignment of LPL derived from *Bos Taurus* (bovine) and *Homo Sapiens* (Human). Sequence alignment was run by an alignment tool provided by Uniprot.org database showing 92.21% homology. Uniprot IDs: P11151 for Bovine LPL (in blue) and P06858 for Human LPL (in black). Conserved amino acids indicated with *. Similar amino acids indicated with " : " , somewhat similar amino acids indicated with ". " . Tryptophan-rich loop indicated in purple box.

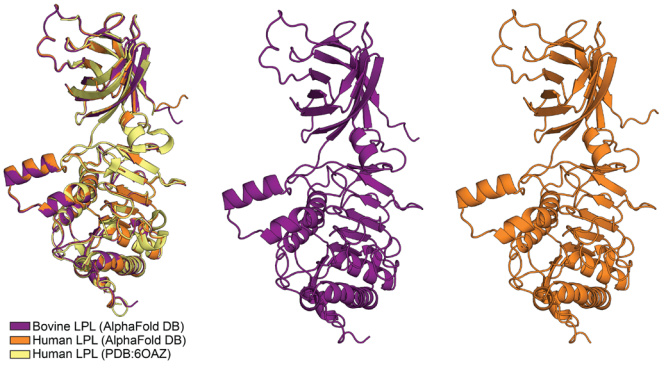

Figure S26. AlphaFold and X-ray protein structures overlap. The AlphaFold DB [72,73] models of bovine and human LPL closely overlap with the human LPL crystal structure (PDB: 6OAZ).[51]

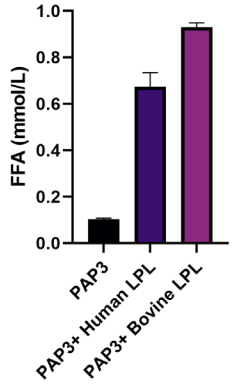

Figure S27. Release of FFA from PAP3 liposomes incubating with Human LPL and Bovine LPL. PAP3 liposomes incubating at 37 °C with LPL for 120 min.

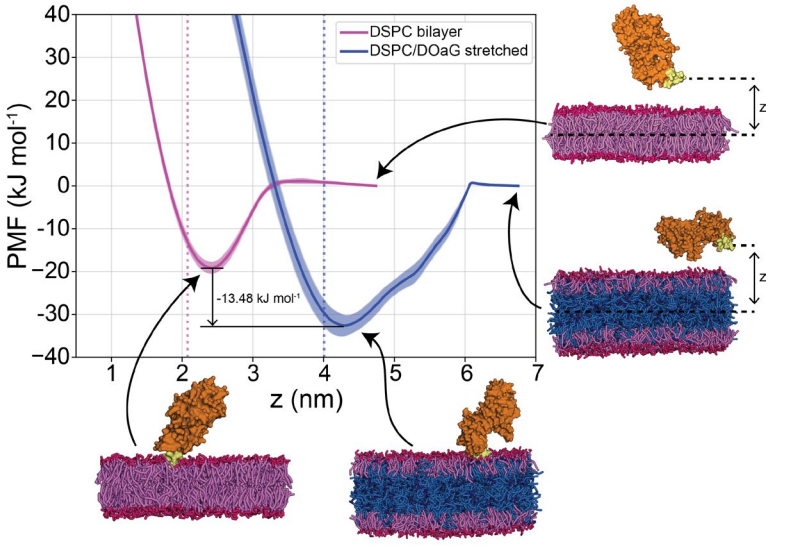

Figure S28. Potential of mean force (PMF) profiles of human LPL binding to a DSPC bilayer (in red-pink) and a DSPC/DOaG phase-separated membrane (in red-pink/blue). The US reaction coordinate is the z-distance between the COM of the Trp-rich loop (in yellow) and the COM of the lipids (i.e., center plane of the membrane). Snapshots are the final frames of the trajectories and indicate that the protein is completely unbound at high z (free energy = 0 kJ mol^{-1}) and membrane-bound through the Trp-rich loop at the minima. Dotted lines indicate the position of the DSPC head groups (NC3 beads).

Table S1. Physicochemical properties of liposomes

Formulation	Size (nm)	PDI	T (°C)	Formulation	Size (nm)	PDI	T (°C)
PAP3	± 143.2	0.294	25	PAP3 + LPL:XEN445 0 µM	±147.5	0.124	37
PAP3 30 min	± 151.8	0.330	37	PAP3 + LPL:XEN445 50 µM	±146.9	0.117	37
PAP3 120 min	± 154.4	0.370	37	PAP3 + LPL:XEN445 100 µM	±147.4	0.110	37
PAP3 300 min	± 150.8	0.350	37	PAP3 + LPL:XEN445 500 µM	±141.2	0.116	37
PAP3 + LPL 30 min	± 159.5	0.085	37	PAP3 + LPL:XEN445 1000 µM	±136.7	0.099	37
PAP3 + LPL 120 min	± 158.5	0.104	37	PAP3 (10% DOaG)	±97.5	0.051	25
PAP3 + LPL 300 min	± 166.0	0.200	37	PAP3 (20% DOaG)	±139.3	0.230	25
PAP3 + inactive LPL 30 min	± 146.3	0.275	37	PAP3 (30% DOaG)	±109.3	0.140	25
PAP3 + inactive LPL 120 min	± 141.5	0.256	37	PAP3 (10% DOaG) + LPL	±106.5	0.072	37
PAP3 + inactive LPL 300 min	± 140.4	0.269	37	PAP3 (20% DOaG) + LPL	±104.5	0.047	37
DSPC	± 135.7	0.344	37	PAP3 (30% DOaG) + LPL	±115.3	0.103	37
DSPC + LPL 30 min	± 142.0	0.265	37	PAP3 + LPL:5D2	±151.8	0.184	37
DSPC + LPL 120 min	± 148.4	0.382	37	PAP3 + LPL:IgG	±158.7	0.182	37
DSPC + LPL 300 min	± 128.1	0.208	37	PAP3 + bacterial LPL	±155.0	0.156	37
Myocet®-like (POPC:CHO_55:45) + LPL	± 114.2	0.065	37	PAP3 + bacterial LPL:5D2	±149.4	0.143	37

3.6 References

1. Bulbake, U.; Doppalapudi, S.; Kommineni, N.; Khan, W. Liposomal Formulations in Clinical Use: An Updated Review. *Pharmaceutics* **2017**, *9* (2), 12.
2. Cullis, P. R.; Hope, M. J. Lipid Nanoparticle Systems for Enabling Gene Therapies. *Mol Ther* **2017**, *25* (7), 1467–1475.
3. Akinc, A.; Maier, M. A.; Manoharan, M.; Fitzgerald, K.; Jayaraman, M.; Barros, S.; Ansell, S.; Du, X.; Hope, M. J.; Madden, T. D.; Mui, B. L.; Semple, S. C.; Tam, Y. K.; Ciufolini, M.; Witzigmann, D.; Kulkarni, J. A.; van der Meel, R.; Cullis, P. R. The Onpattro Story and the Clinical Translation of Nanomedicines Containing Nucleic Acid-Based Drugs. *Nat Nanotechnol* **2019**, *14* (12), 1084–1087.
4. Kulkarni, J. A.; Darjuan, M. M.; Mercer, J. E.; Chen, S.; van der Meel, R.; Thewalt, J. L.; Yi Tam, Y. C.; Cullis, P. R. On the Formation and Morphology of Lipid Nanoparticles Containing Ionizable Cationic Lipids and siRNA. *ACS Nano* **2018**, *12* (5), 4787–4795.
5. Schoenmaker, L.; Witzigmann, D.; Kulkarni, J. A.; Verbeke, R.; Kersten, G.; Jiskoot, W.; Crommelin, D. J. A. mRNA-Lipid Nanoparticle COVID-19 Vaccines: Structure and Stability. *Int J Pharm* **2021**, *601*, 120586.
6. Hou, X.; Zaks, T.; Langer, R.; Dong, Y. Lipid Nanoparticles for mRNA Delivery. *Nat Rev Mat* **2021**, *6* (12), 1078–1094.
7. Francia, V.; Schiffelers, R. M.; Cullis, P. R.; Witzigmann, D. The Biomolecular Corona of Lipid Nanoparticles for Gene Therapy. *Bioconjug Chem* **2020**, *31* (9), 2046–2059.
8. Pattipeiluhu, R.; Crielaard, S.; Klein-Schiphorst, I.; Florea, B. I.; Kros, A.; Campbell, F. Unbiased Identification of the Liposome Protein Corona Using Photoaffinity-Based Chemoproteomics. *ACS Cent Sci* **2020**, *6* (4), 535–545.
9. Hadjidemetriou, M.; Mcadam, S.; Garner, G.; Thackeray, C.; Knight, D.; Smith, D.; Al-Ahmady, Z.; Mazza, M.; Rogan, J.; Clamp, A.; Kostarelos, K.; Hadjidemetriou, M.; Al-Ahmady, Z.; Mazza, M.; Kostarelos, K.; Mcadam, S.; Garner, G.; Rogan, J.; Thackeray, C.; Clamp, A.; Knight, D.; Smith, D. The Human in vivo Biomolecule Corona onto PEGylated Liposomes: A Proof-of-Concept Clinical Study. *Adv Mater* **2019**, *31* (4), 1803335.
10. Hadjidemetriou, M.; Kostarelos, K. Evolution of the Nanoparticle Corona. *Nat Nanotechnol* **2017**, *12* (4), 288–290.
11. Holme, M. N.; Rashid, M. H.; Thomas, M. R.; Barriga, H. M. G.; Herpoldt, K. L.; Heenan, R. K.; Dreiss, C. A.; Bañuelos, J. L.; Xie, H. N.; Yarovsky, I.; Stevens, M. M.

Fate of Liposomes in the Presence of Phospholipase C and D: From Atomic to Supramolecular Lipid Arrangement. *ACS Cent Sci* **2018**, *4* (8), 1023–1030.

12. Fong, W. K.; Sánchez-Ferrer, A.; Rappolt, M.; Boyd, B. J.; Mezzenga, R. Structural Transformation in Vesicles upon Hydrolysis of Phosphatidylethanolamine and Phosphatidylcholine with Phospholipase C. *Langmuir* **2019**, *35* (46), 14949–14958.
13. Arias-Alpizar, G.; Papadopoulou, P.; Rios, X.; Pulagam, K. R.; Moradi, M. A.; Pattipeiluhu, R.; Bussmann, J.; Sommerdijk, N.; Llop, J.; Kros, A.; Campbell, F. Phase-Separated Liposomes Hijack Endogenous Lipoprotein Transport and Metabolism Pathways to Target Subsets of Endothelial Cells in vivo. *Adv Healthc Mater* **2023**, *12* (10), e2202709.
14. Bolen, E. J.; Sando, J. J. Effect of Phospholipid Unsaturation on Protein Kinase C Activation. *Biochemistry* **1992**, *31* (25), 5945–5951.
15. Goñi, F. M.; Alonso, A. Structure and Functional Properties of Diacylglycerols in Membranes. *Prog Lipid Res* **1999**, *38* (1), 1–48.
16. Goldberg, E. M.; Lester, D. S.; Borchardt, D. B.; Zidovetzki, R. Effects of Diacylglycerols on Conformation of Phosphatidylcholine Headgroups in Phosphatidylcholine/Phosphatidylserine Bilayers. *Biophys J* **1995**, *69* (3), 965–973.
17. Campomanes, P.; Zoni, V.; Vanni, S. Local Accumulation of Diacylglycerol Alters Membrane Properties Nonlinearly Due to Its Transbilayer Activity. *Commun Chem* **2019**, *2* (1), 1–8.
18. Alwarawrah, M.; Hussain, F.; Huang, J. Alteration of Lipid Membrane Structure and Dynamics by Diacylglycerols with Unsaturated Chains. *Biochim Biophys Acta Biomembr* **2016**, *1858* (2), 253–263.
19. Vanni, S.; Hirose, H.; Barelli, H.; Antonny, B.; Gautier, R. A Sub-Nanometre View of How Membrane Curvature and Composition Modulate Lipid Packing and Protein Recruitment. *Nat Commun* **2014**, *5* (1), 1–10.
20. Alwarawrah, M.; Dai, J.; Huang, J. Modification of Lipid Bilayer Structure by Diacylglycerol: A Comparative Study of Diacylglycerol and Cholesterol. *J Chem Theory Comput* **2012**, *8* (2), 749–758.
21. Goldberg, E. M.; Lester, D. S.; Borchardt, D. B.; Zidovetzki, R. Effects of Diacylglycerols and Ca2+ on Structure of Phosphatidylcholine/Phosphatidylserine Bilayers. *Biophys J* **1994**, *66*, 382–393.
22. Vamparys, L.; Gautier, R.; Vanni, S.; Bennett, W. F. D.; Tieleman, D. P.; Antonny, B.; Etchebest, C.; Fuchs, P. F. J. Conical Lipids in Flat Bilayers Induce Packing Defects Similar to That Induced by Positive Curvature. *Biophys J* **2013**, *104* (3), 585–593.

23. Drin, G.; Casella, J.-F.; Gautier, R.; Boehmer, T.; Schwartz, T. U.; Antonny, B. A General Amphipathic A-Helical Motif for Sensing Membrane Curvature. *Nat Struct Mol Biol* **2007**, *14* (2), 138–146.
24. Hatzakis, N. S.; Bhatia, V. K.; Larsen, J.; Madsen, K. L.; Bolinger, P. Y.; Kunding, A. H.; Castillo, J.; Gether, U.; Hedegård, P.; Stamou, D. How Curved Membranes Recruit Amphipathic Helices and Protein Anchoring Motifs. *Nat Chem Biol* **2009**, *5* (11), 835–841.
25. Vanni, S.; Vamparys, L.; Gautier, R.; Drin, G.; Etchebest, C.; Fuchs, P. F. J.; Antonny, B. Amphipathic Lipid Packing Sensor Motifs: Probing Bilayer Defects with Hydrophobic Residues. *Biophys J* **2013**, *104* (3), 575–584.
26. Wildermuth, K. D.; Monje-Galvan, V.; Warburton, L. M.; Klauda, J. B. Effect of Membrane Lipid Packing on Stable Binding of the ALPS Peptide. *J Chem Theory Comput* **2019**, *15* (2), 1418–1429.
27. Kim, S.; Oh, M. I.; Swanson, J. M. J. Stressed Lipid Droplets: How Neutral Lipids Relieve Surface Tension and Membrane Expansion Drives Protein Association. *J Phys Chem B* **2021**, *125* (21), 5572–5586.
28. Barlič, A.; Gutiérrez-Aguirre, I.; Caaveiro, J. M. M.; Cruz, A.; Ruiz-Argüello, M. B.; Pérez-Gil, J.; González-Mañas, J. M. Lipid Phase Coexistence Favors Membrane Insertion of Equinatoxin-II, a Pore-Forming Toxin from Actinia Equina. *J Biol Chem* **2004**, *279* (33), 34209–34216.
29. Ahyayauch, H.; Sot, J.; Collado, M. I.; Huarte, N.; Requejo-Isidro, J.; Alonso, A.; Goñi, F. M. End-Product Diacylglycerol Enhances the Activity of PI-PLC through Changes in Membrane Domain Structure. *Biophys J* **2015**, *108* (7), 1672–1682.
30. Bohr, S. S. R.; Thorlaksen, C.; Kühnel, R. M.; Günther-Pomorski, T.; Hatzakis, N. S. Label-Free Fluorescence Quantification of Hydrolytic Enzyme Activity on Native Substrates Reveals How Lipase Function Depends on Membrane Curvature. *Langmuir* **2020**, *36* (23), 6473–6481.
31. Fuki, I. V.; Blanchard, N.; Jin, W.; Marchadier, D. H. L.; Millar, J. S.; Glick, J. M.; Rader, D. J. Endogenously Produced Endothelial Lipase Enhances Binding and Cellular Processing of Plasma Lipoproteins via Heparan Sulfate Proteoglycan-Mediated Pathway. *J Biol Chem* **2003**, *278* (36), 34331–34338.
32. Merkel, M.; Kako, Y.; Radner, H.; Cho, I. S.; Ramasamy, R.; Brunzell, J. D.; Goldberg, I. J.; Breslow, J. L. Catalytically Inactive Lipoprotein Lipase Expression in Muscle of Transgenic Mice Increases Very Low Density Lipoprotein Uptake: Direct Evidence That Lipoprotein Lipase Bridging Occurs in vivo. *PNAS* **1998**, *95* (23), 13841–13846.

33. Connelly, P. W. The Role of Hepatic Lipase in Lipoprotein Metabolism. *Clin Chim Acta* **1999**, *286* (1–2), 243–255.
34. Mead, J. R.; Irvine, S. A.; Ramji, D. P. Lipoprotein Lipase: Structure, Function, Regulation, and Role in Disease. *J Mol Med* **2002**, *80* (12), 753–769.
35. Jaye, M.; Lynch, K. J.; Krawiec, J.; Marchadier, D.; Maugeais, C.; Doan, K.; South, V.; Amin, D.; Perrone, M.; Rader, D. J. A Novel Endothelial-Derived Lipase That Modulates HDL Metabolism. *Nat Genet* **1999**, *21* (4), 424–428.
36. Wang, Z.; Li, S.; Sun, L.; Fan, J.; Liu, Z. Comparative Analyses of Lipoprotein Lipase, Hepatic Lipase, and Endothelial Lipase, and Their Binding Properties with Known Inhibitors. *PLOS One* **2013**, *8* (8), 72146.
37. Choi, S. Y.; Hirata, K.; Ishida, T.; Quertermous, T.; Cooper, A. D. Endothelial Lipase. *J Lipid Res* **2002**, *43* (11), 1763–1769.
38. Lookene, A.; Groot, N. B.; Kastelein, J. J. P.; Olivecrona, G.; Bruin, T. Mutation of Tryptophan Residues in Lipoprotein Lipase. Effects on Stability, Immunoreactivity, and Catalytic Properties. *J Biol Chem* **1997**, *272* (2), 766–772.
39. Williams, S. E.; Inoue, I.; Tran, H.; Fry, G. L.; Pladet, M. W.; Iverius, P. H.; Lalouel, J. M.; Chappell, D. A.; Strickland, D. K. The Carboxyl-Terminal Domain of Lipoprotein Lipase Binds to the Low Density Lipoprotein Receptor-Related Protein/Alpha 2-Macroglobulin Receptor (LRP) and Mediates Binding of Normal Very Low Density Lipoproteins to LRP. *J Biol Chem* **1994**, *269* (12), 8653–8658.
40. Goulbourne, C. N.; Gin, P.; Tatar, A.; Nobumori, C.; Hoenger, A.; Jiang, H.; Grovenor, C. R. M.; Adeyo, O.; Esko, J. D.; Goldberg, I. J.; Reue, K.; Tontonoz, P.; Bensadoun, A.; Beigneux, A. P.; Young, S. G.; Fong, L. G. The GPIHBP1-LPL Complex Is Responsible for the Margination of Triglyceride-Rich Lipoproteins in Capillaries. *Cell Metab* **2014**, *19* (5), 849–860.
41. Yu, J. E.; Han, S. Y.; Wolfson, B.; Zhou, Q. The Role of Endothelial Lipase in Lipid Metabolism, Inflammation, and Cancer. *Histol Histopathol* **2018**, *33* (1), 1–10.
42. Borén, J.; Lookene, A.; Makoveichuk, E.; Xiang, S.; Gustafsson, M.; Liu, H.; Talmud, P.; Olivecrona, G. Binding of Low Density Lipoproteins to Lipoprotein Lipase Is Dependent on Lipids but Not on Apolipoprotein B. *J Biol Chem* **2001**, *276* (29), 26916–26922.
43. De Man, F. H. A. F.; De Beer, F.; Van Der Laarse, A.; Smelt, A. H. M.; Havekes, L. M. Lipolysis of Very Low Density Lipoproteins by Heparan Sulfate Proteoglycan-Bound Lipoprotein Lipase. *J Lipid Res* **1997**, *38* (12), 2465–2472.

44. Perdomo, G.; Kim, D. H.; Zhang, T.; Qu, S.; Thomas, E. A.; Toledo, F. G. S.; Slusher, S.; Fan, Y.; Kelley, D. E.; Dong, H. H. A Role of Apolipoprotein D in Triglyceride Metabolism. *J Lipid Res* **2010**, *51* (6), 1298–1311.
45. Batist, G.; Barton, J.; Chaikin, P.; Swenson, C.; Welles, L. Myocet (Liposome-Encapsulated Doxorubicin Citrate): A New Approach in Breast Cancer Therapy. *Expert Opin Pharmacother* **2002**, *3* (12), 1739–1751.
46. Sun, S.; Dean, R.; Jia, Q.; Zenova, A.; Zhong, J.; Grayson, C.; Xie, C.; Lindgren, A.; Samra, P.; Sojo, L.; Van Heek, M.; Lin, L.; Percival, D.; Fu, J. M.; Winther, M. D.; Zhang, Z. Discovery of XEN445: A Potent and Selective Endothelial Lipase Inhibitor Raises Plasma HDL-Cholesterol Concentration in Mice. *Bioorg Med Chem* **2013**, *21* (24), 7724–7734.
47. Rigoni, M.; Caccin, P.; Gschmeissner, S.; Koster, G.; Postle, A. D.; Rossetto, O.; Schiavo, G.; Montecucco, C. Neuroscience: Equivalent Effects of Snake PLA2 Neurotoxins and Lysophospholipid - Fatty Acid Mixtures. *Science* **2005**, *310* (5754), 1678–1680.
48. Souza, P. C. T.; Alessandri, R.; Barnoud, J.; Thallmair, S.; Faustino, I.; Grünewald, F.; Patmanidis, I.; Abdizadeh, H.; Bruininks, B. M. H.; Wassenaar, T. A.; Kroon, P. C.; Melcr, J.; Nieto, V.; Corradi, V.; Khan, H. M.; Domański, J.; Javanainen, M.; Martinez-Seara, H.; Reuter, N.; Best, R. B.; Vattulainen, I.; Monticelli, L.; Periole, X.; Tieleman, D. P.; de Vries, A. H.; Marrink, S. J. Martini 3: A General Purpose Force Field for Coarse-Grained Molecular Dynamics. *Nat Methods* **2021**, *18* (4), 382–388.
49. Liu, Y.; de Vries, A. H.; Pezeshkian, W.; Marrink, S. J. Capturing Membrane Phase Separation by Dual Resolution Molecular Dynamics Simulations. *J Chem Theory Comput* **2021**, *17* (9), 5876–5884.
50. Van Hilten, N.; Stroh, K. S.; Risselada, H. J. Efficient Quantification of Lipid Packing Defect Sensing by Amphipathic Peptides: Comparing Martini 2 and 3 with CHARMM36. *J Chem Theory Comput* **2022**, *18* (7), 4503–4514.
51. Arora, R.; Nimonkar, A. V.; Baird, D.; Wang, C.; Chiu, C. H.; Horton, P. A.; Hanrahan, S.; Cubbon, R.; Weldon, S.; Tschantz, W. R.; Mueller, S.; Brunner, R.; Lehr, P.; Meier, P.; Ottl, J.; Voznesensky, A.; Pandey, P.; Smith, T. M.; Stojanovic, A.; Flyer, A.; Benson, T. E.; Romanowski, M. J.; Trauger, J. W. Structure of Lipoprotein Lipase in Complex with GPIHBP1. *PNAS* **2019**, *116* (21), 10360–10365.
52. Gunn, K. H.; Roberts, B. S.; Wang, F.; Strauss, J. D.; Borgnia, M. J.; Egelman, E. H.; Neher, S. B. The Structure of Helical Lipoprotein Lipase Reveals an Unexpected Twist in Lipase Storage. *PNAS* **2020**, *117* (19), 10254–10264.

53. Wong, H.; Davis, R. C.; Thuren, T.; Goers, J. W.; Nikazy, J.; Waite, M.; Schotz, M. C. Lipoprotein Lipase Domain Function. *J Biol Chem* **1994**, *269* (14), 10319–10323.
54. van Hilten, N.; Methorst, J.; Verwei, N.; Risselada, H. J. Physics-Based Generative Model of Curvature Sensing Peptides; Distinguishing Sensors from Binders. *Sci Adv* **2023**, *9* (11), eade8839.
55. Cui, H.; Lyman, E.; Voth, G. A. Mechanism of Membrane Curvature Sensing by Amphipathic Helix Containing Proteins. *Biophys J* **2011**, *100* (5), 1271–1279.
56. Santamarina-Fojo, S.; Dugi, K. A. Structure, Function and Role of Lipoprotein Lipase in Lipoprotein Metabolism. *Curr Opin Lipidol* **1994**, *5* (2), 117–125.
57. Prévost, C.; Sharp, M. E.; Kory, N.; Lin, Q.; Voth, G. A.; Farese, R. V.; Walther, T. C. Mechanism and Determinants of Amphipathic Helix-Containing Protein Targeting to Lipid Droplets. *Dev Cell* **2018**, *44* (1), 73-86.e4.
58. Kim, S.; Swanson, J. M. J.; Voth, G. A. Computational Studies of Lipid Droplets. *J Phys Chem B* **2022**, *126* (11), 2145–2154.
59. Luz, J. G.; Beigneux, A. P.; Asamoto, D. A. K.; He, C.; Song, W.; Allan, C. M.; Morales, J.; Tu, Y.; Kwok, A.; Cottle, T.; Meiyappan, M.; Fong, L. G.; Kim, J. E.; Ploug, M.; Young, S. G.; Birrane, G. The Structural Basis for Monoclonal Antibody 5D2 Binding to the Tryptophan-Rich Loop of Lipoprotein Lipase. *J Lipid Res* **2020**, *61* (10), 1347–1359.
60. Chang, S. F.; Reich, B.; Brunzell, J. D.; Will, H. Detailed Characterization of the Binding Site of the Lipoprotein Lipase-Specific Monoclonal Antibody 5D2. *J Lipid Res* **1998**, *39* (12), 2350–2359.
61. Kristensen, K. K.; Leth-Espensen, K. Z.; Mertens, H. D. T.; Birrane, G.; Meiyappan, M.; Olivecrona, G.; Jørgensen, T. J. D.; Young, S. G.; Ploug, M. Unfolding of Monomeric Lipoprotein Lipase by ANGPTL4: Insight into the Regulation of Plasma Triglyceride Metabolism. *PNAS* **2020**, *117* (8), 4337–4346.
62. Wu, S. A.; Kersten, S.; Qi, L. Lipoprotein Lipase and Its Regulators: An Unfolding Story. *Trends Endocrinol Metab* **2021**, *32* (1), 48–61.
63. Kersten, S. Physiological Regulation of Lipoprotein Lipase. *Biochim Biophys Acta* **2014**, *1841* (7), 919–933.
64. Cornell, C. E.; Mileant, A.; Thakkar, N.; Lee, K. K.; Keller, S. L. Direct Imaging of Liquid Domains in Membranes by Cryo-Electron Tomography. *PNAS* **2020**, *117* (33), 19713–19719.
65. Heberle, F. A.; Doktorova, M.; Scott, H. L.; Skinkle, A. D.; Waxham, M. N.; Levental, I. Direct Label-Free Imaging of Nanodomains in Biomimetic and Biological Membranes by Cryogenic Electron Microscopy. *PNAS* **2020**, *117* (33), 19943–19952.

66. Khetarpal, S. A.; Vitali, C.; Levin, M. G.; Klarin, D.; Park, J.; Pampana, A.; Millar, J. S.; Kuwano, T.; Sugasini, D.; Subbaiah, P. V.; Billheimer, J. T.; Natarajan, P.; Rader, D. J. Endothelial Lipase Mediates Efficient Lipolysis of Triglyceride-Rich Lipoproteins. *PLoS Genet* **2021**, *17* (9), e1009802.

67. Olivecrona, G.; Olivecrona, T. Triglyceride Lipases and Atherosclerosis. *Curr Opin Lipidol* **2010**, *21* (5), 409–415.

68. Watt, M. J.; Spriet, L. L. Triacylglycerol Lipases and Metabolic Control: Implications for Health and Disease. *Am J Physiol Endocrinol Metab* **2010**, *299* (2), 162–168.

69. Abraham, M. J.; Murtola, T.; Schulz, R.; Páll, S.; Smith, J. C.; Hess, B.; Lindahl, E. GROMACS: High Performance Molecular Simulations through Multi-Level Parallelism from Laptops to Supercomputers. *SoftX* **2015**, *1*, 19–25.

70. Martinez, L.; Andrade, R.; Birgin, E. G.; Martínez, J. M. PACKMOL: A Package for Building Initial Configurations for Molecular Dynamics Simulations. *J Comput Chem* **2009**, *30* (13), 2157–2164.

71. Gautier, R.; Bacle, A.; Tiberti, M. L.; Fuchs, P. F.; Vanni, S.; Antonny, B. PackMem: A Versatile Tool to Compute and Visualize Interfacial Packing Defects in Lipid Bilayers. *Biophys J* **2018**, *115* (3), 436–444.

72. Jumper, J.; Evans, R.; Pritzel, A.; Green, T.; Figurnov, M.; Ronneberger, O.; Tunyasuvunakool, K.; Bates, R.; Žídek, A.; Potapenko, A.; Bridgland, A.; Meyer, C.; Kohl, S. A. A.; Ballard, A. J.; Cowie, A.; Romera-Paredes, B.; Nikolov, S.; Jain, R.; Adler, J.; Back, T.; Petersen, S.; Reiman, D.; Clancy, E.; Zielinski, M.; Steinegger, M.; Pacholska, M.; Berghammer, T.; Bodenstein, S.; Silver, D.; Vinyals, O.; Senior, A. W.; Kavukcuoglu, K.; Kohli, P.; Hassabis, D. Highly Accurate Protein Structure Prediction with AlphaFold. *Nature* **2021**, *596* (7873), 583–589.

73. Varadi, M.; Anyango, S.; Deshpande, M.; Nair, S.; Natassia, C.; Yordanova, G.; Yuan, D.; Stroe, O.; Wood, G.; Laydon, A.; Zídek, A.; Green, T.; Tunyasuvunakool, K.; Petersen, S.; Jumper, J.; Clancy, E.; Green, R.; Vora, A.; Lutfi, M.; Figurnov, M.; Cowie, A.; Hobbs, N.; Kohli, P.; Kleywegt, G.; Birney, E.; Hassabis, D.; Velankar, S. AlphaFold Protein Structure Database: Massively Expanding the Structural Coverage of Protein-Sequence Space with High-Accuracy Models. *Nucleic Acids Res* **2022**, *50* (D1), D439–D444.

74. Cock, P. J. A.; Antao, T.; Chang, J. T.; Chapman, B. A.; Cox, C. J.; Dalke, A.; Friedberg, I.; Hamelryck, T.; Kauff, F.; Wilczynski, B.; De Hoon, M. J. L. Biopython: Freely Available Python Tools for Computational Molecular Biology and Bioinformatics. *Bioinformatics* **2009**, *25* (11), 1422–1423.

75. Wassenaar, T. A.; Ingólfsson, H. I.; Böckmann, R. A.; Tieleman, D. P.; Marrink, S. J. Computational Lipidomics with Insane: A Versatile Tool for Generating Custom Membranes for Molecular Simulations. *J Chem Theory Comput* **2015**, *11* (5), 2144–2155.
76. Cornelis Kroon, P. Aggregate Assemble Automate. **2020**.
77. Kabsch, W.; Sander, C. Dictionary of Protein Secondary Structure: Pattern Recognition of Hydrogen-Bonded and Geometrical Features. *Biopolymers* **1983**, *22* (12), 2577–2637.
78. Kästner, J.; Thiel, W. Bridging the Gap between Thermodynamic Integration and Umbrella Sampling Provides a Novel Analysis Method: "Umbrella Integration." *J Chem Phys* **2005**, *123* (14), 144104.
79. Bligh, E. G.; Dyer, W. J. A Rapid Method of Total Lipid Extraction and Purification. *Can J Biochem Physiol* **1959**, *37* (8), 911–917.
80. Liu, Y.; de Vries, A. H.; Pezeshkian, W.; Marrink, S. J. Capturing Membrane Phase Separation by Dual Resolution Molecular Dynamics Simulations. *J Chem Theory Comput* **2021**, *17* (9), 5876–5884.
81. Fischer, M.; Pleiss, J. The Lipase Engineering Database: A Navigation and Analysis Tool for Protein Families. *Nucleic Acids Res* **2003**, *31* (1), 319–321.

CHAPTER 4

Structure-function relationship of phase-separated liposomes containing diacylglycerol analogues

Panagiota Papadopoulou[#], Gabriela Arias-Alpizar[#], Pim Weeda, Thijs Poppe, Niels van Klaveren, Tomas Slíva, Dennis Aschmann, Winant van Os, Yun Zhang, Mohammad-Amin Moradi, Nico Sommerdijk, Frederick Campbell, Alexander Kros*

# denotes equal contribution
ready for submission

Abstract | Composition and morphology of lipid-based nanoparticles can influence their overall *in vivo* behavior. Previously, we demonstrated that phase separation in liposomes composed of DSPC and a diacylglycerol lipid analogue (DOaG), drives the *in vivo* biodistribution towards a specific subset of endothelial cells in zebrafish embryos. In the absence of traditional targeting functionalities (*e.g.*, antibodies, ligands), this selectivity is mediated solely by the unique liposome morphology, characterized by a DOaG-rich lipid droplet within the DSPC-rich phospholipid bilayer. The phase separationis induced due to the geometry of DOaG lipid and its ability to create non-bilayer phases in lipid membranes. To investigate the underlying principles of phase separation and to optimize the liposome colloidal stability, we performed a structure-function relationship study by synthesizing a library of DOaG analogues varying molecular properties, such as the number, length and *sn*-position of the acyl chains, as well as the degree of saturation or carbonyl substituents. We assessed the ability of these lipid analogues to assemble into phase-separated liposomes and studied their morphology, colloidal stability, and *in vivo* biodistribution in zebrafish embryos. We found that analogues containing unsaturated, medium length (C16-C18) fatty acids were required to obtain colloidally stable, phase-separated liposomes with cell-specific biodistribution patterns. Moreover, we observed that using the pure DOaG isomer, with acyl chains at the *sn*-1,3 positions leads to more colloidally stable liposomes than when a mixture of *sn*-1,2 and *sn*-1,3 isomers is used. Similarly, we observed that incorporating a DOaG analogue with fatty tails shorter than DSPC, as well as PEGylation, favor liposome long term stability while retaining cell-selective biodistribution. Diacylglycerols are known to promote fusion, lipid polymorphism, signaling and protein recruitment on lipid membranes. In this study we showed that diacylglycerol derivatives can induce phase separation in liposomes, unlocking the potential for cell-specific targeting *in vivo*. We believe these findings can be the foundation for future use of diacylglycerols in lipid-based nanomedicines and could lead to the development of novel targeted delivery strategies.

4.1 Introduction

Composition and molecular properties of lipids used in lipid-based nanoparticles play a pivotal role on their overall *in vivo* behavior. Charge, geometry and degree of saturation, as well as combination of different lipids and molar ratios, dictate lipid nanoparticle size, morphology, rigidity and surface chemistry. Upon *in vivo* administration, these physicochemical properties influence the protein corona formation, clearance, cell uptake and endocytic routes, thereby controlling the overall nanoparticle biodistribution.[1–4] However, the underlying principles are still only understood at a basic level, limiting the effective design of nanomedicines with a high therapeutic efficacy.

Whereas strong surface charge – either anionic or cationic – appears to lead to dominant interactions in the body, [5–10] the fate of neutral lipid nanoparticles appears more nuanced.[1,3,9,10] Geometry of individual lipids contributes to lipid polymorphism[11,12] and controls the morphological and physicochemical properties of lipid-based nanoparticles, which in turn determine the particle - protein interactions and *in vivo* fate. [13–16] Inverted conical lipids with bulky polar head groups result in assemblies with positive curvature (*i.e.*, micelles), while lipids with cylindrical geometry result in planar lamellar bilayers (*i.e.*, liposomes).[11,17] Conical lipids with small polar headgroups increase the negative curvature of membranes providing fusogenic properties in lipid-based nanoparticles[11,18] and facilitate endosomal escape after endocytosis, a crucial event for drug and nucleic acid delivery.[15,19,20] Additionally, conical lipids can lead to non-bilayer phases *i.e.*, inverse hexagonal phase (H_{II}).[17,21–24] One example of such lipids are diacylglycerols (DAGs).[25] DAGs are endogenous lipids found in the cell membrane – mainly after the hydrolysis of phosphatidylinositol – and activate enzymes such Protein Kinase C (PKC) or Phospholipase C, promoting signaling cascade.[25] Lacking a phosphate group, DAGs are hydrophobic conical lipids which can occupy the interleaflet space of lamellar lipid membranes. Above a critical concentration in the bilayer, local accumulation of DAGs disrupts the lamellar properties of membranes, and leads to phase separation and formation of lipid droplets buried within the phospholipid leaflet.[26–30]

In a recent study, we demonstrated how DAG-induced phase separation can drive the biodistribution of liposomes to specific endothelial cell types in zebrafish embryos.[13] The liposome formulation (denoted PAP3) consisting of an equimolar mixture of the saturated, naturally occurring, phospholipid DSPC (1,2-distearyl-*sn*-glycero-3-phosphatidylcholine, T*m* = 55 ºC) and a synthetic DAG analogue, DOaG (2-hydroxy-3-oleamidopropyl-oleate, or dioleoylamidoglycerol), resulted in phase-separated liposomes bearing a single lipid droplet in each bilayer (**Figure 1a, b**). Surprisingly, upon intravenous administration in zebrafish embryos, PAP3 liposomes selectively accumulated within brain endothelial cells (bECs) without the use of traditional targeting ligands (*e.g.*, antibodies, peptides) (**Figure 1c**). The observed liposome recognition and accumulation in bECs was mediated by triglyceride lipase (TGL), which is highly present at the luminal surface of zebrafish bECs during development. Importantly, we showed that this process required the presence of the phase-separated droplet within the liposome bilayer, implying a preferential nanoparticle-protein communication due to unique morphology and composition.[13,14] Additionally, we found that accumulation of DOaG within the DSPC leaflet induced lipid packing defects on the liposome surface, exposing the DOaG to the surrounding environment, a key factor for the specific interaction between PAP3 liposomes and TGL.[14] As with DAGs, DOaG increases the distance between adjacent phospholipids, increasing hydrophobicity and facilitating recognition and binding of TGL on the lipid membrane.[14,29,31]

In this study, we designed a library of close DOaG analogues, to probe how the exact molecular chemistry and structure of DOaG induce phase separation in liposomes and concomitant bEC targeting in embryonic zebrafish. Chain length, degree of saturation, number and *sn*-position of fatty acid chains, and carbonyl substituents on the backbone, were varied to study the effect on lipid assembly and *in vivo* cell-specific targeting (**Figure 1d**). Hence, molecular DOaG analogues were synthesized, mixed with DSPC (analogue/DSPC 1:1) and assembled into liposomes. Long-term stability and morphology of the resulting liposomes were characterized by dynamic light scattering (DLS) and cryo-transmission electron microscopy (cryo-TEM) respectively, and their *in vivo* behavior was assessed in zebrafish embryos (**Figure 1e**).

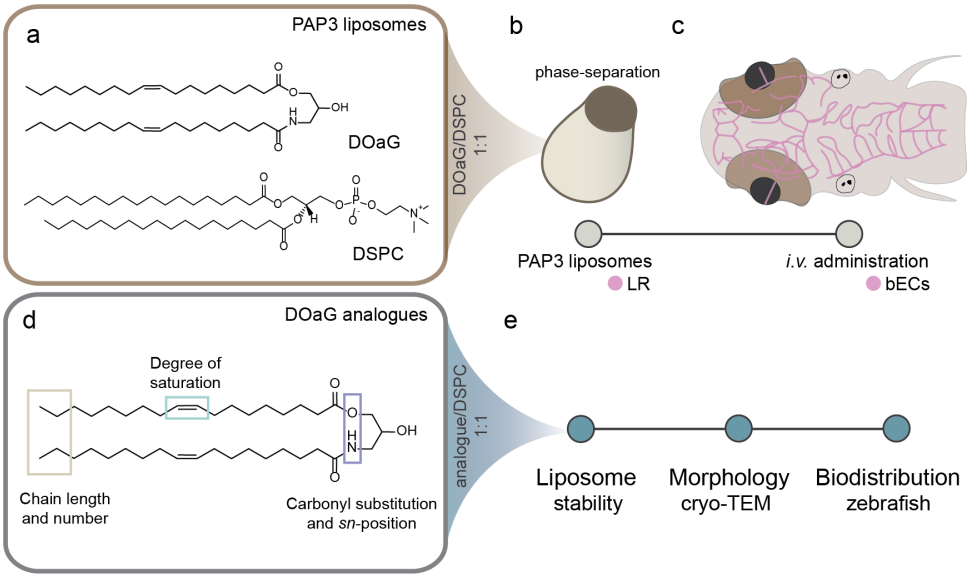

Figure 1. Overview of phase-separated liposomes and timeline of experiments. a) Molecular structures of DOaG and DSPC. **b)** Schematic of phase-separated liposomes containing DOaG and DSPC (1:1). **c)** Schematic dorsal view of zebrafish embryo head. Injected liposomes contained 0.2% mol DOPE-LR (1,2-dioleoyl-sn-glycero-3-phosphoethanolamine-N-[lissamine rhodamine B sulfonyl]) for visualization. (Brain) vasculature depicted in pink, region in which liposomes selectively accumulate. **d)** Molecular properties of DOaG which were altered to generate a library of DOaG analogues. **e)** Overview of DOaG library assessment: Liposomes were formulated from a 1:1 ratio of DSPC:analogue and stability, morphology and biodistribution were assessed by DLS, cryo-TEM and confocal imaging of injected zebrafish embryos, respectively.

Overall, we observed that DOaG analogues with unsaturated, medium length (C16-C18) fatty acid tails – when co-formulated with DSPC – can induce phase separation in colloidally stable liposome formulations, which leads to bEC specific biodistribution patterns in embryonic zebrafish. Monoacyl and triacyl glycerol analogues, as well as diacyl analogues with saturation, or shorter (C14) or longer fatty acid tails (C20-C24), either i) cannot form liposomes, or ii) phase separationexists only in a small fraction of the population, or iii) the formulation cannot interact with bECs. Additionally, we show the naturally occurring dioleoylglycerol (DOG) retains the properties of DOaG, proving the correlation of

the well-studied DAGs in membranes with the DOaG-induced phase-separation. Finally, we show that lipids with fatty acid tails substituting the *sn*-1,3 positions of the backbone result in liposomes with more favorable long-term stability, than when the *sn*-1,2 positional isomer is also present in the formulation. Similarly, PAP3 liposomes could be stabilized by a small amount of DMPE-PEG2k (1,2-dimyristoyl-sn-glycero-3-phosphoethanolamine-N-[methoxy(polyethylene glycol)-2000), or by replacing DOaG with the shorter (C16:1) analogue. This improved the long-term stability and ability to assemble liposomes in physiologically relevant buffers, which is particularly important for the translation towards nanomedicine formulations with high therapeutic efficacy.

4.2 Results and Discussion

Molecular library of DOaG analogues

DOaG is a synthetic, amide-containing analogue of dioleoylglycerol (DOG) (**Figure 2a, b**). It is mainly isolated as a mixture of two positional isomers – something that also occurs in natural lipids – in which the two acyl chains substitute the *sn*-1,3 positions and *sn*-1,2 positions with a 8:2 ratio **(Figure S1**). To understand the influence of individual molecular properties of the DOaG lipid, a library of 12 analogues was created, maintaining the glycerol-like backbone in all newly synthesized lipids (**Figure 2b**). Firstly, a series of changes in chain length was generated, altering the monounsaturated fatty acid chains, from C14:1 to C24:1, resulting in lipids **1-5** (**Figure 2c** and **Figure S2b, g**. Note: lipid 3 is DOaG). Subsequently, degree of saturation was altered (**Figure 2d** and **Figure S2c, g**), with either full saturation on both C18 tails (lipid **6**) one saturated and one monounsaturated tail (lipid **7**) or with di-unsaturation in both tails (lipid **8**). Next, we generated lipids with only one, or three oleic chains and lipids with either two esters (naturally occurring DAG), or two amides (**Figure 2e, f** and **Figure S2d-e, g, lipids 9-12**). Finally, to assess the importance of the regioisomeric mixture of positional isomers, we synthesized the pure DOaG isomer with substitution on the *sn*-1,3 position (~ 95% pure), as a comparison of the mixture that has been studied so far (*sn*-1,3/80%, *sn*-1,2/20%) (lipid **21, Figure 2g** and **Figure S2f, g**).

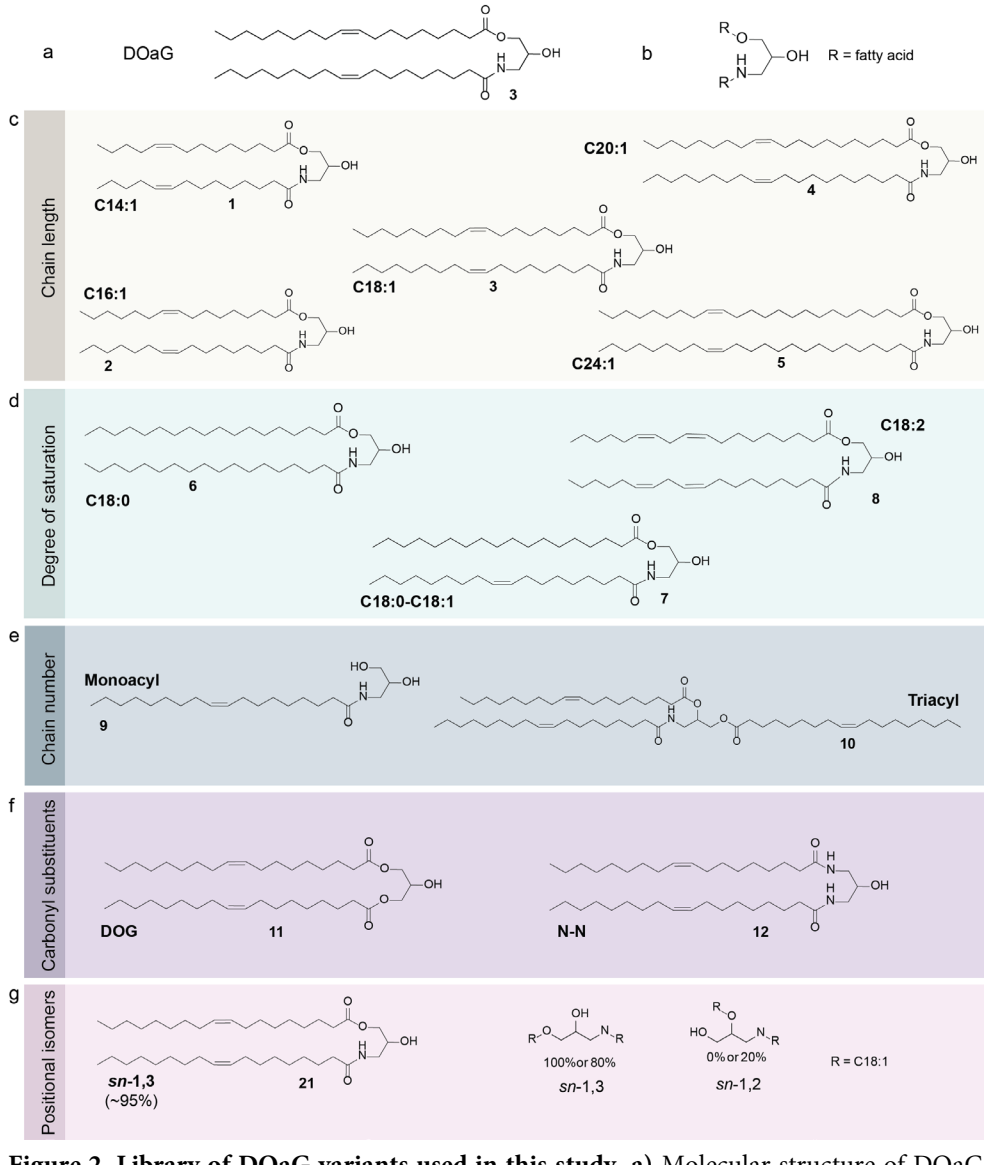

Figure 2. Library of DOaG variants used in this study. a) Molecular structure of DOaG lipid. **b)** DOaG glycerol-like backbone. DOaG analogues varying the: **c)** chain length, **d)** degree of saturation, **e)** number of acyl chains, **f)** carbonyl substituents of the glycerol-like backbone and **g)** *sn*-position of acyl chain substitution. All lipids exist as a regioisomeric mixture of *sn*-1,3 and *sn*-1,2 positional isomers (8:2 ratio), except for (**7**, **9**, **10**, **12**, **21**). Only the *sn*-1,3 isomer is shown for clarity.

Chain length influences stability and bEC targeting

Liposomes containing an equimolar mixture of DSPC and the **C14:1** analogue (**lipid 1**), were stable over a period of ~25 days, maintaining their hydrodynamic diameter below 200 nm albeit with the polydispersity increasing after 6 days (**Figure 3a**). The majority (80%) of the liposomes revealed a phase-separated morphology (**Figure 3b**) as quantified by cryo-TEM (**Figure S3a, d**). Interestingly, real-time biodistribution imaging in zebrafish suggested these liposomes mostly accumulate in a subset of cells located in the tail region of the zebrafish embryo, named as scavenging endothelial cells[6] and in the zebrafish liver, but not in bECs despite their phase-separated morphology (**Figure 3c** and **Figure S4a, b**). We hypothesize the **C14:1** analogue might be too short to create high packing defects at the liposome membrane, resulting in less exposure to the surrounding environment therefore being less recognizable by TGL. Liposomes assembled from the **C16:1** analogue (**lipid 2**) were stable over a period of 30 days and monodisperse (**Figure 3d**). Phase separation was also observed in these liposomes, while the bilayers appeared less cornered (less flat) suggesting a more liquid disordered phase than the **C14:1** containing liposomes (**Figure 3e, Figure S3b**). This indicates that **C16:1** analogues are able to mix with the DSPC-rich membranes more effectively due to a smaller chain length mismatch. Therefore, the membrane becomes more flexible resulting in more spherical liposomes with less corners. Quantification indicated that the large majority of liposomes (~90%) possessed a phase-separated morphology (**Figure S3d**). Liposomes containing the **C16:1** variant were also able to target bECs (**Figure 3f** and **Figure S4c, d)**, similar to the original PAP3 liposomes[13] which contain **C18:1** chains (DOaG, **lipid 3** in figure 2c) (compare **Figure 3f** with **Figure 3i** and **Figure S4e, f)**. Extending the unsaturated chain length by 2 carbons (**C18:1**) decreased the stability of the resulting liposomes, as these were only stable and monodisperse for less than 7 days (**Figure 3g**). The membrane of the phase-separated **C18:1** containing liposomes appeared more fluid as evidenced by the more spherical shape of the liposomes compared to the **C14:1** and **C16:1** variants (**Figure 3h** and **Figure S3c**). Similar to **C16:1** containing liposomes, **C18:1** containing liposomes were predominantly phase-separated (**Figure S3d**). Further extension of the acyl chains to **C20:1** DOaG analogue (**lipid 4**), resulted in

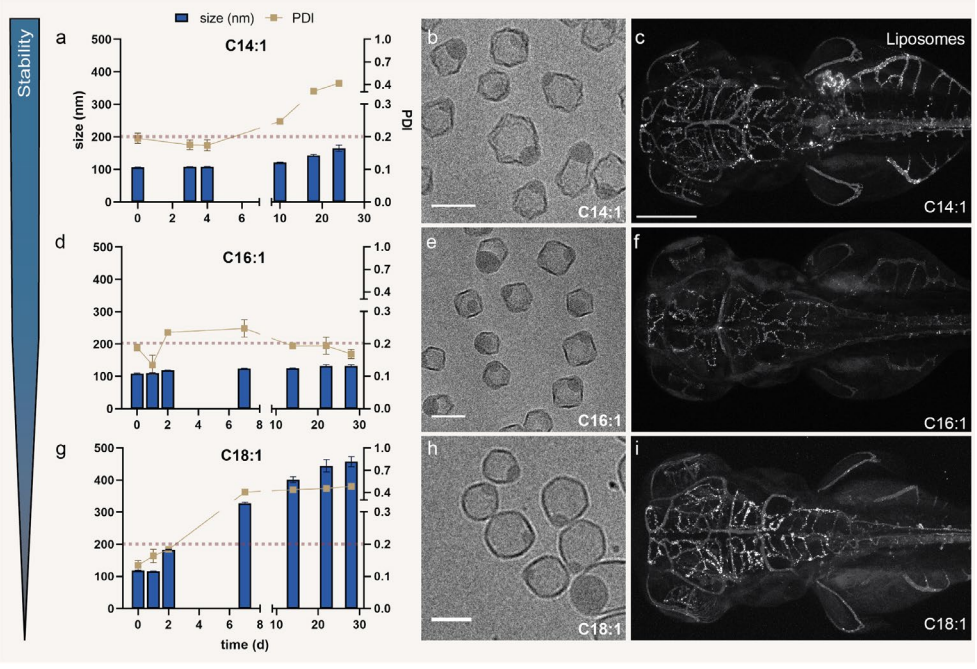

Figure 3. Stability, morphology and biodistribution of liposomes consisting of DSPC and DOaG analogues (1:1) as a function of chain length. Size (nm) and polydispersity index (PDI) of liposomes consisting of DSPC and **a)** C14:1, **d)** C16:1, **g)** C18:1 variant over a period of ~30 days. Cryo-TEM image of liposomes consisting of DSPC and **b)** C14:1, **e)** C16:1, **h)** C18:1 variant. Biodistribution of liposomes (grey) consisting of DSPC and **c)** C14:1, **f)** C16:1, **i)** C18:1 variant in a Tg(*kdrl*:GPF) zebrafish embryo, in dorsal view (10x magnification), 1.5 hour post injection (hpi) at 78 days post fertilization (dpf). Liposomes consisting of 1:1 DSPC/analogue, total lipid concentration 5 mM containing 0.2 mol% DOPE-LR (dioleoyl-phosphatidylethanolamine-lissamine rhodamine). Scale bars: 200 µm for zebrafish and 100 nm for cryo-TEM images. Dynamic light scattering (DLS) was used to obtain data in a, d and g. Size as determined by the measurement of the hydrodynamic diameter (nm). Red dashed line in a, d and g indicates the threshold of size and PDI relevant for *in vivo* use. Cryo-TEM imaging at d=0.

aggregation after only ~6 h (**Figure S5a**), while the **C24:1** variant (**lipid 5**) did not assemble into liposomes at all (**Figure S5b**).

These findings, as well as the instability of the **C18:1**-containing formulation (PAP3), indicate that liposomes progressively aggregate by increasing fatty acid chain length, when mixed with DSPC.

This supports previous findings which show DOaG is exposed to the surrounding environment due to large hydrophobic packing defects induced in the membrane, due to phase-separation.[14] Hence, the longer the fatty acid tail of the variant the more the variant is exposed to the surroundings and therefore the shorter the stability of the overall assembly and vice versa. We have reported previously that packing defects on PAP3 liposomes are a key factor for liposome recognition by TGLs,[14] which in turn influences liposome uptake *in vivo*.[13] Liposomes which contain the shorter chain (**C14:1**) analogue did not target bECs but *are* phase-separated. A possible explanation for this observation is that packing defects on these liposomal membranes are lower throughout.

C14:1 lipids may possibly be more buried within the leaflet and less exposed on the liposome surface, due to their shorter chains and high mismatch with DSPC, therefore the liposome surface is less favorable for protein recruitment. Increasing the chain length by two carbons (**C16:1** analogue) is already enough to create liposomes that target bECs, indicating again the starting point of exposure and accessibility of the lipid. This in turn, indicates **C16:1** creates fewer packing defects than the longer **C18:1** (DOaG) lipid and so forth. This hypothesis is supported by the colloidal stability studies, in which **C16:1** containing liposomes are shown to be more stable and less prone to aggregation, than the **C18:1** containing liposomes. Since liposomes with > C18 chains do not form stable formulations, **C16:1** and **C18:1** lipid seem to be the "sweet spot" for phase-separation, liposome stability and bEC targeting.

Unsaturated analogues favor liposome formation and phase separation

We next assessed the effect that unsaturation in DOaG analogues has on the liposome assembly, by synthesizing a fully saturated variant (**C18:0, lipid 6**). This analogue could not be formulated into liposomes with DSPC as a co-formulant (**Figure S6a**). The intermediate lipid analogue **C18:0-C18:1 (lipid 7)** was also unable to assemble into stable liposomes (**Figure S6b**). This confirmed that both acyl chains must be unsaturated in order to assemble into stable phase-separated liposomes with DSPC. Indeed, as with DOaG, similar results were obtained with the DOaG analogue with two (conjugated) double bonds in each fatty acid tail (**C18:2, lipid 8**). Liposomes made of DSPC/C18:2 (1:1) were stable for at least 30 days, albeit

with a moderate PDI (**Figure 4a**). Cryo-TEM analysis showed these liposomes were predominantly phase-separated (**Figure 4b** and **Figure S7a, e**), but the bilayers appeared to be more in the gel-phase, as evidenced by cornered/flat membranes. The double unsaturation per acyl chain has a strong influence on the lipid's geometry and we assume the packing on this lipid within the DSPC leaflet might be more compact and completely de-mixed from DSPC, resulting in a gel-phase for the bilayer. Liposomes containing **C18:2** were able to target bECs in zebrafish embryos (**Figure 4c and Figure S9a, b**). In conclusion, equimolar mixtures of unsaturated DOaG analogues and DSPC assemble into phase separated liposomes, which in turn are able to selectively target bECs *in vivo*.

Influence of chain number and amide in glycerol-like backbone

Next, we investigated how essential the number of acyl chains per glycerol is for phase-separation. Monoacylglycerols have been studied before for their ability to form inverse hexagonal and (inverse) cubic liquid crystalline phases.[23,24] However, a liposome formulation with (1:1) DSPC and a **monoacyl** variant (**lipid 9**), formed liposomes that were highly unstable, as evidenced by the rapid size increase within ~6 h (**Figure S6d**). The **triacyl** variant (**lipid 10**), formulated with DSPC, formed liposomes that were stable for at least 30 days (**Figure 4d**). Interestingly, these liposomes were predominantly lamellar in morphology (~80%), with some solid particles (~2%) and only a small fraction (~5%) which revealed a phase-separated morphology (**Figure 4e** and **Figure S7b, e**). As a result, the majority of injected liposomes in zebrafish did not accumulate in the brain endothelium (**Figure 4f and Figure S9c, d**). Only a minor fraction was able to target bECs, which might be explained by the fraction of phase-separated liposomes in the formulation. To assess the influence of the ester and amide functionalities of DOaG on phase separation and *in vivo* bEC targeting, we synthesized the naturally occurring dioleoylglycerol (**DOG, lipid 11**). Liposomes containing **DOG** were stable in size and with acceptable PDI values for a period of 20 days (**Figure 4g**). Similar to **PAP3** liposomes, the **DOG** containing-liposomes revealed a phase-separated morphology (**Figure 4h** and **Figure S7c),** albeit for only ~55% of all liposomes (**Figure S7e**). DOG/DSPC liposomes also targeted bECs (**Figure 4i**). Interestingly, the lipid analogue with two amides (coded **N-N, lipid 12**) could not be formulated into stable liposomes (**Figure S6c**). A possible explanation may be an additional hydrogen bond due to the introduction of the extra amide, thereby negatively influencing lipid assembly into defined nanoparticles.

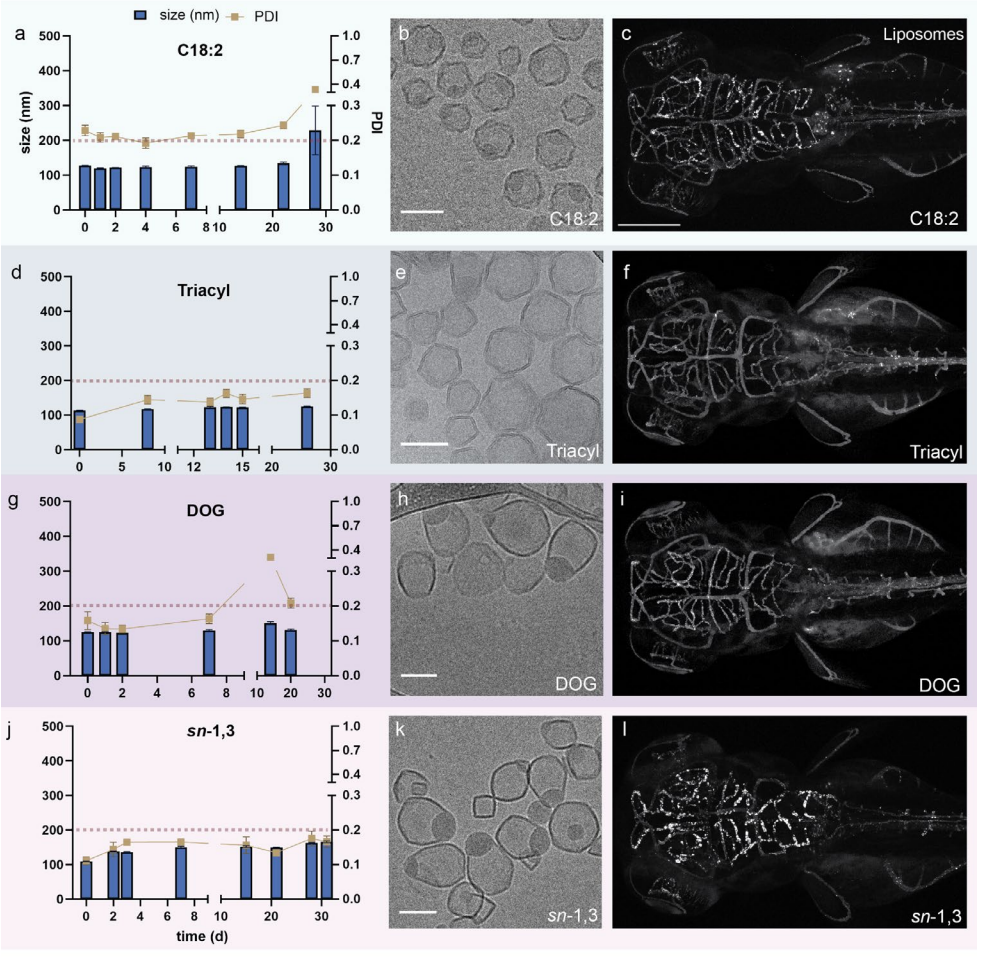

Figure 4. Stability, morphology and *in vivo* behavior of liposomes consisting of DSPC and DOaG analogues (1:1) as a function of saturation, number of fatty acid tails, carbonyl substitution or *sn*-position substitution. Size (nm) and PDI of liposomes consisting of DSPC and **a)** C18:2, **d)** Triacyl, **g)** DOG, **j)** *sn*-1,3 variant over a period of ~30 days. Cryo-TEM image of liposomes consisting of DSPC and **b)** C18:2, **e)** Triacyl, **h)** DOG, **k)** *sn*-1,3 variant. Biodistribution of liposomes (grey) consisting of DSPC and **c)** C18:2, **f)** Triacyl, **i)** DOG, **l)** *sn*-1,3 variant in a Tg(kdrl:GPF) zebrafish embryo, in dorsal view (10x magnification), 1.5 hpi at 78 dpf. Liposomes consisting of 1:1 DSPC/analogue, total lipid concentration 5 mM containing 0.2 mol% DOPE-LR. Scale bars: 200 µm for zebrafish and 100 nm for cryo-TEM images. DLS was used to obtain data in a, d, g and j. Size as determined by the measurement of the hydrodynamic diameter (nm). Red dashed line in a, d, g and j indicates the threshold of size and PDI relevant for *in vivo* use. Cryo-TEM imaging at d=0.

***Sn*-position in fatty acid tails influences stability**

Due to the chosen synthetic strategy, all previously discussed DOaG lipids (except lipid 7, 9, 10 and 12) were a mixture of the *sn*-1,2 and *sn*-1,3 isomers with a ~2:8 ratio. Therefore, we synthesized the *sn*-1,3 isomer in high purity (~95%, coded ***sn*-1,3, lipid 21**) and upon co-assembly with DSPC, stable liposomes were obtained for at least 30 days (**Figure 4j**). In contrast, the original PAP3 liposomes, that contained the *sn*-1,3/*sn*-1,2 mixture, were only stable for 7 days (**Figure 3g**). As expected, liposomes with *sn*-1,3 were phase-separated (**Figure 4k** and **Figure S7d**), with only a small population (3.3%) having an unknown, highly structured liquid-crystalline phase (**Figure S7d, e** and **Figure S8**), with a repeat distance of 4.85 nm as seen by Fast Fourier Transform (FFT) analysis. Biodistribution studies in zebrafish embryos revealed that liposomes containing this isomerically pure DOaG variant were also able to target bECs in a selective manner (**Figure 4l** and **Figure S9g, h**).

C16:1 variant and PEGylation improves long term stability

Despite their interesting morphology and selective *in vivo* behavior, PAP3 liposomes are not stable in physiologically isosmotic and isotonic buffers which contain saline (*i.e.*, phosphate buffered saline [PBS]). This is particularly important for the efficient applicability of these liposomal formulations towards nanomedicine. PAP3 liposomes formulated in water are stable for 7 days, however in PBS rapid aggregation is observed (**Figure 5a, b**). This is likely due to the lack of ability of membranes which contain DAGs to coordinate sodium ions, as described in a previous study;[32] and although formulating liposomes containing the pure ***sn*-1,3** DOaG variant (*i.e.*, excluding the *sn*-1,2 isomer) improves the overall stability of PAP3 liposomes, it does not improve their stability in PBS (**Figure S10**). Interestingly, when co-formulated with DSPC, the shorter (**C16:1**) lipid variant could formulate stable phase-separated liposomes in PBS, with colloidal stability for at least 30 days and with improved PDI values (**Figure 5a, d**). This supports our hypothesis that **C16:1** lipids are less exposed to the aqueous surroundings than DOaG, leading to less membrane instability and aggregation. Alternatively, a low percentage of PEGylated lipid also increased the stability of PAP3 liposomes, while retaining morphology and bEC targeting. Previously, addition of 5% mol of DSPE-PEG2k-(1,2-distearoyl-sn-glycero-3-phosphoethanolamine-N-amino(polyethylene

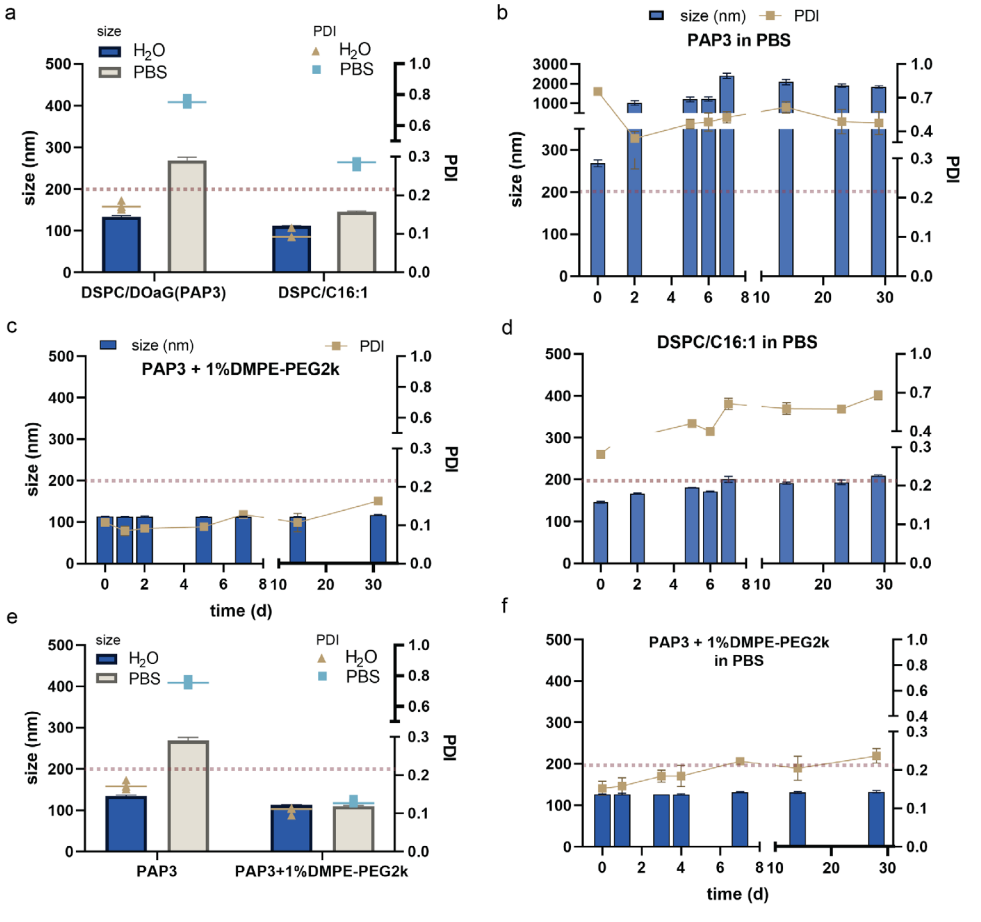

Figure 5. Optimization and stability studies of PAP3 liposomes. a) Size (nm) and PDI of PAP3 liposomes (DSPC/DOaG) or DSPC/C16:1 liposomes, formulated in ddH_2O or PBS. **b)** Size (nm) and PDI of PAP3 liposomes formulated in PBS over a period of ~30 days. **c)** Size (nm) and PDI of PAP3 liposomes incorporating 1 % mol DMPE-PEG2k formulated in ddH_2O over a period of ~30 days. **d)** Size (nm) and PDI of DSPC/C16:1 liposomes formulated in PBS over a period of ~30 days. **e)** Size (nm) and PDI of PAP3 liposomes or PAP3 liposomes incorporating 1 % mol DMPE-PEG2k, formulated in ddH_2O or PBS. **f)** Size (nm) and PDI of PAP3 liposomes incorporating 1 % mol DMPE-PEG2k formulated in PBS over a period of ~30 days. DLS was used to obtain the data depicted in this figure. Size as determined by the measurement of the hydrodynamic diameter (nm). Red dashed line indicates the threshold of size and PDI relevant for *in vivo* use.

glycol)-2000) in PAP3 was observed to abolish the bEC targeting.[13] Addition of only 1% mol of DMPE-PEG2k however, showed to be optimal, keeping the *in vivo* bEC targeting while also improving liposomal stability (**Figure 5c**). PAP3 liposomes with 1% mol DMPE-PEG are phase-separated (**Figure S11)** and target bECs in zebrafish embryos (**Figure S12).** Importantly, when formulated in PBS, stability of PAP3 liposomes incorporating 1% mol of DMPE-PEG2k was improved even further than the **C16:1** variant (**Figure 5e, f**). The information obtained by this effort to optimize the phase-separated liposomes can be the basis for future developments, or use of DAGs and DAG analogues in lipid-based formulations.

Saturation in phospholipid co-formulant is important for phase separation

It is important to mention that liposomes with DOaG and the fluid DOPC (1,2-dioleoyl-sn-glycero-3-phosphocholine) as a co-formulant, instead of DSPC, do not formulate phase-separated liposomes and do not target bECs.[13] It was therefore interesting to assess the significance of saturated DSPC in the phase-separated liposomes. At room temperature, DSPC is a rigid phospholipid (*Tm* 55 °C) that prefers flat orientations and therefore not favoring curvature *i.e.*, spherical liposomes.[33] PAP3 liposomes are formed (above the *Tm* of all lipids, *i.e.*, 65 °C) and slowly reach room temperature, in which DSPC is in the gel-phase. We hypothesized the gel-phase of DSPC is an important factor that induces phase-separation. Indeed, cryo-TEM imaging at 45 °C < T < 65 °C reveals ~50% of liposomes are in a fluid phase and non-phase separated, indicating full mixing of lipids (**Figure S13**). Therefore, phase separationseems to be induced after DSPC is in the gel-phase (< 55 °C).

4.3 Discussion and Conclusions

In this study, we investigate the molecular details of DOaG, a DAG lipid analogue which – when co-formulated with DSPC – leads to unique phase-separated liposomes able to target endothelial cell subsets *in vivo*, and preferentially interact with TGLs *in vivo* and *in vitro*.[13,14] Through our structure-activity relationship screening we are able to show the narrow window of *in vivo* activity of phase-separated liposomes consisting of medium (C16-C18), unsaturated diacylglycerol

analogues. All DAG analogues are summarized in **Figure 6**, depicting the relationship between their chemical character, stability, morphology and *in vivo* fate of resulting liposomes. Briefly, we find that there is increasing instability in the liposome system, directly proportional to the DOaG chain length and degree of saturation. Additionally, we show that monoacylglycerol or triacylglycerol counterparts do not result in liposomes with bEC specific behavior. Therefore, diacylglycerol analogues are the only molecules with the ability to phase-separate in membranes and result in liposomes targeting bECs in zebrafish embryos. Importantly, we show the naturally occurring DAG equivalent has the same ability to form phase-separated liposomes (although in a lower percentage within the liposome population) and target bECs in zebrafish embryos. This gives strength to the basis of our background knowledge for the DOaG lipid, as it correlates with supporting previous studies of DAG properties in lipid membranes.[25,26,29,34]

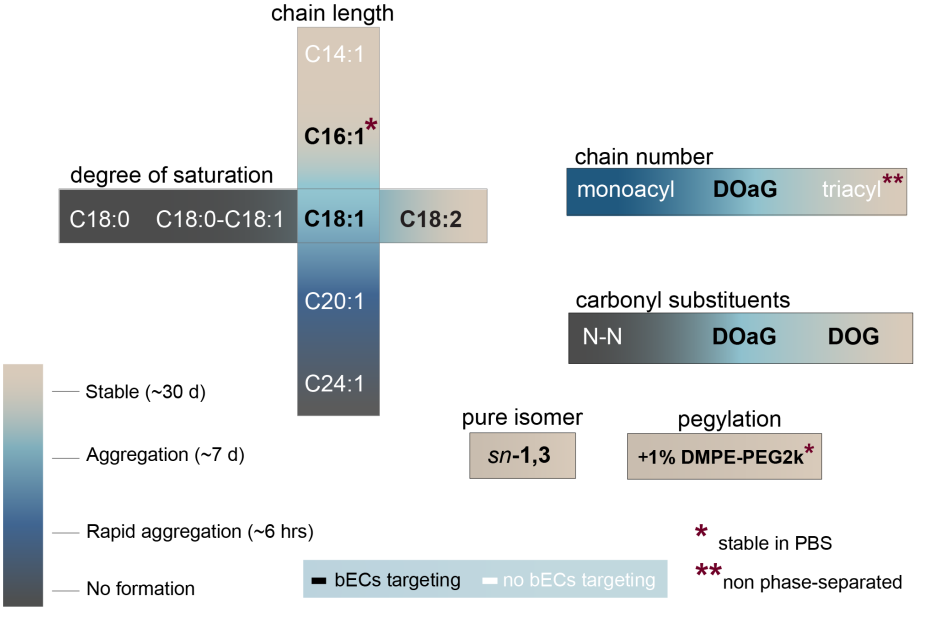

Figure 6. Summary of DOaG analogues and relationship between chemical character and stability, morphology, and *in vivo* behavior of resulting liposomes. Stability: stable for ~30 days (beige), aggregation after ~7 days (light blue), rapid aggregation after ~6 hours (dark blue), no formation (dark grey). Analogues which result in liposomes targeting bECs are written in black letters and not targeting bECs in white letters. * Stable in PBS, **Non phase-separated.

Interestingly, we find phase-separated liposomes that do not target bECs (*i.e.*, **C14:1**). We hypothesize that lipid droplets may not be the only liposome part responsible for bEC targeting, but also all parts of the bilayer which have packing defects, exposing the DOaG analogue. Excess **C14:1** accumulates in the lipid droplet – which may indeed have high packing defects – but other parts of the bilayer may be unaffected due to its shorter chains. Liposomes therefore with only a fraction of their bilayer being defected, may not have the same chance to expose DOaG analogues and be recognized and taken up by bECs, compared to liposomes with high packing defects throughout the bilayer (*i.e.*, **C16:1**, **C18:1**).

Additionally, we observe better long-term stability of liposomes containing the pure *sn*-1,3 positional isomer. The importance and effect of pure lipid isomers in lipid-based nanoparticle properties has been recently reported[35,36] and is an aspect to be considered in their development. Next, we find that liposomes consisting of the **C16:1** variant are overall more stable in PBS than the **C18:1** counterpart (DOaG) and that PEGylation of PAP3 liposomes (1 % mol DMPE-PEG2k) increases the long-term stability even further, while phase separationand bECs targeting is retained. Herein, we display a selection of DOaG analogues co-formulated with DSPC. Combinations of DOaG analogues, DAGs, and co-formulants are virtually endless, nevertheless out of the scope of this study. This work is an effort to comprehend the overall properties of a highly unusual liposome with a specific *in vivo* behavior. Lacking any 'active' targeting ligands, these liposomes depend solely on composition and morphology which dictate the nano-bio interactions. Therefore, this compositionally simple system can offer new perspectives in the design of 'targeted' liposome formulations. This work also highlights the importance of lipid composition in lipid-based nanoparticles, as even the smallest molecular changes in lipid components can greatly affect their macromolecular assembly and *in vivo* behavior.

Finally, diacylglycerols are lipids that have unique properties in lipid membranes. From membrane alteration and phase transitions, to signaling and protein recruitment, these lipids can be proven to be interesting lipid components in lipid-based nanoparticles. They could contribute to novel formulations with unique properties and functions, such as *in vivo* specificity, nanoparticle-protein communication, fusion and enhanced endosomal escape.

4.4 Materials and Methods

General reagents: 1,2-distearoyl-*sn*-glycero-3-phosphocholine (DSPC), 1,2-dioleoyl-*sn*-glycero-3-phosphoethanolamine-N-(lissamine rhodamine B sulfonyl) (DOPE-LR), were purchased from Avanti Polar Lipids (Alabaster, AL, US). Additional DSPC was purchased from Lipoid GmbH. All other chemical reagents were purchased at the highest grade available from Sigma Aldrich and used without further purification. All solvents were purchased from Biosolve Ltd. Ultrapure MilliQ® water, purified by a H_2O Advantage A10 water purification system from MilliPore, was used throughout.

Liposome formulation: Liposomes were formulated by extrusion in ddH_2O at a total lipid concentration of 5 mM, except for the PBS studies for which they were formulated in PBS. Individual lipids as stock solutions (1-10 mM) in chloroform, were combined to the desired molar ratios and dried to a thin film, first under N_2 stream, then >1 h under vacuum. The fluorescent reporter DOPE-LR (1,2-dioleoyl-*sn*-glycero-3-phosphoethanolamine-N-(lissamine rhodamine B sulfonyl) was also added in the lipid film at 0.2% moL. Lipid films were hydrated with 1mL ddH_2O (or PBS) above the T*m* of all lipids (65 °C), with gentle vortexing if necessary, to form a suspension. Large unilamellar vesicles were formed through extrusion (mini extruder, Avanti Polar Lipids) above the T*m* of all lipids (*i.e.* 65 °C). Hydrated lipids were passed 11 times through 2 x 400 nm polycarbonate (PC) membranes (Nucleopore Track-Etch membranes, Whatman), followed by 11 times through 2 x 100 nm PC membranes. All liposomes were freshly made for cryo-TEM imaging and intravenous administration in zebrafish embryos. Subsequently, all formulations were stored at 4 °C for a period of 30 days measuring their size and PDI occasionally.

Hydrodynamic diameter and PDI measurements: The hydrodynamic diameter and PDI of liposomes were obtained by using a Malvern Zetasizer Nano ZS. DLS measurements (operating wavelength = 633 nm), were carried out at room temperature in water at a total lipid concentration of approx. 100 μM. All reported DLS measurements are the average of three measurements.

Zeta potential measurements: Zeta potential of each formulation was measured at 500 μM total lipid concentration, using a dip-cell electrode (Malvern), at room

temperature. For liposomes formulated in water, aq. NaCl was added to the liposome solution prior to the measurement, to a final concentration of 10 mM. Total NaCl concentration was <20 mM for all measurements.

Cryogenic transmission electron microscopy: Liposomes (3 µL, 5 mM total lipid concentration) were applied to a freshly glow-discharged carbon 200 mesh Cu grid (Lacey carbon film, Electron Microscopy Sciences, Aurion, Wageningen, The Netherlands). Grids were blotted for 3 s at 99% humidity in a Vitrobot plunge-freezer (FEI VitrobotTM Mark III, Thermo Fisher Scientific). For PAP3 liposomes imaged at 45 ºC < T < 65 ºC , liposomes were prepared by extrusion at 65 ºC and immediately transferred in a thermomixer with a stable temperature at 65 ºC, without allowing the liposomes to reach room temperature at all times. Subsequently, liposomes were transferred in the plunge-freezer operating at 45 ºC and immediately vitrified. Cryo-TEM images were collected on a Talos L120C (NeCEN, Leiden University) or a Titan (TU Eindhoven) operating at 120 kV or 300kV, respectively. Images acquired on the Talos microscope were recorded manually at a nominal magnification of 13500x or 22000x yielding a pixel size at the specimen of 7.44 or 4.40 ångström (Å), respectively. Images acquired on the KRIOS microscope were recorded manually at a nominal magnification of 6500x or 24000x yielding a pixel size at the specimen of 13.99 or 3.87 ångström (Å), respectively.

Cryo-TEM quantification: Software Fiji (ImageJ) was used for image processing and quantification. One or more low magnification images were used to visualize at least 100 nanoparticles. Particles were counted and divided into categories (lamellar, multilamellar, phase separated, solid particles), according to their morphology. Liposomes whose morphology was not able to be identified were marked as "unidentifiable" and the number obtained was used as standard deviation for the rest of population. Liposomes that were observed to be on top or in close contact with the copper grid or overlapping with each other were excluded from the quantification.

Zebrafish husbandry and injections: Zebrafish (*Danio rerio*, strain AB/TL) were maintained and handled according to the guidelines from the Zebrafish Model Organism Database (http://zfin.org) and in compliance with the directives of the local animal welfare committee of Leiden University. Fertilization was performed by natural spawning at the beginning of the light period, and eggs were raised at 28.5

°C in egg water (60 ug/ mL Instant Ocean sea salts). The previously established zebrafish line Tg*(kdrl:*eGFP*)*^{s843} was used throughout this study.[37] Liposomes were injected into zebrafish embryos (78 hours post fertilization) using a modified microangiography protocol.[38] Embryos were anesthetized in 0.01% tricaine and embedded in 0.4% agarose containing tricaine before injection. To improve reproducibility of microangiography experiments, 1 nL injection volume was calibrated before liposomes were injected into the sinus venosus/Duct of Cuvier. A small injection space was created by penetrating the skin with the injection needle and gently pulling the needle back, thereby creating a small pyramidal space in which the liposomes were injected. Successfully injected embryos were identified through the backward translocation of venous erythrocytes and the absence of damage to the yolk ball. Injection in zebrafish embryos and imaging of biodistribution of each formulation was conducted more than once to obtain n>1. Each time freshly made liposomes were prepared.

Confocal imaging acquisition and editing: Zebrafish embryos were randomly picked from a dish of 20-60 successfully injected embryos. Confocal z-stacks were captured on a Leica TCS SPE or SP8 confocal microscope, using a 10x air objective (HCX PL FLUOTAR), a 40x water-immersion objective (HCX APO L) or 63x water-immersion objective (HC PL APO CS). For whole-embryo views, 3 overlapping z-stacks were captured to cover the complete embryo. Laser intensity, gain and offset settings were identical between stacks and experiments. Images were processed using the Fiji distribution of ImageJ. Confocal image stacks (raw data) are available upon request.

Synthesis and characterization of DAG analogues: Column Chromatography was performed using silica gel (40-63 μm, 60 Å, Screening Devices, The Netherlands). TLC analysis was performed on Merck silica gel 60/Kieselguhr F254, 0.25 mm TLC plates and compounds were visualized using a $KMnO_4$ stain (10 mg/ml $KMnO_4$ and 75 mg/ml K_2CO_3 in H_2O). ^1H spectra were recorded on a Bruker AV 400 MHz spectrometer. Chemical shifts are reported in ppm (δ), relative to the deuterated solvent as internal standard. Data are reported as follows: chemical shifts (δ), multiplets (s = singlet, d = doublet, dd = doublet of doublets, td = triplet of doublets, t = triplet, q = quartet, m = multiplet), coupling constants (J) reported in Hz.

High resolution mass spectra (HRMS) were recorded by direct injection (2 µL of a 1 µM solution in methanol) using a mass spectrometer (Q-Exactive HF Orbitrap) with an electrospray ion source (ESI) run in positive mode (source voltage 3.5 kV, capillary temperature 275 °C, no sheath gas), and with a resolution R = 240000 at m/z = 400 (mass range m/z = 160-2000). Eluents used: MeCN:H_2O (1:1 v/v) supplemented with 0,1% formic acid. For molecules **1** and **16,** high resolution mass spectra were recorded by direct injection (2 µL of a 2 µM solution in methanol) using a mass spectrometer (Synapt G2-Si [Waters]) with an electrospray ion source (ESI-TOF) run in positive mode, with LeuEnk(m/z=556.2771) as "lock mass". Source voltage of 3.5 kV, 275 °C as temperature. Mass range m/z = 160-2000. The high-resolution mass spectrometer was calibrated prior to measurements with a calibration mixture (Thermo Finnigan).

Synthesis of DOaG and DOG lipids: DOaG (**3**) and DOG (**11**) lipids were synthesized as reported in Chapter 2 and reference [13].
All lipids (except lipids **7**, **9**, **10**, **12** and **21**) were isolated as regioisomeric mixtures: 80% isomer where acyl chains substituting the *sn*-1,3 positions of the backbone and 20% isomer where acyl chains substituting the *sn*-1,2 positions of the backbone as determined by ^{1}H NMR.

(1) C14:1; 2-hydroxy-3-((Z)-tetradec-9-enamido)propyl (Z)-tetradec-9-enoate

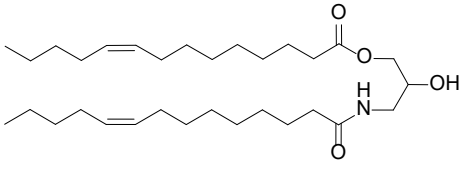

In a round bottom flask, (±)-3-amino-1,2-propane diol (10.59 mg, 0.12 mmoL), DMAP (35.51 mg, 0.29 mmoL), DIPEA (37.49 mg, 0.29 mmoL) and EDC (45.00 mg, 0.29 mmoL) were dissolved in CH_2CL_2 (10 mL). Myristoleic acid (50.00 mg, 0.22 mmoL) was added to the solution and the reaction mixture was allowed to stir overnight. The reaction mixture was washed with sat. NH_4Cl (10 mL), followed by dd. H_2O (3 x 20 mL), brine (20 mL) and subsequently was dried (with Na_2SO_4), filtered and concentrated *in vacuo*. Purification by Column Chromatography (EtOAc: hexane; graduate elution from 0:100 to 20:80) yielded compound **1** as a white solid (26.96 mg, 0.053 mmoL).

^{1}H NMR (400 MHz, $CDCl_3$) δ 6.00 (t, J = 6.0 Hz, 1H), 5.43 – 5.27 (m, 4H), 4.15 (dd, J = 11.5, 5.1 Hz, 1H), 4.05 (dd, J = 11.5, 5.8 Hz, 1H), 3.93 (qd, J = 5.8, 3.4 Hz, 1H), 3.65 – 3.46 (m, 1H), 3.23 (m, 1H), 2.33 (td, J = 7.7, 5.6 Hz, 2H), 2.27 – 2.17 (m, 2H), 2.08 – 1.96 (m, 8H), 1.62 (q, J = 7.1 Hz, 4H), 1.30 (d, J = 4.0 Hz, 24H), 0.94 – 0.81 (t, J = 8 Hz, 6H); **ESI-HRMS** (m/z) [M+H] +: calcd. for $C_{31}H_{57}NO_4$, 507.4360; found 507.4367, delta =1.4 ppm.

(2) C16:1; 3-((Z)-hexadec-9-enamido)-2-hydroxypropyl (Z)-hexadec-9-enoate

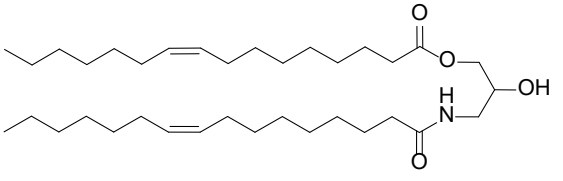

In a round bottom flask, (±)-3-amino-1,2-propane diol (100.0 mg, 1.10 mmoL), DMAP (336.0 mg, 2.75 mmoL), DIPEA (479 µL, 2.75 mmoL) and EDC (427.0 mg, 2.75 mmoL) were dissolved in CH_2Cl_2 (10 mL). Palmitoleic acid (530.5 mg, 2.10 mmoL) was added to the solution and the reaction mixture was allowed to stir overnight. The reaction mixture was washed with sat. NH_4Cl solution (10 mL), followed by dd. H_2O (3 x 10 mL), brine (10 mL) and subsequently was dried (Na_2SO_4), filtered and concentrated *in vacuo*. Purification by Column Chromatography (EtOAc : CH_2CL_2; 10:90 to 20:80) yielded compound **2** as a white solid (247.0 mg, 0.44 mmoL).

^{1}H NMR (400 MHz, $CDCl_3$) δ 6.40 (t, J = 5.8 Hz, 1H), 5.36 – 5.23 (m, 4H), 4.10 – 4.00 (m, 2H), 3.93 – 3.81 (m, 1H), 3.64 – 3.37 (m, 1H), 3.21 (dt, J = 14.1, 6.1 Hz, 1H), 2.34 – 2.24 (m, 2H), 2.17 (dd, J = 9.5, 5.8 Hz, 2H), 1.97 (q, J = 6.3 Hz, 8H), 1.58 (t, J = 7.4 Hz, 4H), 1.25 (d, J = 9.3 Hz, 32H), 0.88 – 0.80 (t, J = 8 hz, 6H). **ESI-HRMS** (m/z) $[M+H]^+$: calcd. for $C_{35}H_{65}NO_4$, 563.4986; found 563.4988, delta =0.4 ppm.

(4) C20:1; 2-hydroxy-3-((Z)-icos-11-enamido)propyl (Z)-icos-11-enoate

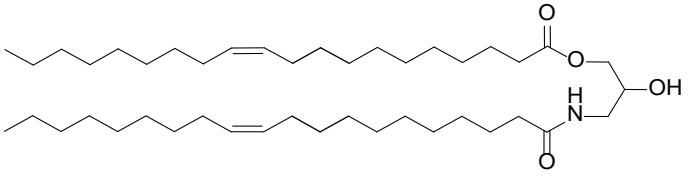

In a round bottom flask, (±)-3-amino-1,2-propane diol (7.70 mg, 0.08 mmoL), DMAP (25.66 mg, 0.21 mmoL), DIPEA (27.14mg, 0.21 mmoL) and EDC (32.60 mg, 0.21 mmoL) were dissolved in CH_2Cl_2 (10 mL). Eicosenoic acid (50 mg, 0.16 mmoL) was added to the solution and the reaction mixture was allowed to stir overnight. The reaction mixture was washed with sat. NH_4Cl solution (10 mL), followed by dd. H_2O (3 x 10 mL), brine (10 mL) and subsequently was dried (Na_2SO_4), filtered and concentrated *in vacuo*. Purification by Column Chromatography (EtOAc : CH_2CL_2; 0:100 to 20:80) yielded compound **4** as a white solid (12.00 mg, 0.02 mmoL).

^{1}H NMR (400 MHz, $CDCl_3$) δ 5.98 (t, J = 5.9 Hz, 1H), 5.39 – 5.28 (m, 4H), 4.16 (dd, J = 11.5, 5.1 Hz, 1H), 4.05 (dd, J = 11.5, 5.9 Hz, 1H), 3.94 (qd, J = 5.9, 3.4 Hz, 1H), 3.65 – 3.46 (m, 1H), 3.24 (dt, J = 14.3, 6.0 Hz, 1H), 2.40 – 2.28 (m, 2H), 2.23 (td, J = 7.6, 4.9 Hz, 2H), 2.01 (q, J = 6.0 Hz, 8H), 1.62 (q, J = 6.5, 4.9 Hz, 4H), 1.26 (d, J = 4.4 Hz, 48H), 0.90 – 0.85 (t, J = 8 hz, 6H). **ESI-HRMS** (m/z) [M+H] +: calcd. for $C_{43}H_{81}NO_4$, 676.6238; found 676.6231, delta =1.0 ppm.

(5) C24:1; 2-hydroxy-3-((Z)-tetracos-15-enamido)propyl (Z)-tetracos-15-enoate

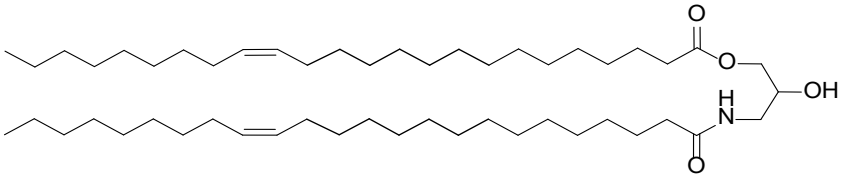

In a round bottom flask containing stirred solution of (±)-3-amino-1,2-propanediol (3.90 mg, 0.04 mmoL) in 10 mL CH_2Cl_2, nervonic acid (31.40 mg, 0.09 mmoL), DMAP (19.80 mg, 0.16 mmoL), DIPEA (13.30 mg, 0.10 mmoL) and EDC (21.84 mg, 0.14 mmoL) were added. To this solution 2 mL THF were added. The reaction mixture was allowed to stir overnight at room temperature and subsequently the mixture was washed with sat. NH_4Cl solution (10 mL), followed by dd. H_2O (3 x 10 mL), brine (10 mL). Next, the mixtrure was dried (Na_2SO_4),

filtered and concentrated *in vacuo*. Purification by Column Chromatography (CH_2Cl_2 to 20% EtOAc in CH_2Cl_2), yielded the target compound **5** (17.30 mg, 0.02 mmoL).

TLC (CH_2Cl_2:EtOAc, 8:2 v/v) : Rf = 0.26 ; **^{1}H NMR** (400 MHz, $CDCl_3$) δ 5.95 (t, J = 10.2 Hz 1H), 5.41 – 5.28 (m, 4H), 4.16 (dd, J = 11.5, 5.2 Hz, 1H), 4.05 (dd, J = 11.5, 5.9 Hz, 1H), 3.93 (dt, J = 9.1, 5.7 Hz, 1H), 3.66 – 3.48 (m, 1H), 3.27 – 3.19 (m, 1H), 2.34 (dq, J = 7.8, 5.7, 5.0 Hz, 2H), 2.22 (td, J = 7.7, 5.7 Hz, 2H), 2.01 (q, J = 6.5 Hz, 8H), 1.62 (d, J = 7.4 Hz, 4H), 1.26 (d, J = 4.0 Hz, 64H), 0.93 – 0.84 (t, J = 8 Hz, 6H). **ESI-HRMS** (m/z) [M+H]+: calcd. for $C_{51}H_{97}NO_4$, 788.7490; found 788.7485, delta = 0.7 ppm.

(6) C18:0; 2-hydroxy-3-stearamidopropyl stearate

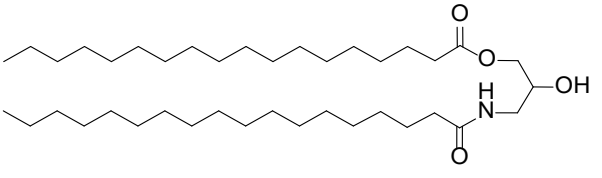

In a round bottom flask containing stirred solution of (±)-3-Amino-1,2-propanediol (100.0 mg, 1.10 mmoL) in THF (~15 mL), stearic acid (594.5 mg, 2.10 mmoL), EDCI (426.9 mg, 2.75 mmoL), DMAP (336.0 mg, 2.75 mmoL) and DIPEA (355.0 mg, 2.75 mmoL) were added. After overnight stirring at RT and subsequent evaporation of THF, the reaction mixture was diluted with $CHCl_3$, washed with sat. NH_4Cl (~15 mL) and brine (~15 mL) and subsequently was dried (Na_2SO_4), filtered *in vacuo* and concentrated. Purification by Column Chromatography (CH_2Cl_2 to 20% EtOAC in CH_2Cl_2) yielded the target material **6**.

R_f: 0.4 (CH_2Cl_2: EtOAc_8:2), **^{1}H NMR** (400 MHz, $CDCl_3$) δ 5.94 (t, J = 8 Hz 1H), 4.16 (dd, J = 11.5, 5.2 Hz, 1H), 4.05 (dd, J = 11.5, 5.8 Hz, 1H), 3.93 (qd, J = 5.7, 3.3 Hz, 1H), 3.56 (m, 1H), 3.23 (dt, J = 14.3, 5.9 Hz, 1H), 2.34 (t, J = 7.6 Hz, 2H), 2.26 – 2.18 (m, 2H), 1.62 (s, 4H), 1.25 (s, 56H), 0.91 – 0.84 (t, J = 8 Hz, 6H).

(8) C18:2; 2-hydroxy-3-((9Z,12Z)-octadeca-9,12-dienamido)propyl (9Z,12Z)-octadeca-9,12-dienoate

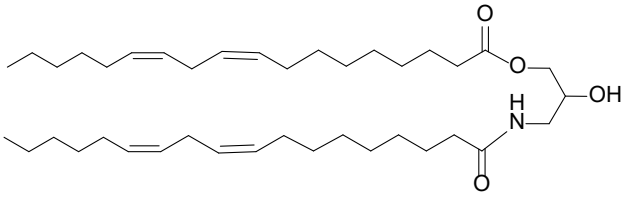

In a round bottom flask containing stirred solution of (+-)-3-amino-1,2-propanediol (54.50 mg, 0.60 mmoL) in 50 mL CH_2Cl_2, linoleic acid (336.5 mg, 1.20 mmoL), DMAP (205.1 mg, 1.68 mmoL), DIPEA (191.3 mg, 1.48 mmoL) and EDC (280.2 mg, 1.80 mmoL) were added. Next, 10 mL THF was added to the solution so that the solvent mixture was in a CH_2Cl_2:THF (5:1) ratio. The reaction mixture was stirred overnight at RT, then it was washed with saturated NH_4Cl solution and brine, and the organic phase was dried with Na_2SO_4, filtered *in vacuo*, and concentrated under reduced pressure. Purification by Column Chromatography (CH_2Cl_2 to 40% EtOAc in CH_2Cl_2) yielded the target compound **8** as a white solid (29.40 mg, 0.05 mmoL).

TLC (CH_2Cl_2:EtOAc, 8:2 v/v) : Rf = 0.45 ; **^{1}H NMR** (400 MHz, $CDCl_3$) δ 6.09 (t, J = 6 Hz, 1H), 5.43 – 5.25 (m, 8H), 4.13 (dd, J = 11.5, 5.1 Hz, 1H), 4.05 (dd, J = 11.5, 5.7 Hz, 1H), 3.92 (qd, J = 5.7, 3.3 Hz, 1H), 3.65 – 3.46 (m, 1H), 3.23 (dt, J = 14.2, 5.9 Hz, 1H), 2.76 (t, J = 6.6 Hz, 4H), 2.37 – 2.27 (m, 2H), 2.21 (td, J = 7.6, 4.8 Hz, 2H), 2.04 (q, J = 6.9 Hz, 8H), 1.61 (dq, J = 11.2, 7.1, 6.3 Hz, 4H), 1.38 – 1.22 (m, 28H), 0.90 – 0.85 (t, J = 8 Hz, 6H) ; **ESI-HRMS** (m/z) [M+H]+: calcd. for $C_{39}H_{69}NO_4$, 616.5299; found 616.5299, delta = 0.1 ppm.

(9) monoacyl; N-(2,3-dihydroxypropyl)oleamide

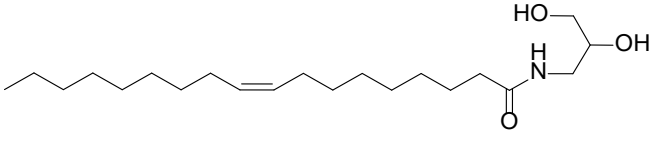

In a round bottom flask containing stirred solution of (±)-3-Amino-1,2-propanediol (200.0 mg, 2.20 mmoL) in CH_2Cl_2:THF (5:1) (50 mL), oleic acid (496.0 mg, 1.76 mmoL), EDC (402.0 mg, 2.60 mmoL), DMAP (268.0 mg, 2.20 mmoL) and DIPEA (284.0 mg, 2.20 mmoL) were added. After overnight stirring at RT and subsequent evaporation of CH_2Cl_2 and THF, the reaction mixture was diluted with $CHCl_3$, washed with sat. NH_4Cl (~25 mL) and brine (~25 mL) and subsequently was dried (Na_2SO_4), filtered in vacuo and concentrated, so the

crude compound was obtained. Purification by Column Chromatography (CH_2Cl_2 to 50% EtOAc in CH_2Cl_2) yielded the target material **9** as a white solid (469.3 mg, 1.32 mmoL).

^{1}H NMR (400 MHz, $CDCl_3$) δ 6.22 (t, J = 6.1 Hz, 1H), 5.42 – 5.26 (m, 2H), 3.75 (t, J = 4.9 Hz, 1H), 3.64 – 3.49 (m, 4H), 3.39 (m, 2H), 2.25 – 2.17 (m, 2H), 2.00 (q, J = 6.4 Hz, 4H), 1.61 (t, J = 7.4 Hz, 2H), 1.27 (d, J = 12.0 Hz, 20H), 0.94 – 0.83 (t, J = 8.0 Hz, 3H). **ESI-HRMS** (m/z) [M+H]+: calcd. for $C_{21}H_{41}NO_3$, 355.3159; found 355.3158, delta = 0.3 ppm.

(10) triacyl; 3-oleamidopropane-1,2-diyl dioleate

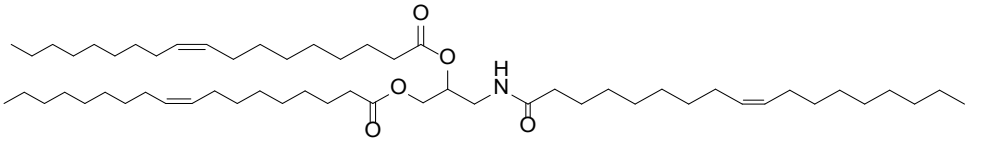

In a round bottom flask containing stirred solution of (±)-3-Amino-1,2-propanediol (92.00 mg, 1.01 mmoL) in CH_2Cl_2 (25 mL), oleic acid (1.0 g, 3.54 mmoL), HCTU (2.0 g, 5.26 mmoL) and DIPEA (1.3 g, 10.23 mmoL) were added. After overnight stirring at RT, the reaction mixture was diluted with CH_2CL_2, washed with sat. NH_4Cl (~30 mL) and brine (~30 mL) and subsequently was dried (Na_2SO_4), filtered *in vacuo* and concentrated. Purification by Column Chromatography (CH_2Cl_2 to 2% EtOAC in CH_2Cl_2) yielded the target material **10** as a white solid (193.0 mg, 0.22 mmoL).

TLC (CH_2Cl_2: EtOAc_8:2) : R_f = 0.9, **^{1}H-NMR** ($CDCl_3$, 400MHz) δ 5.73 (t, J = 5.8 Hz, 1H), 5.39 – 5.27 (m, 6H), 5.09 (m, 1H), 4.25 (dd, J = 12.0, 4.1 Hz, 1H), 4.13 (dd, J = 12.0, 5.7 Hz, 1H), 3.48 (m, 2H), 2.31 (td, J = 7.6, 2.2 Hz, 4H), 2.16 (t, J = 7.6 Hz, 2H), 2.00 (q, J = 6.3 Hz, 12H), 1.60 (s, 6H), 1.28 (d, J = 10.4 Hz, 62H), 0.88 (t, J = 6.8 Hz, 9H); **ESI-HRMS** (m/z) [M+H]+: calcd. for $C_{57}H_{105}NO_5$, 884.8066; found 884.8062, delta = 0.5 ppm.

(12)N-N,(9Z,9'Z)-1,1'-((2-hydroxypropane-1,3-diyl)bis(l2-azanediyl)) bis(octadec-9-en-1-one)

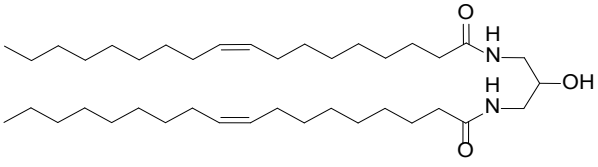

In a round bottom flask containing a stirred solution of 1,3-diamino-2-propanol (102.4 mg, 1.12 mmoL) and oleic acid (595.2 mg, 2.11 mmoL), DMAP (356.9 mg, 2.92 mmoL), EDC (437.1 mg, 2.82 mmoL) and DIPEA (356.7 mg, 2.76 mmoL) were added. The mixture was diluted with 10 mL of CH_2Cl_2 and 3 mL of THF. After stirring overnight at RT, the reaction mixture was diluted with CH_2Cl_2 before washing with saturated NH_4Cl (2x ~15 mL), and brine (~15 mL). Subsequently, the mixture was dried with Na_2SO_4 and filtered *in vacuo* and concentrated. Purification by Column Chromatography (CH_2Cl_2 to 50% EtOAc in CH_2Cl_2), yielded the target material **12** as a white solid (274.5 mg, 0.44 mmoL).

^{1}H NMR (400 MHz, $CDCl_3$) δ 6.79 (t, J = 6.3 Hz, 2H), 5.38 – 5.30 (m, 4H), 3.74 (m, 1H), 3.38 (m, 2H), 3.21 (dt, J = 14.0, 5.5 Hz, 2H), 2.24 – 2.15 (m, 4H), 1.99 (q, J = 6.6 Hz, 8H), 1.60 (m, 4H), 1.26 (d, J = 13.1 Hz, 40H), 0.90 – 0.82 (t, J = 8 Hz, 6H).
ESI-HRMS (m/z) $[M+H]^+$: calcd. for $C_{39}H_{69}NO_4$, 619.5772; found 619.5771, delta = 0.2 ppm.

Synthetic route for lipids 7 and 21. Each *sn*-position of the amino-propanediol was first coupled to a protecting group (PG) in 3 synthetic steps, leading to a full protected amino-propanediol with PG1, PG2 and PG3 protecting the -NH_2 of *sn*-1 position, -OH of the *sn*-3 position and the -OH of the *sn*-2 position, respectively (**Figure S15**). All protecting groups were orthogonal with each other. Synthesis steps: 1) Deprotection of the NH group, 2) subsequent coupling with fatty acid (oleic acid) in *sn*-1 position, 3) deprotection of OH group in *sn*-3 position, 4) subsequent coupling with fatty acid (stearic acid for **7** or oleic acid for **21**) in *sn*-3 position, 5) deprotection of OH group in *sn*-2 position.

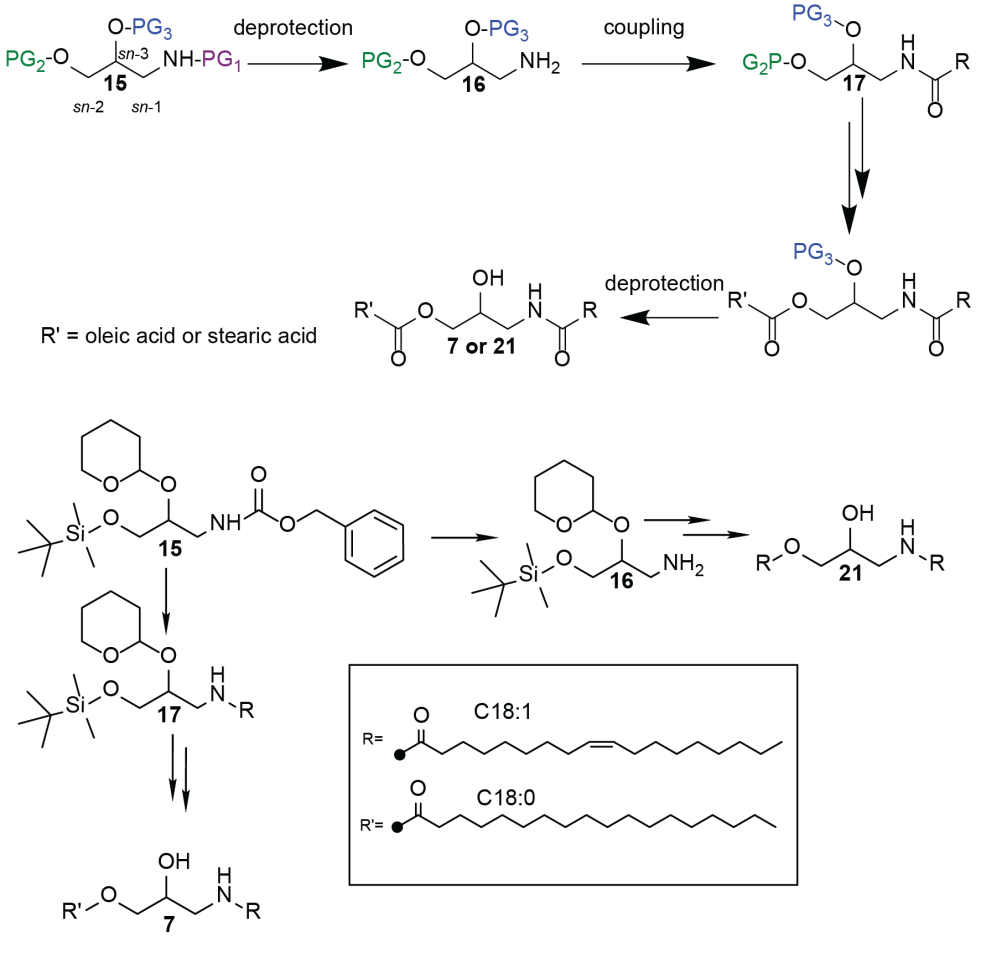

Figure S15. Schematic of synthetic route for lipids 7 and 21.

(13) Benzyl (2,3-dihydroxypropyl) carbamate

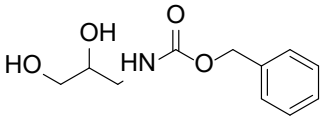

In a round bottom flask, 3-amino-1,2-propane diol (1.5 g, 16.6 mmol) was dissolved in THF (50 mL). Water (25 mL) and potassium carbonate (6.9 g; 49.7 mmol) were added to the solution and the reaction mixture was cooled down to 0 °C. Benzyl chloroformate (3.8 g, 16.5 mmol) was added dropwise over 2 hours and afterwards was allowed to warm to room temperature and left stirring overnight. The reaction mixture was extracted with EtOAc (3 x 25 mL), the combined organic layers were washed with brine (20 mL) and subsequently was dried (Na_2SO_4), filtered and concentrated *in vacuo*. Purification by Column Chromatography (MeOH: CH_2Cl_2; graduate elution from 0:100 to 6:94 in steps of 2%) yielded the title compound **13** as a white solid (3.47 g, 15.4 mmol).

^{1}H NMR (400 MHz, MeOD) δ 7.37 – 7.23 (m, 5H), 5.06 (s, 2H), 3.66 (dq, J = 7.1, 5.1 Hz, 1H), 3.47 (tt, J = 11.4, 6.3 Hz, 2H), 3.29 – 3.21 (m, 1H), 3.12 (dd, J = 13.8, 6.8 Hz, 1H).

(14) Benzyl (3-((tert-butyldimethylsilyl)oxy)-2-hydroxypropyl)carbamate

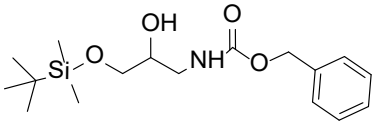

In a 500 mL round bottom flask compound **13** (3.1 g; 13.9 mmol) was dissolved in CH_2Cl_2 (30 mL). Imidazole (2.4 g, 34.7 mmol) was added to the solution and the reaction mixture was cooled down to 0 °C. TBDMS-Cl (3.1 g, 20.8 mmol) was added and the reaction mixture was allowed to stir for 2 hours while maintaining 0 °C. The reaction mixture was quenched with sat. $NaHCO_3$ solution (25 mL) and washed with dd. H_2O (3 x 10 mL) and subsequently was dried (Na_2SO_4), filtered and concentrated *in vacuo*. Purification by Column Chromatography (EtOAc: petroleum ether; 10:90 to 25:75) yielded the title compound **14** as a colorless oil (3.83 g, 11.0 mmol).

^{1}H NMR (400 MHz, MeOD) δ 7.39 – 7.24 (m, 5H), 6.85 (d, J = 5.9 Hz, 1H), 5.07 (s, 2H), 3.70 (dt, J = 10.6, 5.1 Hz, 1H), 3.65 – 3.54 (m, 2H), 3.40 – 3.29 (m, 1H), 3.20 – 3.08 (m, 1H), 0.92 (s, 9H), 0.08 (s, 6H).

(15) Benzyl (3-((tert-butyldimethylsilyl)oxy)-2-((tetrahydro-2H-pyran-2-yl)oxy)propyl) carbamate

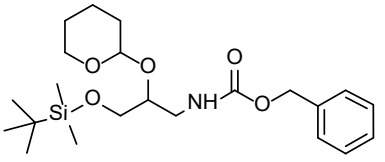

In a round bottom flask, compound **14** (2.9 g, 8.65 mmoL) was dissolved in CH_2Cl_2 alongside pyridinium p-toluenesulfonate (0.22 g, 0.884 mmoL). 3,4-dihydro-pyran (2.2 g, 25.95 mmoL) was added and the reaction was allowed to stir for 3 hours. The reaction mixture was washed with sat. $NaHCO_3$ solution (25 mL), followed by H_2O (2 x 25 mL) and brine (25 mL) and subsequently was dried (Na_2SO_4), filtered and concentrated *in vacuo*. Purification by Column Chromatography (EtOAc: hexane; graduate elution from 1:99 to 10:90 in steps of 1%, followed by a flush of 50:50) yielded the title compound **15** as a colorless oil (3.14 g, 7.40 mmoL).

^{1}H NMR (400 MHz, $CDCl_3$) δ 7.42 – 6.99 (m, 5H), 5.80 – 5.45 (m, 1H), 5.03 (s, 2H), 4.71 – 4.52 (m, 1H), 3.84 (dt, J = 10.5, 4.7 Hz, 1H), 3.73 (dq, J = 16.1, 5.3, 4.9 Hz, 1H), 3.57 (dd, J = 12.9, 4.5 Hz, 1H), 3.50 – 3.33 (m, 2H), 3.29 – 3.08 (m, 1H), 1.83 – 1.56 (m, 2H), 1.51 – 1.36 (m, 4H), 0.86 (s, 9H), 0.02 (d, J = 6.1 Hz, 6H).

(16)3-((tert-butyldimethylsilyl)oxy)-2-((tetrahydro-2H-pyran-2-yl)oxy)propan-1-amine

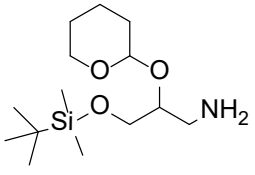

Compound **15** (1.9 g, 4.50 mmoL) was dried in a round bottom flask before use in a vacuum oven (25 °C) for at least 2 hours. Palladium on carbon (191.0 mg) was added and the round bottom flask was flushed with nitrogen gas for 10 minutes. Dry MeOH was added, and to the stirred solution with addition of a nitrogen balloon, triethylsilane (7.9 g, 67.6 mmoL) was added dropwise. The reaction mixture was allowed to stir for 4 hours and then was filtered over Celite, cleansed with MeOH and concentrated *in vacuo*. Excess of triethylsilane was removed under airflow for 30 min. Purification by Column Chromatography (CH_2Cl_2 + 0,5 % isopropylamine with graduate elution to 2.5 % EtOH in CH_2Cl_2 + 0.5 % isopropylamine in steps of 0.5% EtOH) yielded the title compound **16** as a colorless oil (1.16 g, 4.00 mmoL).

^{1}H NMR (400 MHz, $CDCl_3$) δ 4.61 (td, J = 5.7, 5.1, 2.7 Hz, 1H), 3.83 (m, 1H), 3.77 – 3.70 (m, 1H), 3.63 – 3.45 (m, 2H), 3.44 – 3.34 (m, 1H), 2.80 (m, 1H), 2.65 (m, 1H), 1.80 – 1.57 (m, 2H), 1.53 – 1.36 (m, 4H), 1.28 (s, 2H), 0.79 (s, 9H), -0.05 (d, J = 3.2 Hz, 6H). **ESI-HRMS** (m/z) [M+H]+: calcd. for $C_{14}H_{31}NO_3Si$, 289.2146; found 289.2154, delta=2.8 ppm.

(17)N-(3-((tert-butyldimethylsilyl)oxy)-2-((tetrahydro-2H-pyran-2-yl)oxy)propyl) oleamide

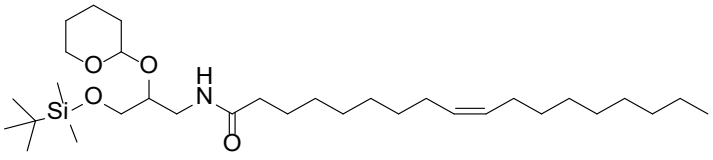

In a round bottom flask, compound **16** (915.3 mg, 3.16 mmoL), DMAP (1.0 g, 8.2 mmoL), DIPEA (1.1 g, 8.2 mmoL) and EDC (1.3 g, 8.2 mmoL) were dissolved in CH_2Cl_2 (20 mL). Oleic acid (1.3 g, 4.74 mmoL) was added to the solution and the reaction mixture was allowed to stir at RT overnight. The reaction mixture was washed with sat. NH_4Cl solution (20 mL), followed by H_2O (3 x 20 mL), brine (20 mL) and subsequently was dried (Na_2SO_4), filtered and concentrated *in vacuo*. Purification by Column Chromatography (EtOAc: hexane; graduate elution from 0:100 to 20:80 in steps of 10%) yielded the title compound **17** as a colorless oil (1.30 g, 2.35 mmoL).

^{1}H NMR (400 MHz, $CDCl_3$) δ 6.67 – 6.01 (m, 1H), 5.38 – 5.25 (m, 2H), 4.62 (m, 1H), 4.00 – 3.83 (m, 1H), 3.83 – 3.67 (m, 2H), 3.64 (dd, J = 9.6, 6.0 Hz, 1H), 3.61 – 3.53 (m, 2H), 3.48 (m, 1H), 3.40 – 2.96 (m, 1H), 2.14 (td, J = 8.3, 6.9 Hz, 2H), 2.05 – 1.94 (m, 4H), 1.88 – 1.67 (m, 2H), 1.64 – 1.55 (m, 2H), 1.54 – 1.46 (m, 4H), 1.26 (d, J = 13.0 Hz, 20H), 0.88 (s, 9H), 0.87 – 0.82 (t, J = 4 Hz, 3H), 0.04 (dd, J = 9.8, 1.4 Hz, 6H).

(18) N-(3-hydroxy-2-((tetrahydro-2H-pyran-2-yl)oxy)propyl)oleamide

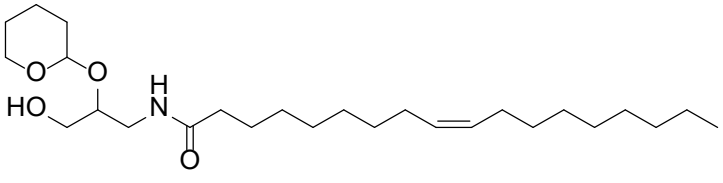

In a round bottom flask, compound **17** (1.2 g; 2.09 mmoL) was dissolved in THF (30 mL) and the reaction mixture was cooled down to 0 °C. TBAF·3 H_2O (2.0 g, 6.27 mmoL) was dissolved in a small amount of THF and was added dropwise. The mixture was allowed to stir for 1 hour. Afterwards the reaction mixture was diluted with H_2O (30 mL) extracted with EtOAc (3 x30 mL) and subsequently was dried (Na_2SO_4), filtered and concentrated *in vacuo*. Purification by Column Chromatography (EtOAc: hexane; elution from 0:100 to 50:50 in steps of 10%) yielded the title compound **18** as a colorless oil (0.78 g, 1.77 mmoL).

^{1}H NMR (400 MHz, $CDCl_3$) δ 6.09 (dt, J = 196.7, 6.1 Hz, 1H), 5.40 – 5.26 (m, 2H), 4.56 (dq, J = 6.2, 2.8 Hz, 1H), 3.95 (dq, J = 13.0, 3.6, 2.9 Hz, 1H), 3.76 (dp, J = 11.0, 5.4 Hz, 1H), 3.58 – 3.33 (m, 5H), 2.19 (q, J = 7.1 Hz, 2H), 1.99 (q, J = 6.4 Hz, 4H), 1.90 – 1.71 (m, 2H), 1.61 (t, J = 7.2 Hz, 2H), 1.58 – 1.46 (m, 4H), 1.27 (d, J = 14.6 Hz, 20H), 0.87 (t, J = 6.7 Hz, 3H).

(19) 3-oleamido-2-((tetrahydro-2H-pyran-2-yl)oxy)propyl stearate

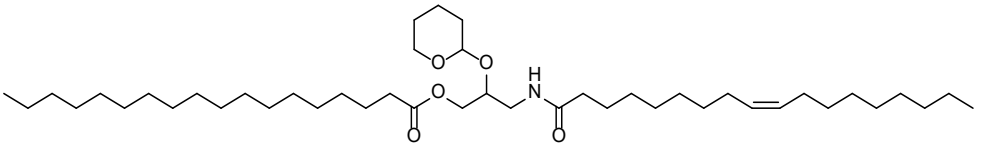

In a round bottom flask, compound **18** (322.7 mg, 0.73 mmoL), DMAP (224.2 mg, 1.83 mmoL), DIPEA (236.5 mg, 1.83 mmoL) and EDC (284.1 mg, 1.83 mmoL) were dissolved in CH_2Cl_2 (10 mL). Stearic acid (31.93 mg, 0.11 mmoL) was added to the solution and the reaction mixture was allowed to stir overnight at RT. The reaction mixture was washed with sat. NH_4Cl solution (10 mL), followed by H_2O (3 x 10 mL), brine (20 mL) and subsequently was dried (Na_2SO_4), filtered and concentrated *in vacuo*. Purification by Column Chromatography (Acetone : CH_2Cl_2, 5:95) yielded the title compound **19** as a white solid (247.2 mg, 0.35 mmoL).

^{1}H NMR (400 MHz, $CDCl_3$) δ 5.38 – 5.27 (m, 2H), 4.74 – 4.47 (m, 1H), 4.28 – 4.05 (m, 2H), 3.99 – 3.83 (m, 2H), 3.65 – 3.42 (m, 3H), 3.35 – 3.08 (m, 1H), 2.31 (q, J = 7.9 Hz, 3H), 2.21 – 2.12 (m, 2H), 1.99 (q, J = 6.8 Hz, 4H), 1.88 – 1.67 (m, 2H), 1.60 (td, J = 7.3, 3.9 Hz, 4H), 1.56 – 1.46 (m, 3H), 1.27 (d, J = 19.3 Hz, 34H), 0.90 – 0.84 (t, J = 8 Hz, 6H).

(7) C18:0-C18:1; 2-hydroxy-3-oleamidopropyl stearate

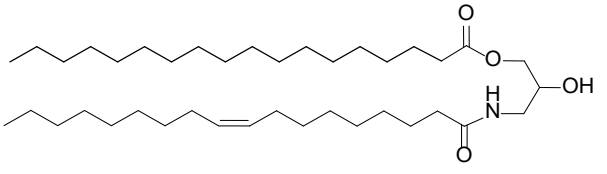

In a round bottom flask, compound **19** (223.0 mg, 0.32 mmoL) and pyridinium p-toluene sulfonate (8.04 mg, 0.032 mmoL) were dissolved in MeOH (5 mL) and the reaction mixture was allowed to stir overnight at 50 °C. The reaction mixture was quenched with sat. NaHCO3 solution (10 mL) and was extracted with EtOAc (3 x 10 mL) and subsequently was dried (Na_2SO_4), filtered and concentrated *in vacuo*. Purification by Column

Chromatography (EtOAc:CH_2Cl_2, graduate elution from 0:100 to 30:70) yielded the final compound **7** as a white solid (168.0 mg, 0.27 mmoL).

^{1}H NMR (400 MHz, $CDCl_3$) δ 6.00 (t, J = 5.9 Hz, 1H), 5.39 – 5.28 (m, 2H), 4.14 (dd, J = 11.5, 5.2 Hz, 1H), 4.05 (dd, J = 11.5, 5.8 Hz, 1H), 3.93 (qd, J = 5.7, 3.3 Hz, 1H), 3.53 (m, 1H), 3.23 (dt, J = 14.3, 6.0 Hz, 1H), 2.33 (t, J = 7.6 Hz, 2H), 2.26 – 2.17 (m, 2H), 2.00 (q, J = 6.5 Hz, 4H), 1.62 (m, 4H), 1.27 (d, J = 19.7 Hz, 48H), 0.91 – 0.83 (m, 6H); **ESI-HRMS** (m/z) [M+H]+: calcd. for $C_{39}H_{75}NO_4$, 622.5769; found 622.5767, delta = 0.5 ppm.

(20) 3-oleamido-2-((tetrahydro-2H-pyran-2-yl)oxy)propyl oleate

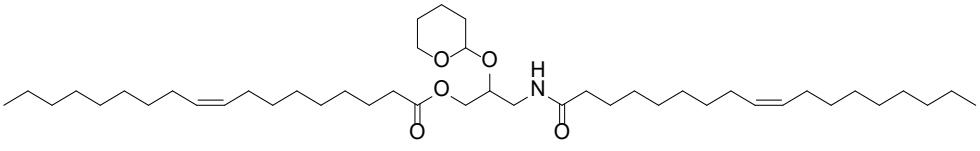

In a round bottom flask, compound **18** (295.1 mg, 0.67 mmoL), DMAP (205.0 mg, 1.68 mmoL), DIPEA (217.1 mg, 1.68 mmoL) and EDC (260.8 mg, 1.68 mmoL) were dissolved in CH_2Cl_2 (10 mL). Oleic acid (282.5 mg, 1.0 mmoL) was added to the solution and the reaction mixture was allowed to stir overnight at RT. The reaction mixture was washed with sat. NH_4Cl solution (10 mL), followed by H_2O (3 x 10 mL), brine (20 mL) and subsequently was dried (Na_2SO_4), filtered and concentrated *in vacuo*. Purification by Column Chromatography (Acetone: CH_2Cl_2, 5:95) yielded the title compound **20** as a colorless oil (308.5 mg, 0.44 mmoL).

^{1}H NMR (400 MHz, $CDCl_3$) δ 6.61 – 6.09 (m, 1H), 5.31 – 5.18 (m, 4H), 4.70 – 4.45 (m, 1H), 4.10 (m, 1H), 4.01 (dd, J = 5.5, 2.5 Hz, 1H), 3.91 – 3.76 (m, 2H), 3.54 – 3.32 (m, 2H), 3.28 – 2.95 (m, 1H), 2.23 (q, J = 7.2 Hz, 2H), 2.09 (q, J = 7.4 Hz, 2H), 1.92 (q, J = 6.4 Hz, 8H), 1.79 – 1.59 (m, 2H), 1.59 – 1.38 (m, 4H), 1.45 (dq, J = 8.6, 5.5, 5.1 Hz, 4H), 1.20 (d, J = 13.5 Hz, 40H), 0.83 – 0.75 (t, J = 8 Hz, 6H).

(21) *sn*-1,3; 2-hydroxy-3-oleamidopropyl oleate

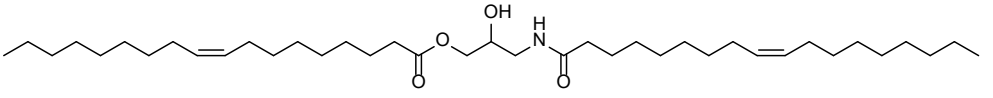

In a round bottom flask, compound **20** (269.3 mg, 0.38 mmoL) and pyridinium p-toluene sulfonate (9.50 mg, 0.038 mmoL) were dissolved in MeOH (5 mL) and the reaction mixture was allowed to stir overnight at 50 °C. The reaction mixture was quenched with sat. NaHCO3 solution (10 mL) and was extracted with EtOAc (3 x 10 mL) and subsequently was dried (Na_2SO_4), filtered and concentrated *in vacuo*. Purification by Column Chromatography (EtOAc:CH_2Cl_2, graduate elution from 0:100 to 30:70) yielded the final compound **21** as a white solid (200.2 mg, 0.32 mmoL).

^{1}H NMR (400 MHz, $CDCl_3$) δ 5.98 (t, J = 6.0 Hz, 1H), 5.40 – 5.27 (m, 4H), 4.15 (dd, J = 11.4, 5.1 Hz, 1H), 4.05 (dd, J = 11.5, 5.8 Hz, 1H), 3.93 (qd, J = 5.8, 3.3 Hz, 1H), 3.53 (m, 1H), 3.23 (dt, J = 14.2, 6.0 Hz, 1H), 2.33 (t, J = 7.6 Hz, 2H), 2.24 – 2.18 (m, 2H), 2.00 (q, J = 6.5 Hz, 8H), 1.62 (m, 1H), 1.28 (d, J = 14.3 Hz, 40H), 0.91 – 0.83 (t, J = 8 Hz, 6H); **ESI-HRMS** (m/z) [M+H]+: calcd. for $C_{39}H_{73}NO_4$, 619.5612; found 619.5610, delta = 0.3 ppm.

4.5 Supporting Figures and ^{1}H-NMR spectra

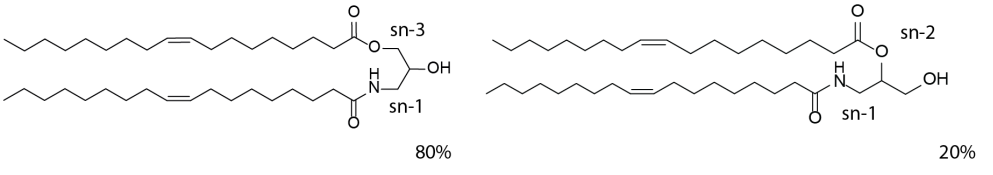

Figure S1. Positional isomers found as a mixture in DOaG lipid. Fatty acid tails substituting the *sn*-1,3 position (80%, majority) and *sn*-1,2 (20%). All lipids are also a racemic mixture.

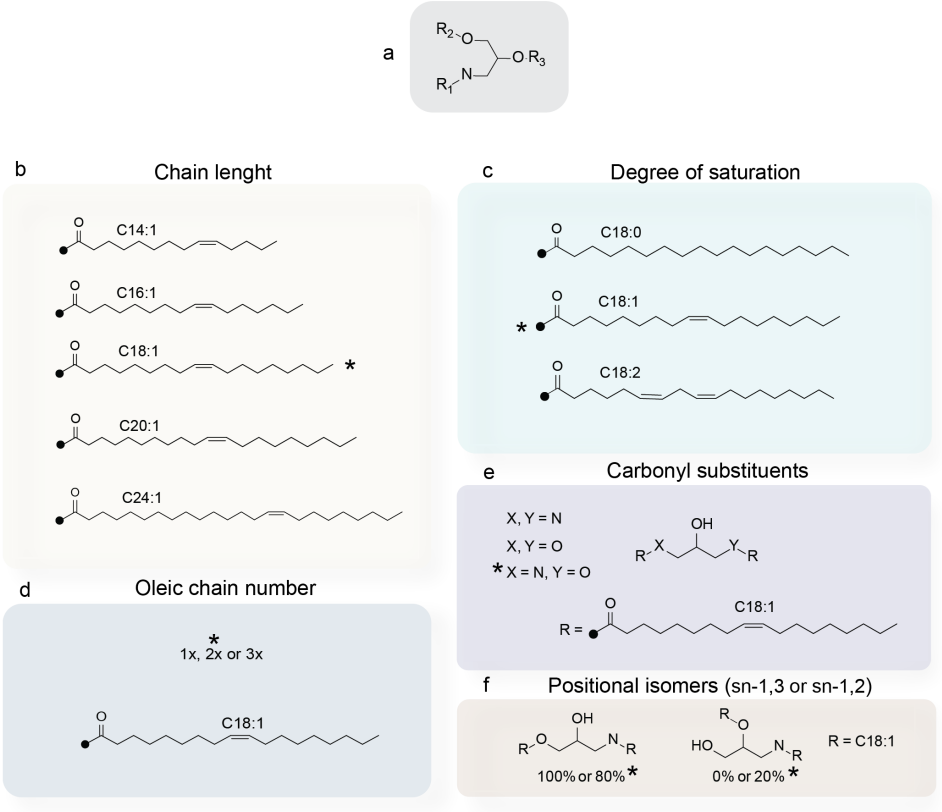

g

No.	Code	R_1	R_2	R_3	No.	Code	R_1	R_2	R_3
1	**C14:1**	C14:1	C14:1	H	8	**C18:2**	C18:2	C18:2	H
2	**C16:1**	C16:1	C16:1	H					
*3	**C18:1**	C18:1	C18:1	H	9	**Monoacyl**	C18:1	H	H
4	**C20:1**	C20:1	C20:1	H	10	**Triacyl**	C18:1	C18:1	C18:1
5	**C24:1**	C24:1	C24:1	H	11	**N-N**	C18:1	C18:1	H
6	**C18:0**	C18:0	C18:0	H	12	**DOG**	C18:1	C18:1	H
7	**C18:0-C18:1**	C18:0	C18:1	H	13	***sn*-1,3**	C18:1	H	C18:1

Figure S2. Library of DOaG analogues. a) Glycerol-like DOaG backbone. DOaG analogues varying **b)** chain length, **c)** degree of saturation, **d)** number of fatty acid tails, **e)** carbonyl substituents of the backbone, **f)** positional isomers. **g)** table depicting the number and code of each lipid and the substitution of each *sn* position of the DOaG backbone. DOaG (as a reference) is indicated with *.

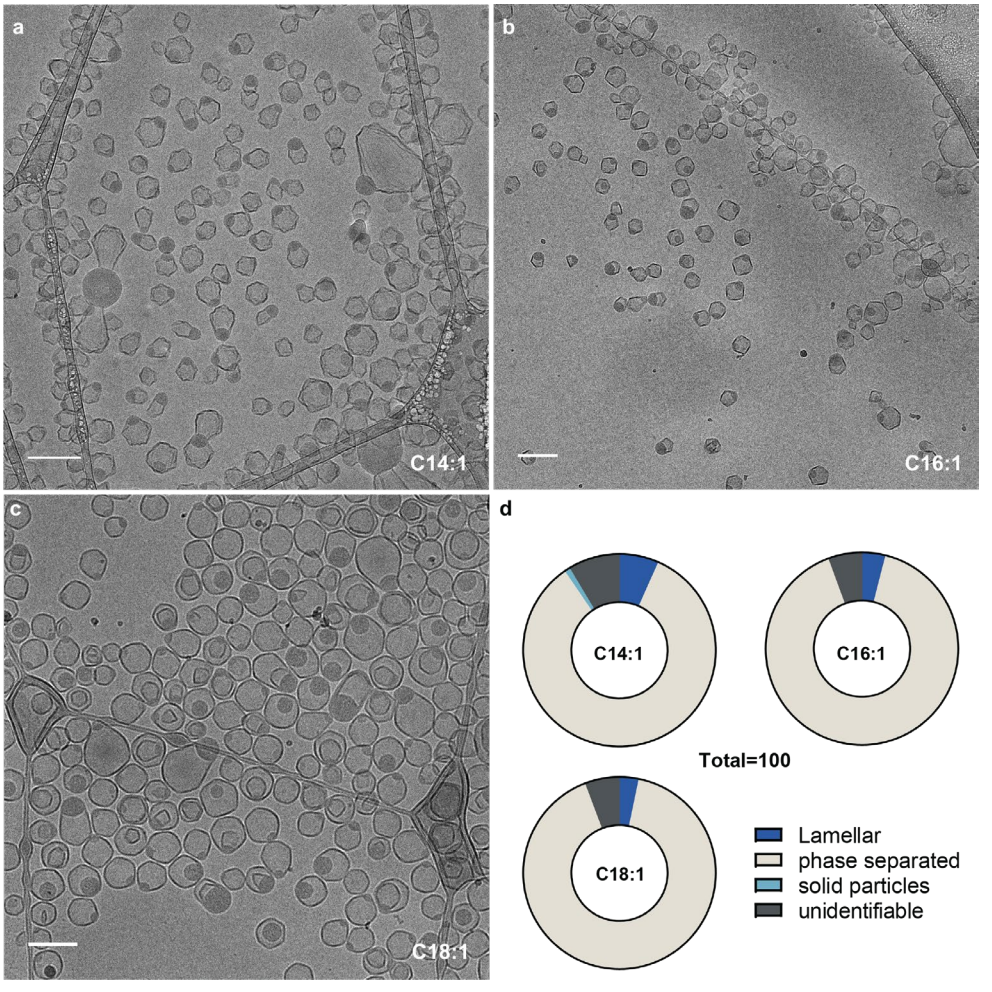

Figure S3. Cryo-TEM images of liposomes containing 1:1 molar ratio of DSPC and a) C14:1, **b)** C16:1, **c)** 18:1 (DOaG). **d)** Quantification of all populations in liposomal formulations containing 1:1 molar ratio of DSPC and C14:1, C16:1 or 18:1 (DOaG). Quantification based on cryo-TEM images a-c (N=100). Scale bars: 200 nm.

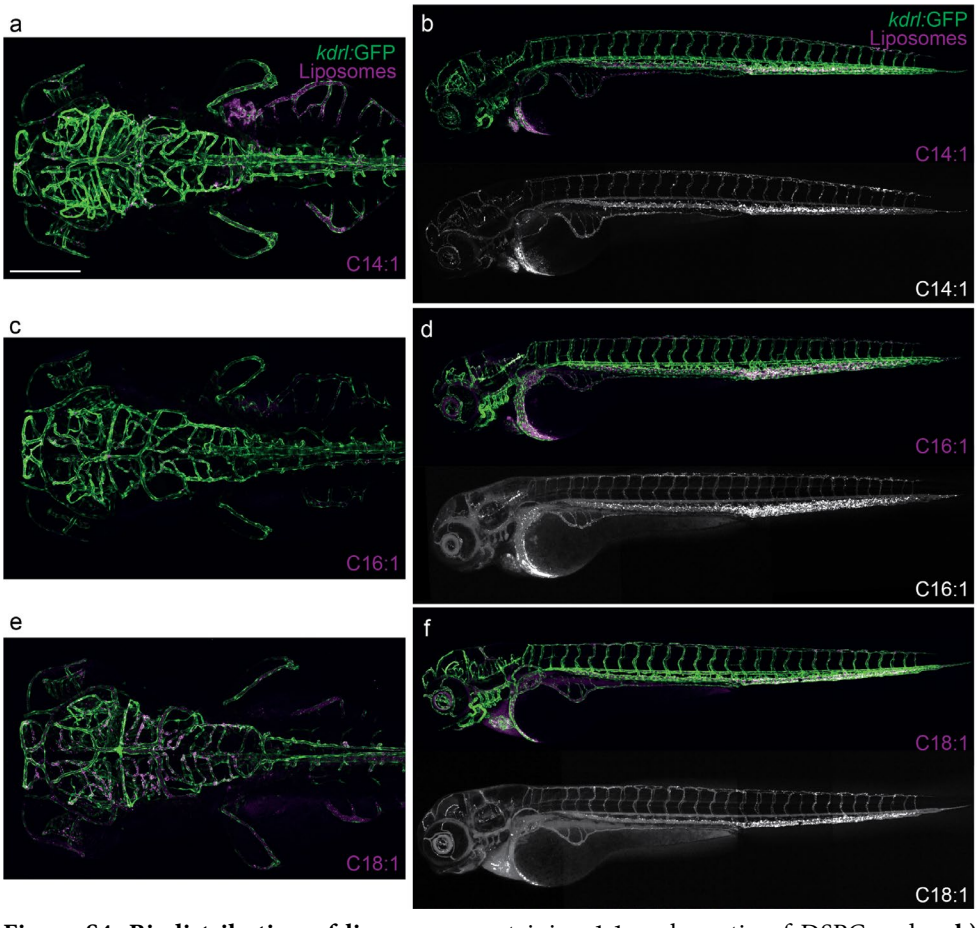

Figure S4. Biodistribution of liposomes containing 1:1 molar ratio of DSPC and **a, b)** C14:1, **c, d)** C16:1 and **e, f)** C18:1 (PAP3 liposomes) in Tg(kdrl:GPF) zebrafish embryos, expressing GFP in all endothelial cells, in dorsal (10x magnification) and lateral view, 1.5 hours post injection (hpi), at 78 days post fertilization (dpf). Liposomes in grey/magenta at 5mM total lipid concentration containing 0.2% DOPE-LR (1,2-dioleoyl-sn-glycero-3-phosphoethanolamine-N-[lissamine rhodamine B sulfonyl]) for visualization. Vasculature in green. Scale bar for a, c, e: 200 µm.

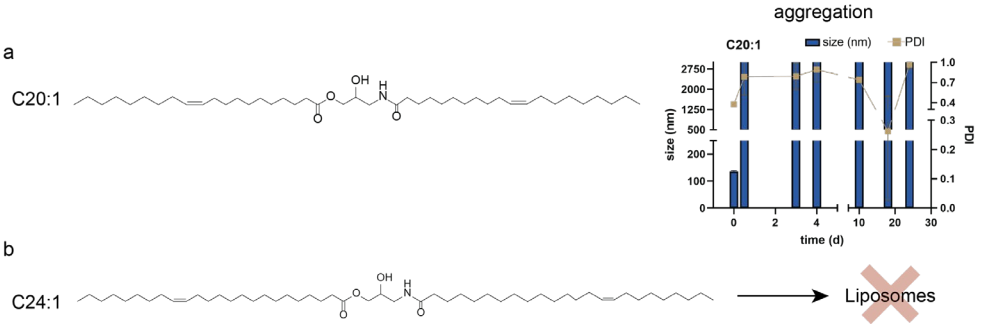

Figure S5. DOaG variants resulting in unstable formulations. a) Liposomes composed with DSPC and C20:1 variant (1:1 molar ratio) aggregate rapidly within ~6 hours as seen by size and polydispersity index (PDI) measurements (size and PDI limit of a formulation relevant for *in vivo* application = 200nm and 0.2, respectively). **b)** A mixture of DSPC and C24:1 (1:1 molar ratio) cannot be formulated into liposomes as the lipid film hydration step failed.

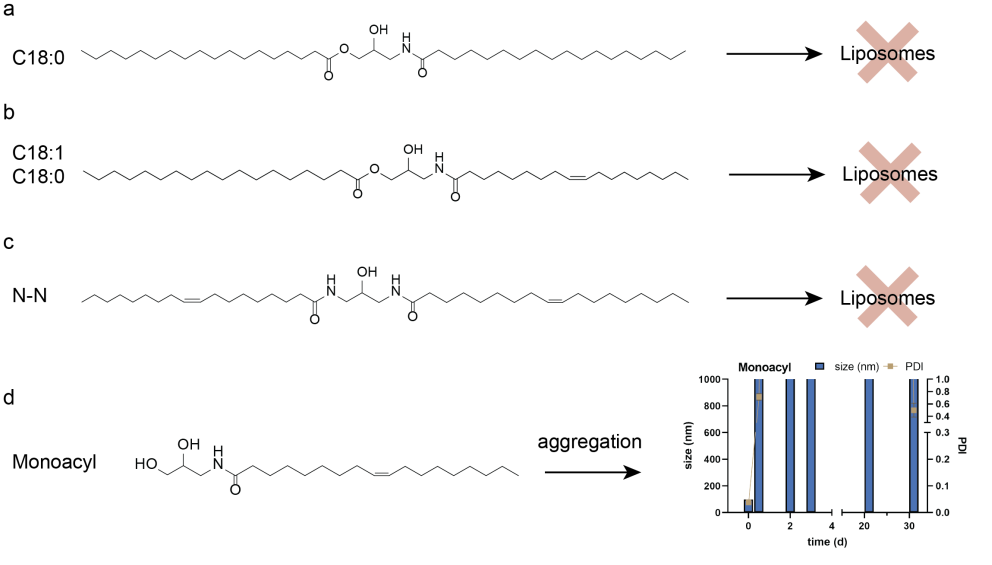

Figure S6. DOaG variants resulting in unstable formulations. Mixture of DSPC and **a)** C18:0, **b)** C18:0-C18:1 or **c)** N-N (in 1:1 molar ratio) cannot be formulated into liposomes as the lipid film hydration step failed. **d)** Liposomes composed with DSPC and monoacyl variant (1:1 ratio) aggregate rapidly within ~6 hours, as seen by size and PDI measurements (size and PDI limit of a formulation relevant for *in vivo* application = 200nm and 0.2, respectively).

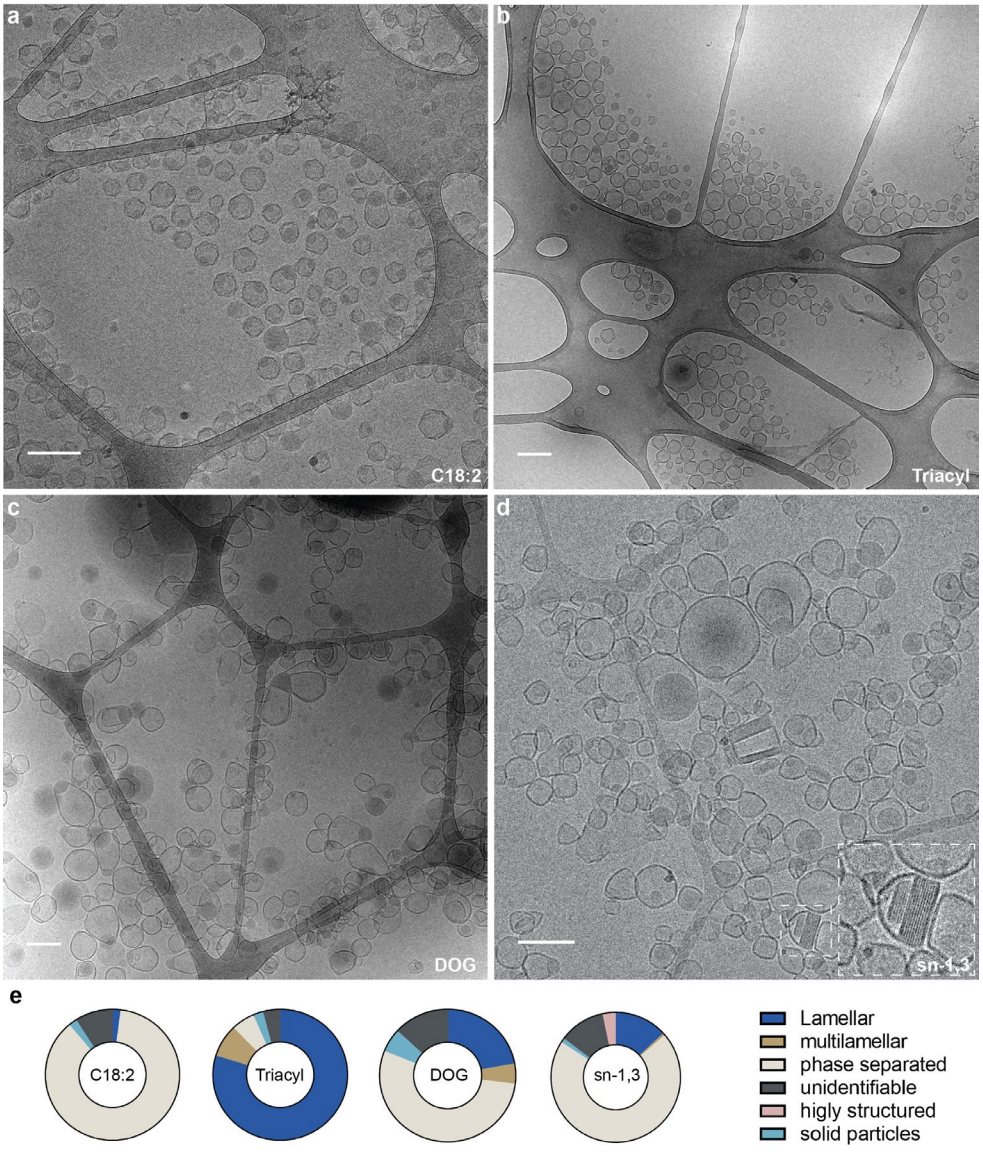

Figure S7. Cryo-TEM images of liposomes containing 1:1 molar ratio of DSPC and a) C18:2, **b)** Triacyl, **c)** DOG or **d)** *sn*-1,3. **e**) Quantification of all populations found in liposomal formulations containing 1:1 molar ratio of DSPC and C18:2, triacyl, DOG or *sn*-1,3. Inset in d depicts highly structured, crystalline assemblies present in the formulation. Quantification based on cryo-TEM images a-d (N=100). Scale bars: 200 nm.

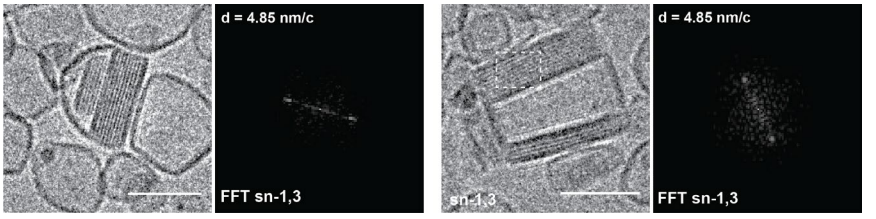

Figure S8. Liquid-crystalline assemblies as seen in *sn*-1,3 containing liposomes. Cryo-TEM images of liposomes containing the liquid-crystalline phases and average repeating distance of the lattice as indicated by FFT (nm per repeating cycle). Scale bars: 100 nm.

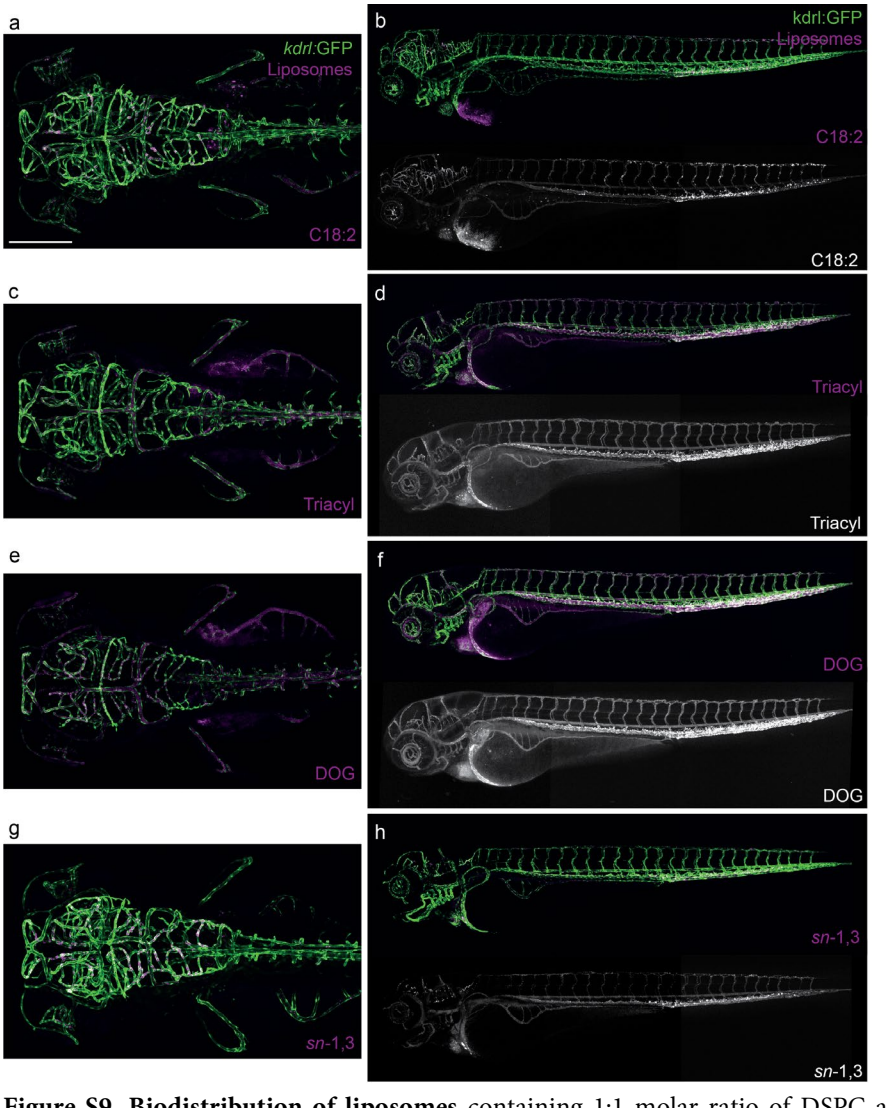

Figure S9. Biodistribution of liposomes containing 1:1 molar ratio of DSPC and **a, b)** C18:2, **c, d)** Triacyl, **e, f)** DOG and **g, h)** *sn*-1,3 in Tg(kdrl:GPF) zebrafish embryos,

expressing GFP in all endothelial cells, in dorsal (10x magnification) and lateral view, 1.5 hpi, at 78 dpf. Liposomes in grey/magenta at 5mM total lipid concentration containing 0.2% DOPE-LR for visualization. Vasculature in green. Scale bar for a, c, e, g: 200 µm.

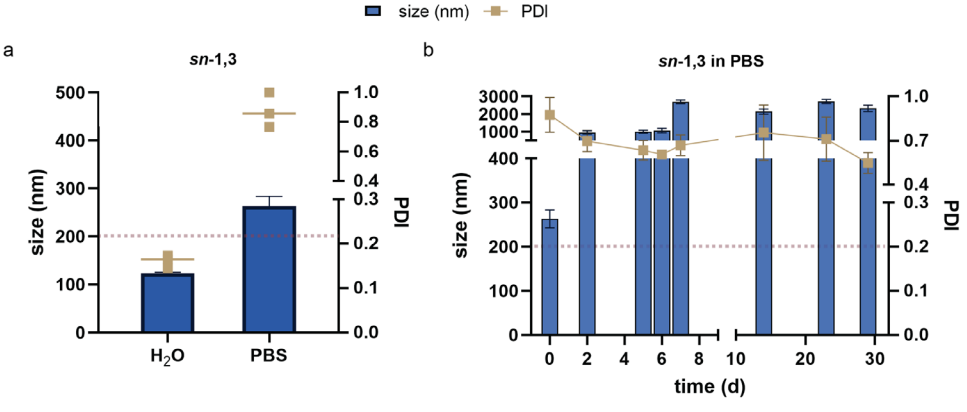

Figure S10. Stability of liposomes containing DSPC and *sn*-1,3 (1:1) made in ddH_2O and PBS. a) Size (nm) and PDI measurement of liposomes containing DSPC and *sn*-1,3 (1:1) made in ddH_2O and PBS. b) Size and PDI of liposomes containing DSPC and *sn*-1,3 (1:1) made in PBS over a period of ~30 days. Red dashed line indicates the threshold of size and PDI relevant for *in vivo* use.

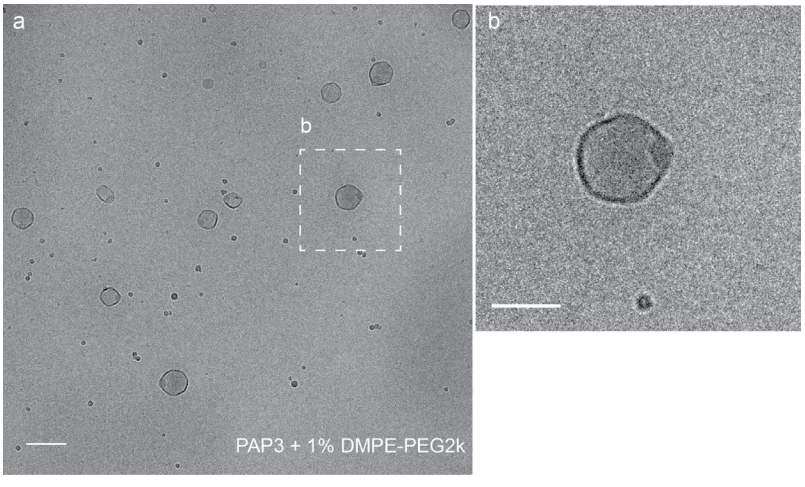

Figure S11. Cryo-TEM images of PAP3 liposomes containing 1% mol DMPE-PEG2k. a) Low magnification image and b) inset from **a** (white box). Scale bars: 200 nm for (a) and 100 nm for (b).

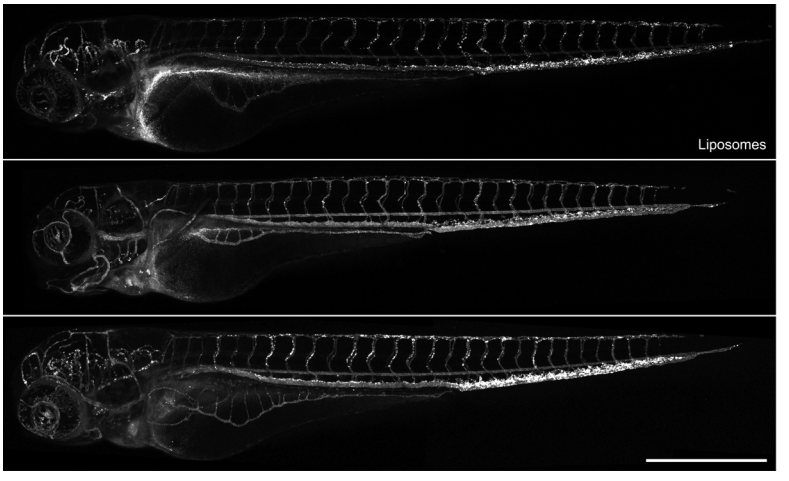

Figure S12. Biodistribution of PAP3 liposomes coated with 1 % mol DMPE-PEG2k in AB/TL zebrafish embryos (wild type), in lateral view, 2.5 hpi at 78 dpf. Liposomes in grey at 5mM total lipid concentration containing 0.2% DOPE-LR for visualization. Scale bar: 500 μm.

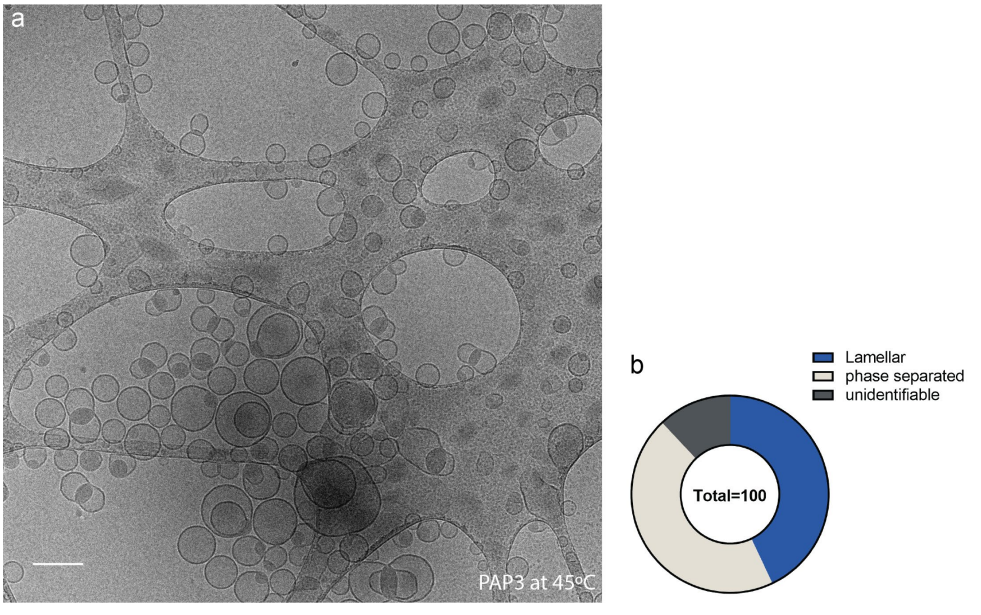

Figure S13. PAP3 liposomes at 45 < T < 65 ºC. a) Cryo-TEM image of PAP3 liposomes cooling to 45 ºC, immediately after formation at 65 ºC. **b)** Quantification of all populations found in the formulation. Quantification based on cryo-TEM image a (N=100). Scale bar = 200 nm.

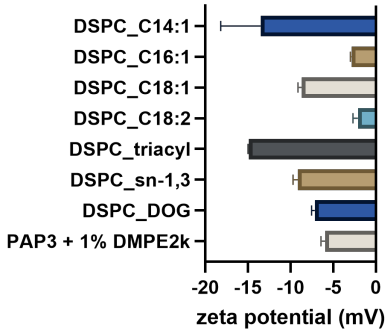

Figure S14. Zeta potential (mV) of stable formulations containing DSPC and DOaG analogues (1:1).

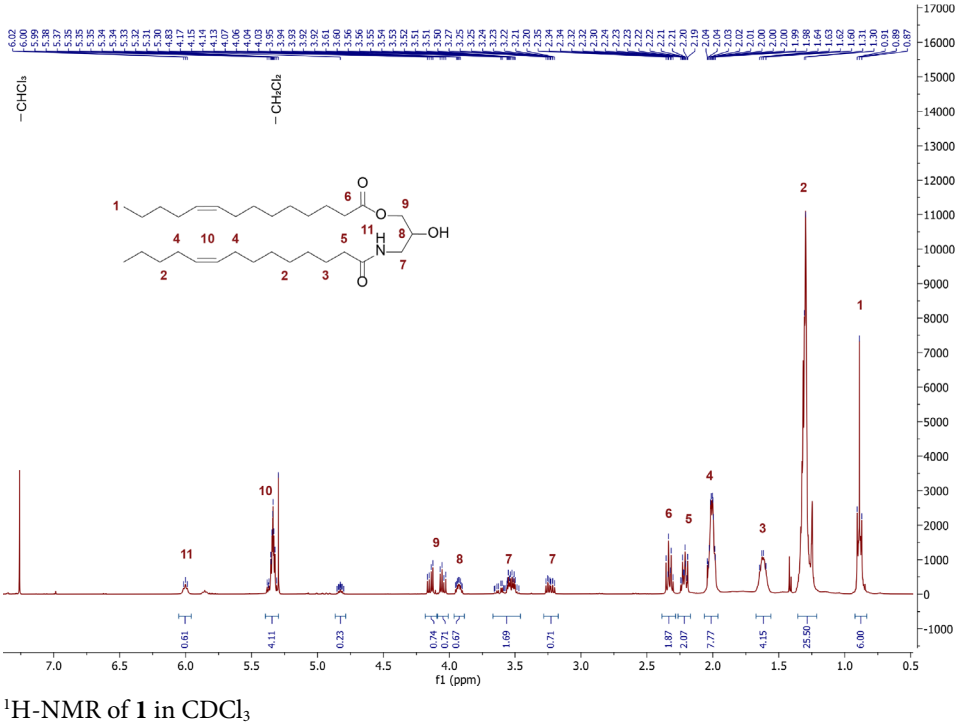

^{1}H-NMR of **1** in $CDCl_3$

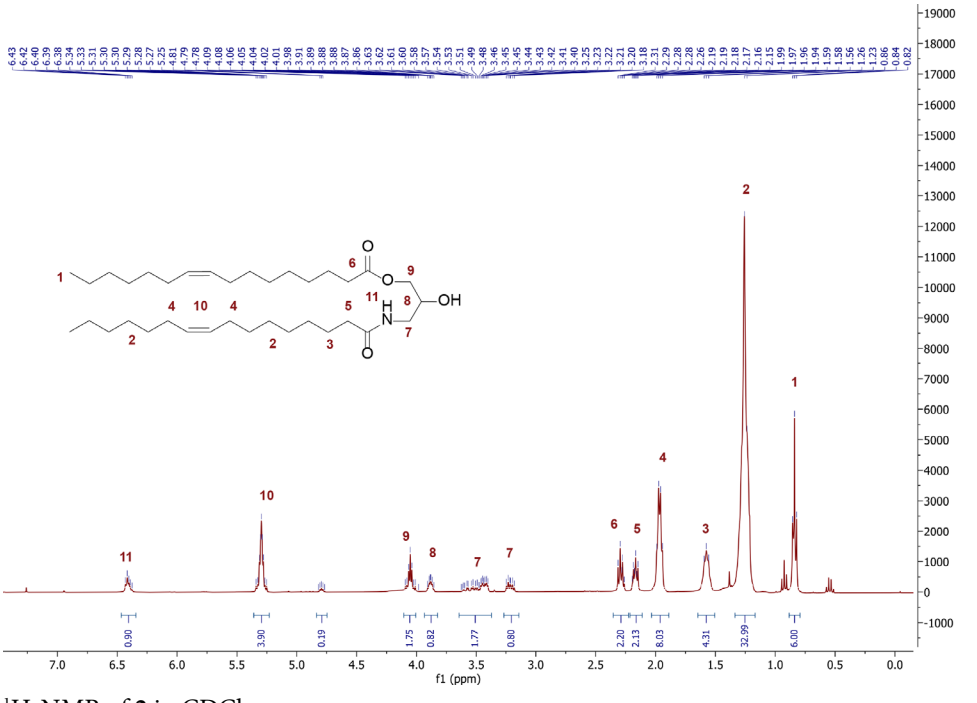

^{1}H-NMR of **2** in $CDCl_3$

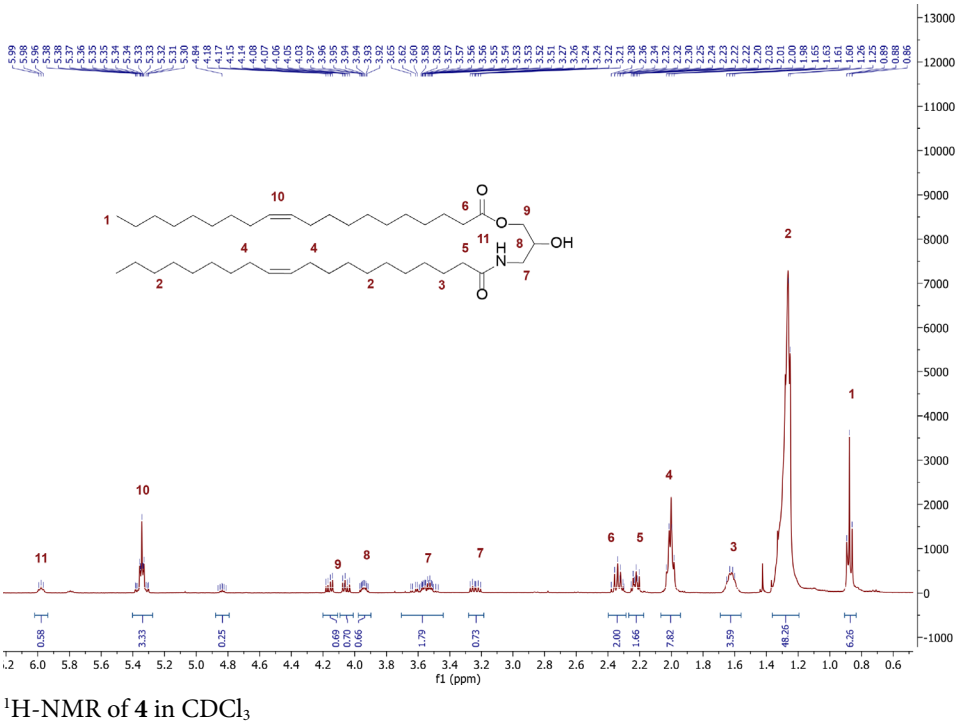

^{1}H-NMR of **4** in $CDCl_3$

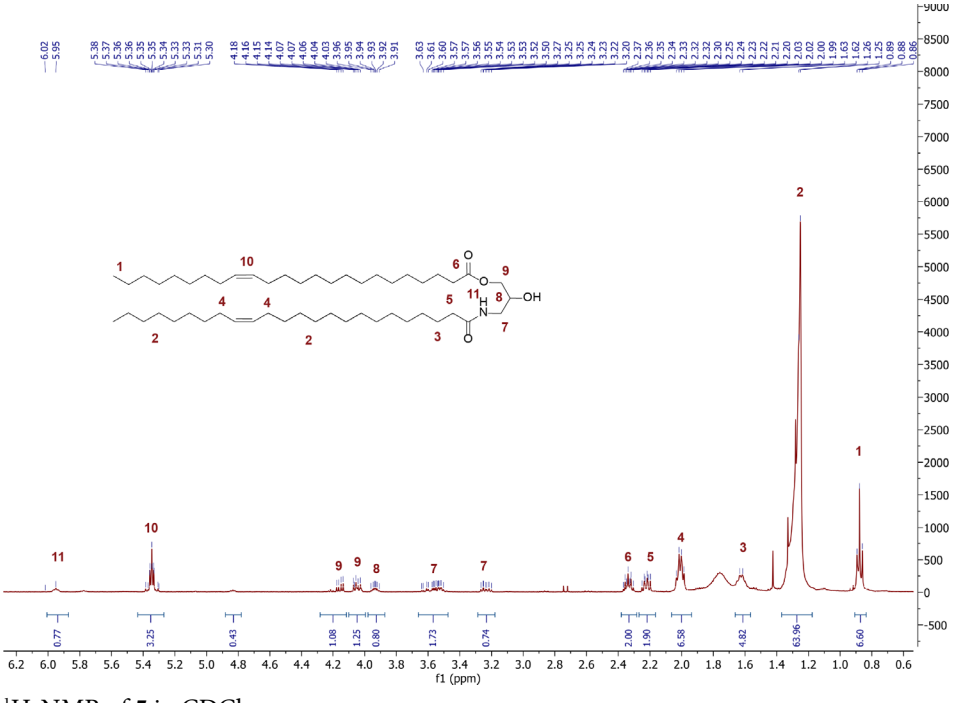

^{1}H-NMR of **5** in $CDCl_3$

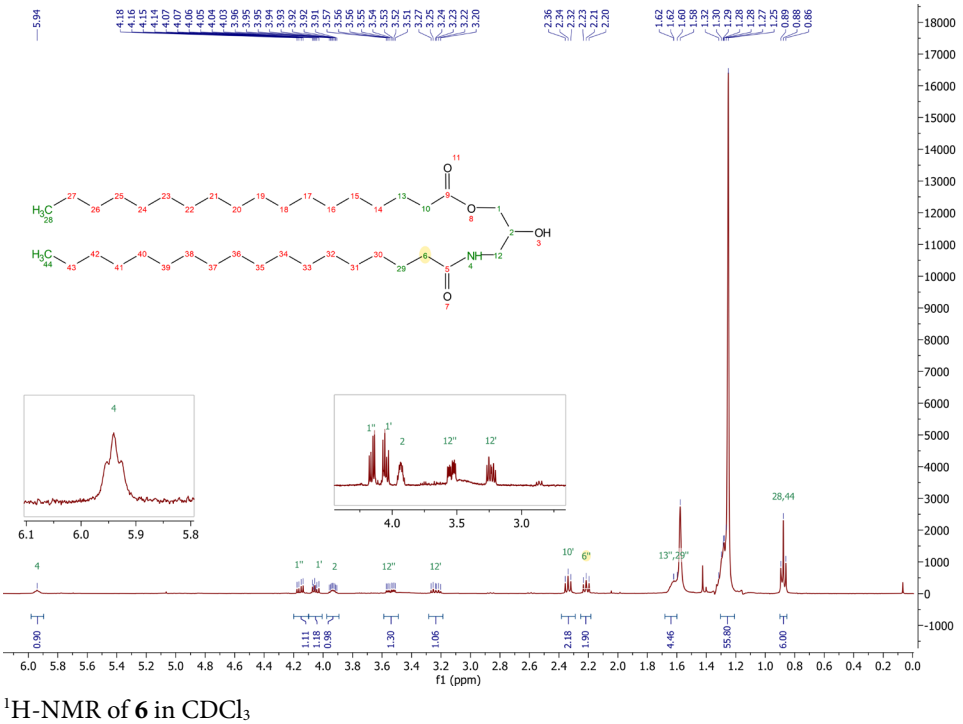

^{1}H-NMR of **6** in $CDCl_3$

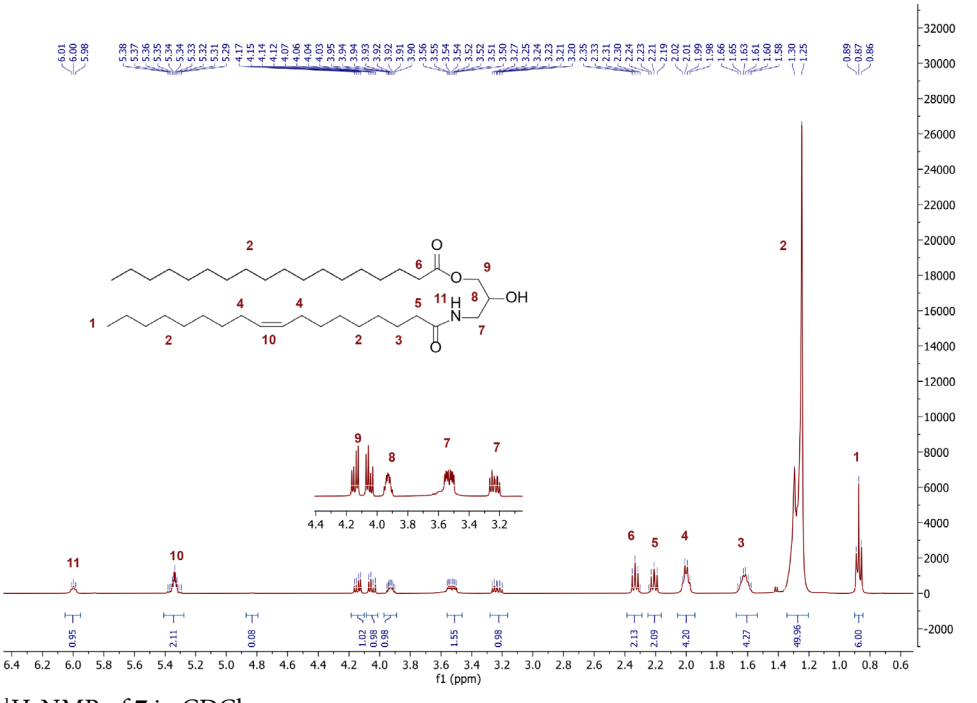

^{1}H-NMR of **7** in $CDCl_3$

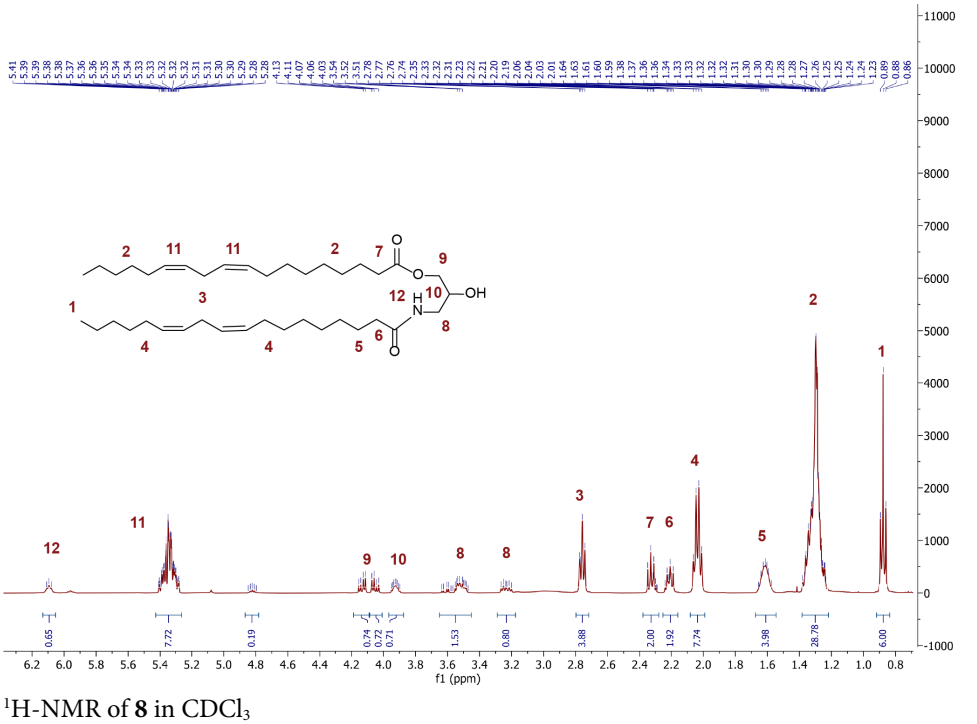

^{1}H-NMR of **8** in $CDCl_3$

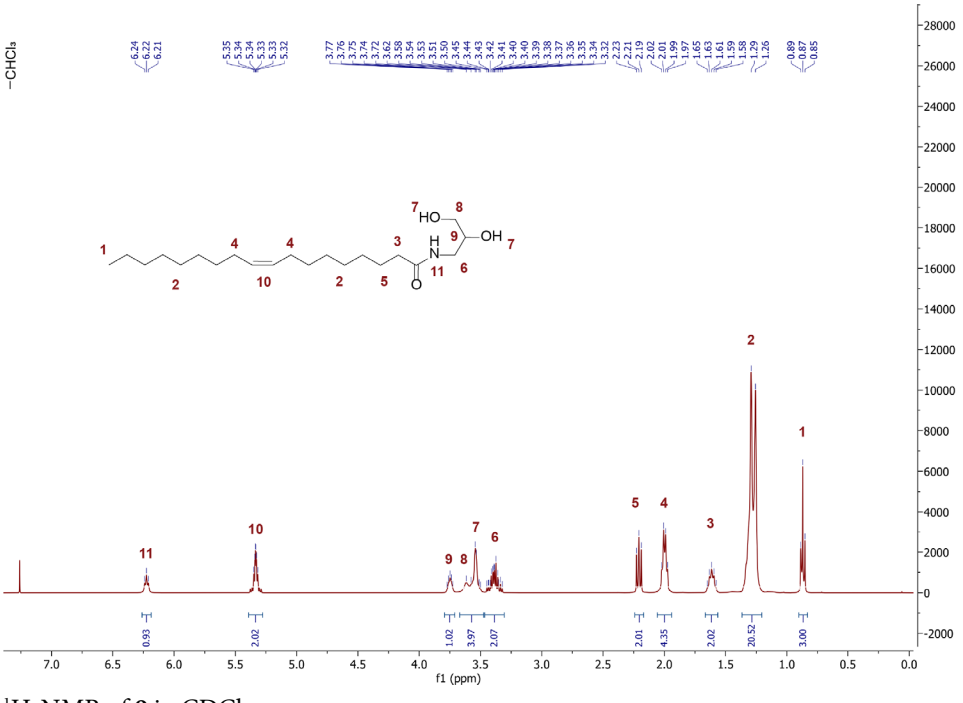

^{1}H-NMR of **9** in $CDCl_3$

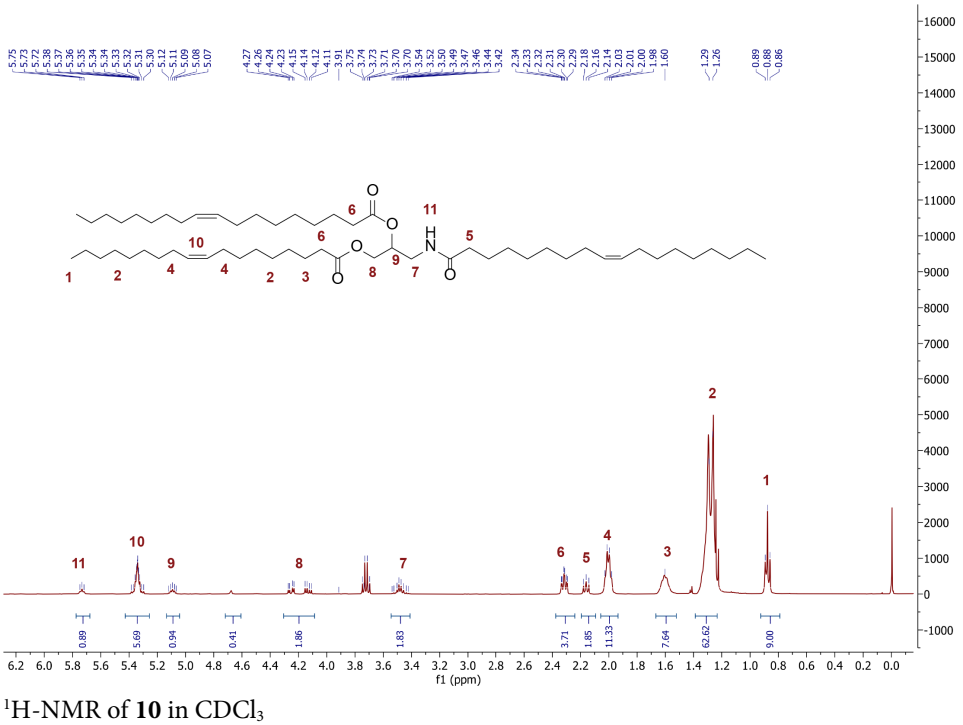

^{1}H-NMR of **10** in $CDCl_3$

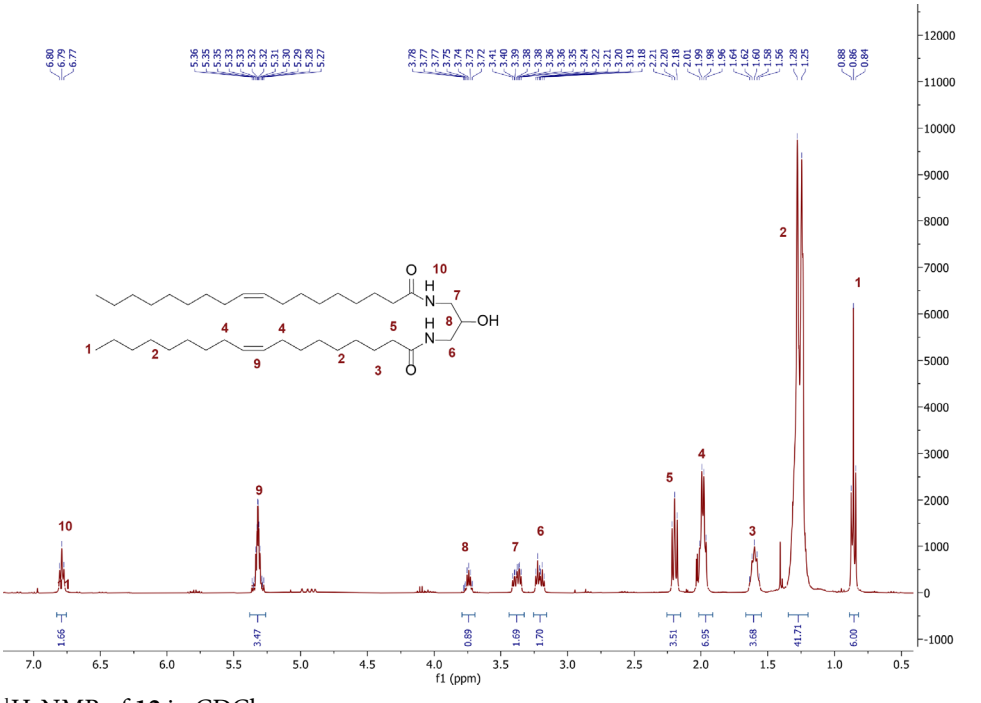

^{1}H-NMR of **12** in $CDCl_3$

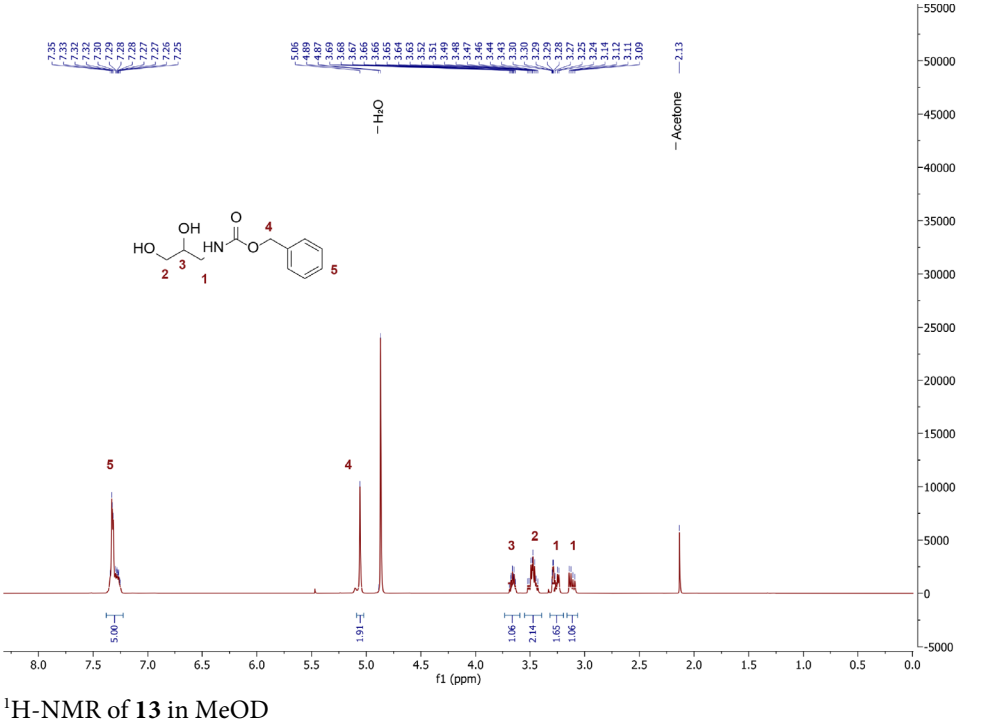

^{1}H-NMR of **13** in MeOD

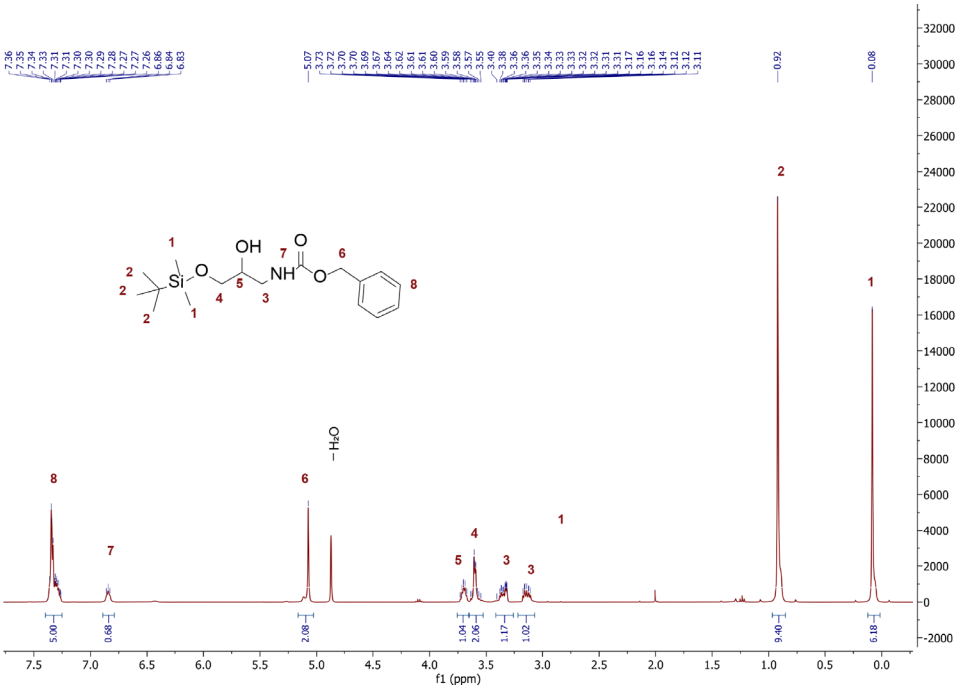

^{1}H-NMR of **14** in MeOD

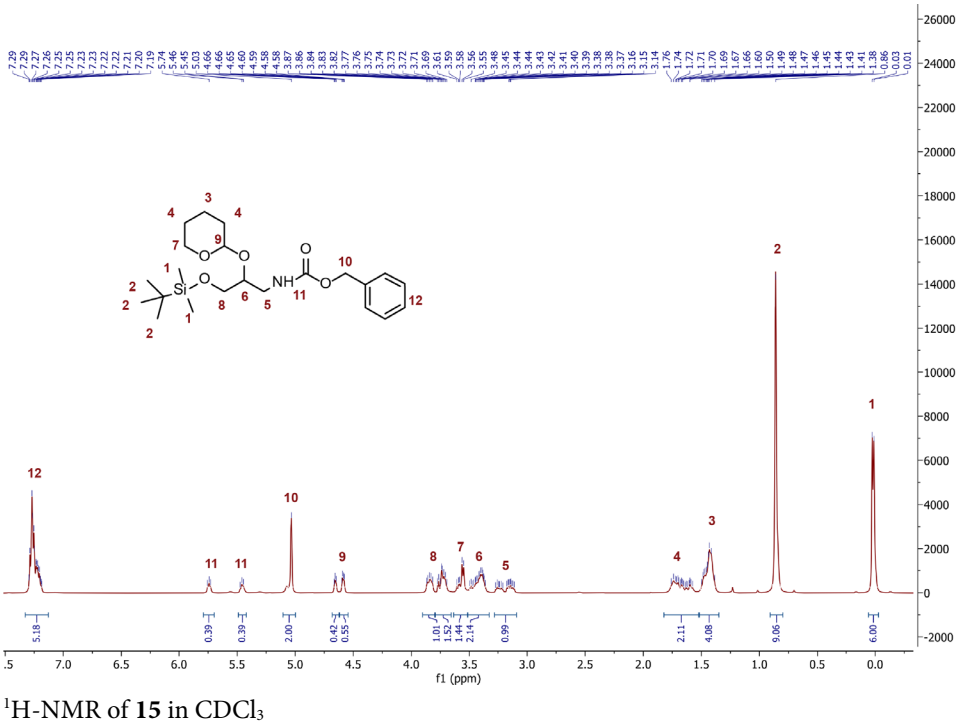

^{1}H-NMR of **15** in $CDCl_3$

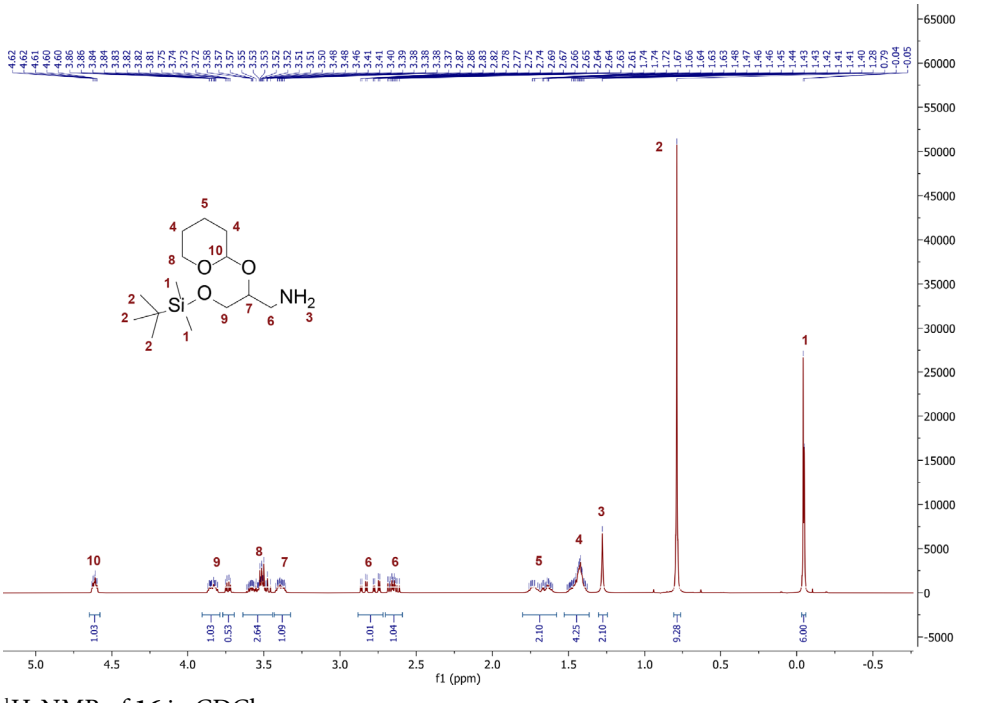

^{1}H-NMR of **16** in $CDCl_3$

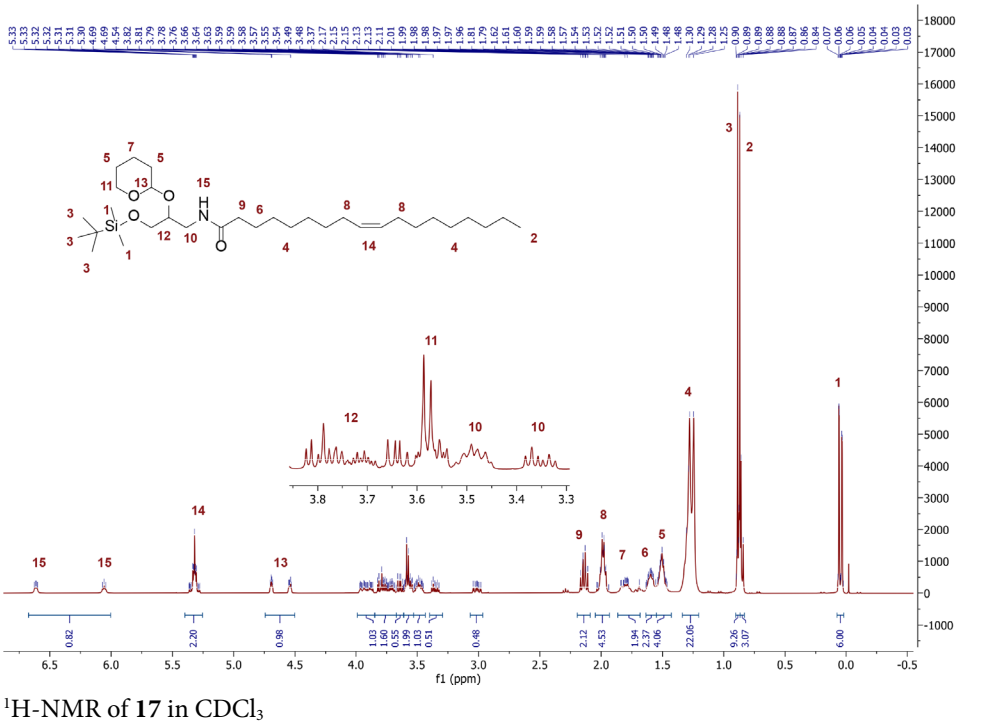

^{1}H-NMR of **17** in $CDCl_3$

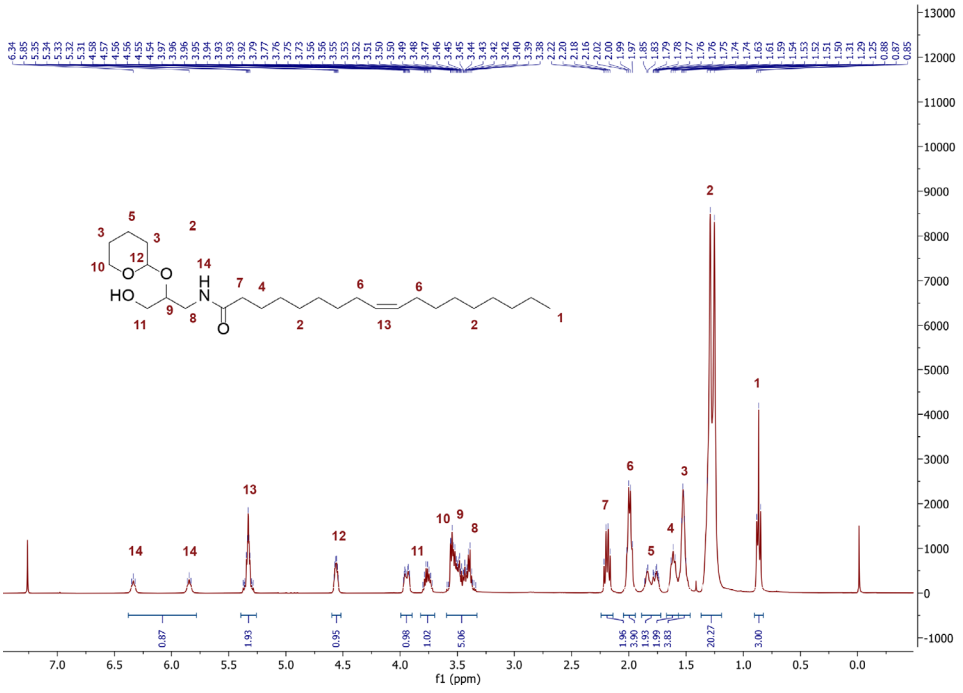

^{1}H-NMR of **18** in $CDCl_3$

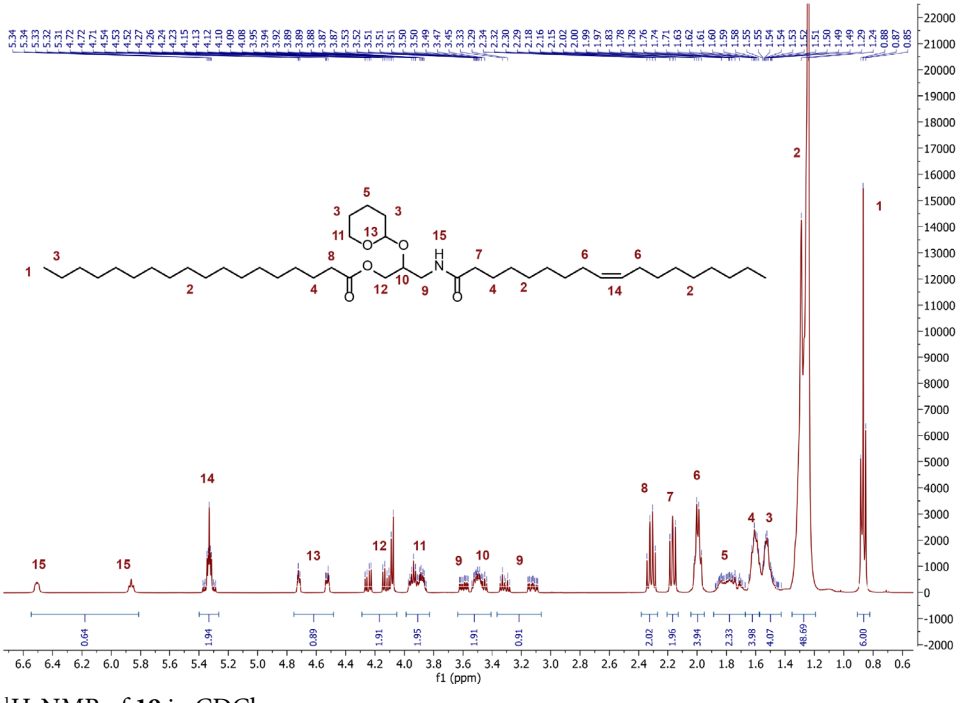

^{1}H-NMR of **19** in $CDCl_3$

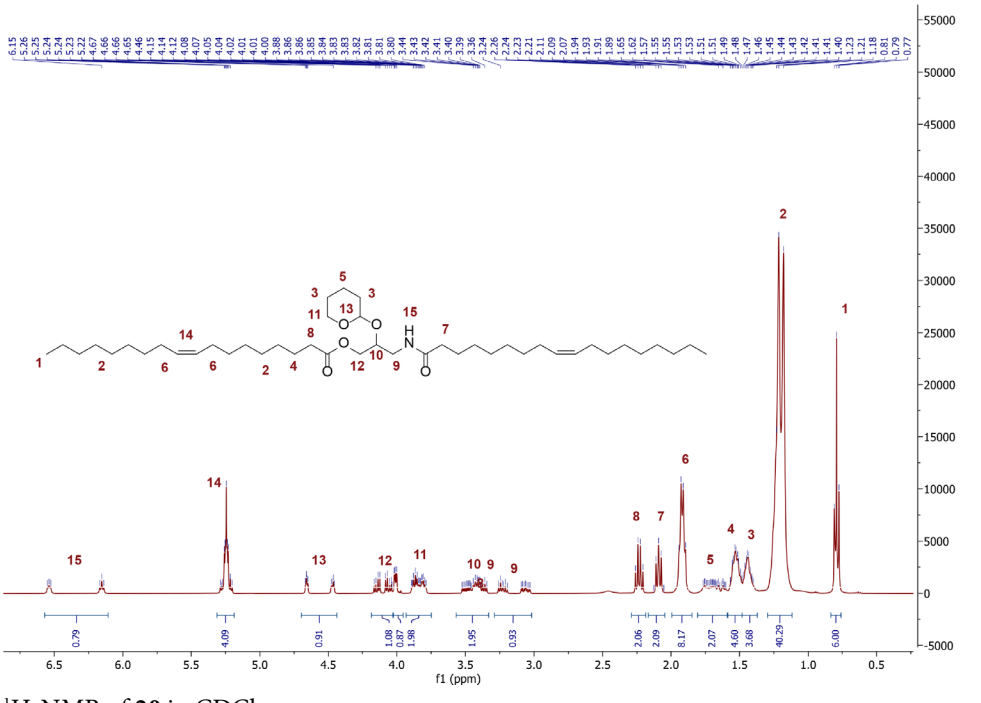

^{1}H-NMR of **20** in $CDCl_3$

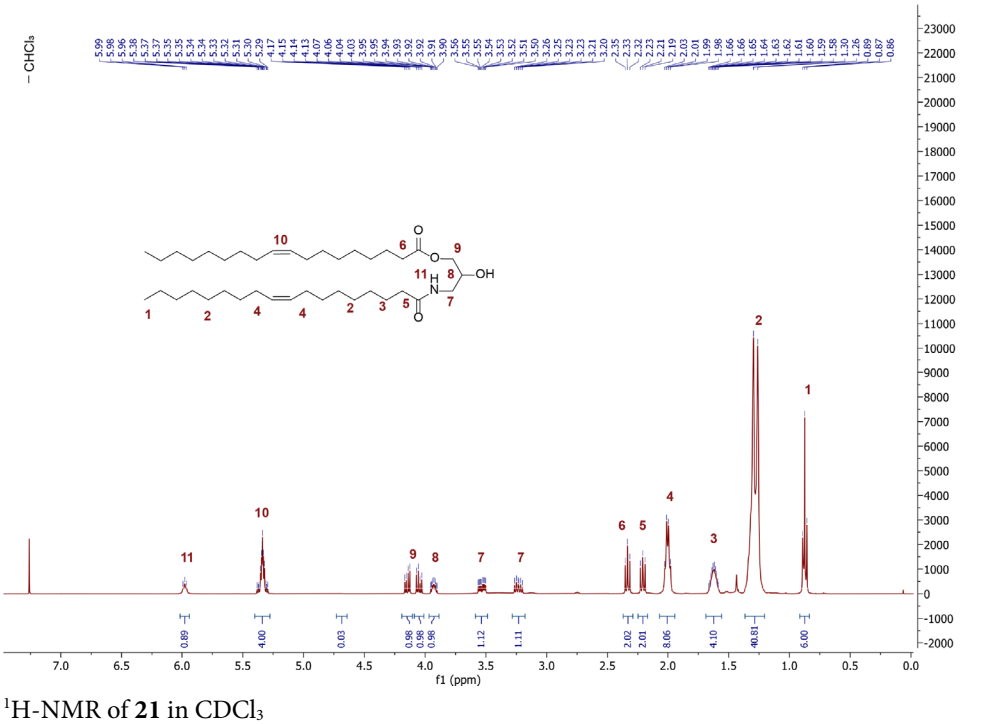

^{1}H-NMR of **21** in $CDCl_3$

4.6 References

1. Duan, X.; Li, Y. Physicochemical Characteristics of Nanoparticles Affect Circulation, Biodistribution, Cellular Internalization, and Trafficking. *Small* **2013**, *9* (9–10), 1521–1532.
2. Mitchell, M. J.; Billingsley, M. M.; Haley, R. M.; Wechsler, M. E.; Peppas, N. A.; Langer, R. Engineering Precision Nanoparticles for Drug Delivery. *Nat Rev Drug Discov* **2020**, *20* (2), 101–124.
3. Blanco, E.; Shen, H.; Ferrari, M. Principles of Nanoparticle Design for Overcoming Biological Barriers to Drug Delivery. *Nat Biotechnol* **2015**, *33* (9), 941–951.
4. Li, M.; Jin, X.; Liu, T.; Fan, F.; Gao, F.; Chai, S.; Yang, L. Nanoparticle Elasticity Affects Systemic Circulation Lifetime by Modulating Adsorption of Apolipoprotein A-I in Corona Formation. *Nat Commun* **2022**, *13* (1), 1–16.
5. Arias-Alpizar, G.; Koch, B.; Hamelmann, N. M.; Neustrup, M. A.; Paulusse, J. M. J.; Jiskoot, W.; Kros, A.; Bussmann, J. Stabilin-1 Is Required for the Endothelial Clearance of Small Anionic Nanoparticles. *Nanomedicine* **2021**, *34*, 102395.
6. Ishiwata, H.; Suzuki, N.; Ando, S.; Kikuchi, H.; Kitagawa, T. Characteristics and Biodistribution of Cationic Liposomes and Their DNA Complexes. *J Control Release* **2000**, *69* (1), 139–148.
7. Cho, E. C.; Xie, J.; Wurm, P. A.; Xia, Y. Understanding the Role of Surface Charges in Cellular Adsorption versus Internalization by Selectively Removing Gold Nanoparticles on the Cell Surface with a I 2/KI Etchant. *Nano Lett* **2009**, *9* (3), 1080–1084.
8. Pattipeiluhu, R.; Arias-Alpizar, G.; Basha, G.; Chan, K. Y. T.; Bussmann, J.; Sharp, T. H.; Moradi, M.-A.; Sommerdijk, N.; Harris, E. N.; Cullis, P. R.; Kros, A.; Witzigmann, D.; Campbell, F. Anionic Lipid Nanoparticles Preferentially Deliver mRNA to the Hepatic Reticuloendothelial System. *Adv Mater* **2022**, *34* (16), e2201095.
9. Campbell, F.; Bos, F. L.; Sieber, S.; Arias-Alpizar, G.; Koch, B. E.; Huwyler, J.; Kros, A.; Bussmann, J. Directing Nanoparticle Biodistribution through Evasion and Exploitation of Stab2-Dependent Nanoparticle Uptake. *ACS Nano* **2018**, *12* (3), 2138–2150.
10. Arias-Alpizar, G.; Kong, L.; Vlieg, R. C.; Rabe, A.; Papadopoulou, P.; Meijer, M. S.; Bonnet, S.; Vogel, S.; van Noort, J.; Kros, A.; Campbell, F. Light-Triggered Switching of Liposome Surface Charge Directs Delivery of Membrane Impermeable Payloads in vivo. *Nat Commun* **2020**, *11*, 3638.

11. Cullis, P. R.; Hope, M. J.; Tilcock, C. P. S. Lipid Polymorphism and the Roles of Lipids in Membranes. *Chem Phys Lipids* **1986**, *40* (2–4), 127–144.
12. Frolov, V. A.; Shnyrova, A. v.; Zimmerberg, J. Lipid Polymorphisms and Membrane Shape. *Cold Spring Harb Perspect Biol* **2011**, *3* (11), a004747.
13. Arias-Alpizar, G.; Papadopoulou, P.; Rios, X.; Pulagam, K. R.; Moradi, M. A.; Pattipeiluhu, R.; Bussmann, J.; Sommerdijk, N.; Llop, J.; Kros, A.; Campbell, F. Phase-Separated Liposomes Hijack Endogenous Lipoprotein Transport and Metabolism Pathways to Target Subsets of Endothelial Cells in vivo. *Adv Healthc Mater* **2023**, *12* (10), e2202709.
14. Papadopoulou, P.; Van Der Pol, R.; Van Hilten, N.; Moradi, M.-A.; Ferraz, M. J.; Aerts, J. M. F. G.; Sommerdijk, N.; Risselada, H. J.; Sevink, G. J. A.; Kros, A. Lipase-Mediated Selective Hydrolysis of Lipid Droplets in Phase-Separated Liposomes. *ChemRxiv* **2023**, DOI : 10.26434/chemrxiv-2023-9q9wh-v3.
15. Semple, S. C.; Akinc, A.; Chen, J.; Sandhu, A. P.; Mui, B. L.; Cho, C. K.; Sah, D. W. Y.; Stebbing, D.; Crosley, E. J.; Yaworski, E.; Hafez, I. M.; Dorkin, J. R.; Qin, J.; Lam, K.; Rajeev, K. G.; Wong, K. F.; Jeffs, L. B.; Nechev, L.; Eisenhardt, M. L.; Jayaraman, M.; Kazem, M.; Maier, M. A.; Srinivasulu, M.; Weinstein, M. J.; Chen, Q.; Alvarez, R.; Barros, S. A.; De, S.; Klimuk, S. K.; Borland, T.; Kosovrasti, V.; Cantley, W. L.; Tam, Y. K.; Manoharan, M.; Ciufolini, M. A.; Tracy, M. A.; De Fougerolles, A.; MacLachlan, I.; Cullis, P. R.; Madden, T. D.; Hope, M. J. Rational Design of Cationic Lipids for siRNA Delivery. *Nat Biotechnol* **2010**, *28* (2), 172–176.
16. Patel, S.; Ashwanikumar, N.; Robinson, E.; Xia, Y.; Mihai, C.; Griffith, J. P.; Hou, S.; Esposito, A. A.; Ketova, T.; Welsher, K.; Joyal, J. L.; Almarsson, Ö.; Sahay, G. Naturally-Occurring Cholesterol Analogues in Lipid Nanoparticles Induce Polymorphic Shape and Enhance Intracellular Delivery of mRNA. *Nat Commun* **2020**, *11* (1), 1–13.
17. Janmey, P. A.; Kinnunen, P. K. J. Biophysical Properties of Lipids and Dynamic Membranes. *Trends Cell Biol* **2006**, *16* (10), 538–546.
18. Siegel, D. P.; Epand, R. M. The Mechanism of Lamellar-to-Inverted Hexagonal Phase Transitions in Phosphatidylethanolamine: Implications for Membrane Fusion Mechanisms. *Biophys J* **1997**, *73* (6), 3089–3111.
19. Cullis, P. R.; Hope, M. J. Lipid Nanoparticle Systems for Enabling Gene Therapies. *Mol Ther* **2017**, *25* (7), 1467–1475.
20. Hafez, I. M.; Cullis, P. R. Roles of Lipid Polymorphism in Intracellular Delivery. *Adv Drug Deliv Rev* **2001**, *47* (2–3), 139–148.

21. Huang, Y.; Gui, S. Factors Affecting the Structure of Lyotropic Liquid Crystals and the Correlation between Structure and Drug Diffusion. *RSC Adv* **2018**, *8*, 6978–6987.
22. Johnsson, M.; Lam, Y.; Barauskas, J.; Tiberg, F. Aqueous Phase Behavior and Dispersed Nanoparticles of Diglycerol Monooleate/Glycerol Dioleate Mixtures. *Langmuir* **2005**, *21* (11), 5159–5165.
23. Popescu, G.; Barauskas, J.; Nylander, T.; Tiberg, F. Liquid Crystalline Phases and Their Dispersions in Aqueous Mixtures of Glycerol Monooleate and Glyceryl Monooleyl Ether. *Langmuir* **2007**, *23* (2), 496–503.
24. Johnsson, M.; Barauskas, J.; Tiberg, F. Cubic Phases and Cubic Phase Dispersions in a Phospholipid-Based System. *J. Am. Chem. Soc.* **2005**, *127* (4), 1076–1077.
25. Goñi, F. M.; Alonso, A. Structure and Functional Properties of Diacylglycerols in Membranes. *Prog Lipid Res* **1999**, *38* (1), 1–48.
26. Campomanes, P.; Zoni, V.; Vanni, S. Local Accumulation of Diacylglycerol Alters Membrane Properties Nonlinearly Due to Its Transbilayer Activity. *Commun Chem* **2019**, *2* (1), 1–8.
27. Alwarawrah, M.; Hussain, F.; Huang, J. Alteration of Lipid Membrane Structure and Dynamics by Diacylglycerols with Unsaturated Chains. *Biochim Biophys Acta Biomembr* **2016**, *1858* (2), 253–263.
28. Goldberg, E. M.; Lester, D. S.; Borchardt, D. B.; Zidovetzki, R. Effects of Diacylglycerols on Conformation of Phosphatidylcholine Headgroups in Phosphatidylcholine/Phosphatidylserine Bilayers. *Biophys J* **1995**, *69* (3), 965–973.
29. Alwarawrah, M.; Dai, J.; Huang, J. Modification of Lipid Bilayer Structure by Diacylglycerol: A Comparative Study of Diacylglycerol and Cholesterol. *J Chem Theory Comput* **2012**, *8* (2), 749–758.
30. Bilayers Edward Goldberg, P. M.; Lester, D. S.; Borchardt, D. B.; Zidovetzki, R. Effects of Diacylglycerols and Ca2+ on Structure of Phosphatidylcholine/Phosphatidylserine Bilayers. *Biophys J* **1994**, *66*, 382–393.
31. Dawson, R. M. C.; Hemington, N. L.; Irvine, R. F. Diacylglycerol Potentiates Phospholipase Attack upon Phospholipid Bilayers: Possible Connection with Cell Stimulation. *Biochem Biophys Res Commun* **1983**, *117* (1), 196–201.
32. Holme, M. N.; Rashid, M. H.; Thomas, M. R.; Barriga, H. M. G.; Herpoldt, K. L.; Heenan, R. K.; Dreiss, C. A.; Bañuelos, J. L.; Xie, H. N.; Yarovsky, I.; Stevens, M. M. Fate of Liposomes in the Presence of Phospholipase C and D: From Atomic to Supramolecular Lipid Arrangement. *ACS Cent Sci* **2018**, *4* (8), 1023–1030.

33. Strijkers, G. J.; Mulder, W. J. M.; van Heeswijk, R. B.; Frederik, P. M.; Bomans, P.; Magusin, P. C. M. M.; Nicolay, K.; Nicolay, · K; Nmr, B.; Bomans, · P. Relaxivity of Liposomal Paramagnetic MRI Contrast Agents. *MAGMA* **2005**, *18*, 186–192.
34. Gómez-Fernández, J. C.; Corbalán-García, S. Diacylglycerols, Multivalent Membrane Modulators. *Chem Phys Lipids* **2007**, *148*, 1–25.
35. Da Silva Sanchez, A. J.; Zhao, K.; Huayamares, S. G.; Hatit, M. Z. C.; Lokugamage, M. P.; Loughrey, D.; Dobrowolski, C.; Wang, S.; Kim, H.; Paunovska, K.; Kuzminich, Y.; Dahlman, J. E. Substituting Racemic Ionizable Lipids with Stereopure Ionizable Lipids Can Increase mRNA Delivery. *J Control Release* **2023**, *353*, 270–277.
36. Hatit, M. Z. C.; Dobrowolski, C. N.; Lokugamage, M. P.; Loughrey, D.; Ni, H.; Zurla, C.; Da Silva Sanchez, A. J.; Radmand, A.; Huayamares, S. G.; Zenhausern, R.; Paunovska, K.; Peck, H. E.; Kim, J.; Sato, M.; Feldman, J. I.; Rivera, M. A.; Cristian, A.; Kim, Y. T.; Santangelo, P. J.; Dahlman, J. E. Nanoparticle Stereochemistry-Dependent Endocytic Processing Improves in vivo mRNA Delivery. *Nat Chem* **2023**, *15*, 508–515.
37. Jin, S. W.; Beis, D.; Mitchell, T.; Chen, J. N.; Stainier, D. Y. R. Cellular and Molecular Analyses of Vascular Tube and Lumen Formation in Zebrafish. *Development* **2005**, *132* (23), 5199–5209.
38. Arias-Alpizar, G.; Bussmann, J.; Campbell, F. Zebrafish Embryos as a Predictive Animal Model to Study Nanoparticle Behavior in vivo. *Bio Protoc* **2021**, *11* (19), e4173.

CHAPTER 5

DOaG-containing mRNA-LNPs specifically target and transfect brain endothelial cells in zebrafish embryos

Parts of this chapter have been used in a research article (currently under revision with Advanced Materials)

Panagiota Papadopoulou[#], Winant L. van Os[#], Roy Pattipeiluhu, Gabriela Arias-Alpizar, Willem Noteborn, Frederick Campbell, Alexander Kros*

# denotes equal contribution

Abstract | Lipid nanoparticle (LNP) technology has unlocked the potential of mRNA therapeutics, and current developments in the field focus on tissue-targeted therapies for disease-specific treatments. However, cell/tissue selectivity for LNPs, accompanied with efficient mRNA delivery and expression, remain a major challenge. Recently, a liposome formulation containing a diacylglycerol lipid analogue (DOaG), led to specific targeting of brain endothelial cells (bECs) in zebrafish embryos. Here, we investigate whether incorporation of DOaG in LNPs, results in cell-specific mRNA delivery and transfection *in vivo*. By incorporating DOaG – or cholesterol as a control – and by using two different ionizable lipids, four mRNA-LNPs were formulated and demonstrated similar physicochemical characteristics (size, surface charge), and mRNA encapsulation efficiency. Cryo-transmission electron microscopy (cryo-TEM) revealed a phase-separated morphology in DOaG-containing LNPs, similarly to prior developed DOaG-containing liposomes. Subsequently, LNP biodistribution, mRNA delivery and translation were screened in zebrafish embryos and strikingly, DOaG-containing LNPs transfected bECs selectively, depending on the combination with the ionizable lipid. Moreover, transfection was solely observed when specific targeting was involved, in contrast to a shotgun approach where higher transfecting, but non-targeting, formulations did not reveal bEC transfection. Finally, we show that selective delivery of functional oligonucleotides to brain vasculature *is* possible, providing hope for novel drug delivery strategies for brain- and cerebrospinal fluid (CSF) related diseases.

5.1 Introduction

RNA therapeutics are rapidly changing the current landscape of medicine. Gene silencing or gene expression through RNA interference (RNAi) or messenger RNA (mRNA) delivery respectively, could potentially treat a plethora of genetic diseases, develop vaccines, or be used in cancer immunotherapy.[1] Small interfering RNA (siRNA), microRNA (miRNA) and antisense oligonucleotides (ASOs), are short strands of nucleotides that are resilient to *in vivo* degradation and therefore are also suitable as therapeutic agents. Moreover, several techniques are already addressing their inability to diffuse through cell membranes and reach the cytoplasm *i.e.*, conjugation with the sugar moiety GalNac induces receptor mediated endocytosis.[2,3] In contrast, the much larger mRNA is prone to enzymatic degradation by nucleases before entering the cell.[4–6] Therefore, mRNA delivery is critically dependent on lipid nanoparticles (LNPs) which protect RNA from degradation, but also facilitate delivery and endosomal escape to the cytoplasm.[7,8] LNP technology has been in the spotlight after their success in the recent mRNA vaccines against SARs-Cov-2, which was an important milestone for mRNA therapeutics.[9,10] Production, large-scale manufacturing and research of mRNA-LNPs are established and rapidly accelerated.[11] Despite this, due to their high assembly complexity and fairly new development, research with basic information on LNPs is still required, including research on lipid organization, morphology and transfection optimization. For example, the molecular mechanism on LNP assembly was elucidated only recently,[12,13] and LNP morphology as well as racemic pure lipid components, have been addressed to influence the mRNA transfection efficiency.[14–18]

Additionally, existing challenges in nanomedicine, including translational gaps, rapid clearance of lipid-based nanoparticles from systemic circulation, and targeting tissues beyond the liver, can hamper their clinical applicability.[19–21] Therefore, understanding fundamental aspects of LNPs *i.e.*, how lipid composition and physicochemical properties affect their biodistribution,[22] as well as selective uptake and transfection, could facilitate overcoming current challenges.

LNPs have a sophisticated ultrastructure based on the synergistic effect of different lipid components comprising the assembly.[16,22] Components include lipids that provide structural integrity (helper lipids), hydrophobic lipids which reside in the LNP core (structural lipids) and lipids which complex with the nucleic acid cargo (ionizable lipids). Lipid components can individually dictate circulation lifetimes, biodistribution, cell selectivity, or transfection potency [23,24] and therefore rational design of LNPs are of great importance for the outcome of each individual therapeutic. The "helper" lipid, typically a phospholipid, comprises the outer lipid layer exposed to the surrounding environment and dictates surface charge and rigidity.[16] Additionally, a lipid-polyethylene glycol (PEG) conjugate is incorporated on the LNP outer lipid layer, providing structural and long-term stability. Depending on the exact chemistry, PEG lipids can improve circulation lifetimes and/or dissociate from the LNP membrane facilitating desired biodistribution and transfection.[23] The ionizable lipid resides in the solid core of LNPs along with other hydrophobic lipids – *i.e.*, cholesterol -, and mRNA. Having an optimal apparent pKa between 6-7, the ionizable amino lipids can complex with mRNA in acidic pH, followed by LNP assembly and mRNA encapsulation.[25,26] Subsequently, in physiological buffers, ionizable lipids are neutral giving LNPs non-cationic net surface charge, which renders them compatible for clinical use. After LNP endocytosis, ionizable lipids are protonated again in the acidic endosome. In turn, protonated ionizable lipids are thought to electrostatically interact with negatively charged phospholipids of the endosomal membrane, facilitating endosomal disruption and escape of mRNA into the cytoplasm.[27–31] DODAP (1,2-dioleoyl-3-dimethylammonium propane) has been one of the first ionizable synthetic aminolipids developed for nucleic acid encapsulation [26,32] and ever since evolution of the lipid chemistry has led to more potent, clinically approved ionizable lipids for siRNA or mRNA-LNPs *i.e.*, DLin-MC3-DMA (dilinoleylmethyl - 4-dimethyl aminobutyrate, in short MC3), ALC-0315 ([(4-hydroxybutyl)azanediyl]di(hexane-6,1-diyl)bis(2-hexyldecanoate)) or SM-102 (Heptadecan-9-yl-8-((2-hydroxy ethyl) (6-oxo-6-(undecyloxy)hexyl)amino) octanoate).[33–36]

Along with the ionizable lipid, the "structural" lipid mainly occupies the solid core of LNPs. Cholesterol has been extensively used in LNP formulations as a structural lipid due to its hydrophobicity and because it improves circulation lifetimes and

facilitates siRNA encapsulation.[37] Additionally, cholesterol exerts the ability to "condense" lipid membranes, pushing them towards the liquid ordered (L_o) phase, increasing stability. Also, it has the propensity to form liquid crystalline phases that can facilitate fusion and transfection.[14,15,38,39] Despite their difference in molecular structure, cholesterol and diacylglycerols (DAGs) exert similar properties in lipid membranes.[40] Due to their hydrophobicity, DAGs mainly reside in between the phospholipid leaflet of the cell membrane. Additionally, they are main components of lipoproteins, especially high-density lipoproteins (HDLs).[41–43] Additionally, DAGs induce condensing effects on lipid membranes (similarly to cholesterol), participate in signaling pathways (*i.e.*, protein kinase C activation) and facilitate protein recruitment.[43–46] Their conical shape perturbs the lamellar structure of a phospholipid bilayer, inducing non-bilayer phases (*i.e.*, inverted hexagonal phase [H_{II}]) and lipid phase separation.[47,48] These in turn can increase the spontaneous negative curvature of membranes, facilitating fusion.[49]

All these properties render DAGs as interesting molecules for lipid-based nanoparticle formulations, nevertheless, have not been explored in LNP development. Recently, the unique properties of DAGs were investigated in a liposomal formulation composed of the synthetic DAG analogue, DOaG (2-hydroxy-3-oleamidopropyl-oleate) and the fully saturated, naturally occurring DSPC (1,2-distearyl-*sn*-glycero-3-phosphatidylcholine).[50] Surprisingly, these liposomes (named PAP3) localized at the brain endothelial cells (bECs) of zebrafish embryos with a great specificity, due to their unique "parachute" liposome morphology. This morphology was a result of lipid phase separation induced by DOaG, creating a lipid droplet within the DSPC leaflet (**Figure 1a-c**). bEC targeting was mediated by triglyceride lipases (TGLs), - capillary lumen-bound enzymes highly present in bECs at this developmental stage - facilitating liposome recognition and uptake. Moreover, it was revealed that TGLs specifically recognize and bind to the lipid droplets of PAP3 liposomes, as mediated by higher lipid packing defects due to phase separation.[51] This highlights the influence that lipid organization in membranes has on the nano-bio interface, resulting in cell-specific biodistribution.

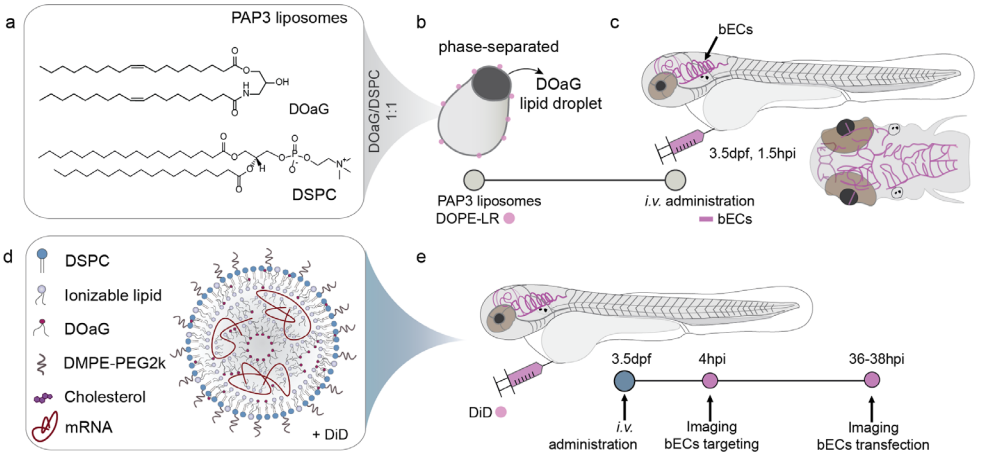

Figure 1. Overview of phase-separated liposomes, mRNA-LNP development strategy, and timeline of experiments. a) Molecular structure of lipids DSPC and DOaG comprising the PAP3 liposomes (in an equimolar mixture). **b)** Schematic of phase-separated morphology of PAP3 liposomes. **c)** Intravenous administration of PAP3 liposomes in 3.5 dpf zebrafish embryos. Brain vasculature depicted in pink, region in which liposomes selectively accumulate at 1.5 hpi. **d)** Schematic representation of an mRNA-LNP and lipids selected for the assembly. Note that cholesterol is not depicted in the LNP schematic. **e)** Timeline of the in vivo assessment of mRNA-LNPs. DOPE-LR = 1,2-dioleoyl-sn-glycero-3-phosphoethanolamine-lissamine rhodamine as a fluorescent tracer, dpf = days post fertilization, hpi = hours post injection.

In this study, we formulated mRNA-LNPs which preferentially target bECs in zebrafish embryos, achieving cell selective mRNA delivery and protein expression. This redirection of nanoparticle biodistribution towards bECs was obtained by replacing cholesterol with DOaG in LNPs, in combination with the ionizable lipid DODAP. Cryo-TEM and cryo-electron tomography (cryo-ET) revealed an unusual mRNA-LNP morphology when DOaG is incorporated in LNP formulations, characterized by two distinct, electron dense, separated phases. This proof-of concept study shows how switching a single lipid component, dramatically affects the morphology and directs biodistribution and transfection of mRNA-LNPs towards specific cell subsets in zebrafish embryos. Finally, this study shows that rational design and selection of lipid composition is important to gain control of nanoparticle *in vivo* behavior.

5.2 Results and Discussion

mRNA-LNPs were successfully formulated with DOaG

Our strategy for the LNP design originates from the DOaG-containing PAP3 liposomes. The two lipid components (DSPC and DOaG) result in phase separation, which leads to bECs specificity in zebrafish embryos (**Figure 1a-c**). Therefore, formulating mRNA-LNPs incorporating DOaG as a structural lipid component could result in formulations that preferentially target bECs of zebrafish embryos, with concomitant mRNA delivery and protein expression. Based on LNP formulations containing standard lipid components (*i.e.*, helper, structural and ionizable lipids), we designed DOaG-based mRNA-LNPs and their biodistribution, bEC targeting, and mRNA expression was qualitatively and quantitively studied in transgenic zebrafish embryos (**Figure 1 d, e**).

Four formulations were designed for the study (**Figure 2a, b)**, investigating the effect of two different ionizable lipids (DODAP and the clinically approved MC3) and replacing the structural lipid cholesterol with DOaG. In all formulations, DSPC was chosen as the helper lipid and the short-chain DMPE-PEG2k was used as the PEG lipid, which is known to desorb from the LNP surface *in vivo*, enabling nanoparticle - protein interactions.[23] LNPs were formulated encapsulating functional mRNA expressing fluorescent reporter protein mCherry, using a Nitrogen to Phosphate ratio of 6 (N/P = 6) (**Figure 2c**). Reporter protein mCherry was preferred over GFP due to its decreased autofluorescence levels (**Figure S1)**, allowing for broader range of fluorescence intensity measurements. For the real time biodistribution studies, all LNPs contained the far-red lipophilic dye DiD (1,1′-dioctadecyl- 3, 3, 3′, 3′ - tetramethylindodicarbo cyanine, 4- chlorobenzene sulfonate). The *kdrl*:GFP zebrafish line (GFP-positive vasculature) was used for vasculature visualization and colocalization studies. All LNPs were fully characterized and found to have properties with comparable values in size, charge, PDI and encapsulation efficiency. LNPs were characterized by dynamic light scattering (DLS) and were found in the range of 100.5-148.4 nm in average hydrodynamic diameter, low polydispersity indices and near neutral to slightly anionic surface charge (**Figure 2d, e**). Additionally, encapsulation efficiency (%EE)

of mRNA was high for all formulations (**Figure 2f**). In summary, replacing cholesterol with DOaG does not significantly alter the LNP assembly, physicochemical properties and mRNA %EE. Hereafter, we use the following nomenclature for the four LNP formulations: LNP-A (*i.e.,* CHO-DODAP), LNP-B (*i.e.,* DOaG-DODAP), LNP-C (*i.e.,* CHO-MC3) and LNP-D (*i.e.,* DOaG-MC3) (**Figure 2b**).

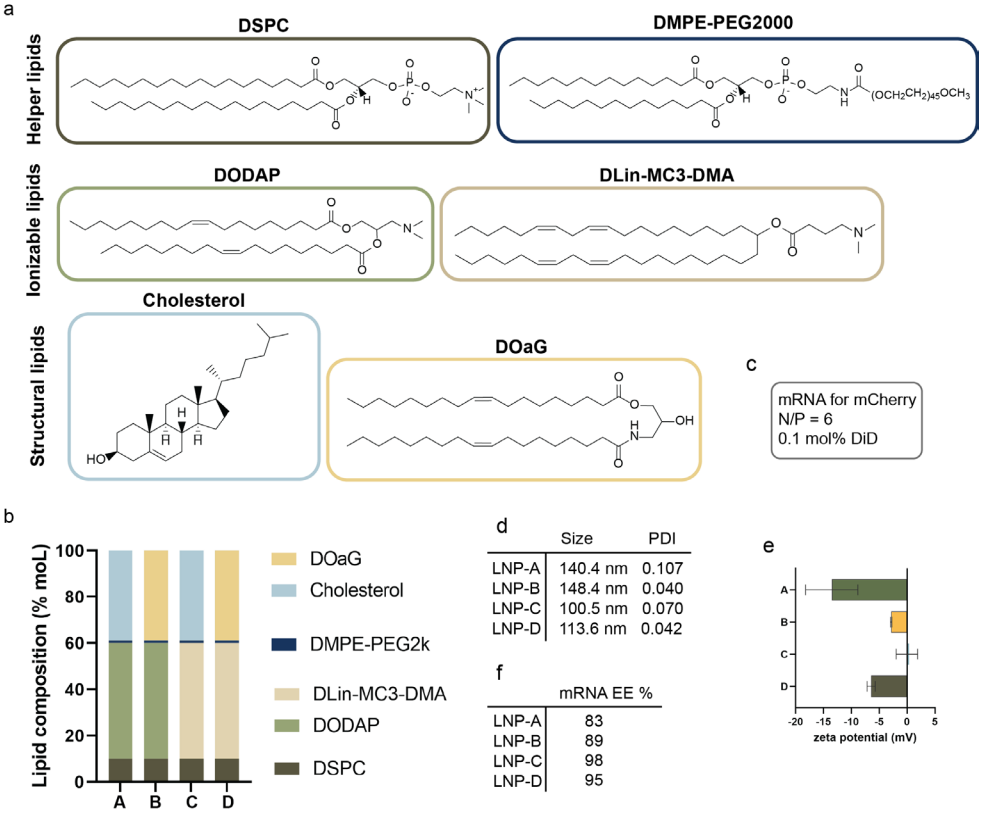

Figure 2. Lipid composition of mRNA-LNP formulations and physicochemical properties. a) Molecular structures of lipid components used for mRNA-LNPs. **b)** Molar ratios of lipid components and composition of the four mRNA-LNP formulations. **c)** Information on functional mRNA, N/P ratio and fluorescent tracer, constant for all LNP formulations. **d)** Size (average hydrodynamic diameter) and PDI of mRNA-LNP formulations as determined by DLS. **e)** Surface charge of LNP formulations, as determined by zeta-potential measurements. **f)** Encapsulation efficiency of mRNA of all mRNA-LNP formulations. e demonstrates three technical replicates.

Cryo-TEM reveals phase-separated morphology on DOaG-based mRNA-LNPs

Previously, PAP3 liposomes were found to accumulate in bECs as a result of their phase-separated morphology.[50] Being a two-component lipid system, it was easy to manipulate molar ratios, revealing that lipid droplets in liposomes were only observed after DOaG reached the phase separation threshold in the membrane. Interestingly, the selective *in vivo* targeting of liposomes to the bECs corelated with phase separation. Thus, morphology played a pivotal role on bEC specificity and therefore we sought to investigate whether DOaG also induced a unique morphology in LNP formulations. Cryo-TEM and cryo-ET was used to assess LNP ultrastructure and identify differences in morphology between all LNP formulations. For LNP-A, most of particles were either solid, or nanoparticles with distinct lamellar lipid compartments, possibly composed of a phospholipid bilayer (**Figure 3a black arrow** and **Figure S2**). Such structures have been previously described as lipid "blebs" for LNP compositions similar to LNP-A, and RNA has been found to localize in the "bleb's" hydrophilic core.[13,52] For LNP-A, a distinct punctuated electron-dense pattern is observed in the hydrophilic core of the bleb, indicating similarly mRNA localization (**Figure 3a, red arrow**). The morphology of LNP-C is characterized by solid lipid particles with a multilamellar lipid partitioning observed for some of the particles (**Figure 3c** and **Figure S2**). This type of morphology for similar lipid compositions has been described before.[53] Interestingly, the DOaG containing LNPs (LNP-B and LNP-D) were found to be solid, however a phase-separated droplet with different electron density was present within the solid particles (**Figure 3b, d** and **Figure S2**). Cryo-ET of LNP-B revealed the morphology in higher resolution, and a bilayer around the phase-separated droplet could be observed **(Figure 3e-g**). It is not known whether this bilayer consists of one or more lipid components. A similar morphology has been recently characterized, where cholesterol was replaced by its analogue fucosterol.[15] It was suggested that phase separation may influence the mRNA localization towards the protruded area, however, no conclusive data was presented to support this claim. The electron density observed in the separate droplet in LNP-B and D is similar to the electron density induced when mRNA is present, which suggests that mRNA is present in the phase-separated droplet.

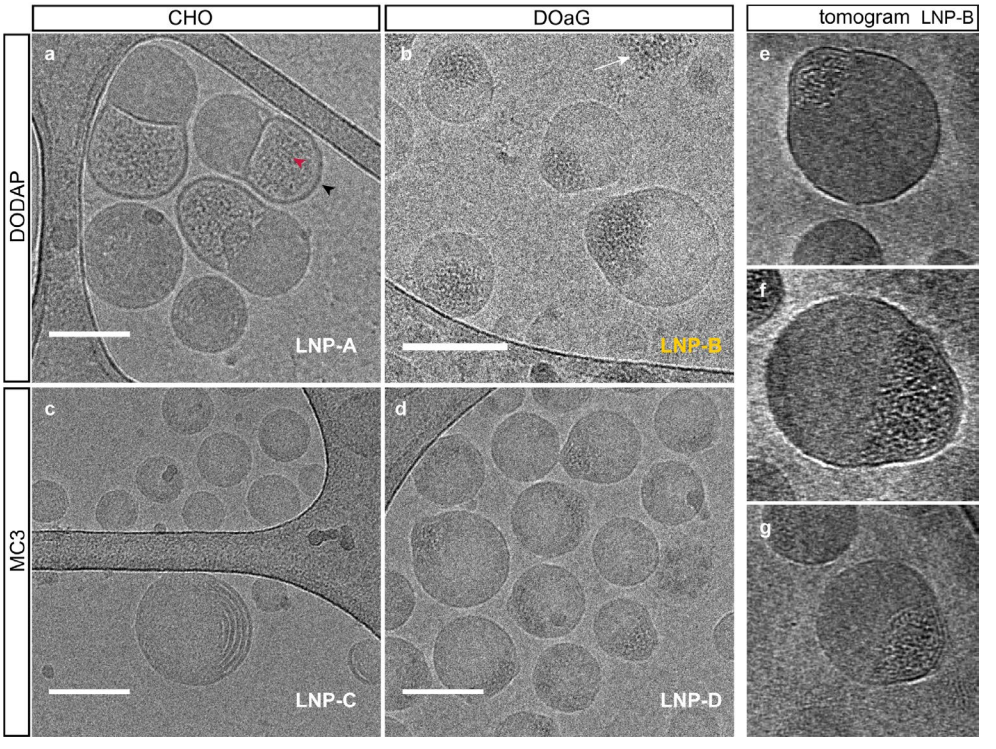

Figure 3. Cryo-electron microscopy images of mRNA-LNP formulations. Cryo-TEM images of **a)** LNP-A, **b)** LNP-B, **c)** LNP-C, **d)** LNP-D. **e-g)** Cryo-ET images of LNP-B. **f** is a cross section. Black arrow depicts the phospholipid bleb. Red and white arrows possibly depict encapsulated and free mRNA, respectively, as described before.[13] Scale bars: 100 nm.

DOaG-DODAP containing LNPs target the bECs of zebrafish embryos

All four LNP formulations shared similar physicochemical properties (size range, PDI, surface charge) allowing us to assess the LNPs' potential to target bECs based on difference in lipid composition and/or morphology. Formulations were intravenously (IV) administered in zebrafish embryos at 3.5 days post fertilization (dpf) and imaged in real time with confocal microscopy (**Figure 4a**). All formulations, revealed to be predominantly in circulation 4 hours post injection (hpi) (**Figure 4b** and **Figure S3a, c, e, g**). To investigate bEC targeting in more detail, cellular localization of LNPs was studied by high resolution confocal z-stack imaging at the hindbrain, from a dorsal perspective (insert **Figure 4a, Figure 4c**). LNP-A and C revealed to be circulating represented by a haze of

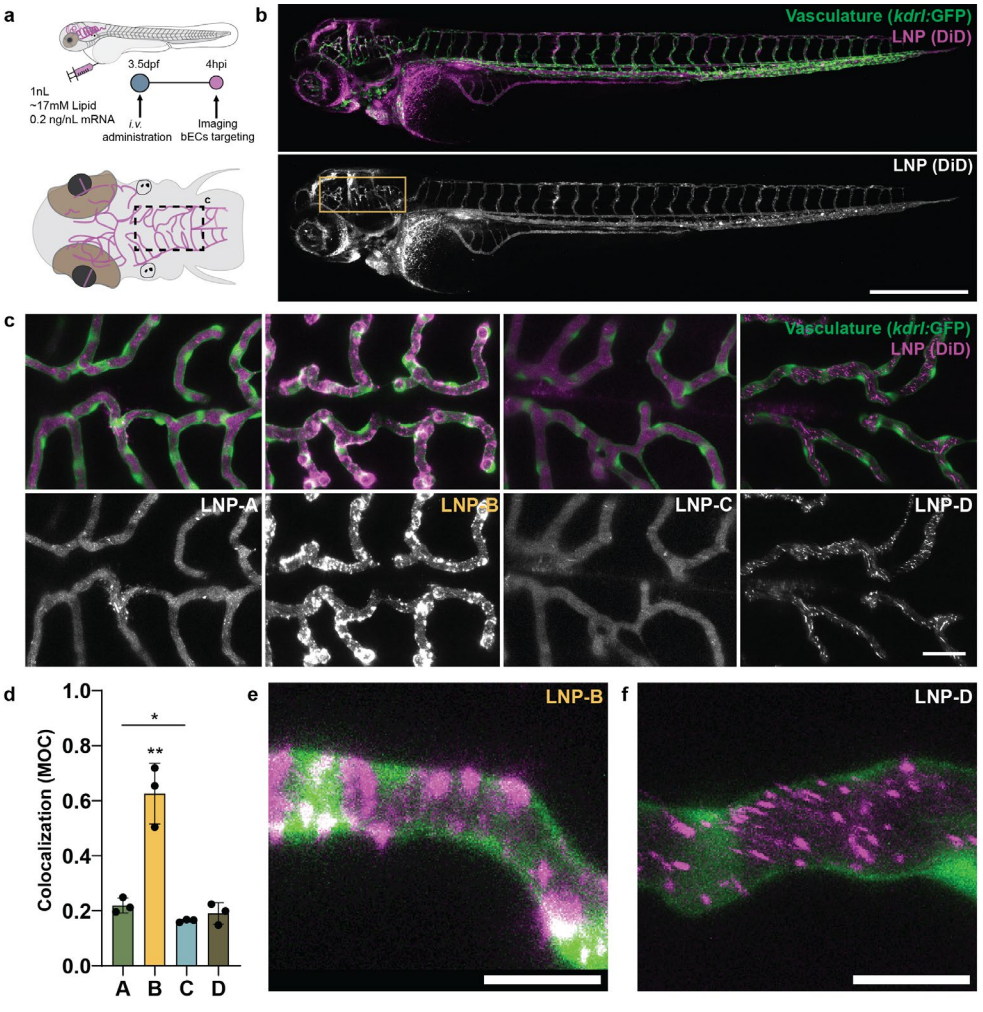

Figure 4. Biodistribution of mRNA-LNPs within zebrafish embryos (3.5 dpf). a) Timeline of experimental setup. **b)** Lateral view on 3.5 dpf zebrafish embryo revealing DiD-represented biodistribution (4 hpi) as an overlay of LNP-B (magenta, single channel white) and GFP positive vasculature (green). Yellow box indicates region of brain vasculature. **c)** Dorsal view on brain vasculature at 4 hpi revealing biodistribution of LNP-A, LNP-B, LNP-C and LNP-D. **d)** Quantification of Mander's Overlap Coefficient (MOC) for DiD signal in relation to GFP-positive vasculature. **e)** LNP-B (magenta) reveals colocalizing clusters with GFP-positive vasculature (green) in contrast to **f)** LNP-D which display clusters in the vasculature lumen. Scale bars: 500 µm (b), 25 µm (c), and 10 µm (e, f). Statistical significance was evaluated as ns: not significant ($p > 0.05$), significantly different *$p < 0.05$, **$p < 0.01$; ***$p < 0.001$. Note that B is significantly different to A, C and D. Exact p-values: A-B = 0.0034, A-C = 0.0263, A-D = 0.3533, B-C = 0.0019, B-D = 0.0030, C-D = 0.3081.

fluorescence within the vasculature lumen (**Figure 4c**). Formulation LNP-D, also revealed to be circulating freely (**Figure S3g**), however in a likely aggregated state represented by clusters localized in the vasculature lumen (**Figure 4c, f**). Strikingly, LNP-B revealed also strong fluorescent clusters, however these were localizing at the bECs, in contrast to LNP-D (**Figure 4c, e**). These dense localizations of DiD could be interpreted as either the result of LNP aggregation at the bECs *or* endosomal uptake. As bECs have a thickness close to the diffraction limit, excluding whether clusters remain intra- or extracellular was limited. Nonetheless, the combination of GFP-positive vasculature and far-red labeled LNPs allowed for quantification of their colocalization by using the Manders' Overlap coefficient (MOC) (**Figure 4d** and **Figure S3b, d, f, h**).[54] Quantification (n = 3) revealed that DiD labeled LNP-B localized preferentially at the bECs, compared to the other LNP formulations ($p<0.01$). This suggests an important, though not decisive, role for both ionizable lipid, as well as DOaG, in LNP-mediated cell selective targeting (no targeting for LNP-D). Moreover, as cryo-TEM revealed similar morphologies for LNP-B and LNP-D, it is suggested that phase separation does not warrant bEC targeting, however appears to be an important component for it, since non-phase separated formulations (LNP-A and C) do not reveal any targeting.

LNP targeting is required for transfection

To assess whether bEC-targeting of LNP-B results in local translation of its mRNA-cargo, we investigated the expression of mCherry protein at 36-38 hpi (**Figure 5a**). Whole fish and head were visualized for transfection **(Figure S4a, b, d, e, g, h, j, k**). Though visualized at n=1, it is worth noticing three findings from these acquisitions. First, DODAP containing formulations revealed overall relatively lower transfection levels in comparison to MC3 containing formulations (**Figure 5c** and **Figure S4a, b, d, e** compared to **4g, h, j, k**). This is in line with literature, where MC3 – compared to DODAP – has been demonstrated as a more potent ionizable lipid resulting in high transfection levels.[33] Secondly, LNP-C revealed high levels of transfection at the head and around the liver-swim bladder (**Figure 5c** and **Figure S4g, h**).

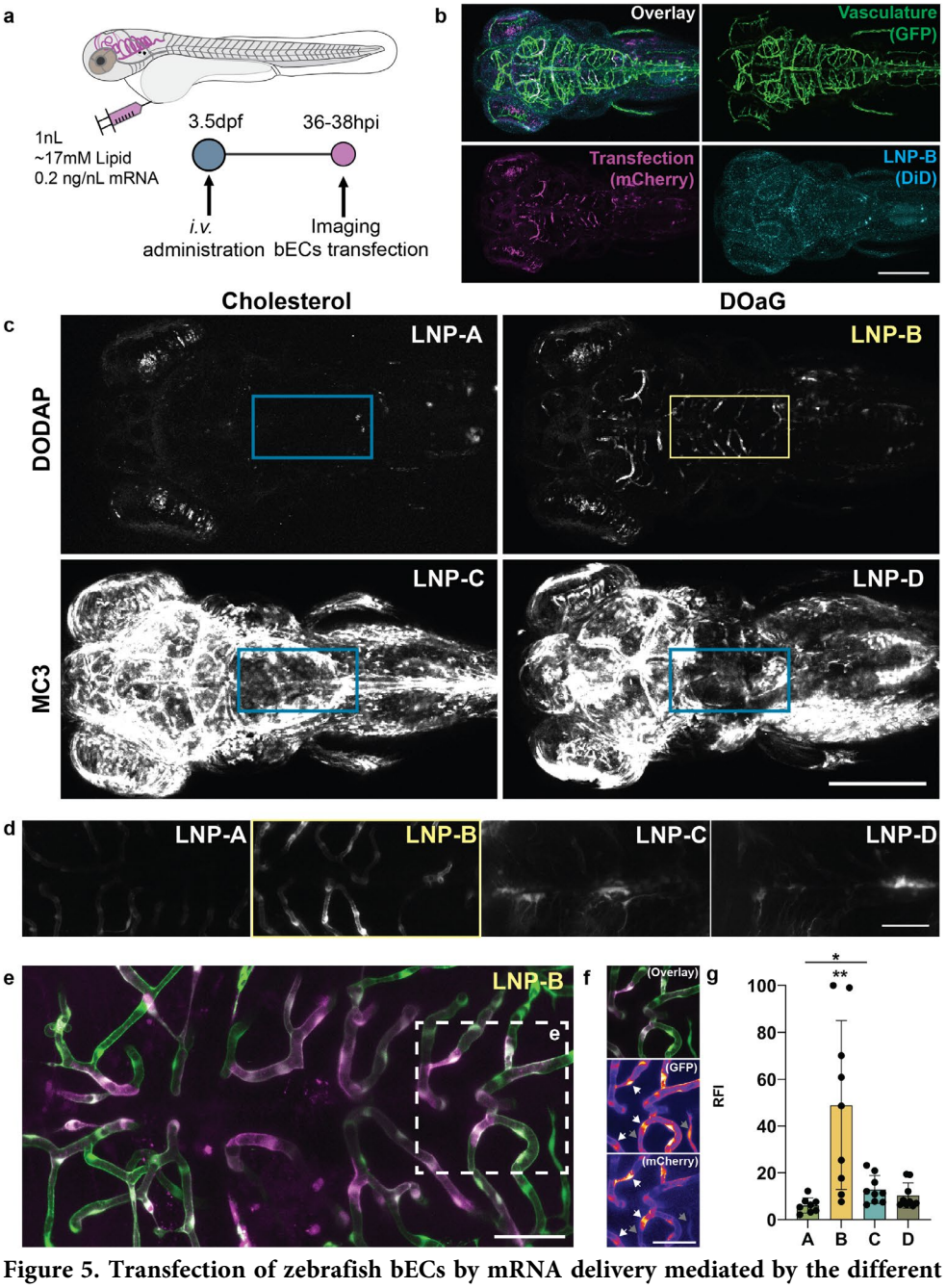

Figure 5. Transfection of zebrafish bECs by mRNA delivery mediated by the different LNP formulations. a) Schematic timeline of experimental setup. **b)** Dorsal view on the embryo's head 36-38 hpi of LNP-B, revealing GFP-positive vasculature (green), mCherry expression as result of transfection (magenta), DiD biodistribution (cyan) and overlay. **c)** mCherry expression as a result of transfection for each formulation in the head region of

the fish. **d)** Insets of (c) depicting confocal z-stacks of brain vasculature regions used for quantification studies. **e)** Overlay of mCherry expression (as mediated by LNP-B) and transgenic GFP positive vasculature. **f)** Inset of (e) depicting co-localization of GFP and mCherry (white arrows) and independent GFP fluorescence (gray arrows) indicating fluorescence as a result of transfection, not channel bleed-through **g)** Quantification of mCherry relative fluorescence intensity as a result of bECs transfection, per formulation. Scale bars: 250 μm (b, c) and 50 μm (d, e, f). Statistical significance was evaluated as ns: not significant ($p > 0.05$), significantly different *$p < 0.05$, **$p < 0.01$; ***$p < 0.001$. Note that B is significantly different to A, C and D. Exact p-values: A-B = 0.0045, A-C = 0.0113, A-D = 0.0742, B-C = 0.0093, B-D = 0.0059, C-D = 0.3460.

For LNP-C, 3D imaging of the head visualized mCherry expression rather at the exterior site of the brain, likely localized at the skin. Third, although with a lower Relative Fluorescence Intensity (RFI) than LNP-C and D, LNP-B revealed mCherry emission in the brain region from both lateral and dorsal perspective (**Figure S4d, e)**. A more detailed view at the brain vasculature (n=9) confirmed that mCherry expression in the head, as mediated by LNP-B, is indeed localized at the bECs with relatively high expression levels of transfection (**Figure 5c, d**). Differing fluorescent intensity- and/or localization profiles (e.g., GFP, mCherry, and DiD) excluded the potential of major channel bleed-through (**Figure 5b**). In contrast, LNP-A, C and D did not seem to result in transfection in bECs, as mCherry fluorescence was very low and likely present as a result of GFP bleed-through (**Figure 5d**). For LNP-B, high-resolution imaging revealed colocalization between GFP positive vasculature and mCherry transfection (**Figure 5e**), displaying specific (non-bleed-through) individual bEC transfection (**Figure 5f**, white arrow for GFP and mCherry positive, grey arrow for only GFP positive). Quantification (n = 9) revealed that mCherry expression in bECs is significantly higher for LNP-B than LNP-A, C and D ($p<0.01$, **Figure 5g** and **Figure S4c, f, i, l**). In summary, LNP-B results in specific bEC targeting compared to non-targeting LNP-A and non-targeting - but highly transfecting - LNP-C and D. Together, this study indicates that specific targeting of bECs in zebrafish embryos is required for mRNA delivery resulting in concomitant protein expression.

5.3 Discussion and Conclusion

This work describes an LNP screening study in zebrafish embryos, in which novel DOaG-containing mRNA-LNPs (LNP-B) are found to selectively target the embryos' bECs, a subset of endothelial cells. After the selective targeting and accumulation of LNPs, selective mRNA delivery, bEC transfection, and concomitant protein expression is observed. Although two of the formulations achieve higher transfection levels throughout the whole fish (LNP-C and D), they lacked selective bEC transfection. This highlights that cell specific LNP targeting is required for cell specific mRNA delivery and translation, in contrast to a shotgun approach where tissue of interest is usually exposed to non-specific, highly potent nanomedicines.

Furthermore, replacement of cholesterol with DOaG resulted in LNPs that target bECs, indicating a potential role of DOaG for this selectivity. However, to achieve selective accumulation, clustering in circulation should be avoided. This is because the two DOaG-containing LNPs (LNP-B and LNP-D) revealed opposing biodistribution patterns, where the non-targeting LNP-D seemed to cluster in circulation, suggesting colloidal instability *in vivo*. Here, the transparent zebrafish model, which enables real time imaging, allowed us to conclude that to achieve cell specific targeting, colloidal stability of LNPs *in vivo* is an important requirement.

Moreover, this proof-of-concept study highlights that switching one only lipid component dramatically affects the LNP biodistribution (*i.e.*, DOaG vs. cholesterol). Similarly, replacing DODAP with MC3 results in a formulation (LNP-D) that cannot achieve cell specific targeting, probably due to clustering in circulation. This suggests that DOaG-related specificity is achieved in combination with the ionizable lipid DODAP. This opens new avenues for exploring different lipid ratios between the LNP-B lipid components, or combinations of DOaG and/or DODAP with different - ideally more potent - ionizable lipids, to enhance the transfection potency. Overall, understanding the effects of lipid composition on LNP properties is vital for rational nanoparticle design. Especially for multicomponent systems such as LNPs, ultrastructure, stability and overall physicochemical properties are a result of specific lipid packing, and therefore a one-fits-all approach for design should not be utilized.

Interestingly, DOaG-containing LNP-B promotes cell selective biodistribution in zebrafish embryos with a yet unknown mechanism. Given that TGL plays a role on selective bEC targeting by DOaG-containing liposomes (PAP3) as previously described,[50] it is likely that a similar mechanism is involved in the LNP-B uptake. However, experiments will have to be conducted to prove this hypothesis.

Although the novel morphology of LNP-B may contribute to the bEC targeting, it is very important to note that LNP-B and D have a very similar macromolecular structure. LNP-B targets the bECs with relatively high specificity, whereas LNP-D is presented as clusters in circulation. We hypothesize that there is a molecular difference between those two formulations that is beyond the resolution of cryo-TEM. This difference at the molecular level could contribute to the clustering of LNP-D which prevents accumulation in bECs. Further studies are required to elucidate the mechanism of targeting and whether the phase-separated LNP morphology is essential.

DAGs are lipids with several interesting properties including fusion promotion, polymorphism, and according to this and our previous studies,[50,51] protein recruitment and cell selectivity. One potential advantage of using DAGs as lipid components in LNPs, is their propensity to form inverse hexagonal phases which can potentially facilitate endosomal escape, leading to higher transfection efficiencies. Also, their general ability to induce phase separation in LNPs could propel higher transfection potencies, similarly to recently described phase-separated blebs in LNP systems.[55]

The initial discovery of phase separation as a novel targeting concept [50] resulted in the development of a second-generation formulation (mRNA-LNP). Combined with previous studies[24,56–58] we demonstrate that zebrafish embryos is a robust *in vivo* screening model for the discovery or bottom-up development of nanoparticle formulations with an enhanced *in vivo* function. This is because zebrafish offer the ability to observe nanoparticle biodistribution and behavior in real time and at a cellular level. Based on a workflow involving thorough nanoparticle characterization (size, polydispersity, charge, morphology, cargo-loading) in combination with this screening model/tool, we have developed mRNA-LNPs that specifically transfect bECs in zebrafish embryos. Additional research is needed to investigate whether the selective gene delivery in zebrafish bECs is translatable in

mammalian animals. Previously on a mouse study, rapid clearance of PAP3 liposomes in organs such as the liver and spleen was observed. [50] Similar clearance may be expected for LNP-B, however, given that LNP-B is more stable than PAP3 liposomes (stable for at least up to 1 month compared to ~7 days) (**Figure S5**) it may circumvent rapid clearance and exhibit different biodistribution patterns. However, if a TGL mediated pathway is involved as with PAP3 liposomes, it is likely that organs such as the liver, but also heart and reproductive organs, may be targeted.

Achieving selective delivery of *functional* oligonucleotide cargo to brain vasculature in zebrafish embryos, demonstrates the potential for disease specific therapies based on design of cell selective LNPs. Although these studies have been performed in only one type of species and differences in expression may be expected across species,[59] the zebrafish embryo can be the starting point for translational studies. Nonetheless, the fact that transfection of brain vasculature *is* possible, provides hope and potential for novel drug delivery strategies for brain- and CSF related diseases. Oligonucleotide delivery to brain vasculature could serve as a *trojan horse* by having brain endothelium selectively produce and secret therapeutic proteins (*e.g.*, monoclonal antibodies[60] or growth factors[61]) at the basolateral side into CSF, thereby reaching brain (diseased) tissue. Recent endeavors support this strategy,[62] where endothelial-specific mouse adeno-associated virus capsids were used to genetically engineer the blood-brain barrier into a functional 'biofactory' to rescue synaptic deficits. Another approach would encompass mRNA- and/or siRNA delivery to brain endothelial cells and could (back) gain control over brain homeostasis in diseased states,[63] thereby providing opportunities for novel, future RNA-based therapies.

In summary, we have successfully demonstrated selective transfection of brain endothelial cells *in vivo*, based on LNP cell-selective targeting. This proof-of-concept LNP formulation provides an intersection from which parallel routes can be taken, including investigation of bEC gene expression/suppression at embryonic stages, translational and mechanistic studies, formulation optimization, structure-activity relationship studies in combination with Cryo-TEM, and exploration of potential role of diacylglycerol lipids in the field of nanomedicine.

5.4 Materials and Methods

General reagents: 1,2-distearoyl-*sn*-glycero-3phosphocholine (DSPC), 1,2-dioleoyl-3-dimethylammonium-propane (DODAP), CHO and DMPE-PEG2k were purchased from Avanti Polar Lipids. Additional DSPC was purchased from Lipoid GmbH. MC3 was purchased from Biorbyt. 1,1'-Dioctadecyl-3,3,3',3'-Tetramethylindodicarbocyanine, 4-Chlorobenzenesulfonate Salt (DiD) was purchased from Thermo Fisher Scientific. mCherry mRNA (CleanCap®, 5moU, 1 mg/mL in 1 mM Sodium Citrate pH=6.4) was purchased from Trilink Biotechnologies, aliquoted in nuclease-free Eppendorf tubes and stored at -80 °C. All other chemical reagents were purchased at the highest grade available from Sigma Aldrich and used without further purification. All solvents were purchased from Biosolve Ltd. Ultrapure MilliQ® water, purified by a H_2O Advantage A10 water purification system from MilliPore, was used throughout. Nuclease-free Ultrapure MilliQ® water was made in house.

Synthesis of DOaG lipid: DOaG lipid was synthesized as reported in Chapter 2.

LNP formulation: Encapsulation of mRNA and simultaneous formation of lipid nanoparticles in a Nitrogen to Phosphate ratio (N/P ratio) of 6, was performed as previously described.[24] In brief, individual lipid components (DSPC, DMPE-PEG2k, DOaG or CHO, DODAP or MC3) as stock solutions in chloroform (1-10 mM), were combined to the desired molar ratios and dried to ensure complete removal of chloroform, first under a stream of N_2, then >1 h under vacuum. The non-exchangeable tracer DiD was also added to the lipid mixtures at a total lipid concentration of 0.1% mol. Lipid films were re-dissolved (with vortrexing) in 200 µL of absolute ethanol at a total lipid concentration of 5.31 mM. In another vial, 30 µL of mRNA encoding mCherry (1 mg/mL) were diluted up to 600 µL with nuclease-free sodium citrate buffer (pH 4, 16.7 mM trisodium citrate dihydrate and 30.5 mM citric acid monohydrate). Controlled rapid mixing of the two solutions was achieved by using a custom-made T-junction mixer, equipped with syringe pumps (fusion 100-X, Chemyx Inc., Stafford, USA) and syringes with an inner diameter of 4.78 mm. The total flow rate was 2 mL/min, with a flow rate ratio of 3:1 v/v citrate buffer: ethanol). The resulting LNP formulations were dialyzed overnight against nuclease-free PBS (pH=7.4). After that, they were

concentrated at 4 °C to the lowest volume possible by centrifugation at 2000-3000 g using 100K MWCO centrifugal filters (Amicon® Ultra, Merck) resulting in mRNA-LNPs with [total lipid] ~16-18 mM. Microfluidic mixing and mRNA were handled with nuclease-free lab consumables and gloves throughout.

Encapsulation efficiency and mRNA concentration determination after LNP formation: Encapsulation efficiency and mRNA concentration were determined using the high range assay of Quant-iT™ RiboGreen® RNA assay kit (Invitrogen®, ThermoFisher Scientific) with nuclease-free TE buffer throughout. Briefly, to determine the unencapsulated mRNA [$mRNA_{free}$] in the sample, 10 µL of each LNP formulation (100x diluted with nuclease-free, filtered PBS) was added in a 96 well plate (Greiner, black). To determine the total mRNA in each sample [$mRNA_{total}$], 10 µL of each formulation was added to wells mixing in 10 µL of 1% triton X-100 (prepared with nuclease-free H_2O). The samples were diluted to 100 µL with TE buffer and subsequently 100 µL of RiboGreen reagent was added. Fluorescence intensity (λ_{ex} = 485 nm, λ_{em} = 530 nm) was determined using a fluorescence microplate reader (Infinite®, M1000 pro, TECAN) 5 min after adding the RiboGreen reagent. The mRNA concentration (mg/ml) was determined for every individual experiment using a calibration curve. Encapsulated mRNA was determined with the following equation: [$mRNA_{encapsulated}$] = [$mRNA_{total}$] – [$mRNA_{free}$] and encapsulation efficiency by: EE% = $(\frac{[mRNAencapsulated]}{[mRNAtotal]})$ x 100%. All measurements were conducted in triplicate. All preparations were handled with nuclease-free lab consumables and gloves throughout. For administration in embryonic zebrafish ($V_{injection}$ = 1 nL) the LNP formulations were diluted to contain [mRNA] = 0.2 mg/mL.

Size and zeta potential measurements: Particle size and PDI values were obtained by using a Malvern Zetasizer Nano ZS. DLS measurements (operating wavelength = 633 nm), were carried out at room temperature in PBS (pH=7.4) at a [total lipid] = 100 µM. Zeta potential of each LNP formulation was measured at [total lipid] = 500 µM, using a dip-cell electrode (ZEN1002, Malvern), at room temperature and at [NaCl] <20 mM. All reported DLS and zeta potential measurements are the average of three measurements.

Cryogenic transmission electron microscopy: mRNA-LNP formulations (3.5 µL) were applied to a freshly glow-discharged carbon 200 mesh Cu grid (Lacey carbon film, Electron Microscopy Sciences, Aurion, The Netherlands). Grids were blotted for 3 s at 99% humidity in a Vitrobot plunge-freezer (FEI VitrobotTM Mark III, Thermo Fisher Scientific), with a waiting time of 30 sec before blotting. Cryo-TEM images were collected on a Talos L120C (NeCEN, Leiden University) operating at 120 kV, equipped with a Ceta camera and LaB6 filament. Images were recorded manually at a nominal magnification of 11000 or 13500x for low magnification images yielding a pixel size at the specimen of 9.47 or 7.44 ångström (Å), respectively. For high magnification images a nominal magnification of 28000 or 36000x was used, yielding a pixel size at the specimen of 3.46 or 2.84 ångström (Å), respectively.

Cryo-electron tomography: Cryo-ET was performed on a Titan Krios microscope operating at 300 kV equipped with a K3 direct electron detector and BioQuantum energy filter (NeCEN, Leiden University). Tilt series were collected without the use of fiducials with SerialEM[64] at a nominal magnification of 19500x (4.4 Å/pixel) and 42000x (2.17 Å /pixel), respectively, using a dose-symmetric tilt scheme from -50° to 50° with 2° increments and a total dose of 100 e-/ $Å^2$. Tomograms were reconstructed using the IMOD software package.[65]

Zebrafish husbandry and injections: Zebrafish (*Danio rerio*, Tg (*kdrl*:GFP)^{s843})[66] were, in compliance with the directives of the local animal welfare committee of Leiden University, handled and maintained according to Zebrafish Model Organism Database guidelines (http://zfin.org, 2023). Natural spawning at beginning of light period was used for fertilized egg collection, which were subsequently grown at 28.5 °C in egg water (60 g/ml Instant Ocean Sea salts). Zebrafish embryos were anesthetized and embedded in 0.4% (w/v) agarose containing 0.01% tricaine. Screening studies from injection to image analysis were kept blind. Formulations were injected in the Duct of Cuvier at 3.5 dpf stage as previously described [67] ($V_{injection}$ = 1 nL volume, [mRNA] = 0.2 mg/mL per embryo). Zebrafish were qualified as correctly injected when formulation fluorescence correlated with vasculature and no backward translocation of erythrocytes and/or yolk damage was detected. Fish were randomly selected from a group of correctly injected embryos. Confocal microscopy was performed at 4 hpi

and 36-38 hpi and embryos were imaged by overlapping z-plane. Images for quantification were performed using a Leica TCS SP8 confocal microscope, with a 40X water-immersion objective (HCX APO L) and photon count as detection method. Laser intensity, gain, and offset settings were kept identical for unbiased quantification.

Confocal imaging and processing: Images were processed using software (Fiji) ImageJ 2.9.0/1.53t; Java 1.8.0_172 (64- bit). To enhance visualization of the biodistribution in lateral 10× images, mCherry/DiD channel 'Diplay Range Max' was manually optimized; for 40X quantification all settings were kept equal. For targeting studies (4 hpi, DiD channel) number of embryos per group was kept at n=3 due to logistic trade-off in imaging time and hpi, whereas for transfection studies (36-38 hpi, mCherry channel) number of embryos per group was set at n=9. Number of embryos for group A was n=8, as one of the injected embryos was excluded due to damaging of the embryo during transfer.

Quantification of bEC targeting and transfection: Quantification was performed as described in macros using Fiji (see Supplementary Information). Briefly, two methods of quantification were performed: i) GFP positive bEC colocalization with DiD at 4hpi, and ii) quantification of mCherry Fluorescence Intensity that colocalized with GFP positive bEC. For first colocalization studies images were processed in Fiji using Plugin "JACOP" [68] and expressed in a bar plot as a result of MOC. For transfection studies, a mask was created as described in macro, to exclude bEC-negative mCherry from quantification, whereafter leftover fluorescence intensity was quantified and displayed as RFI in a bar plot.

5.5 Supplementary Information

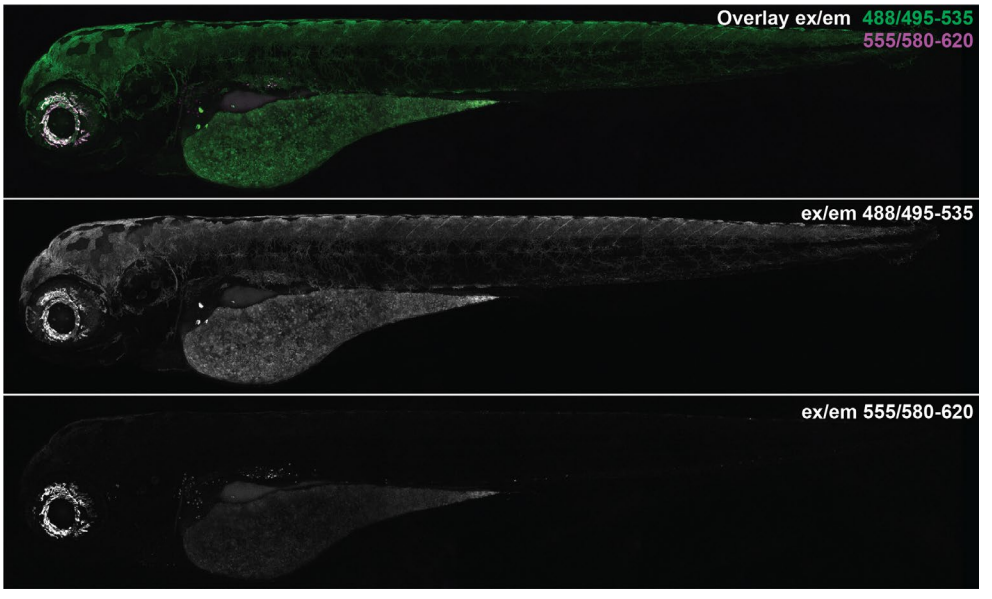

Figure S1. Autofluorescence levels of a 3.5 dpf ABTL zebrafish embryo (wild type) in green (ex/em: 488/495-535 nm) and red channels (ex/em: 555/580-620 nm) and overlay thereof.

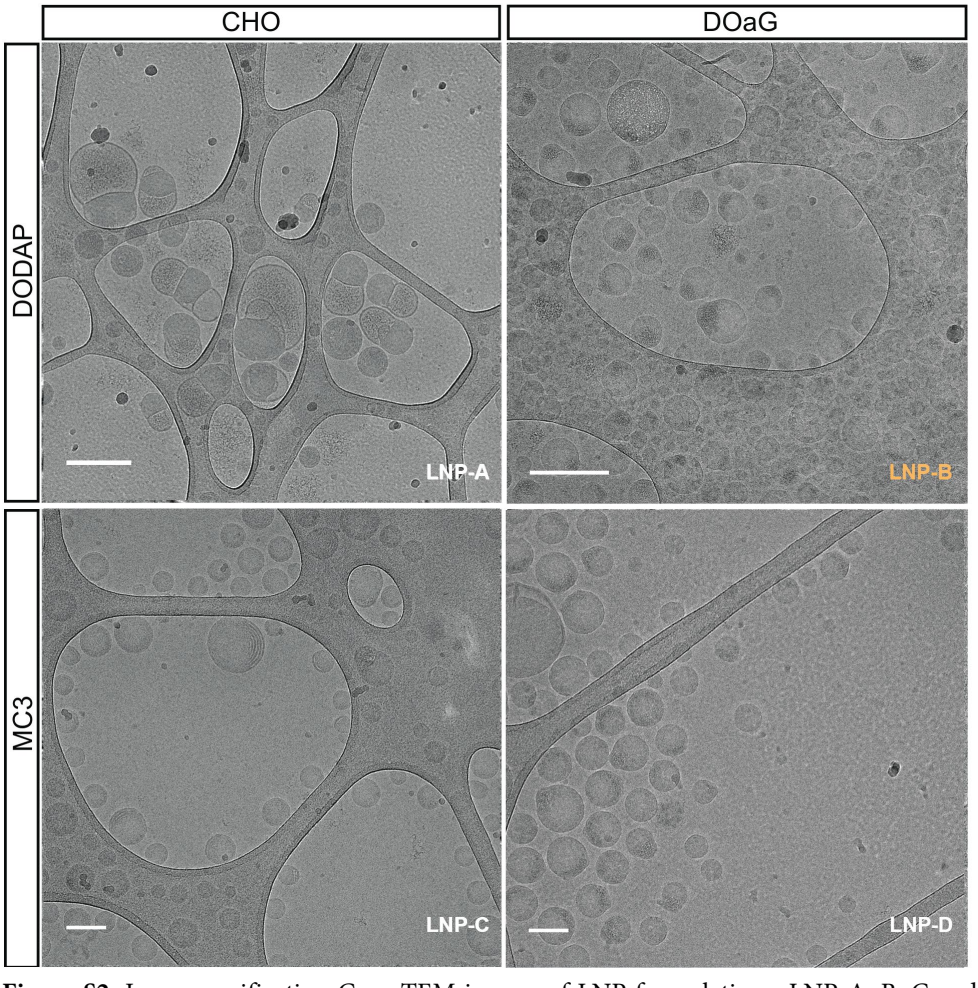

Figure S2. Low magnification Cryo-TEM images of LNP formulations, LNP-A, B, C and D. Scale bars: 200 nm.

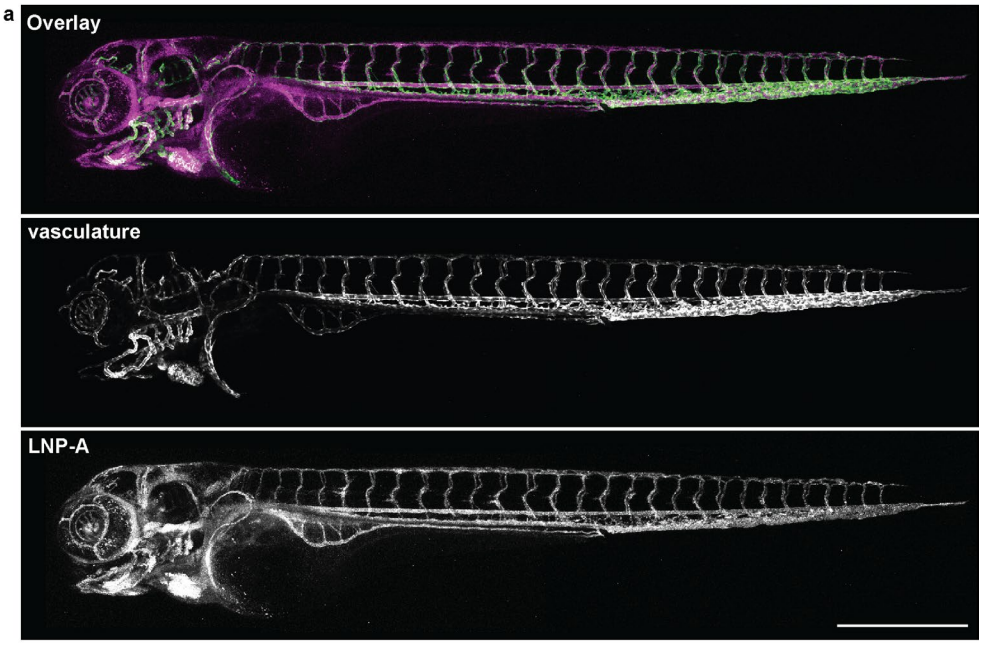
a
Overlay
vasculature
LNP-A

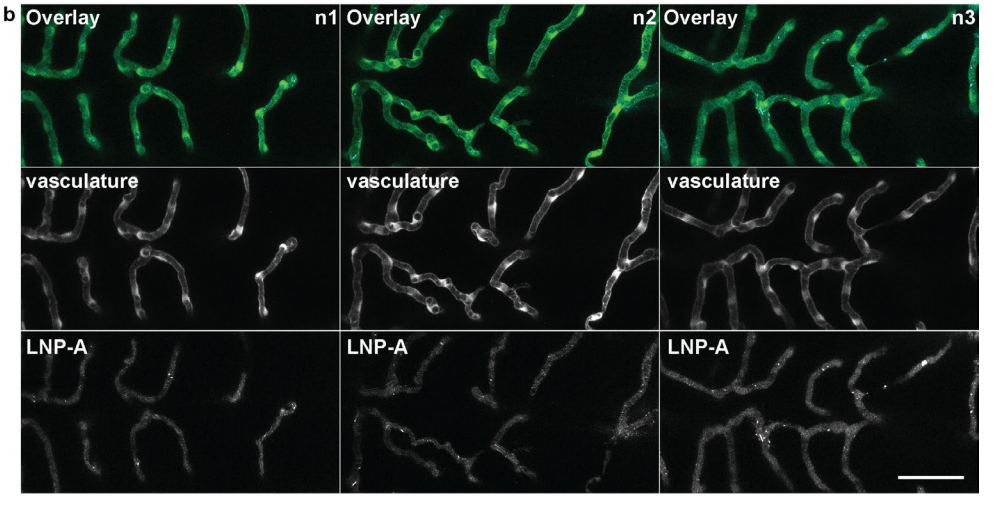
b
Overlay
n1
Overlay
n2
Overlay
n3
vasculature
vasculature
vasculature
LNP-A
LNP-A
LNP-A

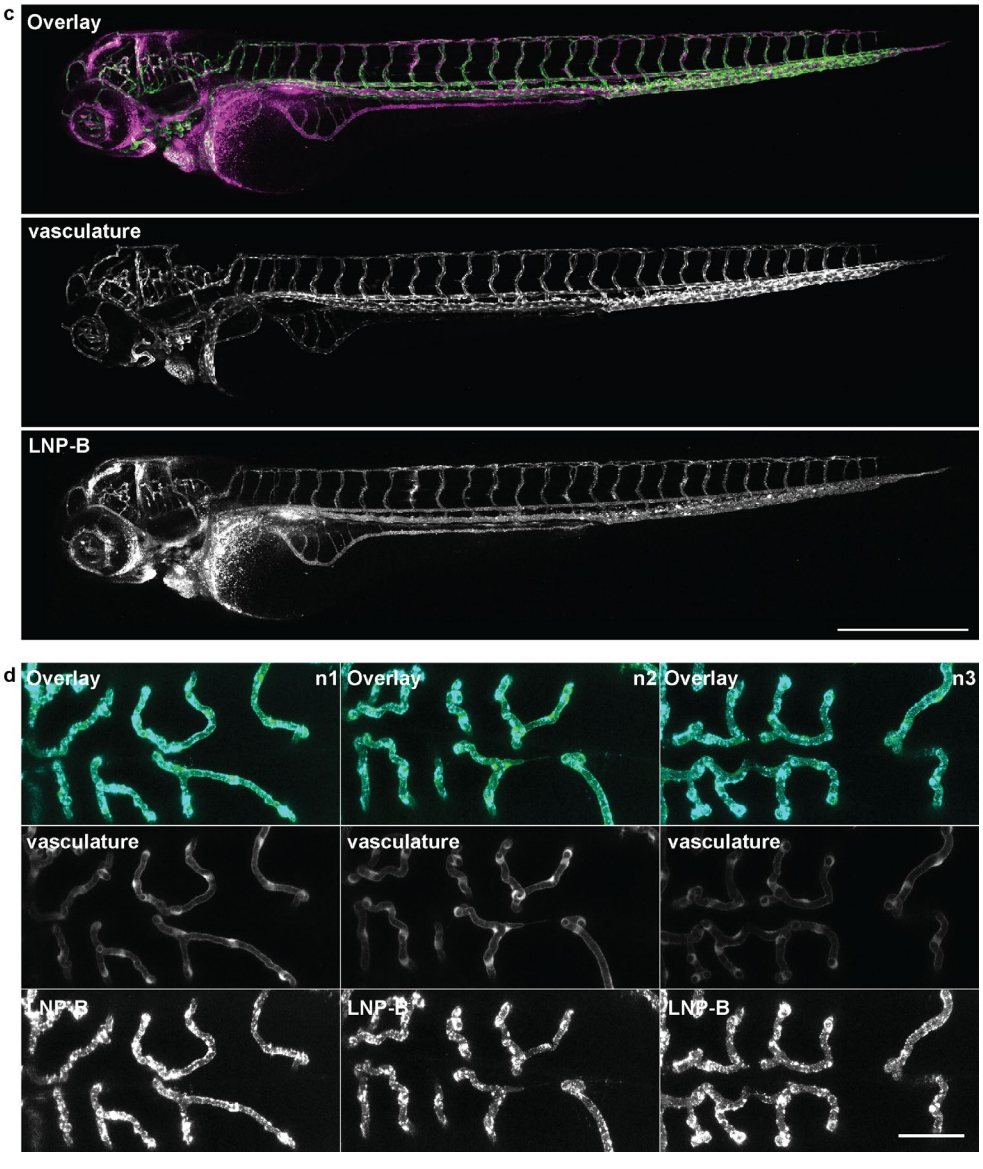
c
Overlay
vasculature
LNP-B
d
Overlay
n1
Overlay
n2
Overlay
n3
vasculature
vasculature
vasculature
LNP-B
LNP-B
LNP-B

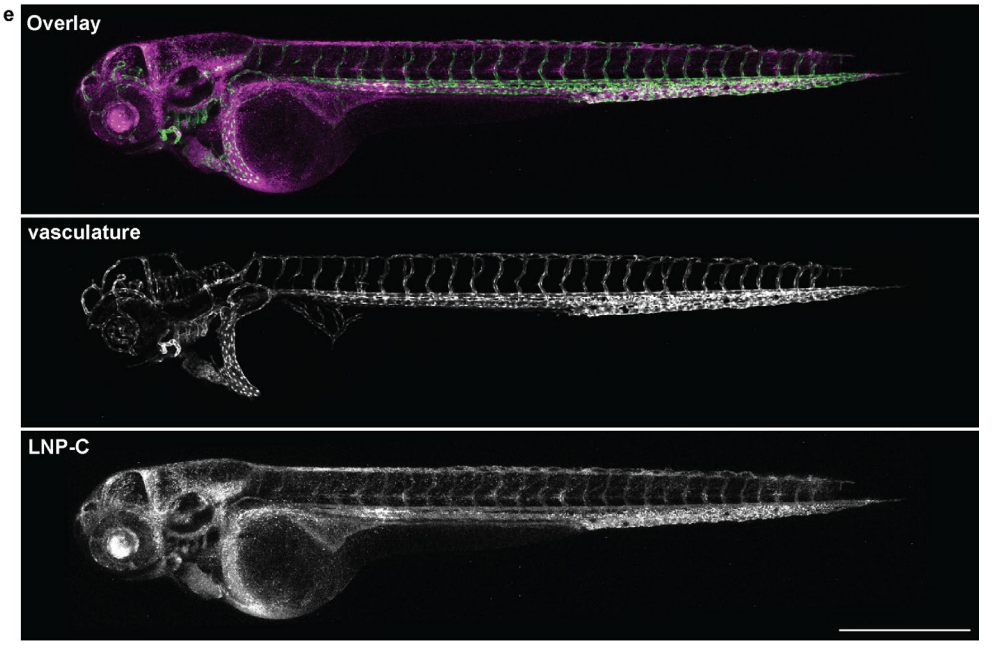
e
Overlay
vasculature
LNP-C

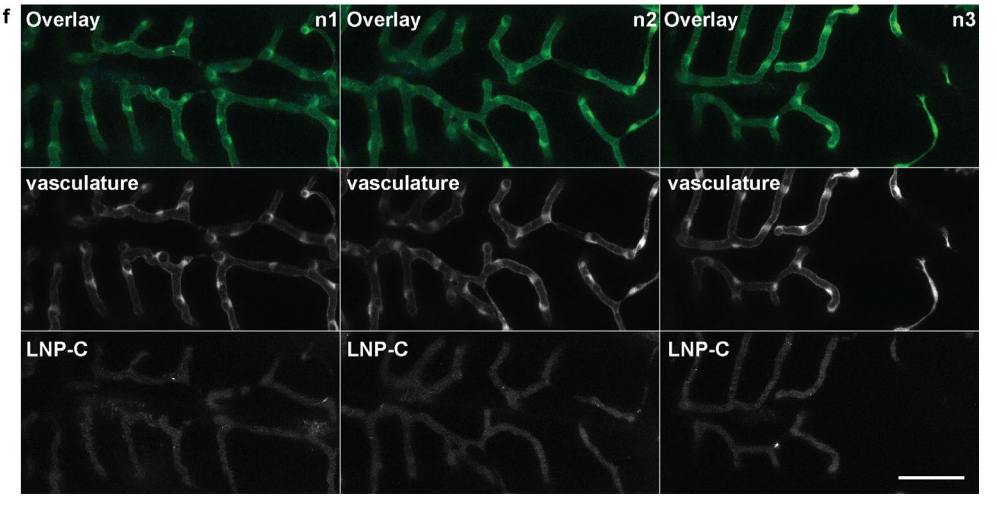
f
Overlay
n1
Overlay
n2
Overlay
n3
vasculature
vasculature
vasculature
LNP-C
LNP-C
LNP-C

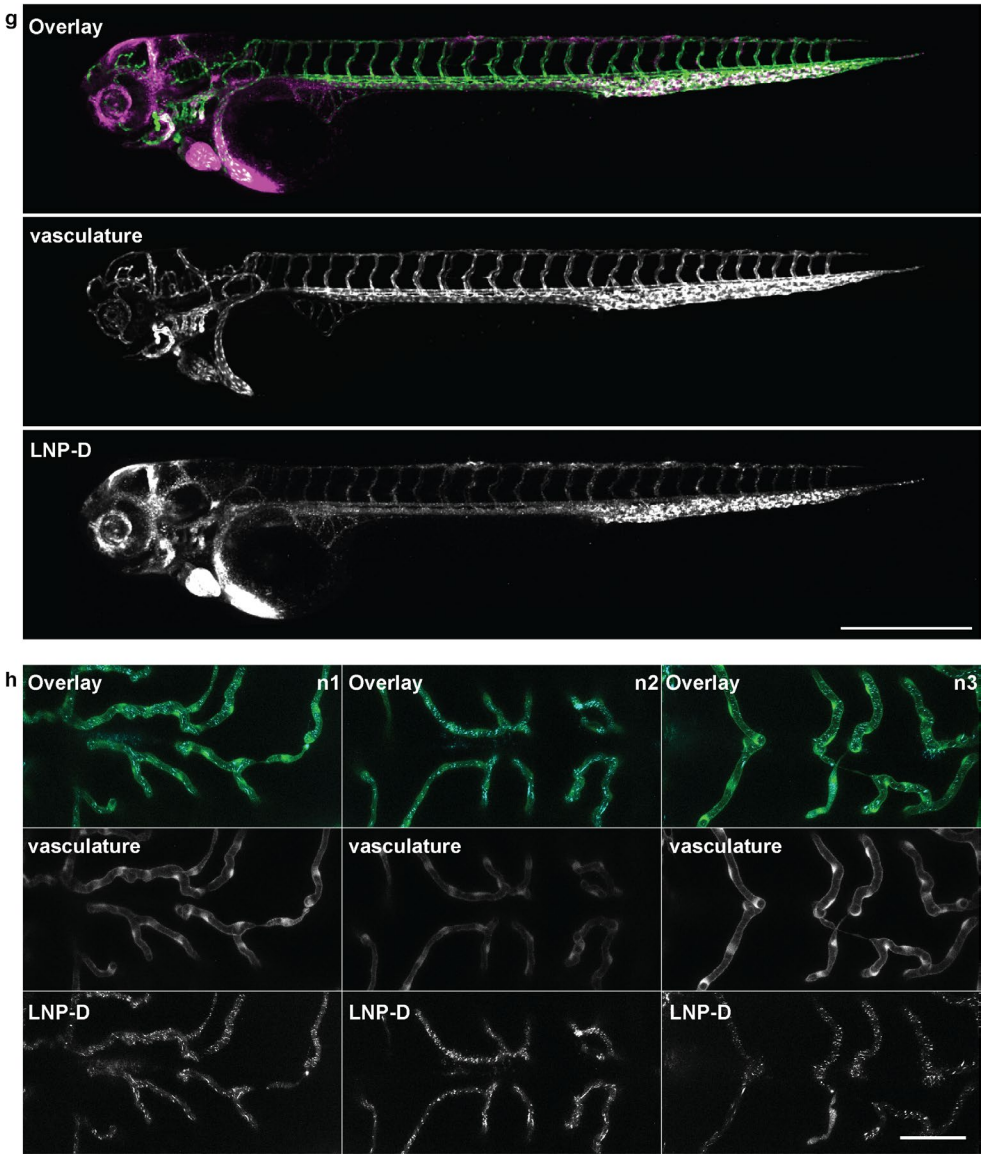

Figure S3. Biodistribution studies of LNP-A (**a, b**), -B (**c, d**), -C (**e, f**), and -D (**g, h**), in which (**a, c, e, g**) represent LNP biodistribution in lateral view on whole embryo, whereas (**b, d, f, h**) represent dorsal view on brain vasculature and LNP localization. Scale bars: 500 μm (a, c, e, g) and 50 μm (b, d, f, h).

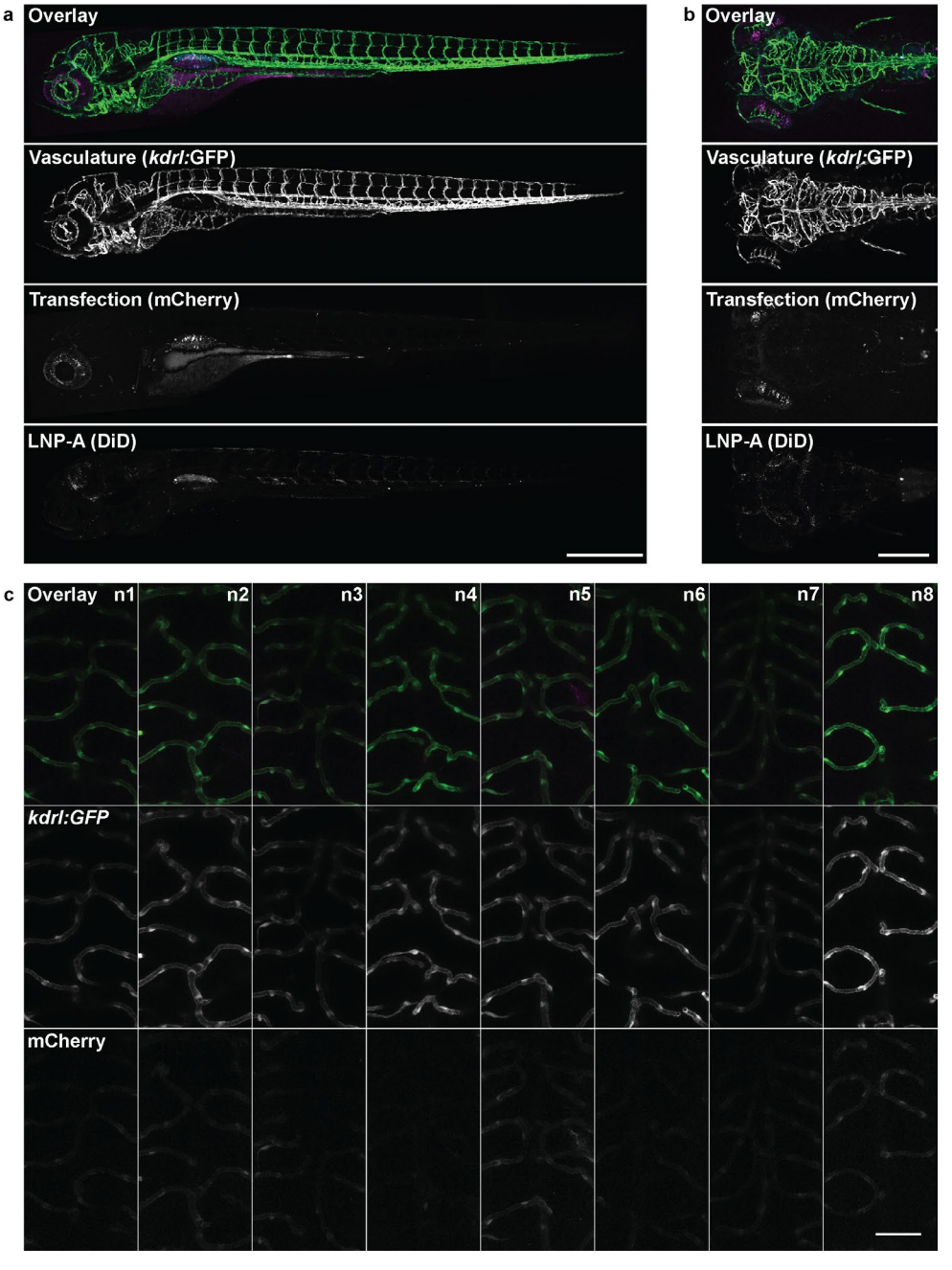
a
Overlay
Vasculature (kdrl:GFP)
Transfection (mCherry)
LNP-A (DiD)
b
Overlay
Vasculature (kdrl:GFP)
Transfection (mCherry)
LNP-A (DiD)
c
Overlay
n1
n2
n3
n4
n5
n6
n7
n8
kdrl:GFP
mCherry

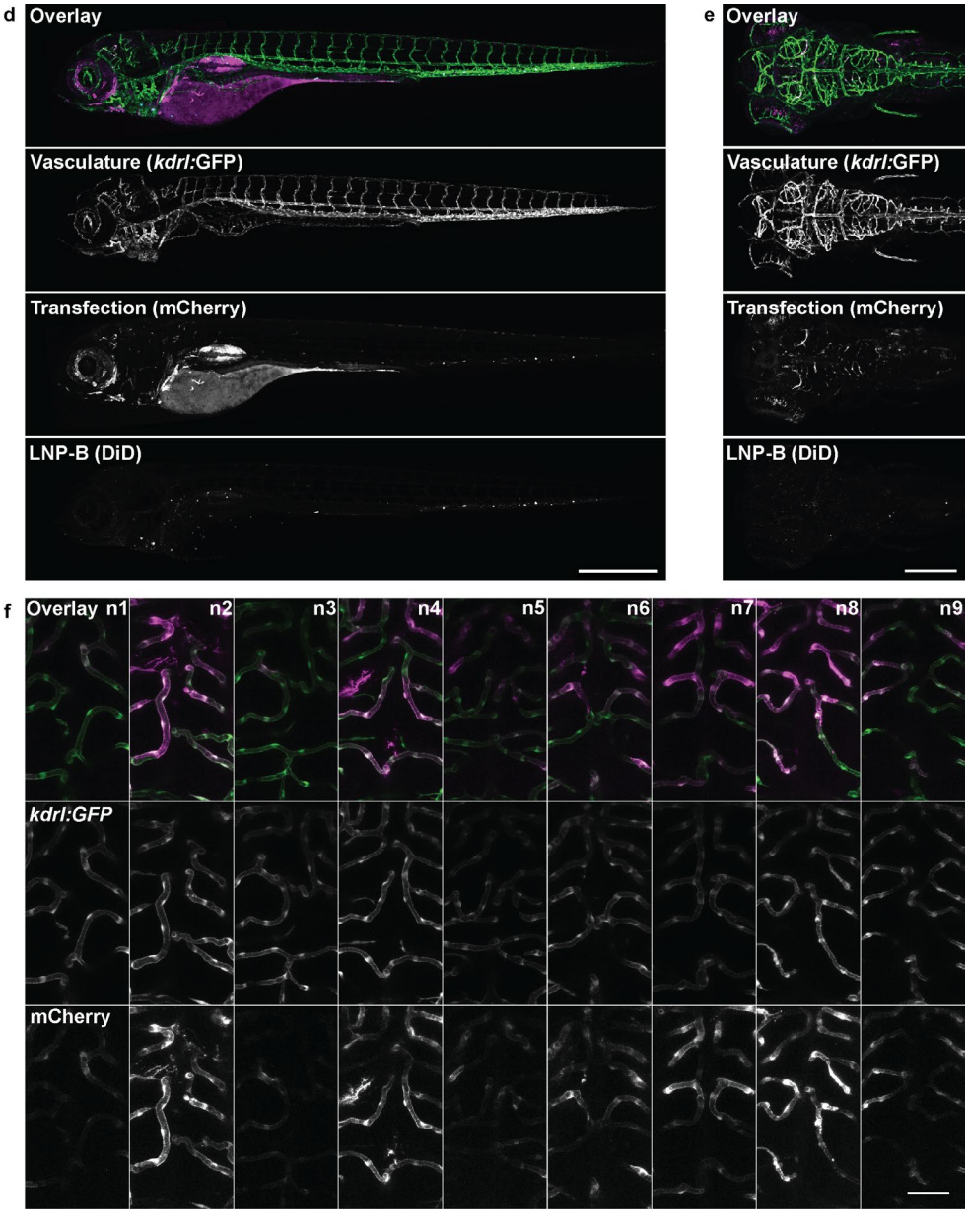
d
Overlay
Vasculature (kdrl:GFP)
Transfection (mCherry)
LNP-B (DiD)
e
Overlay
Vasculature (kdrl:GFP)
Transfection (mCherry)
LNP-B (DiD)
f
Overlay
n1
n2
n3
n4
n5
n6
n7
n8
n9
kdrl:GFP
mCherry

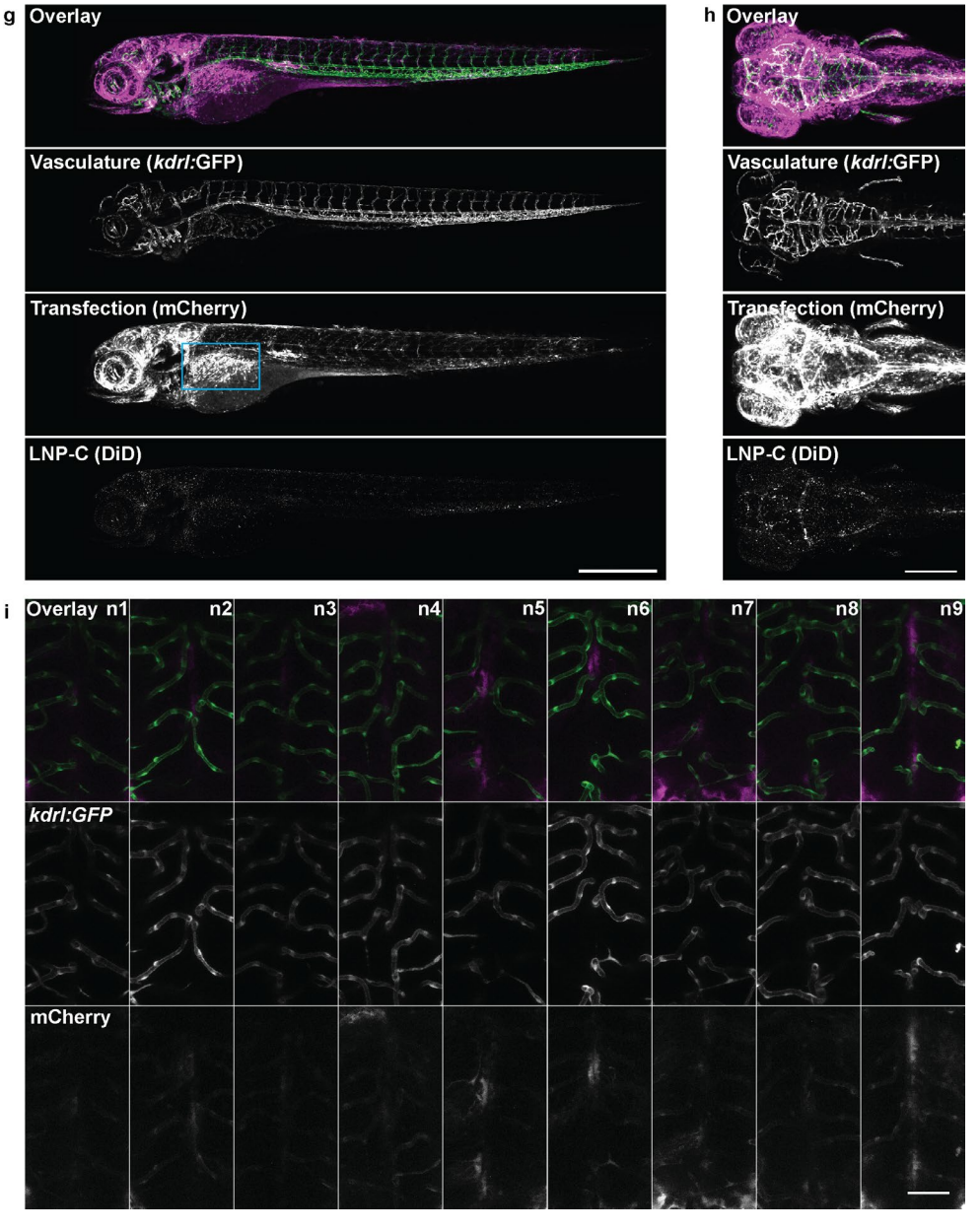
g
Overlay
Vasculature (kdrl:GFP)
Transfection (mCherry)
LNP-C (DiD)
h
Overlay
Vasculature (kdrl:GFP)
Transfection (mCherry)
LNP-C (DiD)
i
Overlay n1
n2
n3
n4
n5
n6
n7
n8
n9
kdrl:GFP
mCherry

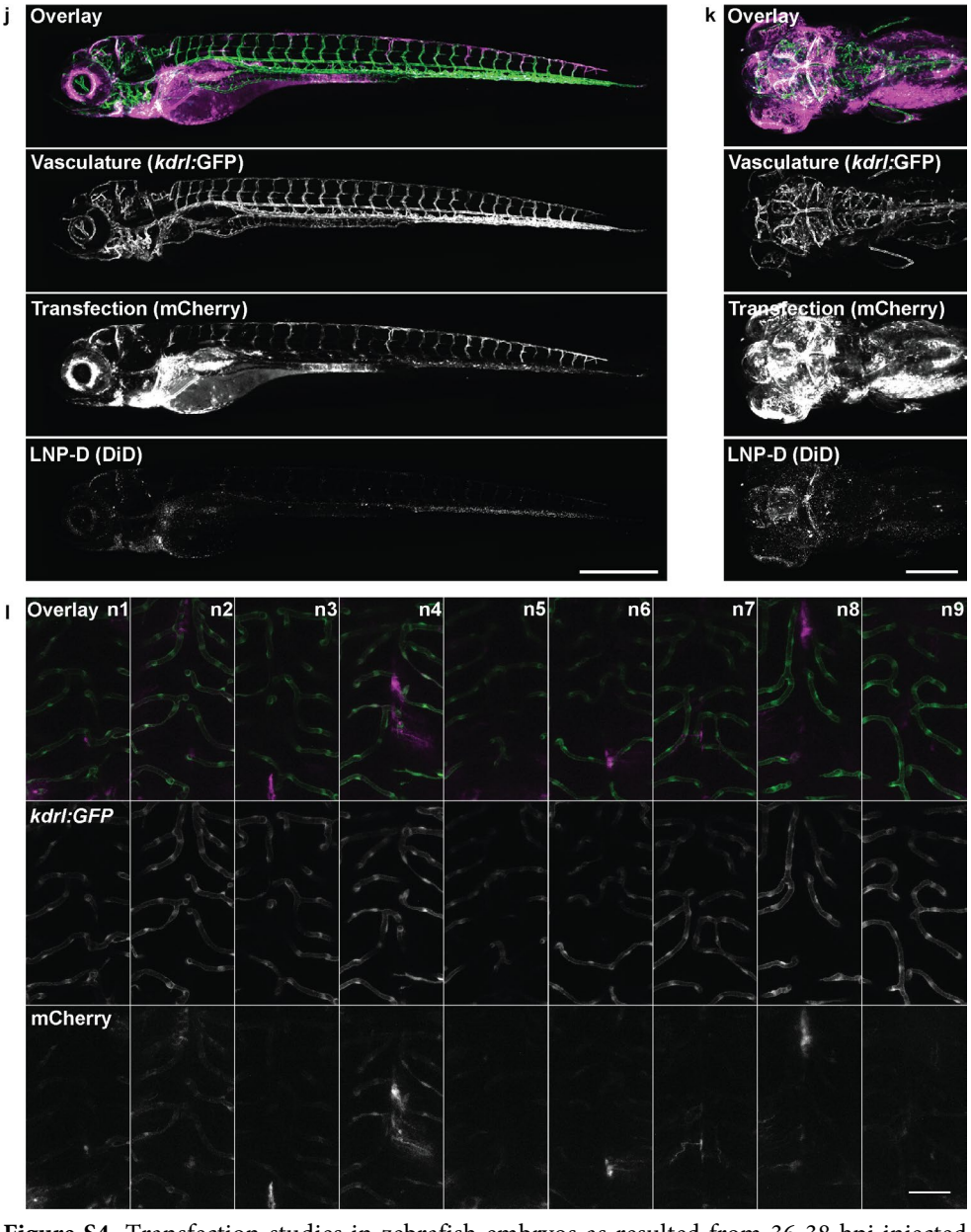

Figure S4. Transfection studies in zebrafish embryos as resulted from 36-38 hpi injected LNP-A (**a-c**), B (**d-f**), C (**g-i**), and D (**j-l**) in which (**a, d, g, j**) represent lateral whole embryo biodistribution and transfection, (**b, e, h, k**) represent dorsal biodistribution and transfection in zebrafish head region, and (**c, f, i, l**) display dorsal view on brain vasculature and transfection levels. Blue box in g indicates the liver/swim bladder. Scale bars: 500 μm (a, d, g, j), 250 μm (b, e, h, k), and 50 μm (c, f, i, l).

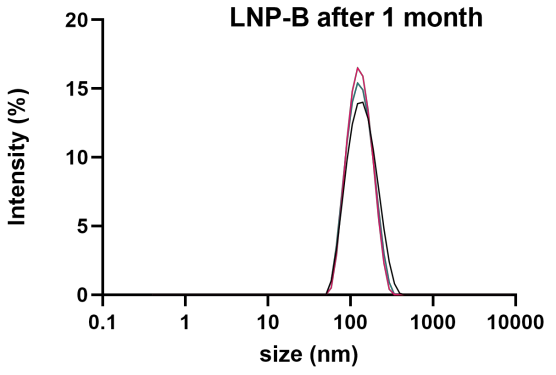

Figure S5. Stability of LNP-B. LNP-B as measured by DLS 1 month after formulation. Average diameter: 124.4 nm, PDI: 0.103.

Image acquisition and settings

Lateral: Leica SP8, 10X 0.4NA magnification, HyD detector

Dorsal: Leica SP8, 10X 0.4NA or 40X 0.8NA magnification, HyD detector

GFP detection: 488 nm laser excitation in 506-526 nm emission window

mCherry detection: 552 nm laser excitation in 600-620 nm emission window

DiD detection: 638 nm laser excitation in 650-670 nm emission window

Lateral: 1024x800 pixels, zoom 1.0, image speed 400, z-step 3.6 um, pinhole 1.0

Dorsal: 1024x500 pixels, zoom 1.28, image speed 700, z-step 3.6 um, pinhole 1.0

Stored as: '20210428 kdrlGFP 3.5dpf formulations bbbtargeting 18mM 4hpi DiD (2)'

Fiji Image reconstruction

For 4 hpi, DiD vs GFP colocalization

```
rename("stack1");
run("Make Substack...", "channels=1,3 slices=1-45");
run("Split Channels");
close("stack1");
run("JACoP ");
selectWindow("C2-stack1-1");
```

```
selectWindow("C1-stack1-1");
selectWindow("C2-stack1-1");
selectWindow("C1-stack1-1");
run("JACoP ", "imga=C1-stack1-1 imgb=C2-stack1-1 thra=50 thrb=130 pearson mm");
```

For 38 hpi, mCherry vs GFP colocalization

```
run("Make Substack...", "channels=1,3 slices=1-43");
run("Z Project...", "projection=[Max Intensity]");
Stack.setDisplayMode("grayscale");
run("Split Channels");
//for quantification mCherry, use 'Sum slices' instead of 'Max Intensity', and only make substack of mCherry (e.g., channel 3)
run("Make Substack...", "channels=3 slices=1-43");
run("Z Project...", "projection=[Sum Slices]");
//save images, make merges and montages for supplementary information, close images
//Open GFP positive image to create mask for specific endothelial cell colocalization
setOption("BlackBackground", false);
run("Convert to Mask");
run("Dilate");
run("Despeckle");
run("Divide...", "value=255");
//Open mCherry positive image
run("Image Calculator...");
//Multiply GFP mask from mCherry positive image
```

5.6 References

1. Kulkarni, J. A.; Witzigmann, D.; Thomson, S. B.; Chen, S.; Leavitt, B. R.; Cullis, P. R.; van der Meel, R. The Current Landscape of Nucleic Acid Therapeutics. *Nat Nanotechnol* **2021**, *16* (6), 630–643.
2. Springer, A. D.; Dowdy, S. F. GalNAc-siRNA Conjugates: Leading the Way for Delivery of RNAi Therapeutics. *Nucleic Acid Ther* **2018**, *28* (3), 109–118.
3. Nair, J. K.; Willoughby, J. L. S.; Chan, A.; Charisse, K.; Alam, M. R.; Wang, Q.; Hoekstra, M.; Kandasamy, P.; Kelin, A. V.; Milstein, S.; Taneja, N.; Oshea, J.; Shaikh, S.; Zhang, L.; Van Der Sluis, R. J.; Jung, M. E.; Akinc, A.; Hutabarat, R.; Kuchimanchi, S.; Fitzgerald, K.; Zimmermann, T.; Van Berkel, T. J. C.; Maier, M. A.; Rajeev, K. G.; Manoharan, M. Multivalent N -Acetylgalactosamine-Conjugated siRNA Localizes in Hepatocytes and Elicits Robust RNAi-Mediated Gene Silencing. *J Am Chem Soc* **2014**, *136* (49), 16958–16961.
4. Tsui, N. B. Y.; Ng, E. K. O.; Dennis Lo, Y. M. Stability of Endogenous and Added RNA in Blood Specimens, Serum, and Plasma. *Clin Chem* **2002**, *48* (10), 1647–1653.
5. Probst, J.; Brechtel, S.; Scheel, B.; Herr, I.; Jung, G.; Rammensee, H. G.; Pascolo, S. Characterization of the Ribonuclease Activity on the Skin Surface. *Genet Vaccines Ther* **2006**, *4* (1), 1–9.
6. Qin, S.; Tang, X.; Chen, Y.; Chen, K.; Fan, N.; Xiao, W.; Zheng, Q.; Li, G.; Teng, Y.; Wu, M.; Song, X. mRNA-Based Therapeutics: Powerful and Versatile Tools to Combat Diseases. *Signal Transduct Target Ther* **2022**, *7* (1), 166.
7. Khurana, A.; Allawadhi, P.; Khurana, I.; Allwadhi, S.; Weiskirchen, R.; Banothu, A. K.; Chhabra, D.; Joshi, K.; Bharani, K. K. Role of Nanotechnology behind the Success of mRNA Vaccines for COVID-19. *Nano Today* **2021**, *38*, 101142.
8. Pardi, N.; Tuyishime, S.; Muramatsu, H.; Kariko, K.; Mui, B. L.; Tam, Y. K.; Madden, T. D.; Hope, M. J.; Weissman, D. Expression Kinetics of Nucleoside-Modified mRNA Delivered in Lipid Nanoparticles to Mice by Various Routes. *J Control Release* **2015**, *217*, 345-351.
9. Szabó, G. T.; Mahiny, A. J.; Vlatkovic, I. COVID-19 mRNA Vaccines: Platforms and Current Developments. *Mol Ther* **2022**, *30* (5), 1850–1868.
10. Schoenmaker, L.; Witzigmann, D.; Kulkarni, J. A.; Verbeke, R.; Kersten, G.; Jiskoot, W.; Crommelin, D. J. A. mRNA-Lipid Nanoparticle COVID-19 Vaccines: Structure and Stability. *Int J Pharm* **2021**, *601*, 120586.

11. Tenchov, R.; Bird, R.; Curtze, A. E.; Zhou, Q. Lipid Nanoparticles from Liposomes to mRNA Vaccine Delivery, a Landscape of Research Diversity and Advancement. *ACS Nano* **2021**, *15* (11), 16982–17015.
12. Li, S.; Hu, Y.; Li, A.; Lin, J.; Hsieh, K.; Schneiderman, Z.; Zhang, P.; Zhu, Y.; Qiu, C.; Kokkoli, E.; Wang, T. H.; Mao, H. Q. Payload Distribution and Capacity of mRNA Lipid Nanoparticles. *Nat Commun* **2022**, *13* (1), 1–13.
13. Brader, M. L.; Williams, S. J.; Banks, J. M.; Hui, W. H.; Hong Zhou, Z.; Jin, L. Encapsulation State of Messenger RNA inside Lipid Nanoparticles. *Biophysj* **2021**, *120*, 2766–2770.
14. Patel, S.; Ashwanikumar, N.; Robinson, E.; Xia, Y.; Mihai, C.; Griffith, J. P.; Hou, S.; Esposito, A. A.; Ketova, T.; Welsher, K.; Joyal, J. L.; Almarsson, Ö.; Sahay, G. Naturally-Occurring Cholesterol Analogues in Lipid Nanoparticles Induce Polymorphic Shape and Enhance Intracellular Delivery of mRNA. *Nat Commun* **2020**, *11* (1), 1–13.
15. Eygeris, Y.; Patel, S.; Jozic, A.; Sahay, G.; Sahay, G. Deconvoluting Lipid Nanoparticle Structure for Messenger RNA Delivery. *Nano Lett* **2020**, *20* (6), 4543–4549.
16. Hald Albertsen, C.; Kulkarni, J. A.; Witzigmann, D.; Lind, M.; Petersson, K.; Simonsen, J. B. The Role of Lipid Components in Lipid Nanoparticles for Vaccines and Gene Therapy. *Adv Drug Deliv Rev* **2022**, *188*, 114416.
17. Da Silva Sanchez, A. J.; Zhao, K.; Huayamares, S. G.; Hatit, M. Z. C.; Lokugamage, M. P.; Loughrey, D.; Dobrowolski, C.; Wang, S.; Kim, H.; Paunovska, K.; Kuzminich, Y.; Dahlman, J. E. Substituting Racemic Ionizable Lipids with Stereopure Ionizable Lipids Can Increase mRNA Delivery. *J Control Release* **2023**, *353*, 270–277.
18. Hatit, M. Z. C.; Dobrowolski, C. N.; Lokugamage, M. P.; Loughrey, D.; Ni, H.; Zurla, C.; Da Silva Sanchez, A. J.; Radmand, A.; Huayamares, S. G.; Zenhausern, R.; Paunovska, K.; Peck, H. E.; Kim, J.; Sato, M.; Feldman, J. I.; Rivera, M. A.; Cristian, A.; Kim, Y. T.; Santangelo, P. J.; Dahlman, J. E. Nanoparticle Stereochemistry-Dependent Endocytic Processing Improves in Vivo mRNA Delivery. *Nat Chem 2023* **2023**, 1–8.
19. Stirland, D. L.; Nichols, J. W.; Miura, S.; Bae, Y. H. Mind the Gap: A Survey of How Cancer Drug Carriers Are Susceptible to the Gap between Research and Practice. *J Control Release* **2013**, *172* (3), 1045–1064.
20. Guidolin, K.; Zheng, G. Nanomedicines Lost in Translation. *ACS Nano* **2019**, *13* (12), 13620–13626.

21. Blanco, E.; Shen, H.; Ferrari, M. Principles of Nanoparticle Design for Overcoming Biological Barriers to Drug Delivery. *Nature Biotechnol* **2015**, *33* (9), 941-951.
22. Horejs, C. From Lipids to Lipid Nanoparticles to mRNA Vaccines. *Nat Rev Mater* **2021**, *6* (12), 1075-1076.
23. Allison, S. J.; Milner, J. Influence of Polyethylene Glycol Lipid Desorption Rates on Pharmacokinetics and Pharmacodynamics of siRNA Lipid Nanoparticles. *Mol Ther Nucleic Acids* **2013**, *2* (12), e139.
24. Pattipeiluhu, R.; Arias-Alpizar, G.; Basha, G.; Chan, K. Y. T.; Bussmann, J.; Sharp, T. H.; Moradi, M.-A.; Sommerdijk, N.; Harris, E. N.; Cullis, P. R.; Kros, A.; Witzigmann, D.; Campbell, F. Anionic Lipid Nanoparticles Preferentially Deliver mRNA to the Hepatic Reticuloendothelial System. *Adv Mater* **2022**, *34* (16), 2201095.
25. Patel, P.; Ibrahim, N. M.; Cheng, K. The Importance of Apparent pKa in the Development of Nanoparticles Encapsulating siRNA and mRNA. *Trends Pharmacol Sci* **2021**, *42* (6), 448–460.
26. Cullis, P. R.; Hope, M. J. Lipid Nanoparticle Systems for Enabling Gene Therapies. *Mol Ther* **2017**, *25* (7), 1467–1475.
27. Zheng, L.; Bandara, S. R.; Leal, C. Lipid Nanoparticle Topology Regulates Endosomal Escape and Delivery of RNA to the Cytoplasm. *PNAS* **2023**, *120* (27), e2301067120.
28. Liu, S.; Cheng, Q.; Wei, T.; Yu, X.; Johnson, L. T.; Farbiak, L.; Siegwart, D. J. Membrane-Destabilizing Ionizable Phospholipids for Organ-Selective mRNA Delivery and CRISPR–Cas Gene Editing. *Nat Mater* **2021**, *20* (5), 701–710.
29. Meng, N.; Grimm, D. Membrane-Destabilizing Ionizable Phospholipids: Novel Components for Organ-Selective mRNA Delivery and CRISPR–Cas Gene Editing. *Signal Transduct Target Ther* **2021**, *6* (1), 1–3.
30. Hafez, I. M.; Maurer, N.; Cullis, P. R. On the Mechanism Whereby Cationic Lipids Promote Intracellular Delivery of Polynucleic Acids. *Gene Ther* **2001**, *8* (15), 1188–1196.
31. Dowdy, S. F.; Setten, R. L.; Cui, X. S.; Jadhav, S. G. Delivery of RNA Therapeutics: The Great Endosomal Escape! *Nucleic Acid Ther* **2022**, *32* (5), 361–368.
32. Semple, S. C.; Klimuk, S. K.; Harasym, T. O.; Dos Santos, N.; Ansell, S. M.; Wong, K. F.; Maurer, N.; Stark, H.; Cullis, P. R.; Hope, M. J.; Scherrer, P. Efficient Encapsulation of Antisense Oligonucleotides in Lipid Vesicles Using Ionizable Aminolipids: Formation of Novel Small Multilamellar Vesicle Structures. *Biochim Biophys Acta - Biomembr* **2001**, *1510* (1–2), 152–166.

33. Jayaraman, M.; Ansell, S. M.; Mui, B. L.; Tam, Y. K.; Chen, J.; Du, X.; Butler, D.; Eltepu, L.; Matsuda, S.; Narayanannair, J. K.; Rajeev, K. G.; Hafez, I. M.; Akinc, A.; Maier, M. A.; Tracy, M. A.; Cullis, P. R.; Madden, T. D.; Manoharan, M.; Hope, M. J. Maximizing the Potency of siRNA Lipid Nanoparticles for Hepatic Gene Silencing In Vivo. *Angew Chem Int Ed Engl* **2012**, *51* (34), 8529-8533.

34. Semple, S. C.; Akinc, A.; Chen, J.; Sandhu, A. P.; Mui, B. L.; Cho, C. K.; Sah, D. W. Y.; Stebbing, D.; Crosley, E. J.; Yaworski, E.; Hafez, I. M.; Dorkin, J. R.; Qin, J.; Lam, K.; Rajeev, K. G.; Wong, K. F.; Jeffs, L. B.; Nechev, L.; Eisenhardt, M. L.; Jayaraman, M.; Kazem, M.; Maier, M. A.; Srinivasulu, M.; Weinstein, M. J.; Chen, Q.; Alvarez, R.; Barros, S. A.; De, S.; Klimuk, S. K.; Borland, T.; Kosovrasti, V.; Cantley, W. L.; Tam, Y. K.; Manoharan, M.; Ciufolini, M. A.; Tracy, M. A.; De Fougerolles, A.; MacLachlan, I.; Cullis, P. R.; Madden, T. D.; Hope, M. J. Rational Design of Cationic Lipids for siRNA Delivery. *Nat Biotechnol* **2010**, *28* (2), 172–176.

35. Ansell, S. M. Lipids and Lipid Nanoparticle Formulations for Delivery of Nucleic Acids. **2016**.

36. Hou, X.; Zaks, T.; Langer, R.; Dong, Y. Lipid Nanoparticles for mRNA Delivery. *Nat Rev Mater* **2021**, *6* (12), 1078–1094.

37. Kulkarni, J. A.; Witzigmann, D.; Leung, J.; Tam, Y. Y. C.; Cullis, P. R. On the Role of Helper Lipids in Lipid Nanoparticle Formulations of siRNA. *Nanoscale* **2019**, *11* (45), 21733–21739.

38. Veatch, S. L.; Keller, S. L. Separation of Liquid Phases in Giant Vesicles of Ternary Mixtures of Phospholipids and Cholesterol. *Biophys J* **2003**, *85* (5), 3074–3083.

39. Tenchov, B. G.; MacDonald, R. C.; Siegel, D. P. Cubic Phases in Phosphatidylcholine-Cholesterol Mixtures: Cholesterol as Membrane "Fusogen." *Biophys J* **2006**, *91* (7), 2508–2516.

40. Alwarawrah, M.; Dai, J.; Huang, J. Modification of Lipid Bilayer Structure by Diacylglycerol: A Comparative Study of Diacylglycerol and Cholesterol. *J Chem Theory Comput* **2012**, *8* (2), 749–758.

41. Vieu, C.; Jaspard, B.; Barbaras, R.; Manent, J.; Chap, H.; Perret, B.; Collet, X. Identification and Quantification of Diacylglycerols in HDL and Accessibility to Lipase. *J Lipid Res* **1996**, *37* (5), 1153–1161.

42. Coffill, C. R.; Ramsamy, T. A.; Hutt, D. M.; Schultz, J. R.; Sparks, D. L. Diacylglycerol Is the Preferred Substrate in High Density Lipoproteins for Human Hepatic Lipase. *J Lipid Res* **1997**, *38* (11), 2224–2231.

43. Goñi, F. M.; Alonso, A. Structure and Functional Properties of Diacylglycerols in Membranes. *Prog Lipid Res* **1999**, *38* (1), 1–48.
44. Bilayers Edward Goldberg, P. M.; Lester, D. S.; Borchardt, D. B.; Zidovetzki, R. Effects of Diacylglycerols and Ca2+ on Structure of Phosphatidylcholine/Phosphatidylserine Bilayers. *Biophys J* **1994**, *66*, 382–393.
45. Dawson, R. M. C.; Hemington, N. L.; Irvine, R. F. Diacylglycerol Potentiates Phospholipase Attack upon Phospholipid Bilayers: Possible Connection with Cell Stimulation. *Biochem Biophys Res Commun* **1983**, *117* (1), 196–201.
46. Heinonen, S.; Lautala, S.; Koivuniemi, A.; Bunker, A. Insights into the Behavior of Unsaturated Diacylglycerols in Mixed Lipid Bilayers in Relation to Protein Kinase C Activation—A Molecular Dynamics Simulation Study. *Biochim Biophys Acta - Biomembr* **2022**, *1864* (9), 183961.
47. Alwarawrah, M.; Hussain, F.; Huang, J. Alteration of Lipid Membrane Structure and Dynamics by Diacylglycerols with Unsaturated Chains. *Biochim Biophys Acta - Biomembr* **2016**, *1858* (2), 253–263.
48. Campomanes, P.; Zoni, V.; Vanni, S. Local Accumulation of Diacylglycerol Alters Membrane Properties Nonlinearly Due to Its Transbilayer Activity. *Commun Chem* **2019**, *2* (1), 1–8.
49. Basáñez, G.; Nieva, J. L.; Rivas, E.; Alonso, A.; Goñi, F. M. Diacylglycerol and the Promotion of Lamellar-Hexagonal and Lamellar-Isotropic Phase Transitions in Lipids: Implications for Membrane Fusion. *Biophys J* **1996**, *70* (5), 2299–2306.
50. Arias-Alpizar, G.; Papadopoulou, P.; Rios, X.; Pulagam, K. R.; Moradi, M. A.; Pattipeiluhu, R.; Bussmann, J.; Sommerdijk, N.; Llop, J.; Kros, A.; Campbell, F. Phase-Separated Liposomes Hijack Endogenous Lipoprotein Transport and Metabolism Pathways to Target Subsets of Endothelial Cells In Vivo. *Adv Healthc Mater* **2023**, *12* (10), e2202709.
51. Papadopoulou, P.; Van Der Pol, R.; Van Hilten, N.; Moradi, M.-A.; Ferraz, M. J.; Aerts, J. M. F. G.; Sommerdijk, N.; Risselada, H. J.; Sevink, G. J. A.; Kros, A. Lipase-Mediated Selective Hydrolysis of Lipid Droplets in Phase Separated-Liposomes. *ChemRxiv* **2023**.
52. Leung, A. K. K.; Tam, Y. C.; Chen, S.; Hafez, I. M.; Cullis, P. R. Microfluidic Mixing: A General Method for Encapsulating Macromolecules in Lipid Nanoparticle Systems. *J. Phys. Chem. B* **2015**, *119* (28), 8698-8706.
53. Arteta, M. Y.; Kjellman, T.; Bartesaghi, S.; Wallin, S.; Wu, X.; Kvist, A. J.; Dabkowska, A.; Székely, N.; Radulescu, A.; Bergenholtz, J.; Lindfors, L. Successful

Reprogramming of Cellular Protein Production through mRNA Delivered by Functionalized Lipid Nanoparticles. *PNAS* **2018**, *115* (15), E3351–E3360.

54. Manders, E. M. M.; Verbeek, F. J.; Aten, J. A. Measurement of Co-Localization of Objects in Dual-Colour Confocal Images. *J Microsc* **1993**, *169* (3), 375–382.
55. Cheng, M. H. Y.; Leung, J.; Zhang, Y.; Strong, C.; Basha, G.; Momeni, A.; Chen, Y.; Jan, E.; Abdolahzadeh, A.; Wang, X.; Kulkarni, J. A.; Witzigmann, D.; Cullis, P. R. Induction of Bleb Structures in Lipid Nanoparticle Formulations of mRNA Leads to Improved Transfection Potency. *Adv Mater* **2023**, e2303370.
56. Arias-Alpizar, G.; Kong, L.; Vlieg, R. C.; Rabe, A.; Papadopoulou, P.; Meijer, M. S.; Bonnet, S.; Vogel, S.; van Noort, J.; Kros, A.; Campbell, F. Light-Triggered Switching of Liposome Surface Charge Directs Delivery of Membrane Impermeable Payloads in Vivo. *Nat Commun* **2020**, *11*, 3638.
57. Sieber, S.; Grossen, P.; Bussmann, J.; Campbell, F.; Kros, A.; Witzigmann, D.; Huwyler, J. Zebrafish as a Preclinical in Vivo Screening Model for Nanomedicines. *Adv Drug Deliv Rev* **2019**, *151–152*, 152–168.
58. Arias-Alpizar, G.; Bussmann, J.; Campbell, F. Zebrafish Embryos as a Predictive Animal Model to Study Nanoparticle Behavior in Vivo. *Bio Protoc* **2021**, *11* (19), e4173.
59. Hatit, M. Z. C.; Lokugamage, M. P.; Dobrowolski, C. N.; Paunovska, K.; Ni, H.; Zhao, K.; Vanover, D.; Beyersdorf, J.; Peck, H. E.; Loughrey, D.; Sato, M.; Cristian, A.; Santangelo, P. J.; Dahlman, J. E. Species-Dependent in vivo mRNA Delivery and Cellular Responses to Nanoparticles. *Nat Nanotechnol* **2022**, *17* (3), 310–318.
60. Sevigny, J.; Chiao, P.; Bussière, T.; Weinreb, P. H.; Williams, L.; Maier, M.; Dunstan, R.; Salloway, S.; Chen, T.; Ling, Y.; O'Gorman, J.; Qian, F.; Arastu, M.; Li, M.; Chollate, S.; Brennan, M. S.; Quintero-Monzon, O.; Scannevin, R. H.; Arnold, H. M.; Engber, T.; Rhodes, K.; Ferrero, J.; Hang, Y.; Mikulskis, A.; Grimm, J.; Hock, C.; Nitsch, R. M.; Sandrock, A. The Antibody Aducanumab Reduces Aβ Plaques in Alzheimer's Disease. *Nature* **2016**, *537* (7618), 50–56.
61. Mitra, S.; Behbahani, H.; Eriksdotter, M. Innovative Therapy for Alzheimer's Disease-with Focus on Biodelivery of NGF. *Front Neurosci* **2019**, *13*, 38.
62. Chen, X.; Wolfe, D. A.; Bindu, D. S.; Zhang, M.; Taskin, N.; Goertsen, D.; Shay, T. F.; Sullivan, E. E.; Huang, S. F.; Ravindra Kumar, S.; Arokiaraj, C. M.; Plattner, V. M.; Campos, L. J.; Mich, J. K.; Monet, D.; Ngo, V.; Ding, X.; Omstead, V.; Weed, N.; Bishaw, Y.; Gore, B. B.; Lein, E. S.; Akrami, A.; Miller, C.; Levi, B. P.; Keller, A.; Ting, J. T.; Fox, A. S.; Eroglu, C.; Gradinaru, V. Functional Gene Delivery to and

across Brain Vasculature of Systemic AAVs with Endothelial-Specific Tropism in Rodents and Broad Tropism in Primates. *Nat Commun* **2023**, *14* (1), 1–19.

63. Weiss, N.; Miller, F.; Cazaubon, S.; Couraud, P. O. The Blood-Brain Barrier in Brain Homeostasis and Neurological Diseases. *Biochim Biophys Acta - Biomembr* **2009**, *1788* (4), 842–857.
64. Mastronarde, D. N. Automated Electron Microscope Tomography Using Robust Prediction of Specimen Movements. *J Struct Biol* **2005**, *152* (1), 36–51.
65. Kremer, J. R.; Mastronarde, D. N.; McIntosh, J. R. Computer Visualization of Three-Dimensional Image Data Using IMOD. *J Struct Biol* **1996**, *116* (1), 71–76.
66. Jin, S. W.; Beis, D.; Mitchell, T.; Chen, J. N.; Stainier, D. Y. R. Cellular and Molecular Analyses of Vascular Tube and Lumen Formation in Zebrafish. *Development* **2005**, *132* (23), 5199–5209.
67. Campbell, F.; Bos, F. L.; Sieber, S.; Arias-Alpizar, G.; Koch, B. E.; Huwyler, J.; Kros, A.; Bussmann, J. Directing Nanoparticle Biodistribution through Evasion and Exploitation of Stab2-Dependent Nanoparticle Uptake. *ACS Nano* **2018**, *12* (3), 2138-2150.
68. Bolte, S.; Cordelières, F. P. A Guided Tour into Subcellular Colocalization Analysis in Light Microscopy. *J Microsc* **2006**, *224* (3), 213–232.

CHAPTER 6

Summary and Closing remarks

"Αυτός ο κόσμος, ο μικρός, ο μέγας" – Odysseas Elytis, 1959

Lipid-based nanoparticles are the most clinically advanced drug delivery systems; however, a persistent and limited understanding of their assembly properties and the key nano-bio interactions hampers their clinical translation, which mainly relies on trial-error approaches and labor-intensive empirical screenings. In this doctoral dissertation, lipid chemistry, composition and morphology, are all connected to provide a comprehensive picture of novel phase separated lipid-based nanoparticles with specific behavior at the nano-bio interface. This behavior is characterized by selective nanoparticle-protein communications and the hijacking of endogenous biological mechanisms for cell specificity *in vivo*. To achieve nanoparticle-mediated targeted therapies, a better understanding on how lipid composition determines morphology and influences (desired) nano-bio interactions is needed. Therefore, the information provided in this thesis broadens current, fundamental knowledge on lipid nanoparticle assembly and *in vivo* behavior, and can be the foundation for rationally optimized nanoparticle designs.

This Chapter summarizes and discusses the key findings and relevance of this thesis followed by future perspectives.

6.1 Summary and outlook

In **Chapter 2** a novel liposomal formulation (named PAP3) with cell-selective *in vivo* behavior is described, and found to specifically accumulate in brain endothelial cells (bECs) of embryonic zebrafish. PAP3 liposomes consist of only two lipids, the natural phospholipid DSPC and the synthetic diacylglycerol (DAG) analogue DOaG, without using traditional targeting functionalities, *e.g.*, antibodies, peptides (**Table 1**). In contrast, cell-specific uptake was mediated by a unique "parachute morphology" which was characterized by a single lipid droplet within each DSPC leaflet, as created by lipid phase-separation. While DSPC has a cylindrical geometry and favors assembly into a flat bilayer, DOaG has a conical geometry preferring non-bilayer phases. As a result, upon mixing, these two lipids phase separate.

Table 1. Molecular structures of lipid components in PAP3 liposomes (compared to natural DAGs).

Lipid	Molecular structure	
DOG Natural DAG	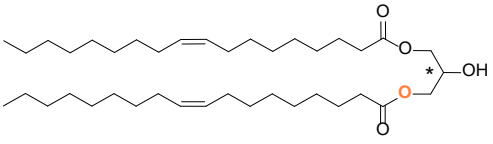	
DOaG synthetic	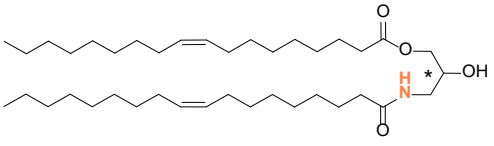	**PAP3 liposomes (1:1)**
DSPC Natural phospholipid	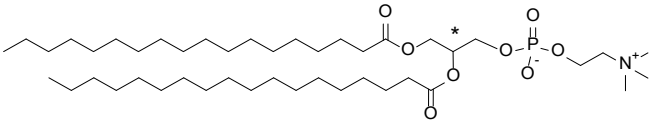	

Atomic differences between DOG and DOaG are shown in orange. Abbreviations in table 1: DOG=Dioleoylglycerol, DOaG=Dioleoylamidoglycerol, DSPC= Distearoylphosphocholine.

By varying the molar ratio of DOaG in the DSPC formulation, it was revealed that phase-separation only occurs at high DOaG concentrations. At a low DOaG/DSPC ratio the lipids mix, while above a threshold concentration DOaG phase-separates into a lipid droplet surrounded by a DSPC monolayer. Strikingly, it was shown that bEC targeting occurred only when liposomes where phase-separated. Mechanistic studies using zebrafish revealed the involvement of a triglyceride lipase-mediated mechanism in the cell selective uptake. At this developmental stage, zebrafish embryos have high lipid and metabolic demands and therefore lipases, such as endothelial (EL) and lipoprotein lipase (LPL), are highly present in the zebrafish head region. Indeed, in the presence of a small molecule lipase inhibitor (XEN445), liposome bEC uptake was abolished. Although in a different tissue (liver), the involvement of triglyceride lipase (TGL) in the uptake, was also found to be (partially) conserved in mice. Here, competing clearance mechanisms lead to the rapid accumulation of PAP3 liposomes in the liver and spleen.

Nevertheless, it was important to identify the involvement of TGL as a mechanism for the clearance of PAP3 liposomes by the liver, which has not been described before. Since TGLs are regulated in both time and space and are highly present in certain disease states such as cancer, they are potentially novel targets to achieve selective nanoparticle *in vivo* uptake and be exploited in a therapeutic setting.

In **Chapter 3**, the lipase-liposome interaction was studied in more detail, revealing the DOaG-rich lipid droplet is specifically hydrolyzed by TGLs, leaving the lamellar liposome membrane intact. By combining cryo-transmission electron microscopy (cryo-TEM), mass spectrometry, enzymatic analysis and molecular dynamic (MD) simulations, the exact mechanism of this interaction was discovered. Phase-separation due to DOaG, results in membranes with lipid packing defects – areas where the distance of adjacent phospholipids is increased – exposing hydrophobic patches rich in DOaG to the aqueous environment. These defects facilitate TGL binding to the liposome surface resulting in DOaG hydrolysis. It was also shown that the so-called tryptophan loop – the natural lipoprotein binding domain of the enzyme – acts as a packing defect sensor, implying that TGLs preferentially bind to phase-separated membranes as compared to flat lamellar membranes.

The observed mechanism of TGL-mediated hydrolysis of PAP3 liposomes has similarities to the endogenous mechanism that takes place on lipoproteins: Involved in natural lipid transport and metabolism pathways, TGLs either 1) hydrolyze di- and triglycerides and cholesterol esters in lipoproteins, or 2) facilitate lipoprotein cell uptake.[1–3] In summary, Chapters 2 and 3 show that phase-separated PAP3 liposomes hijack a biological pathway of lipid transport and/or metabolism, mediated by TGLs.

Chapter 3 demonstrated that, *in vitro*, the droplet of PAP3 liposomes undergo lipolysis by TGL; while Chapter 2 described the TGL-mediated endocytosis of PAP3 liposomes *in vivo*. An unanswered question was whether PAP3 liposomes undergo lipolysis before endocytosis *in vivo*. An indication for this, may lie on the inhibition of TGL by the XEN445 inhibitor, which is usually used to inhibit the catalytic activity of TGLs. *In vitro*, XEN445 inhibits the lipolysis of PAP3 droplets (Chapter 3). In zebrafish, XEN445 treatment inhibits the uptake (Chapter 2). Hence, the

lipolysis of PAP3 liposomes could play a role in the cell uptake *in vivo*. Another interesting question posed in Chapter 3 is whether PAP3 liposome metabolites could still target zebrafish bECs. Indeed, preliminary data show PAP3 metabolites still accumulate in bECs (**Figure 1**).

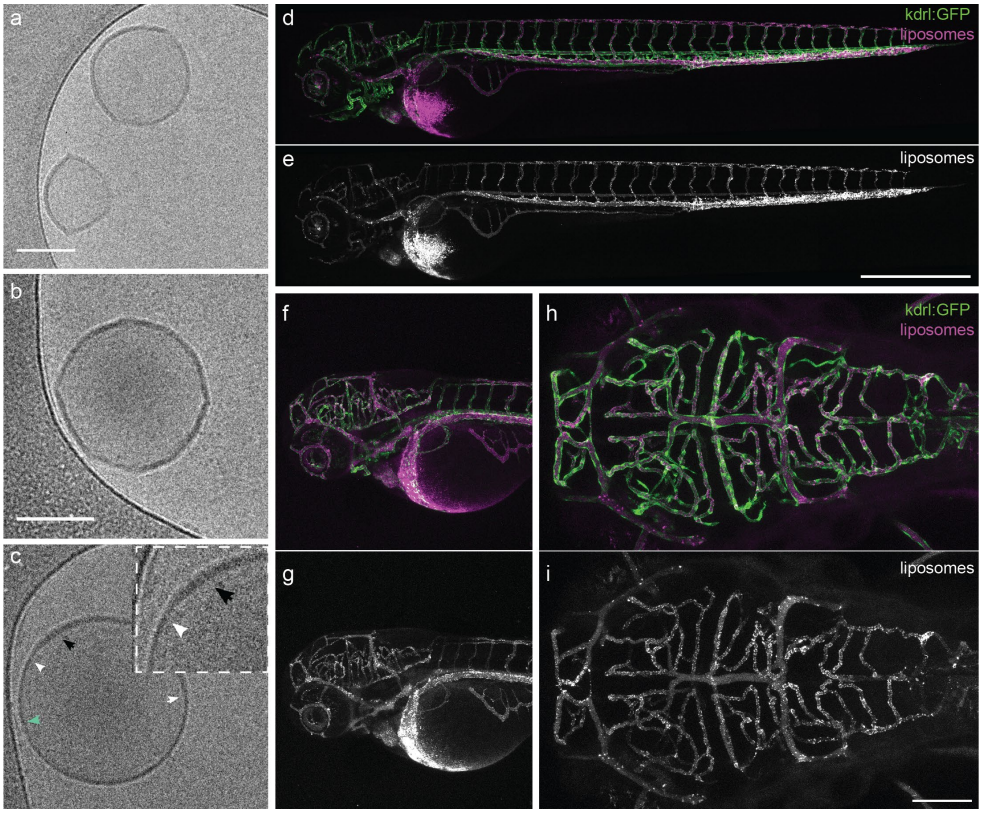

Figure 1. Cryo-TEM images and biodistribution of PAP3 liposomes after droplet hydrolysis in a zebrafish embryo (*kdrl*:GFP, 78 dpf, 2.5 hpi). a-c) Liposomes appear rounder than typical DSPC liposomes and with thicker membranes (8-9 nm compared to 3-4 nm, respectively, as suggested by quantification of N=20). Also, membrane mismatch and co-existence of two phases (gel and fluid) in the membrane can be seen in all images, suggesting the existence of DOaG (or DOaG metabolites). Difference of bilayer thickness is indicated with black (thicker part) or green (thinner part) arrows. The point of thickness mismatch is indicated with white arrows. Biodistribution of PAP3 liposomes after droplet hydrolysis indicating bEC targeting patterns, **d, e**) whole body lateral view**, f, g**) 10x magnification in the head region, lateral view, **h, i**) 10x magnification in the head region, dorsal view. Liposomes prepared by extrusion, at 5 mM total lipid concentration containing 0.2% DOPE-LR for visualization. Scale bars: 100 nm for cryo-TEM, 500 μm for zebrafish lateral view and 100 μm for dorsal view.

This might indicate that lipid droplets are not required for bEC recognition. A small fraction of unhydrolyzed DOaG could still induce packing defects and DOaG exposure throughout the bilayer and could already be enough for TGL recognition and bEC uptake. In Figure 1 such nanodomains can be confirmed: i) the DSPC membrane is observed to be in a liquid disordered (L_d) phase (more fluid) – something uncommon for liposomes made of DSPC only – indicating the existence of a small fraction of DOaG (or DOaG metabolite) that could alter rigid DSPC membranes. ii) A clearly observed membrane thickness mismatch (arrows), have been recently described to be nanodomains in such instances.[4] SANS and cryo-TEM could be used in the future to solidly verify the existence of such domains in the liposome metabolites.[5]

Chapter 4 describes an in-depth investigation of the DOaG's molecular details underpinning the phase-separation and bEC targeting in zebrafish embryos. A library of DOaG analogues was synthesized and the structure-function relationship was investigated. Medium (C16:1 or C18:1) unsaturated chains are necessary to induce phase-separation in liposomes, when DOaG analogues are co-formulated with DSPC, and achieve selective *in vivo* targeting. In contrast, fully saturated DOaG variants did not form liposomes. Variants containing the long acyl chains C20:1 or C24:1, mixed with DSPC, formed liposomes albeit with high instability, or did not form liposomes at all, respectively. Surprisingly, the short acyl chain variant (C14:1) *did* induce phase-separation in DSPC membranes but the resulting liposomes *did not* target bECs.

Chapter 3 illustrates that DOaG lipids induce phase separation in DSPC membranes and TGLs recognize the exposed DOaG molecules due to high membrane packing defects. Since the TGL recognition and binding relies on the exposure of DOaG lipid, the length of DOaG acyl chain may be particularly important. Short chain lipids may not be exposed sufficiently, whereas longer chain DOaG variants may be exposed enough (for TGL recognition), or even too much (potential aggregation risk). The fact that liposomes containing C16:1 or C18:1 variants target bECs, and liposomes containing longer chain DOaG variants (C20:1, C24:1) are colloidally unstable (*i.e.*, massive aggregation or no assembly at all) supports this hypothesis.

In contrast, the shorter C14:1 lipid variant induces phase-separation in stable liposomes, but the chains may be too short to be recognized by TGLs, therefore bEC targeting is not observed. Further investigation is needed to prove this hypothesis.

An alternative explanation why phase-separated liposomes with short C14:1 lipid variants do not target bECs, may lie on the amount of total packing defects they induce throughout the liposome membrane. Due to extreme curvature, the lipid droplet may inevitably induce packing defects exposing the C14:1 lipids locally. However, the lamellar part of DSPC seems to be in a liquid ordered (L_o) phase (gel phase, cornered) in the case of C14:1 liposomes (Figure 3, Chapter 4). This is in contrast to C16:1 and C18:1 liposomes which are more in a L_d phase (Figure 3, Chapter 4). Therefore, the C14:1 liposomes may have less defects throughout due to the shorter chain of C14:1 exposing the lipid less. Hence, in an *in vivo* setting, liposomes with only a small region of C14:1 lipids exposed to the surrounding environment, may have a lower probability to be recognized by TGLs with subsequent bEC uptake, than liposomes with more packing defects throughout the bilayer (*i.e.*, C16:1, C18:1). Besides, liposomes which do not bear a lipid droplet but seem to still be defected throughout retain their bEC targeting, as previously mentioned (Figure 1), supporting this hypothesis.

Other DOaG variants

As previously mentioned (Chapter 3), it is not yet clear whether TGL hydrolysis takes place *in vivo* prior to bEC uptake. Since TGLs endogenously hydrolyze ester bonds in di- and triglycerides to release free fatty acids (FFA), and DOaG contains an ester in the *sn*-3 position, an ether variant of DOaG could be useful to elucidate this mechanism. More specifically, if bEC uptake of liposomes was abolished by replacing the DOaG ester with an ether, then this would indicate hydrolysis prior to PAP3 uptake *in vivo*. However, liposomes containing the ether analogue must have similar physicochemical properties to PAP3 liposomes and not show hydrolysis by TGLs *in vitro*, to prevent false conclusions.

PAP3 Liposome optimization

In Chapter 4, an effort to optimize the PAP3 formulation is described. PAP3 liposomes are only stable for up to ~7 days (Chapter 2) and importantly are not stable when formulated in buffers containing saline (*i.e.*, PBS), which mimic the physiological environment. By assessing the influence of *sn*-isomeric mixtures of DOaG in liposome stability, it is found that DOaG existing in the pure *sn*-1,3 isomer improves long-term stability of PAP3 liposomes. Despite that the presence of a small amount of *sn*-1,2 isomer (20% of the mixture) seems to contribute negatively on the liposome stability, it is important to assess its influence on the liposome assembly when it is in its pure form (*i.e.*, 100% *sn*-1,2). Similar studies have to be performed for other DOaG isomers, such as the *sn*-2,3 (where the amide bond is located on the *sn*-2 position) and racemically pure isomers of DOaG and DSPC.

Additionally, acyl chain length mismatch between DSPC (C18:0) and a DOaG variant (C16:1) improved the stability and ability to assemble the liposomes in PBS with acceptable PDI values and size. This also supports the hypothesis that shorter variants than DOaG (C18:1) are less exposed to the solvent. PEGylation of the liposomes also improved the stability while retaining bECs targeting. Here, it is therefore important to test whether a PEGylated formulation (1% DMPE-PEG2k) with the pure *sn*-1,3 isomer of C16:1 will result in an even more improved, clinically suitable formulation.

Chapter 2-4 illustrates that phase-separation induced by DOaGs is a novel, functional *in vivo* targeting modality, that can be of interest for other lipid-based nanoparticle systems. **Chapter 5** illustrates the applicability of DOaG lipid in mRNA-based lipid nanoparticle formulations and serves as a proof-of-concept on the employment of DOaG in LNPs, to achieve specific cell targeting and mRNA delivery. In this study, four mRNA-LNP formulations were created, and their *in vivo* behavior was assessed in zebrafish embryos. A phase-separated mRNA-LNP containing DOaG, in combination with the ionizable lipid DODAP, was successfully formulated encapsulating sufficient amount of mRNA. This formulation specifically targeted and accumulated in bECs of zebrafish embryos, resulting in mRNA delivery and protein expression. Interestingly, the similarly phase-separated LNP formulation with DOaG and MC3 did not target bECs.

The DOaG-MC3 LNP was observed to cluster in circulation, which could indicate a thermodynamically unstable formulation, and therefore its colloidal instability might prevent bEC targeting. This indicates that a simple ionizable lipid switching could massively influence the nanoparticle assembly and stability, by molecular details that are not captured by cryo-TEM, and signifies the complexity of mRNA-LNP assemblies. More experiments are needed to investigate whether DOaG-MC3 LNPs are unstable, or whether phase-separation plays a role in bEC uptake, possibly via a TGL-mediated pathway.

Importantly, this study was able to determine that highly transfecting but not cell-specific formulations result in potent transfections, however not at the desired site; while less potent but more selective formulations achieve the desired cell-specific transfection. This contrasts with an often-used shotgun approach where potent therapeutics are administered in the overall tissue, aiming to target the desired site within this tissue.

The DOaG-LNP formulation exhibiting cell selectivity can be the starting point for future research. Firstly, formulation optimization can be explored to enhance transfection potency. Different molar ratios between DOaG and rest of lipid components, as well as different ionizable lipids, can be used. Additionally, translational studies in healthy and diseased animal models should be performed, as well as studies to reveal the selective uptake mechanism (*i.e.*, investigating the role of TGL in bEC uptake). Finally, a general exploration of the potential of other diacylglycerol lipids in mRNA-LNP developments *i.e.,* in cell specificity or enhanced endosomal escape through fusion, is of interest.

6.2 Other formulations targeting bECs

During this PhD study, some other lipid-based formulations were also observed to target bECs. siRNA-loaded LNPs using DOPE as a helper lipid (DODAP:DOPE:CHO:DMPE-PEG1k_5:1:3.9:0.1), as well as DOPC:DSPC:CHO_5:2:3, (to a lesser extent) were observed to target bECs in zebrafish embryos (data not included). This could suggest that nanoparticles exhibiting lipid nanodomains could utilize the same TGL-mediated mechanism

and/or have similar protein coronas with PAP3 liposomes. DOPE is a lipid with similar conical geometry of that of DOaG, therefore it may induce similar packing defects in lipid membranes. DOPC:DSPC:CHO is a known formulation to create phase-separation in giant unilamellar vesicles (GUVs) [6,7] hence nanodomains may exist in large unilamellar vesicles (LUVs) in a similar fashion. Further investigation is required here to elucidate the exact mechanisms and composition which could be used for predictable TGL-mediated *in vivo* interactions.

6.3 Potential involvement of DOaG in membrane fusion

DAGs are known to decrease the spontaneous negative curvature of lipid bilayers and induce inverse hexagonal liquid crystalline phases due to their conical geometry, perturbing lamellar phases. Therefore, a small amount of DAGs in lipid bilayers could promote fusion.[8–13] Fusogenicity in DOaG-containing lipid nanoparticles (liposomes and LNPs) is an interesting aspect for future investigation. Preliminary results show that membrane docking takes place (**Figure 2**) in a PAP3 varied formulation, containing DSPC:DOaG:CHO (4:4:2). Interestingly, cholesterol increases the L_d phase of DSPC bilayers and make them more fluid, consequently DOaG can mix with a DSPC membrane, and PAP3 liposomes are mostly observed to no longer phase-separate.

Also, preliminary data showed high levels of lipid mixing when DOaG is present in a liposome formulation (DOPC:DOaG:CHO_2:1:1 containing the fusion promoting coiled coil lipopeptides CPE_4 and CPK_4[14] – data not included in this thesis –) comparable to lipid mixing levels reported for other fusogenic liposomal formulations (*i.e.*, DOPC:DOPE:CHO_2:1:1 with CPE_4 and CPK_4).[15,16] This result indicates a potential role of DOaG in lipid nanoparticle fusion, which can be particularly important for facilitating endosomal escape or drug delivery. Since the DOaG-based liposome formulations that were observed to dock or undergo lipid mixing also contain cholesterol – which literature has characterized as a potential fusogen [17,18] – further investigation is needed to understand its influence in combination with DOaG.

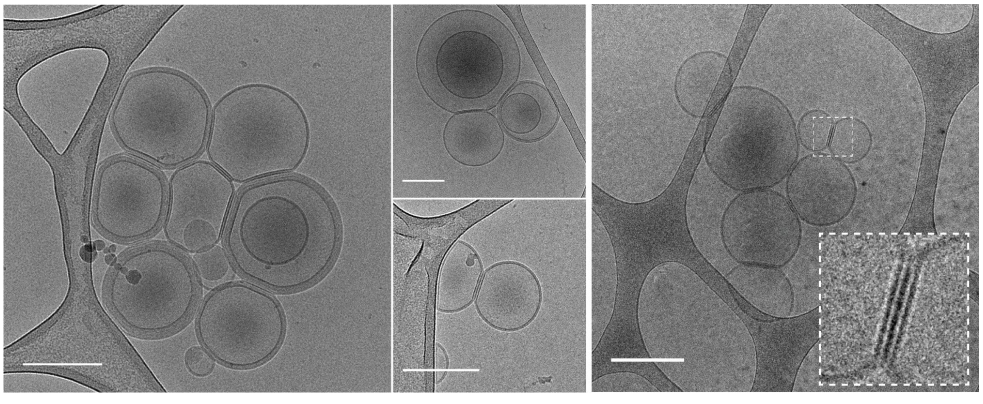

Figure 2. Cryo-TEM images of cholesterol-containing PAP3 liposomes (DSPC:DOaG:CHO_4:4:2) showing membrane docking similarly to other cryo-TEM studies showing docking.[19] Scale bars: 200 nm.

DOaG (or DAGs in general) could be very promising lipid components in mRNA-LNPs and their potential to enhance endosomal escape rates by promoting fusion, should be examined. Molar ratios of DOaG in mRNA-LNPs could vary from the one used in Chapter 5 and can be fine-tuned to promote *i.e.*, liquid crystalline hexagonal phases. It would be interesting to see whether 1-10% mol of DOaG (or variants) in combination (or not) with cholesterol in LNP formulations, may be enough to increase transfection efficiency, retaining ideally specific nano-bio interactions.

6.4 Closing Remarks

Based on the main findings of this thesis and the discussion above, it would be of interest to investigate whether DAG derivatives utilized as lipid components in lipid-based nanoparticles have further potential in selective *in vivo* behavior, nano-protein interactions, fusion and/or enhanced cytoplasmic drug delivery.

Moreover, despite that liposomes have been studied for decades and entered the clinic, this thesis signifies that there is still a large window for exploration at the nano-bio interface, even for simple two-component lipid systems. More importantly, arising multicomponent lipid systems with more intricate supramolecular assemblies such as the ionizable LNPs – which are successfully utilized in the mRNA vaccines against SARs-CoV-2 - [20,21] cannot follow a one-fits-all approach. Rather, a detailed understanding of the properties of each individual lipid component, is vital for rational design strategies leading to more precise targeted therapies.

Finally, this doctoral dissertation describes the novel concept of cell-specific nanoparticle targeting by directly hijacking an endogenous TGL pathway, based on composition and morphology. TGLs are highly involved in lipid transport and metabolism and constitute a rational strategy to promote nanoparticle selectivity *in vivo*, something that has not been widely explored. In contrast, the current practice for targeted nanoparticle discovery relies on large nanoparticle libraries and empirical screenings. Often however, this practice disregards weak *in vitro* "performers", due to exhaustive large-scale experiments and ethical considerations, and therefore a plethora of formulations is not assessed further. To this end, this thesis offers fundamental knowledge on lipid nanoparticle properties at the nano-bio interface to achieve selective *in vivo* behavior. This knowledge can benefit the prediction, development or clinical translation of cell-selective drug delivery systems.

6.5 References

1. De Man, F. H. A. F.; De Beer, F.; Van Der Laarse, A.; Smelt, A. H. M.; Havekes, L. M. Lipolysis of Very Low Density Lipoproteins by Heparan Sulfate Proteoglycan-Bound Lipoprotein Lipase. *J Lipid Res* **1997**, *38* (12), 2465–2472.
2. Khetarpal, S. A.; Vitali, C.; Levin, M. G.; Klarin, D.; Park, J.; Pampana, A.; Millar, J. S.; Kuwano, T.; Sugasini, D.; Subbaiah, P. V.; Billheimer, J. T.; Natarajan, P.; Rader, D. J. Endothelial Lipase Mediates Efficient Lipolysis of Triglyceride-Rich Lipoproteins. *PLOS Genet* **2021**, *17* (9), e1009802.
3. Merkel, M.; Kako, Y.; Radner, H.; Cho, I. S.; Ramasamy, R.; Brunzell, J. D.; Goldberg, I. J.; Breslow, J. L. Catalytically Inactive Lipoprotein Lipase Expression in Muscle of Transgenic Mice Increases Very Low Density Lipoprotein Uptake: Direct Evidence That Lipoprotein Lipase Bridging Occurs in Vivo. *PNAS* **1998**, *95* (23), 13841–13846.
4. Heberle, F. A.; Doktorova, M.; Scott, H. L.; Skinkle, A. D.; Waxham, M. N.; Levental, I. Direct Label-Free Imaging of Nanodomains in Biomimetic and Biological Membranes by Cryogenic Electron Microscopy. *PNAS* **2020**, *117* (33), 19943–19952.
5. Heberle, F. A.; Petruzielo, R. S.; Pan, J.; Drazba, P.; Kučˇ, N.; Standaert, R. F.; Feigenson, G. W.; Katsaras, J. Bilayer Thickness Mismatch Controls Domain Size in Model Membranes. *J. Am. Chem. Soc.* **2013**, *135* (18), 6853–6859.
6. Zhao, J.; Wu, J.; Heberle, F. A.; Mills, T. T.; Klawitter, P.; Huang, G.; Costanza, G.; Feigenson, G. W. Phase Studies of Model Biomembranes: Complex Behavior of DSPC/DOPC/Cholesterol. *Biochim Biophys Acta* **2007**, *1768* (11), 2764–2776.
7. Veatch, S. L.; Keller, S. L. Separation of Liquid Phases in Giant Vesicles of Ternary Mixtures of Phospholipids and Cholesterol. *Biophys J* **2003**, *85* (5), 3074–3083.
8. Rørvig-Lund, A.; Bahadori, A.; Semsey, S.; Bendix, P. M.; Oddershede, L. B. Vesicle Fusion Triggered by Optically Heated Gold Nanoparticles. *Nano Lett* **2015**, *15* (6), 4183–4188.
9. Ibarguren, M.; Bomans, P. H. H.; Ruiz-Mirazo, K.; Frederik, P. M.; Alonso, A.; Goñi, F. M. Thermally-Induced Aggregation and Fusion of Protein-Free Lipid Vesicles. *Colloids Surf B Biointerfaces* **2015**, *136*, 545–552.
10. Siegel, D. P.; Burns, J. L.; Chestnut, M. H.; Talmon, Y. Intermediates in Membrane Fusion and Bilayer/Nonbilayer Phase Transitions Imaged by Time-Resolved Cryo-Transmission Electron Microscopy. *Biophys J* **1989**, *56* (1), 161–169.
11. Nieva, J. L.; Alonso, A.; Basáñez, G.; Goñi, F. M.; Gulik, A.; Vargas, R.; Luzzati, V. Topological Properties of Two Cubic Phases of a Phospholipid : Cholesterol:

Diacylglycerol Aqueous System and Their Possible Implications in the Phospholipase C-Induced Liposome Fusion. *FEBS Lett* **1995**, *368* (1), 143–147.

12. Basáñez, G.; Nieva, J. L.; Rivas, E.; Alonso, A.; Goñi, F. M. Diacylglycerol and the Promotion of Lamellar-Hexagonal and Lamellar-Isotropic Phase Transitions in Lipids: Implications for Membrane Fusion. *Biophys J* **1996**, *70* (5), 2299–2306.
13. Siegel, D. P.; Banschbach, J.; Alford, D.; Bentz, J.; Ellens, H.; Lis, L. J.; Quinn, P. J.; Yeagle, P. L. Physiological Levels of Diacylglycerols in Phospholipid Membranes Induce Membrane Fusion and Stabilize Inverted Phases. *Biochemistry* **1989**, *28* (9), 3703–3709.
14. Marsden, H. R.; Elbers, N. A.; Bomans, P. H. H.; Sommerdijk, N. A. J. M.; Kros, A. A Reduced SNARE Model for Membrane Fusion. *Angew Chem Int Ed Engl* **2009**, *48* (13), 2330–2333.
15. Yang, J.; Bahreman, A.; Daudey, G.; Bussmann, J.; Olsthoorn, R. C. L.; Kros, A. Drug Delivery via Cell Membrane Fusion Using Lipopeptide Modified Liposomes. *ACS Cent Sci* **2016**, *2* (9), 621–630.
16. Zheng, T.; Voskuhl, J.; Versluis, F.; Zope, H. R.; Tomatsu, I.; Robson Marsden, H.; Kros, A. Controlling the Rate of Coiled Coil Driven Membrane Fusion. *Chem Comm* **2013**, *49* (35), 3649–3651.
17. Coorssen, J. R.; Rand, R. P. Effects of Cholesterol on the Structural Transitions Induced by Diacylglycerol in Phosphatidylcholine and Phosphatidylethanolamine Bilayer Systems. *Biochem Cell Biol* **1990**, *68* (1), 65–69.
18. Tenchov, B. G.; MacDonald, R. C.; Siegel, D. P. Cubic Phases in Phosphatidylcholine-Cholesterol Mixtures: Cholesterol as Membrane "Fusogen." *Biophys J* **2006**, *91* (7), 2508–2516.
19. Hernandez, J. M.; Stein, A.; Behrmann, E.; Riedel, D.; Cypionka, A.; Farsi, Z.; Walla, P. J.; Raunser, S.; Jahn, R. Membrane Fusion Intermediates via Directional and Full Assembly of the SNARE Complex. *Science (1979)* **2012**, *336* (6088), 1581–1584.
20. Schoenmaker, L.; Witzigmann, D.; Kulkarni, J. A.; Verbeke, R.; Kersten, G.; Jiskoot, W.; Crommelin, D. J. A. mRNA-Lipid Nanoparticle COVID-19 Vaccines: Structure and Stability. *Int J Pharm* **2021**, *601*, 120586.
21. Szabó, G. T.; Mahiny, A. J.; Vlatkovic, I. COVID-19 mRNA Vaccines: Platforms and Current Developments. *Mol Ther* **2022**, *30* (5), 1850–1868.

Appendix I

Protocol for *in situ* formation of gold nanoparticles in phase-separated liposomes

Herein, a protocol to achieve *in situ* formation of gold nanoparticles (AuNPs) inside the phase-separated PAP3 liposome core, is introduced. The protocol is adapted and modified from a previously described method.[1]

Materials

Tris(hydroxymethyl)aminomethane (Tris), Trisodium Citrate Dihydrate ($HOC(COONa)(CH_2COONa)_2 \cdot {}_2H_2O$), Gold(III) chloride trihydrate ($HAuCl_4 \cdot 3H_2O$) and 1,2-distearoyl-sn-glycero-3-phosphatidylcholine (DSPC) were purchased from Sigma Aldrich. DOaG was synthesized as described in Chapter 2 and in reference [2]. $HAuCl_4 \cdot 3H_2O$ was stored in a dark place.

Method

1. Tris buffer was prepared at 10 mM concentration and pH was adjusted to 7.4 with 1M HCl.
2. Using a volumetric flask (50 mL), an aqueous stock solution of 50.1 mM $HAuCl_4 \cdot 3H_2O$ was prepared immediately after opening the manufacturer's bottle (using all the content from the bottle). From this stock, a stock of 5 mM was prepared.
3. Using a volumetric flask (50 mL), an aqueous stock solution of 20.4 mM trisodium citrate dihydrate was prepared.
4. Individual lipids as stock solutions of DSPC and DOaG (10 mM) in chloroform, were combined in a glass vial to 1:1 molar ratio and dried to a thin film, first under N_2 stream, then >1 h under vacuum.
5. Lipid films were redissolved in 50 µL absolute ethanol with gentle vortexing if necessary, to a total lipid concentration of 50 mM.
6. Using the stock solutions prepared in steps 2 and 3 an queous solution of $HAuCl_4$: Sodium Citrate was prepared at a 1 : 4.08 ratio (Turkevich solution).[3] Two concentrations of $HAuCl_4$ have been successfully used: 1.75 mM or 2.5 mM. Turkevich solution is prepared fresh every time and is used immediately after preparation to ensure prevention of premature AuNP formation prior to liposome formation.
7. Using a (pre-heated) glass micro-syringe (Hamilton, syringe series 700, volume 50), 35.7 µL of the ethanolic lipid solution (warm after submersion in a water bath of 50 °C for 5 sec) was rapidly injected in a glass vial containing 2.5 mL of Turckevic solution (1:71 v/v; EtOH:Turkevich solution) submerged in a 50 °C water bath (freshly made and submerged only for ~2-3 min before injection), under constant vigorous stirring (650 rpm – stirring bar dimensions: 12 x 4 x 4 cm), to form large unilamellar vesicles.
8. Liposomal solution (2.5 mL) was immediately passed through a size exclusion chromatography column (Illustra™ NAP25, GE Healthcare, Thermofischer Scientific)

equilibrated with Tris buffer 10 mM pH = 7.4, to replace the unencapsulated Turkevic solution with buffer.

9. Liposomes encapsulating Turkevich solution in their core were then transferred in an eppendorf tube (1.5 mL) and placed in a thermomixer with a stable temperature at 75 ^{o}C for 10 min to ensure initiation of gold reduction from Au^{+3} to Au^{0} and subsequent nucleation and growth of AuNPs.
10. Liposomes containing formed AuNPs were transferred to a dialysis tube (Float-a-lyzer® G2, 1 mL capacity, 1000 kDa MWCO, Spectrum labs) and dialyzed against Tris buffer 10 mM pH = 7.4 overnight at 4 ^{o}C, to ensure complete removal of ethanol.
11. The hydrodynamic diameter and polydispersity index (PDI) of liposomes containing AuNPs were characterized by Dynamic Light Scattering (DLS) (Malvern Zetasizer Nano ZS). DLS measurements were carried out at room temperature in 10 mM Tris buffer (pH = 7.4) at a total lipid concentration of approx. 100 μM. Reported DLS measurements are the average of three measurements.
12. Liposomes containing AuNPs (3 μL) were applied to a freshly glow-discharged carbon 200 mesh Cu grid (Lacey carbon film, Electron Microscopy Sciences, Aurion, The Netherlands). Grids were blotted for 3 sec at 99% humidity in a Vitrobot plunge-freezer (FEI VitrobotTM Mark III, Thermo Fisher Scientific). Cryo-Transmission Electron Microscopy (cryo-TEM) images were collected on a Talos L120C (NeCEN, Leiden University) or a TITAN (Eindhoven University of Technology) operating respectively at 120 kV or 300kV. In the case of Talos, images were recorded manually at a nominal magnification of 17500x or 36000x yielding respectively a pixel size of 5.87 or 2.89 ångström (Å) at the specimen. In the case of TITAN, images were recorded manually at a nominal magnification of 24000x or 30000x yielding a pixel size of 3.87 or 2.81 ångström (Å) at the specimen, respectively.
13. Cryo-electron tomography (cryo-ET) was performed on a Talos L120C (NeCEN, Leiden University) operating at 120kV. Tomographic tilt series acquisition was performed with Tomo4 software from Thermo Fisher Scientific with a total electron dose of less than 100 e^{-}/nm^{2}. Alignment and reconstruction of the series were performed using IMOD.[4]
14. Liposomes containing AuNPs were concentrated up to 5 mM total lipid concentration (relevant for *in vivo* use) with a Vivaspin® 2 centrifugal concentrator (2 mL volume, 300k MWCO). Note: to prevent liposomes from aggregating, centrifugal forces were not used. Briefly, liposomes were transferred in the concentrator which was let in an upright position. Solvent was slowly removed by gravity and by occasional shaking.

Characterization

Size (nm)	PDI
157.7	0.301

Cryo-TEM images

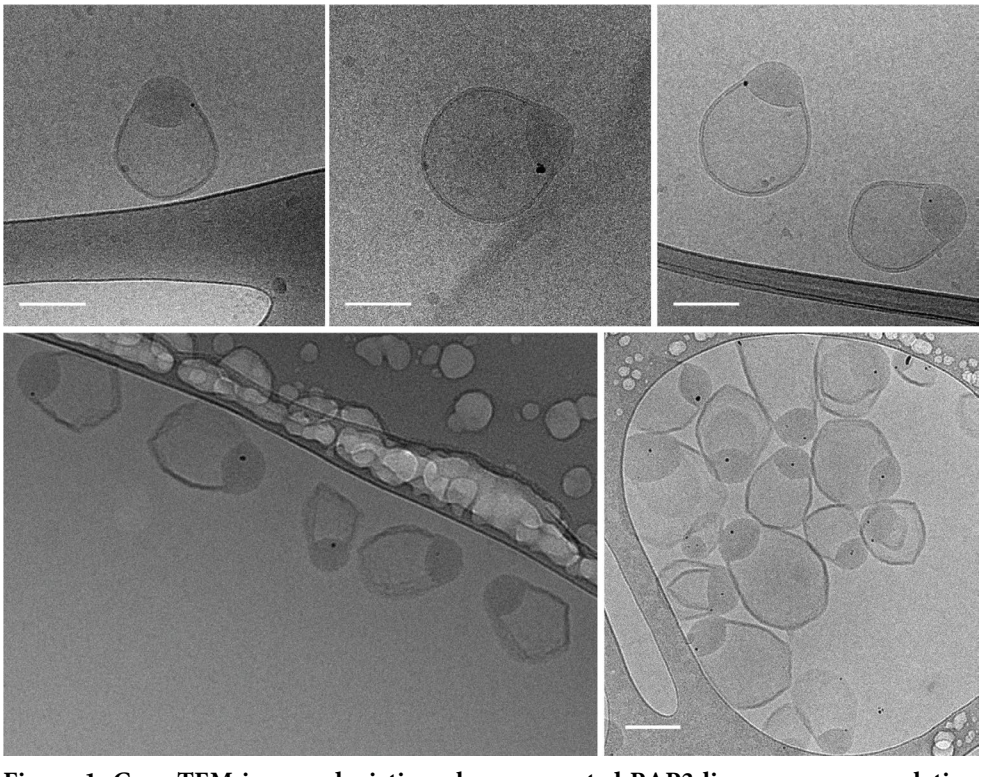

Figure 1: Cryo-TEM images depicting phase-separated PAP3 liposomes encapsulating AuNPs (black, electron dense dots) after *in situ* formation (Turkevich solution used: 1.75 mM $HAuCl_4$: 7.14 mM Sodium Citrate). Average AuNP size = 9.95 nm based on quantification (N = 103). Scale bars = 100 nm. Sample is free of unencapsulated AuNPs.

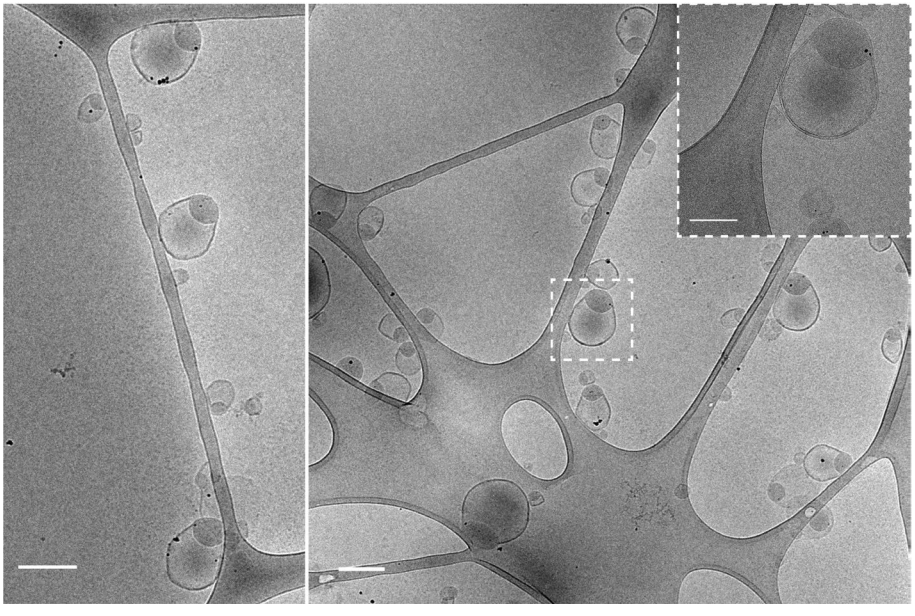

Figure 2: Cryo-TEM images depicting phase-separated PAP3 liposomes encapsulating AuNPs (black, electron dense dots) after *in situ* formation (Turkevich solution used: 2.5 mM $HAuCl_4$: 10.2 mM Sodium Citrate). Scale bars = 200 nm for low magnification images and 100 nm for insert. Sample is free of unencapsulated AuNPs.

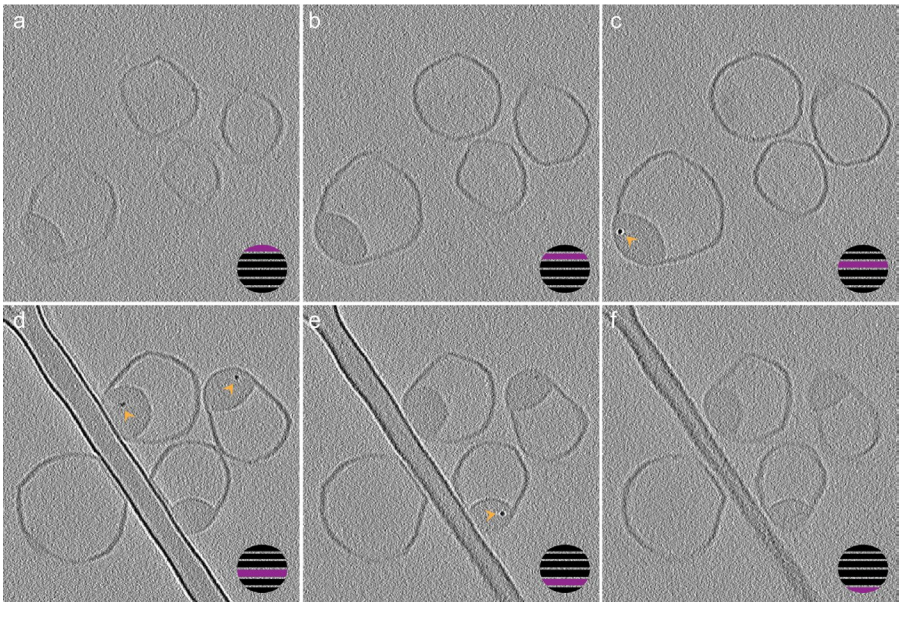

Figure 3. Cryo-electron tomography of PAP3 liposomes containing AuNPs. a-f) Representative slices of the tomogram showing AuNPs (orange arrows) reside in the inner

core of liposomes and show a preference for the liposome lipid droplet. Slice schematic (right bottom corner) shows which slice (in purple) corresponds to each image (a, f = top and bottom slices, b-e = middle slices). Turkevich solution used: 1.75 mM $HAuCl_4$: 7.14 mM Sodium Citrate.

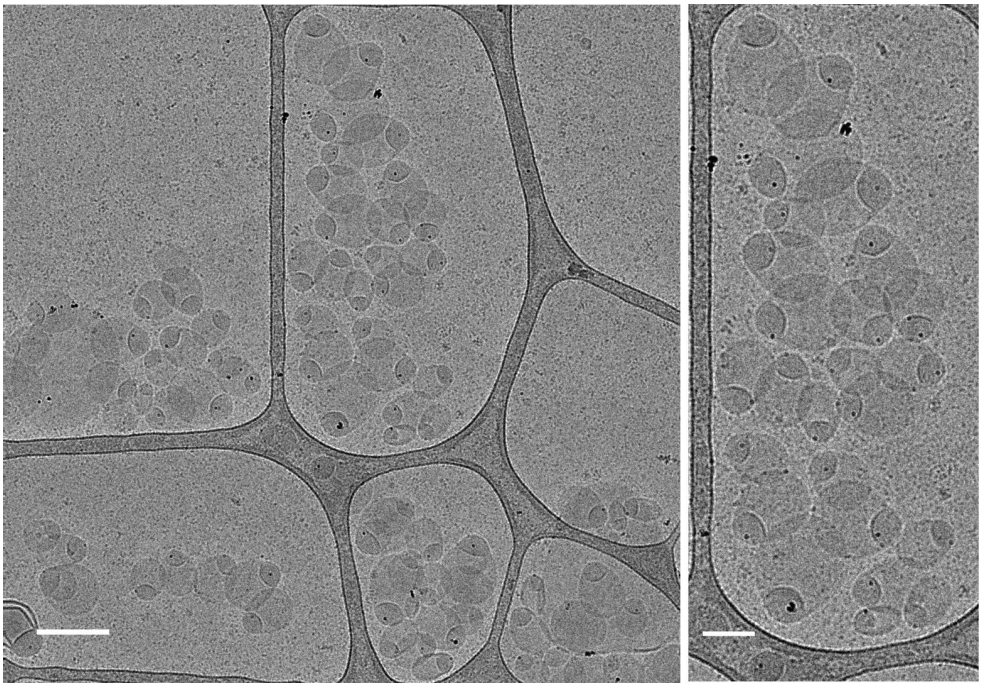

Figure 4. PAP3 liposomes containing AuNPs (black, electron dense dots) after incubation with human serum (1:1) for 10 min. Liposome morphology is preserved and AuNPs remain encapsulated (Turkevich solution used: 1.75 mM $HAuCl_4$: 7.14 mM Sodium Citrate). Average AuNP size = 9.62 nm based on quantification (N = 70). Scale bars = 200 nm for low magnification image and 100 nm for high magnification image.

References

1. Witzigmann, D.; Sieber, S.; Porta, F.; Grossen, P.; Bieri, A.; Strelnikova, N.; Pfohl, T.; Prescianotto-Baschong, C.; Huwyler, J. Formation of Lipid and Polymer Based Gold Nanohybrids Using a Nanoreactor Approach. *RSC Adv* **2015**, *5* (91), 74320–74328.
2. Arias-Alpizar, G.; Papadopoulou, P.; Rios, X.; Pulagam, K. R.; Moradi, M. A.; Pattipeiluhu, R.; Bussmann, J.; Sommerdijk, N.; Llop, J.; Kros, A.; Campbell, F. Phase-Separated Liposomes Hijack Endogenous Lipoprotein Transport and Metabolism Pathways to Target Subsets of Endothelial Cells In Vivo. *Adv Healthc Mater* **2023**, *12* (10), e2202709.
3. Turkevich, J.; Stevenson, P. C.; Hillier, J. A Study of the Nucleation and Growth Processes in the Synthesis of Colloidal Gold. *Discuss Faraday Soc* **1951**, *11*, 55–75.
4. Kremer, J. R.; Mastronarde, D. N.; McIntosh, J. R. Computer Visualization of Three-Dimensional Image Data Using IMOD. *J Struct Biol* **1996**, *116* (1), 71–76.

List of Abbreviations

apoAI apolipoprotein AI
apoCII apolipoprotein CII
ApoE apolipoprotein E
ASOs antisense oligonucleotides
Asp asparagine
ATTR transthyretin amyloidosis
BA basilar artery
BBB blood brain barrier
bECs brain endothelial cells
CE cholesteryl ester
CG coarse grained
CHO cholesterol
CHT caudal hematopoietic tissue
COM center of mass
CSF cerebrospinal fluid
CT computed tomography
CtA cerebral arteries
CV caudal vein
DAG diacylglycerol
DCM dichloromethane
DIPEA diisopropylethylamine
DLS dynamic light scattering
DLV dorsal longitudinal vein
DMAP dimethylaminopyridine
DMSO dimethylsulfoxide
DOaG dioleoylamidoglycerol
DODAP dioleoyldimethylammonium propane
DOE design of experiment
DOG dioleoylglycerol
DOPC dioleoylphosphatidylcholine
DOPS dioleoylphosphatidylserine
DOTMA dioctadecenyl-trimethylammonium propane
dpf days post fertilization
DSPC distearoylphosphatidylcholine
EL endothelial lipase
EMA European medicine agency
EPC phosphatidylcholine (egg)
EPG phosphatidylglycerol (egg)
EPR enhanced permeation-retention
ESI electron spray ionization
ET electron tomography
EV extracellular vesicle
FDA food and drug administration
FFA free fatty acid
FFT fast Fourier transform
GPIHBP1 lycosylphosphatidylinositol anchored high density lipoprotein binding protein 1
GUVs giant unilamellar vesicles
HDL high-density lipoprotein
H_{II} hexagonal phase
His histidine
HL hepatic lipase
hpi hours post injection
HRMS hight resolution mass spectrometry
HSPG heparan sulfate proteoglycans
ID injected dose
IV intravenous
KC Kupffer cells
L_d liquid disordered
LDL low-density lipoprotein
LDLr LDL receptor
LNP lipid nanoparticle

L_o	liquid ordered
LPL	lipoprotein lipase
LR	lissamine rhodamine
LSECs	liver sinusoidal endothelial cells
LUVs	large unilamellar vesicles
MCeV	middle cerebral vein
MD	molecular dynamics
MMCtA	mid.mesencephalic central artery
MPS	mononuclear phagocyte system
mRNA	messenger RNA
MS	mass spectrometry
MsA	mesencephalic artery
MsV	mesencephalic vein
NMR	nuclear magnetic resonance
NN	neural network
PBS	phosphate buffered saline
PC	phosphatidylcholine
PDI	polydispersity index
PEG	polyethylene glycol
PHBC	primordial hindbrain channel
PKC	protein kinase C
PMBC	primordial midbrain channel
PMF	potential mean force
POPC	palmitoyl-oleoyl-phosphocholine
RES	reticuloendothelial system
RNAi	RNA interference
rt	room temperature
SASA	solvent-accessible surface area
SEC	size exclusion chromatography
SECs	scavenging endothelial cells
Ser	serine
siRNA	small interfering RNA
SRB1	scavenger receptor B1
TEM	transmission electron microscopy
TG	triglyceride (or triacylglycerol)
TGL	triacylglycerol lipase
THF	tetrahydrofuran
TLC	thin layer chromatography
Trp	tryptophan
US	umbrella sampling
VLDL	very-low density lipoprotein
VLP	virus-like particle

Samenvatting

Nanomedicijnen gebaseerd op lipiden worden gebruikt als een geavanceerd systeem om medicatie gecontroleerd op de juiste locatie in het lichaam af te leveren. Desalniettemin is er nog veel onbekend hoe deze nanodeeltjes zich gedragen in een biologische omgeving en welke interacties van belang om translatie naar klinische toepassingen mogelijk te maken. Een beter begrip over hoe de samenstelling van nanodeeltjes de fysische eigenschappen beïnvloedt zoals bijvoorbeeld de morfologie en daarmee de interactie met de biologische omgeving kunnen helpen bij de ontwikkeling van efficiënte nanomedicijnen. In dit proefschrift werd de morfologie van lipide nanodeeltjes en de interactie met een biologische omgeving als functie van de lipide structuur onderzocht en dan met name van lipide nanodeeltjes met fase-scheiding. Deze unieke morfologie resulteerde in selectieve nanodeeltje-eiwit interacties en het gebruik maken van endogene biologische systemen voor cel-specifieke aflevering van medicatie *in vivo*. Dit proefschrift beschrijft een fundamentele studie over hoe de samenstelling van lipide deeltjes gebruikt kan worden om het gedrag *in vivo* te controleren, wat kan leiden tot de rationele ontwikkeling van effectieve nanomedicijnen.

Hoofdstuk 1 introduceert het onderzoeksveld van lipide gebaseerde nanomedicijnen. De invloed van lipide structuur op de fysicochemische eigenschappen, het ontwerpen van geoptimaliseerde nanodeeltjes voor medicijnafgifte en een historisch perspectief worden behandeld. De meest recente ontwikkelingen in het veld van nanomedicijnen en hoe een rationele wetenschappelijke benadering kan bijdragen tot nieuwe oplossingen wordt beschreven. Tenslotte wordt de motivatie van dit proefschrift toegelicht.

Hoofdstuk 2 van dit proefschrift beschrijft de ontdekking van de nieuwe liposomale formulering "PAP3", welke bestaat uit een mengsel van het natuurlijke lipide DSPC en het synthetische diacylglycerol (DAG) analoog, DOaG. Deze formulering bevat geen traditionele cel-specifieke peptiden of antilichamen om celspecificiteit te verkrijgen. PAP3-liposomen accumuleerde specifiek in brein endotheelcellen (bECs) van zebravis embryo's door gebruik te maken van endogene lipide transport- en metabolisme mechanismen, gemedieerd door het enzym triglyceride lipase (TGL). Analyse van deze liposomen met elektronen microscopie in bevroren staat

(Cryo-TEM) liet zien dat deze deeltjes een unieke fase-gescheiden morfologie hebben waarbij een DOaG rijke druppel zich bevindt in een bilaag van DSPC. Deze studie toonde aan dat deze morfologie verantwoordelijk was voor de selectieve *in vivo* accumulatie. Deze studies werden uitgevoerd in zebravis embryo's om in detail de specifieke opname van de nanodeeltjes te relateren aan de zogenaamde "nano-bio interface". Deze embryo's hebben een hoge metabolische vraag naar lipiden en daarom een hoge expressie van endotheel- en lipoproteïne lipase (EL en LPL), voornamelijk in de bloedvaten van het brein. In de aanwezigheid van de lipase inhibitor XEN445 werden de lipases geinhibiteerd resulterend in een verlies van celspecificiteit. Het voorgestelde mechanisme en de rol van TGL voor deze bevindingen werd bevestigd met additionele studies in muizen.

Hoofdstuk 3 werd het mechanisme van celspecificteit en de rol van TGL's en fasescheiding verder bestudeerd. Door gebruik te maken van een combinatie van cryo-TEM, massa spectrometrie, enzym analyse en moleculaire dynamische (MD) simulaties, werd aangetoond dat de morfologie van liposomen van verandert na interactie met lipases. Tevens werd aangetoond dat het gebruik van het lipide DOaG in deze liposomen resulteerde in membranen met zogenaamde lipide 'packing defects', dit zijn domeinen in het lipide membraan waarbij de afstand tussen fosfolipiden vergroot is wat leidt tot contact van water met de hydrofobe delen van het membraan in DOaG-rijke domeinen. Tevens werd aangetoond dat de zogenaamde "tryptophane-loop" in lipases verantwoordelijk is voor de binding aan de PAP3-liposomen. Hierdoor gedraagt het enzym zich als een sensor voor de genoemde "packing defects", waardoor TGL's voorkeur hebben om fase-gescheiden liposomen te binden wat de *in vivo* celspecificteit verklaart.

Hoofdstuk 4 beschrijft een uitvoerig onderzoek betreffende de moleculaire principes achter de fase-scheiding en selectieve binding aan bEC's *in vivo*, geïnduceerd door DOaG in liposomale membranen. Varianten van DOaG werden gesynthetiseerd waarna de structuur-functie relatie onderzocht werd. Met behulp van een combinatie van Cryo-TEM analyse van de nanodeeltjes en biodistributiestudies in zebravis embryo's werd duidelijk dat DOaG-analoga met medium-lengte onverzadigde koolstofketens (C16:1, C18:1) in combinatie met DSPC nodig waren om fase-scheiding te induceren, welke noodzakelijk was om liposomen te verkrijgen die selectieve binden aan bEC's in zebravissen. DOaG analoga met verzadigde koolstofketens vertoonden niet deze celspecificiteit. DOaG

analoga met lange koolstofketens (C20:1, C24:1) gemengd met DSPC bleken geen stabiele liposomen te vormen. Fasescheiding in liposomen werd waargenomen voor DOaG analoga/DSPC mengsels, maar dit resulteerde niet in selectieve bEC accumulatie. Het gebruik van alleen het sn-1,3 isomeer van DOaG verhoogde de stabiliteit van de PAP3 liposomen. De stabiliteit van liposomen werd ook verhoogd na pegylering of wanneer DOaG variant (C16:1) gemengd werd met DSPC en deze formuleringen konden ook gevormd worden in PBS met behoud van gemiddelde grootte en lage polydispersiteit.

De in hoofdstuk 2-4 beschreven fase-scheiding in DOaG/DSPC liposomen resulterend in bEC-selectiviteit is ook van interesse voor andere lipide-gebaseerde nanodeeltjes. **Hoofdstuk 5** laat de toepasbaarheid zien van DOaG in mRNA gebaseerde lipide nanodeeltjes (LNPs) en dient als 'proof-of-concept' voor de toepassing van DOaG in LNPs om zo celspecifieke mRNA-afgifte te verkrijgen. In deze studie werden vier mRNA-LNP formuleringen gemaakt en getest in zebravis embryo's. Fase-gescheiden mRNA-LNP's die DOaG bevatten, in combinatie met het ioniseerbare lipide DODAP, werden succesvol geformuleerd met een goede mRNA encapsulatie-efficientie. Deze formulering liet specifieke opname en expressie zien in de bECs van de zebravis embryo's.

Hoofdstuk 6 vat alle bevindingen van dit promotieonderzoek samen en geeft suggesties voor toekomstig onderzoek en toepassingen.

Appendix I beschrijft een gemodificeerd protocol voor de *in-situ* formatie en encapsulering van goud nanodeeltjes in fase-gescheiden DOaG-DSPC liposomen.

Περίληψη

Τα λιπιδικά νανοσωματίδια είναι κλινικά τα πιο προηγμένα συστήματα μεταφοράς φαρμάκων. Ωστόσο, η περιορισμένη κατανόηση των ιδιοτήτων αυτοδόμησης τους και των βασικών νανο-βιο-αλληλεπιδράσεων εμποδίζει την μετάφρασή τους κλινικά, η οποία βασίζεται κυρίως σε προσεγγίσεις δοκιμής-σφάλματος και εντατικούς εμπειρικούς ελέγχους. Επομένως, η εξέλιξη νανολιπιδικών στοχευμένων θεραπειών απαιτεί πληρέστερη κατανόηση του τρόπου με τον οποίο η λιπιδική σύσταση καθορίζει τη μορφολογία και οδηγεί σε (επιθυμητές) νανο-βιο-αλληλεπιδράσεις. Στην παρούσα διδακτορική διατριβή, η χημεία των λιπιδίων, η σύσταση και η νανοσωματιδιακή μορφολογία, συσχετίζονται για να παρέχουν μια ολοκληρωμένη εικόνα καινοτόμων λιπιδικών νανοσωματιδίων διαχωρισμένης φάσης, με εξειδικευμένη συμπεριφορά στη νανο-βιο διεπαφή. Η εξιδεικευμένη αυτή συμπεριφορά χαρακτηρίζεται απο την εκλεκτική αλληλεπίδραση νανοσωματίδιων-πρωτεϊνών και τη προσπέλαση ενδογενών βιολογικών μηχανισμών για κυτταρική εξειδίκευση *in vivo*. Οι πληροφορίες που παρέχονται σε αυτή τη διατριβή διευρύνουν τις τρέχουσες, θεμελιώδεις γνώσεις σχετικά με την αυτοδόμηση λιπιδικών νανοσωματιδίων και την *in vivo* συμπεριφορά τους, θέτοντας τις βάσεις για τον ορθολογικά βελτιστοποιημένο σχεδιασμό τους.

Στο **Κεφάλαιο 1** παρουσιάζεται ο τομέας της νανοϊατρικής βασιζόμενος σε λιπιδικά νανοσωματίδια, εξηγώντας τις μοριακές αρχές των λιπιδίων, τα φυσικοχημικά χαρακτηριστικά τους, την αρχιτεκτονική των λιπιδικών νανοσωματιδίων, ενώ αναφέρεται και η ιστορική ανάδρομή της εξέλιξης τους. Επιπλέον, συζητούνται ενδελεχώς οι πρόσφατες εξελίξεις στη στοχευμένη μεταφορά φαρμάκων στο τομέα αυτό, μαζί με τις υπάρχουσες προκλήσεις, και παρουσιάζονται διάφορες επιστημονικές προσεγγίσεις για την αντιμετώπισή τους. Τέλος, παρουσιάζονται οι βλέψεις και το κίνητρο της παρούσας διδακτορικής διατριβής.

Στο **Κεφάλαιο 2** της διατριβής, περιγράφεται η ανακάλυψη ενός καινοτόμου είδους λιποσωμάτων (αναφερόμενα ως PAP3), που αποτελείται από δύο μόνο λιπίδια - το φυσικό φωσφολιπίδιο DSPC και το συνθετικό ανάλογο διακυλογλυκερόλης (DAG) DOaG - χωρίς τη χρήση κοινώς χρησιμοποιούμενων παραγόντων στόχευσης, π.χ. αντισώματα ή πεπτίδια. Το λιπόσωμα αυτό είναι ικανό να συσσωρεύεται επιλεκτικά στα ενδοθηλιακά κύτταρα του εγκεφάλου εμβρύων ζεβρόψαρων, προελαύνοντας ένα μονοπάτι μεταφοράς λιπιδίων και λιπιδικού μεταβολισμού, με τη μεσολάβηση της τριγλυκεριδικής λιπάσης (TGL). Η απεικόνιση με κρυοηλεκτρονική

μικροσκοπία διέλευσης (cryo-TEM) αποκάλυψε μια νέα μορφολογία λιποσωμάτων που χαρακτηρίζεται από διαχωρισμό φάσης λιπιδίων, παρουσία ενός λιπιδικού σταγονιδίου πλούσιου σε DOaG εντός της διπλοστιβάδας DSPC, το οποίο βρέθηκε ότι είναι υπεύθυνο για την επιλεκτική στόχευση. Τα έμβρυα ζεβρόψαρα χρησιμοποιήθηκαν ως το πρωτογενές μοντέλο *in vivo* για την αποσαφήνιση του βιολογικού μηχανισμού που υποστηρίζει τη επιλεκτική νανοσωματιδιακή στόχευση εγκεφαλικών ενδοθηλιακών κυττάρων. Σε αυτό το αναπτυξιακό στάδιο, τα έμβρυα ζεβρόψαρα έχουν υψηλές απαιτήσεις σε λιπίδια και ως εκ τούτου οι ενζυμικές λιπάσες, όπως η ενδοθηλιακή (EL) και η λιποπρωτεϊνική λιπάση (LPL), έχουν έντονη παρουσία στην περιοχή του κεφαλιού των ζεβρόψαρων. Πράγματι, παρουσία ενός μικρού μορίου αναστολέα λιπάσης (XEN445), η στόχευση των λιποσωμάτων στα ενδοθηλιακά κύτταρα αποτράπηκε. Ομοίως, όταν ποντίκια χρησιμοποιήθηκαν ως μοντέλο *in vivo* μελέτης, η συμμετοχή της TGL στην πρόσληψη βρέθηκε επίσης ότι συντηρείται (μερικώς), παρόλαυτα σε διαφορετικό ιστό (ήπαρ).

Στο **Κεφάλαιο 3** περιγράφεται μια εις βάθος μηχανιστική κατανόηση των μεταβολλών σύστασης και μορφολογίας που υφίστανται τα διαχωρισμένα σε φάση λιποσώματα παρουσία TGL. Συνδυάζοντας διαφορετικές τεχνικές π.χ., cryo-TEM, φασματομετρία μάζας (LC-MS/MS), ενζυματική ανάλυση και προσομοιώσεις μοριακής δυναμικής (MD), αποκαλύφθηκε ότι τα λιποσώματα υφίστανται αναδιαμόρφωση μετά από αλληλεπίδραση λιποσώματος-λιπάσης. Επίσης, ο διαχωρισμός φάσης λόγω DOaG, βρέθηκε ότι έχει ως αποτέλεσμα μεμβράνες με ελαττώματα στο πακετάρισμα των λιπιδίων τους - περιοχές όπου η απόσταση των παρακείμενων φωσφολιπιδίων είναι αυξημένη - εκθέτοντας υδρόφοβα τμήματα πλούσια σε DOaG στο υδατικό περιβάλλον. Αυτά τα ελαττώματα διευκολύνουν τη σύνδεση της TGL στην επιφάνεια του λιποσώματος με αποτέλεσμα την υδρόλυση του DOaG. Αποδείχθηκε επίσης οτι η φυσική περιοχή δέσμευσης λιποπρωτεΐνών του ενζύμου – που είναι πλούσια σε τρυπτοφάνες - δρα ως αισθητήρας αυτών των ελλατωμάτων, υπονοώντας ότι η TGL δεσμεύεται κατά προτίμηση σε μεμβράνες διαχωρισμένης φάσης, σε σύγκριση με επίπεδες λιπιδικές μεμβράνες.

Στο **Κεφάλαιο 4** περιγράφεται μια εμπεριστατωμένη διερεύνηση των υποκείμενων μοριακών αρχών που υποστηρίζουν τον διαχωρισμό φάσης και την επιλεκτική *in vivo* στόχευση, όπως αυτά προκύπτουν από το DOaG σε λιποσωμιακές μεμβράνες. Μια βιβλιοθήκη μοριακών αναλόγων DOaG με ποικίλες μοριακές ιδιότητες συντέθηκε και διερευνήθηκε η σχέση μοριακής δομής-λειτουργίας. Οι μελέτες cryo-

TEM και βιοκατανομής σε έμβρυα ζεβρόψαρα αποκάλυψαν ότι μεσαίου μεγέθους (C16:1, C18:1), μη κορεσμένες λιπιδικές αλυσίδες ήταν απαραίτητες για να προκληθεί διαχωρισμός φάσης στα λιποσώματα - όταν τα ανάλογα DOaG συνδυαζόταν με DSPC - και να επιτευχθεί επιλεκτική *in vivo* στόχευση. Αντίθετα, πλήρως κορεσμένα μοριακά ανάλογα DOaG δεν σχημάτισαν λιποσώματα. Ανάλογα που περιείχαν τις (μακριές) ακυλικές αλυσίδες C20:1 ή C24:1, αναμεμειγμένα με DSPC, σχημάτισαν λιποσώματα αν και με υψηλή αστάθεια, ή δεν σχημάτισαν καθόλου λιποσώματα, αντίστοιχα. Παραδόξως, το ανάλογο με μικρή ακυλική αλυσίδα (C14:1) προκάλεσε διαχωρισμό φάσης στις μεμβράνες DSPC, αλλά τα ανακύπτοντα λιποσώματα δεν στόχευαν τα εγκεφαλικά ενδοθηλιακά κύτταρα. Επίσης, αξιολογώντας την επίδραση των μιγμάτων *sn*-ισομερών του DOaG ως προς τη σταθερότητα των λιποσωμάτων, βρέθηκε ότι το DoaG που παρουσιάζεται στο καθαρό ισομερές *sn*-1,3, βελτιώνει τη μακροπρόθεσμη σταθερότητα των λιποσωμάτων PAP3. Επιπλέον, η πεγκυλίωση και η αναντιστοιχία μήκους ακυλικής αλυσίδας μεταξύ DSPC (C18:0) και αναλόγου DOaG (C16:1) βελτίωσαν τη σταθερότητα και την ικανότητα αυτοδόμησης των λιποσωμάτων σε PBS με αποδεκτές τιμές PDI και μεγέθους.

Το Κεφάλαιο 2-4 αναδεικνύει ότι ο διαχωρισμός φάσης που προκαλείται από τα DOaG λιπίδια είναι μια νέα, λειτουργική μέθοδος στόχευσης *in vivo*, η οποία μπορεί να είναι ενδιαφέρουσα και για άλλα συστήματα λιπιδικών νανοσωματιδίων. Στο **Κεφάλαιο 5** παρουσιάζεται η δυνατότητα εφαρμογής του λιπιδίου DOaG σε συνθέσεις λιπιδικών νανοσωματιδίων που ενθυλακώνουν mRNA (mRNA-LNP) και χρησιμεύει ως απόδειξη της ιδέας για τη χρήση του DOaG σε LNP για την επίτευξη εξειδικευμένης στόχευσης κυττάρων και μεταφοράς mRNA. Σε αυτή τη μελέτη, δημιουργήθηκαν τέσσερα σκευάσματα mRNA-LNP και αξιολογήθηκε η *in vivo* συμπεριφορά τους σε έμβρυα ζεβρόψαρα. Ένα διαχωρισμένης φάσης mRNA-LNP που περιείχε DOaG, σε συνδυασμό με το ιονιζόμενο λιπίδιο DODAP, διαμορφώθηκε επιτυχώς ενθυλακώνοντας επαρκή ποσότητα mRNA. Αυτό το σκεύασμα βρέθηκε να στοχεύει και να συσσωρεύεται εκλεκτικά στα εγκεφαλικά ενδοθηλιακά κύτταρα εμβρύων ζεβρόψαρων, με αποτέλεσμα την μεταφορά mRNA και την έκφραση πρωτεΐνης.

Το **Κεφάλαιο 6** περιλαμβάνει τη σύνοψη όλων των κύριων ευρημάτων που προέκυψαν κατά τη διάρκεια αυτής της έρευνας και υπογραμμίζει τη σημασία τους για μελλοντικές μελέτες και εφαρμογές.

List of publications

1. Arias-Alpizar, G.[#]; **Papadopoulou, P.[#]**; Rios, X.; Reddy Pulagam, K.; Moradi, M.-A.; Pattipeiluhu, R.; Bussmann, J.; Sommerdijk, N.; Llop, J.; Kros, A.; Campbell, F. Phase-separated liposomes hijack endogenous lipoprotein transport and metabolism pathways to target subsets of endothelial cells *in vivo*. *Advanced Healthcare Materials* **2022**, *12* (10), 2202709.

2. **Papadopoulou, P.[#]**; van der Pol. R.[#]; van Hilten, N.[#]; Moradi, M.A.; Ferraz, M.J.; Aerts, J.M.F.G.; Sommerdijk, N.; Risselada, H.J.; Sevink, G.J.A.; Kros, A. Lipase-mediated selective hydrolysis of lipid droplets in phase-separated liposomes. *ChemRxiv* **2023**, DOI: 10.26434/chemrxiv-2023-9q9wh-v3. **In revision with Advanced Materials**

3. **Papadopoulou, P.[#]**; Arias-Alpizar, G.[#]; Weeda, P; Poppe, T.; van Klaveren, N.; Slíva, T.; Aschmann, D.; van Os, W.L.; Zhang, Y.; Moradi, M.A.; Sommerdijk, N.; Campbell, F.; Kros, A. Structure-function relationship of phase-separated liposomes containing diacylglycerol analogues. **Ready for submission**

4. Escalona Rayo, O.[#]; **Papadopoulou, P.[#];** Slutter, B.; Kros, A. Biological recognition of RNA-lipid nanoparticles. *Current Opinion in Biotechnology* **2023**.

5. Zhou, X.; Wang, P.; Ramu, V.; Zhang, L.; Jiang, S.; Li, X.; Abyar, S.; **Papadopoulou, P.**; Shao, Y.; Bretin, L.; Siegler, M.A.; Buda, F.; Kros, A.; Fan, J.; Peng, X.; Sun, W.; Bonnet, S.; *In vivo* metallophilic self-assembly of a light-activated anticancer drug. *Nature Chemistry* **2023**, *15*, 980–987.

6. Zeng, Y.; Senti, M. E.; Labonia, M.C.I.; **Papadopoulou, P.**; Brans, M.A.D; Dokter, I.; Fens, M.H.; van Mil, A.; Sluijter, J.P.G.; Schiffelers, R.; Vader, P.; Kros, A. Fusogenic coiled-coil peptides enhance lipid nanoparticle-mediated mRNA delivery upon intramyocardial administration. **In revision with ACS Nano**

7. Xie, Y.; **Papadopoulou, P.**; Wit, B. de; D'Engelbronner, J.C.; Hage, P. van.; Kros, A.; Schaaf, M.J.M. Two types of liposomal formulations improve the therapeutic ratio of prednisolone phosphate in a zebrafish model for inflammation. *Cells* **2022**, *11*(4), 671.

8. Zhou, X.Q.; Mytiliniou, M.; Hilgendorf, J.; Zeng, Y.; **Papadopoulou, P.**; Shao, Y.; Dominguez, M.P.; Zhang, L.; Hesselberth, M.B.S.; Bos, E.; Siegler, M.A.; Buda, F.; Brouwer, A.M.; Kros, A.; Koning, R.I.; Heinrich, D.; Bonnet, S. Intracellular dynamic assembly of deep-red emitting supramolecular nanostructures based on the Pt…Pt metallophilic interaction. *Advanced materials* **2021**, *33*(37), 2008613.

9. Arias-Alpizar, G.[#]; Kong, L.[#]; Vlieg, R.C.; Rabe, A.; **Papadopoulou, P.**; Meijer, M.S.; Bonnet, S.; Vogel, S.; van Noort, J.; Kros, A.; Campbell, F; Light-triggered switching of liposome surface charge directs delivery of membrane impermeable payloads in vivo, *Nature Communications* **2020**, *11*, 3638.

10. Zhou X.Q.; Xiao M.; Ramu V.; Hilgendorf J.; Li X. Z.; **Papadopoulou, P.**; Siegler, M.A.; Kros, A.; Sun, W; Bonnet, S. The self-assembly of a cyclometalated palladium photosensitizer into protein-stabilized nanorods triggers drug uptake *in vitro* and *in vivo*. *Journal of the American Chemical Society* **2020**, *142*(23): 10383-10399.

11. Bąk, K.M.; van Kolck, B.; Maslowska-Jarzyna, K.; **Papadopoulou, P.**; Kros, A.; Chmielewski, M.J.; Oxyanion transport across lipid bilayers: direct measurements in large and giant unilamellar vesicles. *Chemical Communications* **2020**, *56*(36): 4910-4913.

#These authors contributed equally

Conferences and Symposia

NanoBio conference 2023, Heraklion Greece (oral presentation)
LACDR spring symposium 2023, Leiden University (invited oral presentation)
ICMS meeting 2023, Eindhoven Institute of Technology (poster presentation)
CHAINS 2022, Veldhoven the Netherlands (oral presentation)
TIDES 2022, Vienna Austria (poster presentation)
CHAINS 2019, Veldhoven the Netherlands (poster presentation)
NanoBioMed 2019, Barcelona Spain (poster presentation)
Figon Dutch Medicine Days 2018, Twente the Netherlands (poster presentation)

Biography

Panagiota Papadopoulou obtained her B.Sc. in Chemistry in 2014 from the National Kapodistrian University of Athens, Greece. Her diploma thesis, titled "Qualitative Determination of Azo-Dyes in Vegetable Oil by LC-MS/MS" was conducted at the department of Analytical Chemistry, in the lab of Prof. dr. Nikolaos Thomaidis.
In parallel with her bachelor's studies, she gained work experience as a QC laboratory assistant at the BIOCHALKO group of companies in 2012 for 9 months, and worked as an external intern at the National Center for Scientific Research (NCSR) "Demokritos" at the Institute of Nanoscience and Nanotechnology in 2014 for 8 months. As a QC assistant, Panagiota gained experience on the chemical analysis of industrial waste and ISO accreditation processes. In NCSR, she gained experience on the application of nanotechnology in the field of renewable energy.
In 2017, she received her M.Sc. degree in Life Science and Technology with specialization in Research and Development from the Leiden Institute of Chemistry at Leiden University, the Netherlands. She finalized her M.Sc. diploma thesis with the title "Development of Liposomes for Targeting the Blood-Brain Barrier *in vivo*." During her M.Sc. studies, she also worked as a laboratory assistant at the university for 2 months.
In the same year (2017), she began her Ph.D. journey at the Supramolecular and Biomaterials Chemistry group at Leiden Institute of Chemistry, after receiving the 2017 Leiden/Huygens Fellowship prize. Her Ph.D. supervisors were Prof.dr. Alexander Kros and Prof.dr.ir. John van Noort. During her Ph.D., she focused on the investigation of the physicochemical properties of lipid-based nanoparticles and their influence on nanoparticle behavior. Specifically, her research aimed to understand nanoparticle - protein interactions *in vivo* and *in vitro*, and how lipid phase separation can result in cell selectivity. For her observations, Panagiota incorporated various chemical and biological methods and utilized characterization techniques such as cryo-electron microscopy, for which she received certified training from the Eindhoven Institute of Technology (TUE) and the Netherlands Center of Electron Nanoscopy (NeCEN). Since 2022, Panagiota is working as a post-doctoral researcher at the same department in Leiden University, collaborating closely with Liposoma Ltd. and the Netherlands Cancer Institute (NKI).

"We are all time travelers, journeying together into the future. Let us work together to make that future a place we want to visit. Be brave, be determined, overcome the odds. It can be done."

Stephen Hawkin, 2018